Investigation of the Thermal Decomposition Mechanism and Kinetics of Molecules Relevant to Chemical Vapor Deposition in a Microreactor Using VUV i^{2}PEPICO

Von der Fakultät für Ingenieurwissenschaften, Abteilung Maschinenbau und Verfahrenstechnik der

Universität Duisburg-Essen

zur Erlangung des akademischen Grades

eines

Doktors der Ingenieurwissenschaften

Dr.-Ing.

genehmigte Dissertation

von

Sebastian Grimm
aus
Essen

Gutachter Univ.-Prof. Dr. rer. nat. Burak Atakan
Univ.-Prof. Dr. rer. nat. Tina Kasper

Tag der mündlichen Prüfung: 23.06.2023

Dedication

This thesis work is dedicated to my wife, Sarah, who has been a constant source of support and encouragement during the challenges of graduate school and life. I am truly thankful for having you in my life. I also dedicate this work to the one who made me a dad, my son Jakob. Finally, I also dedicate my dissertation to my parents, Heiko and Cornelia Grimm, who have always loved me unconditionally and whose good examples have taught me to work hard for the things that I aspire to achieve. And last but not least I want to present a funny prayer, which ironically reflects some of my feelings during the almost five years of work which I spent on a cross-disciplinary topic between engineering, chemistry and physics:

The Reactor Prayer
Our reactor,
who art in my lab,
leak-free be thy piping,
thy heater may work,
thy thermocouples may not shift,
thy computer may not freeze,
thy wall may not break,
during experiments, as it should work in theory.
Give us this day our daily result, and help us quickly fix the problems,
as the problems will inevitably come against us.
Lead us not into insanity, but prevent us from equipment failure, for thine is the hope,
the promise of graduation.
Forever and ever (or until my defense)
Amen

Acknowledgements

The work for this thesis is the product of my work as a research assistant in the “Thermodynamik“ department at the University of Duisburg-Essen starting in July 2018. It was performed within the framework of the first period of the project “Gasphasenkinetik von CVD-Vorläufern“, funded by the German Research Foundation (DFG). The outcome benefited a lot from those research grants and especially the measurement campaigns in Switzerland would not have been possible without the financial support by the DFG.

I want to use the following lines to thank all the people who were involved and helped me within the almost five years working on an insightful and fascinating topic. I gratefully acknowledge my supervisor Prof. Dr. Burak Atakan, whose door was always open for discussions on scientific questions, but also on topics dealing with everyday life, such as house prices. Although the first year and especially the corona pandemic was quite challenging for the project, he never lost faith and supported me and my work with valuable suggestions and discussions. I am particularly grateful that he allowed me to work on a topic rooted in materials science, despite my background in mechanical engineering. This has pushed my knowledge to a broader and higher level, while becoming acquainted with fields such as physical chemistry. This process was always insightful and rewarding. I would like to thank him for giving me the opportunity to present my research at many interesting conferences and network with inspiring researchers around the globe. I would like to thank Prof. Dr. Tina Kasper not only for agreeing to be my second examiner, but also for the constant scientific exchange and support during various campaigns at the Swiss Light Source. Tina, in particular, I would like to thank you for your efforts in working on our joint publications. Without your support the present thesis in this form would have not been possible.

I am grateful to my project collaborator Dr. Seung-Jin Baik who provided me with numerical data on the characterization of the microreactors flow field. I am looking forward to continue with our valuable cooperation in the second phase of the project and having many Korean tees together while we rack our brains finding the link between simulation and experiment. I further thank Prof. Dr. Andreas Kempf for his excellent cooperation within the framework of this project.

I gratefully acknowledge Dr. Patrick Hemberger and Dr. Andras Bodi for their help and advice, as well as for always providing perfect conditions at the Swiss Light Source (SLS). Both of you proved great flexibility when we were facing the challenges of COVID and ran a remote experiment on a synchrotron lightsource

together. Patrick, I especially thank you for the weekends you came to the beamline to refill the precursor and for your very quick response times on urgent topics. It was always a pleasure to meet you in Switzerland and discuss scientific but also child-related topics.

I would also like to thank my former office mate Dr. Sascha Lau for the funny moments in our office, such as when a bird hit our window on the fourth floor and creeped the hell out of us ;-), but also for fruitful scientific exchange. Thanks are also due to the technical staff Andreas Görnt and Stephan Steinbrink who did not only keep the coffee machine running but also constantly supported me in all IT-related and technical problems. Thank you, Andreas, for ordering chemicals as fast as light speed, even if the availability was unclear, and thank you, Stephan, for discussions on the precision of our Garmin watches and running in general, but also for constantly supporting me in building the experimental setups. I would like to additionally thank Dr. Ulf Bergmann for his advice. Discussing the teaching concept was always fun. Thank you Lisa Meiers for helping me out with administrative work. Special thanks goes to Dr. Dennis Kaczmarek and Dr. Thomas Bierkandt with whom the measurement campaigns, while eating a lot of chicken tikka masala, would have been as half as successful and fruitful. I would also like to thank all the colleges at the thermodynamics department for the badminton and swimming sessions as well as many coffee rounds in the "Mikroskopie-Labor".

I especially thank Asst. Prof. Dr. Alexander Heinlein, Louisa Laudien, Dr. Arno Knieschewski, Dr. Patrick Hemberger and Dominik Freund for proofreading parts of the thesis. Alexander, not only being my best man, but also helping me out in any part of my life starting from being competitive during our joint time in the swim club, as well as being a role model for my academic carreer. Spending numerous carnival sessions with you have contributed to making you one of the most valuable things in life, a very good friend. Louisa, being a outstanding teacher in English, this thesis would have only been as half as good linguistically as it is in its final version, thank you! Finally I would like to thank my family and friends. Thank you for everything. I want to highlight my beloved wife Sarah who also supported me, even when I was in doubt to reach my final goal. She never lost faith in me and cleared every possible minute, especially after our son was born, which made it possible to finish this work on time. The last word goes for Jakob, my little boy, whose birth, besides the published papers ;-), represents my first lasting action in this world. I hope that someday you will be as proud of your dad, for reaching his goal, as he is of you every second.

Abstract

For the majority of innovations, the tailored synthesis of functional materials is essential, making thin film deposition techniques like chemical vapor deposition (CVD) important for a sustainable future. Investigating the manufacturing characteristics of the CVD method used to create thin films is crucial since precise control and modeling of the process is important for its long-term viability.

Thin film deposition often has its origin in a gas-phase decomposition of the precursor and any reactants involved, forming the "true" precursors responsible for film growth. A major obstacle in the characterization of these deposition processes is the difficulty to detect highly complex initial reactive intermediates and primary pyrolysis products with lifetimes of a few hundreds of microseconds. The goal of this thesis was the fundamental understanding of the gas-phase chemistry and kinetics upon thermal decomposition of three metal-organic precursors, $Al(C_5H_7O_2)_3$, $Zr(C_5H_7O_2)_4$ and $Fe(C_5H_5)_2$, which are commonly used in the synthesis of thin metal oxide films and functional nanomaterials. This includes the identification and characterization of reactive intermediates that are generated upon the thermal decomposition of these metal-organic complexes. In each experiment, the precursor was pyrolytically decomposed in a resistively heated silicon-carbide (SiC) microreactor up to a temperature of 1500 K. The gaseous sample leaving the SiC microreactor was subsequently analyzed by vacuum ultraviolet double imaging photoelectron photoion coincindence spectroscopy (VUV-i^{2}PEPICO). Given the capabilities of i^{2}PEPICO coupled to a tunable synchrotron lightsource providing VUV photons, intermediates, such as radicals, but also metal-containing species were successfully assigned based on their ionization thresholds (PIE) and molecular fingerprints (ms-TPES). Temperature-dependent species profiles were derived which give hints on the underlying chemistry.

In the case of the metal β-diketonate precursors, the results show that the precursor is decomposed at lower temperatures below 600 K mainly due to surface reactions with the wall. This primary decomposition channel affords the formation of $Al(OH)_2(C_5H_7O_2)$ or $Zr(OH)_2(C_5H_7O_2)_2$ together with $C_{10}H_{12}O_2$. The analysis of the dataset at temperatures above 600 K hints on a change in the mechanism, where the gas-phase decomposition of $Al(C_5H_7O_2)_3$ and $Zr(C_5H_7O_2)_4$ becomes dominant. In the case of $Al(C_5H_7O_2)_3$ the major reaction pathway was rationalized where the precursor decomposes in the gas-phase forming $Al(C_5H_7O_2)(C_5H_6O_2)$ and acetylacetone ($C_5H_8O_2$) at temperatures above 600 K in inert atmosphere. Kinetic parameters were determined and are in good agreement with literature

values at similar conditions. It is demonstrated that the thermal decomposition of $Al(acac)_3$ follows first-order kinetics in the gas-phase with an activation energy of $57 \pm 4\,kJ\,mol^{-1}$ and a reasonable pre-exponential factor.

In the second reaction system, using $Zr(C_5H_7O_2)_4$, six important Zr-intermediates such as $Zr(C_5H_7O_2)_2(C_5H_6O_2)$ were assigned for the first time and a complete gas-phase reaction scheme in the temperature range from 400 to 900 K is presented. First, in a primary decomposition step $Zr(C_5H_7O_2)_2(C_5H_6O_2)$ is formed. Based on this the mechanism proceeds in a parallel and consecutive manner which finally forms $ZrO(C_5H_6O_2)$, the final intermediate before subsequent surface reactions lead to film growth at temperatures higher than 850 K. Additionally, adiabatic ionization thresholds of the Zr-intermediates were determined which can be used to identify metal-containing reactive intermediates in CVD processes using zirconium precursors. For both precursors, several hydrocarbons and oxygenated by-products such as *m/z* 100 acetylacetone, *m/z* 82 acetylallene and *m/z* 58 acetone were characterized and reaction pathways were rationalized.

In a third experiment, the thermal decomposition behavior of the ferrocene ($Fe(Cp)_2$) was investigated in inert and reductive atmosphere. The reaction mechanism is a two-step process. The initial decomposition takes place at temperatures below 900 K. Here, cyclopentadienyl radicals and cyclopentadiene are released to the gas-phase, but no iron containing intermediate was found in the gas-phase. This is most likely because the iron-containing intermediate is adsorbed on the surface. At higher temperatures a rapid decomposition of $Fe(Cp)_2$ in the gas-phase and the formation of atomic iron was observed. The addition of 10% hydrogen significantly changes the reaction mechanism. First, the addition of hydrogen adds up to the hydrogen pool on the surface. This in turn enhances the reaction of the cyclopentadienyl radicals with hydrogen on the surface forming cyclopentadiene in excess. Second, catalytic H-losses lead to a rupture of the ligand and a high carbon content on the surface which was rationalized by a black residue on the surface, as well as the formation of C_5H_x hydrocarbons that were released to the gas-phase. The activation energy for these reaction steps was determined and aligns well with previously published literature values using alternative reactor models and detection techniques.

The results of this thesis show that by combing experimental data with numerical simulations of the flow field, one can elaborate on the thermal decomposition pathways of CVD precursors, when the lifetime of the intermediates is on the order of microseconds. The data provided can be used to identify reactive molecules in CVD reaction systems and model the process. Modeling the process helps to improve the understanding of reaction mechanisms in CVD reactors and decrease possible impurities or parasitic side reactions which in turn are detrimental for the film growth rate.

Zusammenfassung

Im Rahmen der meisten technischen Innovationen hin zu einer nachhaltigeren Zukunft werden funktionelle Materialien eingesetzt. Zur Synthese dieser Materialien werden häufig Dünnschichttechnologien, wie exemplarisch die chemische Gasphasenabscheidung (CVD) genutzt. Um ein CVD-Verfahren zu modellieren, zu skalieren und funktionelle Materialien mit den gewünschten Eigenschaften zu erzeugen ist ein grundlegendes Verständnis der beteiligten chemischen Prozesse von großer Bedeutung.

Häufig ist die Zersetzung des Vorläufers in der Gasphase der erste Schritt des Abscheideprozesses. Die Charakterisierung der anfänglichen Reaktionsprozesse in der Gasphase gestaltet sich jedoch aufgrund der hohen Reaktivität und damit kurzen Lebensdauer der primären Pyrolyseprodukte schwierig. Das primäre Ziel dieser Arbeit war daher die Untersuchung und das grundlegende Verständnis der Gasphasenchemie und -kinetik der thermischen Zersetzung dreier metallorganischer Vorläufer, $Al(C_5H_7O_2)_3$, $Zr(C_5H_7O_2)_4$ und $Fe(C_5H_5)_2$, die üblicherweise bei der Synthese von dünnen Metalloxid-Filmen und funktionellen Nanomaterialien verwendet werden. Dies beeinhaltet die Identifizierung und Charakterisierung reaktiver Zwischenprodukte, die bei der thermischen Zersetzung dieser metallorganischen Komplexe entstehen. Die Vorläufer wurden dazu zunächst in einem widerstandsbeheizten Siliziumkarbid (SiC)-Mikroreaktor bei Temperaturen bis zu 1500 K thermisch zersetzt und die gasförmige Probe am Austritt des SiC-Mikroreaktors mittels der isomerselektiven vakuum-ultravioletten Photoelektronen-Photoionen-Koinzidenzspektroskopie (VUV-i^{2}PEPICO) analysiert. Mit Hilfe dieser Methode konnten reaktive organische Zwischenprodukte, sowie metallhaltige Intermediate anhand ihrer Ionisationsschwellen (PIE Kurven) und der spektroskopischen Fingerabdrücke (ms-TPES) erfolgreich detektiert und zugeordnet werden. Auf Basis dieser Charakterisierung wurden temperaturabhängige Speziesprofile abgeleitet, die Hinweise auf die zugrunde liegende Chemie geben.

Im Falle der untersuchten β-Diketonat Metallkomplexe, $Al(C_5H_7O_2)_3$ und $Zr(C_5H_7O_2)_4$, konnten zwei Temperaturbereiche identifizieren. Die Ergebnisse zeigen, dass der Vorläufer bei niedrigeren Temperaturen unter 600 K hauptsächlich aufgrund von Oberflächenreaktionen an der Wand zersetzt wird. Dieser primäre Zersetzungskanal ermöglicht jeweils die Bildung von $Al(OH)_2(C_5H_7O_2)$ und $Zr(OH)_2(C_5H_7O_2)_2$ zusammen mit $C_{10}H_{12}O_2$. Die Analyse der Datensätze bei Temperaturen oberhalb von 600 K deutet auf eine Änderung des Mechanismuses hin, bei der die Gasphasenzersetzung von $Al(C_5H_7O_2)_3$ und $Zr(C_5H_7O_2)_4$ dominant wird.

Im Fall von $Al(C_5H_7O_2)_3$ lässt sich der Hauptreaktionsweg mit der Bildung des Intermediates $Al(C_5H_7O_2)(C_5H_6O_2)$ und Acetylaceton ($C_5H_8O_2$) bei Temperaturen über 600 K beschreiben. Die kinetischen Parameter für diese Gasphasenreaktion wurden bestimmt und die erste Reaktionsordnung wurde experimentell bestätigt.

Bei der Zersetzung von $Zr(C_5H_7O_2)_4$ wurde eine komplexere Gasphasenchemie beobachtet. Basierend auf der Charakterisierung von sechs wichtigen Zr–Zwischenprodukten wurde zum ersten Mal ein umfassendes Gasphasen-Reaktionsschema im Temperaturbereich von 400 bis 900 K aufgestellt. Zunächst wird in einem primären Zersetzungsschritt $Zr(C_5H_7O_2)_2(C_5H_6O_2)$ gebildet. Darauf aufbauend verläuft der Mechanismus vornehmlich konsekutiv, wodurch in drei Schritten schließlich $ZrO(C_5H_6O_2)$ gebildet wird. Dieses Intermediat fungiert als Vorläufer für die nachfolgende Oberflächenreaktionen, die schlussendlich zum Filmwachstum bei Temperaturen über 850 K führen. Darüber hinaus wurden die adiabatischen Ionisierungsschwellen der Zr–Zwischenprodukte bestimmt, die zukünftig zur Identifizierung metallhaltiger reaktiver Zwischenprodukte verwendet werden können. Für beide Ausgangsstoffe wurden mehrere Kohlenwasserstoffe und sauerstoffhaltige Nebenprodukte wie m/z 100 Acetylaceton, m/z 82 Acetylallene und m/z 58 Aceton charakterisiert und die jeweiligen Reaktionswege zur Bildung derselben diskutiert.

In einem dritten Experiment wurde das thermische Zersetzungsverhalten des Ferrocens ($Fe(Cp)_2$) mit und ohne Zugabe von 10% Wasserstoff untersucht. Zunächst ließ sich eine oberflächenkatalytische Zersetzung bei Temperaturen unterhalb von 900 K beobachten. Dabei werden Cyclopentadienyl-Radikale und Cyclopentadien in die Gasphase freigesetzt. Bei höheren Temperaturen wurde eine schnelle Zersetzung von $Fe(Cp)_2$ in der Gasphase und die Bildung von atomarem Eisen beobachtet. Die Zugabe von 10% Wasserstoff verändert den Reaktionsmechanismus. Erstens wird durch die Zugabe von Wasserstoff die Anzahl der Wasserstoffatome an der Oberfläche vergrößert. Dies wiederum verstärkt die bimolekulare Reaktion der Cyclopentadienyl-Radikale mit dem an der Oberfläche adsorbiertem Wasserstoff, wobei große Mengen Cyclopentadien gebildet werden. Zweitens führen katalytische H-Verluste zu einem Bruch des C_5H_5-Liganden und somit zu einem hohen Kohlenstoffgehalt auf der Oberfläche. Sowohl für die unimolekulare Zersetzung, als auch für die bimolekulare Reaktion mit Wasserstoff wurden kinetische Parameter bestimmt, die gut mit den bisher veröffentlichen Daten übereinstimmen.

Die Ergebnisse dieser Arbeit zeigen, dass eine Untersuchung der thermischen Zersetzung von CVD-Vorläufern in der Gasphase in einem Mikroreaktor unter Zuhilfenahme von Simulationen des Strömungsfeldes möglich ist und metallhaltige reaktive Zwischenprodukte mit einer Lebensdauer in der Größenordnung von Mikrosekunden erfolgreich nachgewiesen werden können. Die bereitgestellten kinetischen und mechanistischen Daten können verwendet werden, um reaktive Moleküle in CVD-Reaktionssystemen zu identifizieren und den Prozess zu modellieren. Die Modellierung des Prozesses trägt zu einem besseren Verständnis der Reaktionsmechanismen in CVD-Reaktoren bei und verringert durch geeignete Wahl der Reaktionsparameter mögliche Verunreinigungen oder parasitäre Nebenreaktionen, die sich wiederum nachteilig auf die Filmwachstumsrate auswirken.

Contents

List of Figures

List of Tables

Glossary

AE Appearance energy 23, 24, 99, 101

BDE Bond dissociation energy 119, 120

BG Background 51, 69

BM Bending magnet 17–19

CCVD Catalytic chemical vapor deposition 8, 117, 118

CFD Computational fluid dynamics 9, 10, 41, 44, 56, 60, 64, 66, 69, 75, 81, 84–87, 92–94, 103, 110, 114, 134–136, 141, 143, 146, 151, 194, 195

CNT Carbon nanotube 8, 117, 118

CRF-PEPICO Combustion reactions followed by double imaging photoelectron photoion coincidence 40, 45, 49, 53

CVD Chemical vapor deposition 1–5, 9–13, 23, 25, 27, 28, 33, 36, 39, 42, 46, 56, 59, 91, 92, 94, 111, 118, 128, 140, 145–150

CVS Chemical vapor synthesis 2, 3

DLD Delayed-line anode 44, 45

DPI Dissociative ionization 13, 23–25, 27, 66, 68–70, 75, 119, 121, 191

EI-MBMS Electron ionization molecular-beam mass spectrometry . 5, 9, 84, 86, 137

FC Franck-Condon 62, 69, 73, 74, 98–100, 102, 112, 142, 204

FTIR Fourier-transform infrared spectroscopy 5, 9, 33, 59, 73, 84

GC-MS Gas chromatography-mass spectrometry 5, 9, 33, 59

i^{2}PEPICO Double imaging photoelectron photoion spectroscopy . 11–13, 21, 27, 28, 39, 42, 44, 48, 50, 52, 53, 55, 56, 59–61, 70, 76, 86, 89, 92, 101, 106, 107, 110–112, 115, 118, 119, 126, 127, 130, 139, 141, 142, 146–150

ID Insertion device 17

IE Ionization energy 11, 21, 22, 24, 25, 69, 99, 113, 185

IR-LPHP Infrared laser powered homogeneous pyrolysis 33

LINAC Linear accelerator 16

MBMS Molecular beam mass spectrometry 5

MCP Micro/multi-channel plate 44, 45, 48

MM Multi-start multiple stop 46, 47

MOCVD Metal-organic chemical vapor deposition 58, 59

ms-TPE Mass-selected threshold photoelectron 66, 69, 95, 98–100, 102, 110, 123–125, 131, 186–189, 191, 204

ms-TPES Mass-selected threshold photoelectron spectra 46, 50, 52, 53, 60, 62, 66–70, 72–74, 77, 78, 86, 92, 95, 97–99, 102–104, 106, 112, 113, 119, 120, 122–126, 129–131, 147, 185, 186, 190, 191, 197, 199, 204, 205

PES Photoelectron spectroscopy 13, 24–27, 45, 73, 186

PIE Photoionization efficiency 21–24, 48, 72, 92, 99, 102–104, 110, 119, 120, 129, 148, 186, 188, 190, 204

PIMS Photoionization mass spectrometry . . 13, 21, 23, 24, 26, 45, 48, 60, 62, 70

PSD Position-sensitive detector 45, 48

PSI Paul Scherrer Institute 111, 140

RANS Reynolds averaged Navier-Stokes 41, 193

RF Radiofrequency cavity 18

ROI Region-of-interest 49–51, 62, 69, 112, 141, 142, 202

SiC Silicon-carbide 10, 13, 33, 39, 43, 60, 64, 67, 90, 111, 121, 141, 183

SLS Swiss Light Source 13, 17–20, 39, 40, 46, 50, 60, 92, 111, 140

SR Synchrotron radiation 11, 15, 16

SSR Sum of squared residuals 136

TD-DFT Time-dependent density functional theory 63, 69, 75

ToF Time-of-flight 26, 27, 46–49, 121

TPES Threshold photoelectron spectroscopy 21, 26, 50, 63, 142

TPM Threshold photoionization matrix 70, 123

VMI Velocity map imaging . . 11, 26, 27, 44, 51, 59, 61, 62, 68–70, 75, 92, 95, 96, 102, 103, 105, 110, 112, 118, 120, 121, 130, 141, 142, 148, 201

VUV Vacuum ultraviolet 11, 13, 15, 18–20, 40, 59–61, 70, 86, 92, 101, 107, 110–112, 118, 127, 130, 139–141, 146

Chapter 1

Introduction and Motivation

In high-tech societies thin films and coatings are embedded in almost everything around us and affect every aspect of our life. The annual worldwide market for thin film technology in 2020 was worth 27.6 billion US dollars and is expected to grow in excess of 8.3% per annum in the forecast period from 2021 to 2028, reaching 53.2 billion US dollars by 2028 [1]. A major factor for that growth is that thin films have distinct advantages over bulk material because their properties are not restrained to the design and control of heat treatment procedures to tune the properties of alloys using phase diagrams. In contrast, by using thin film technologies, numerous compositions of thin films can be engineered which modify the functionality of the bulk material by amplifying or adding new desired properties, with respect to a specific demand.

Various approaches exist to deposit thin films on substrates and to tailor materials for a specific application, such as physical vapor deposition or sputtering. The final objective of any deposition methodology is to produce a thin film of high quality in a reproducible manner on industrial scale. A scalable, high-throughput manufacturing process to deposit solid materials on surfaces at high temperatures from gaseous precursors is called chemical vapor deposition (CVD) [2]. The method is characterized by a sequence of complex homogeneous-heterogeneous reactions and meets the aforementioned criteria because of its numerous advantages. These include adjustable deposition rates and conditions, the scalability and the ability to control and minimize the critical deposition parameters, such as temperature and pressure. With respect to film quality aspects, CVD ensures reproducibility in film thickness, composition and purity. Considering the chemical compounds used to perform CVD, a high flexibility to use a wide range of precursors, such as halides, hydrides and organometallic compounds, is ensured, which expands the variety of films to be deposited [2, 3]. Especially its non-line-of-sight nature demarks CVD from other deposition methods, such as physical vapor deposition or sputtering, with beneficial effects on a uniform thickness of coatings of complicated shapes.

This is why many of the largest multi-billion dollar industries use CVD methods, or their products, in manufacturing and tailoring their devices [3, 4]. This includes, but is not limited to the fields of energy conversion [5, 6, 7, 8, 9] and storage

[10, 11, 12, 13], electronics [14, 15, 16], optoelectronics [17, 18, 19], sensors [20], thermal insulation barriers [21, 22, 23], surface hardening [24, 25] and nanomaterials [26, 27, 28]. In order to obtain a fundamental understanding of the processes underlying the synthesis and functionalization of materials produced by CVD, much attention was paid on these topics by researchers over the last two decades. This is mainly because the underlying chemical processes are a major factor influencing the efficiency and properties of the functional materials obtained. Previous findings regarding the role of gas-phase chemistry in CVD processes underlined that the decomposition pathways and reactions in the gas-phase are a central issue among the whole chemical process [29].

1.1 The Role of Gas-Phase Reactions

1.1.1 Overview

The synthesis of thin films by CVD and functional nanomaterials by chemical vapor synthesis (CVS) is driven by the complex chemistry of the metal-organic precursor used. Unlike in atomic layer deposition, where the process is easily controlled by surface reactions, in CVD the chemical mechanism is complicated by preceding gas-phase reactions that are often parasitic when the goal is surface growth [30, 31, 32]. Usually the reaction sequence in CVD involves both gas-phase and surface reactions [33]. A simplified model consisting of the sequential physical and chemical steps involved in the formation of thin layers by the thermal CVD method is shown in Fig. 1.1. The most important process steps can be summarized as follows [29]:

(1) **Gas-phase reactions**: After evaporation and transport of the reagents (i.e., precursor and reactive gases) into the reactor, the precursor is partially decomposed in a unimolecular homogeneous gas-phase reaction or, if reactive gases are present, in a bimolecular reaction. This leads to the formation of various stable and unstable metal-organic intermediates as well as gaseous by-products, including short-lived free radicals.

(2) **Mass transport**: The reactants formed by the initial decomposition reactions diffuse through the boundary layer towards the substrate surface.

(3) **Adsorption and surface reactions**: After diffusion through the boundary layer, the intermediates may adsorb on the surface where they can undergo subsequent heterogeneous surface reactions that may lead to a release of by-products into the gas-phase.

(4) **Surface diffusion**: The adsorbed species diffuse on the surface to growth sites, where nucleation and surface reactions form a thin film.

(5) **Desorption**: Organic by-products from surface reactions could desorb and be released into the gas-phase by mass transport through the boundary layer during any step between (3) and (5).

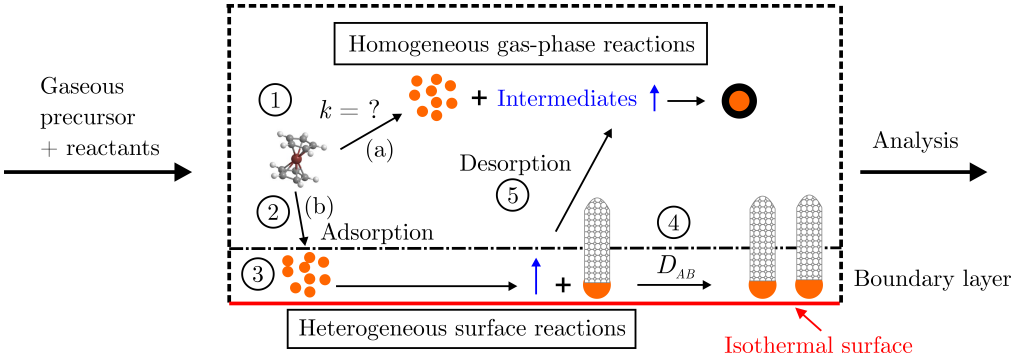

Figure 1.1: Schematic of typical CVD and CVS process using an iron precursor (ferrocene), based on [29]. The precursor molecule is used for two purposes, (a) the growth of encapsulated nanoparticles in the gas-phase by CVS and (b) the surface growth of carbon nanotubes on catalytic iron particles by CVD. The numbers from (1) to (5) are explained in the text.

It is the richness of chemistry of the precursors that makes layers with various properties possible. However, with variety comes complexity. This is mainly valid for the associated deposition parameters that are not easy to control and handle. In general, three regions of film growth as a function of temperature are defined for a CVD process, where the growth rate is either controlled by the kinetics or by mass transport. At high temperatures, desorption of the precursor or prereactions in the gas-phase may lower the growth rate. Often process parameters encompassed within the kinetically controlled regime are chosen for synthesis, which is located at relatively low temperatures, where the surface deposition is either controlled by surface or gas-phase reactions.

From the process scheme in Fig. 1.1, we can anticipate that the extent of gas-phase reactions primarily depends on macroscopic parameters such as temperature, pressure and composition. The influence is increased with increasing temperature and reactant concentration as well as in low pressure environments, due to larger mean free paths of molecules [34]. While for low partial pressures of the reactants and at relatively low temperature, surface reactions dominate, at high partial pressure and high temperature the gas-phase reactions, which are in some cases necessary to form the desired surface-active growth species [35], are an important factor [36, 37]. At sufficiently high temperatures, the precursor already reacts in the gas-phase and may form particles (gas-phase nucleation/ particle formation/ generation of nanoparticles) by CVS [38] (see Fig. 1.1 (a)). In some cases, this is desired, for example to form powders with high purity [39]. Yet in many cases, these prereactions lead to a contamination of the thin film by fractional parts of the precursor ligands and are therefore detrimental when the goal is surface growth [40]. In the case of carbon nanotube synthesis, the catalyst, promoting the growth of these functional materials, could be deactivated by reaction intermediates and products that stem from gas-phase reactions [41].

In summary, not only properties of a thin film, such as the phase formation, crystalline orientation, surface morphology, and stochiometry depend on the ther-

modynamics and kinetics of the reaction system, but also a detrimental defect concentration and poor film adhesion, as well as quality and functionality of the film are influenced by the underlying chemical mechanism, especially in the gas-phase [42, 43]. Therefore, controlling the whole process requires a complete understanding of its initial steps in the gas-phase to obtain materials, having the required physical and chemical properties. Popular examples, where gas-phase reactions play an important role in the deposition process, are the growth of graphite and diamond from hydrocarbon precursors [44]. But also when using metal-organic precursors the analysis of gas-phase reactions should not be omitted [27, 45, 46]. Because of this an accurate description of the gas-phase kinetics is of great importance to model and understand film growth processes. This holds true especially for modeling the whole deposition process, where a complete set of reactions is necessary.

Likewise the analysis of gas-phase reactions is of great importance for the exemplary metal β-diketonate and organometallic precursors investigated in this study; aluminium(III)acetylacetonate $Al(C_5H_7O_2)_3$[1], zirconium(IV)acetylacetonate $Zr(C_5H_7O_2)_4$[2] and ferrocene $Fe(C_5H_5)_2$[3]. Given the high metal-oxygen bond strengths of metal β-diketonates [47], the homogeneous decomposition of the first two precursors is considered as the rate-limiting step for film growth [40], while ferrocene has an even higher bond dissociation energy of 382 kJ mol^{-1}[48]. Consequently, the characterization and role of the gas-phase chemistry and kinetics of these precursors is of particular interest. In the following, a short literature review on the most important aspects of gas-phase related studies in general and with respect to the aforementioned precursors in particular, is presented.

1.1.2 Mechanism & Kinetics

In general, there exist various approaches to model the gas-phase part of a CVD process thermodynamically, but also kinetically. While equilibrium calculations answer general questions about the feasibility of a given reaction path and phase diagrams can be constructed for preselection of precursor concentrations and reaction conditions [2, 49, 50], a more precise and accurate analysis of a CVD system requires the consideration of the chemical kinetics and mass transport phenomena [49]. The first one is frequently tackled using *ab-initio* molecular dynamic simulations based on the density functional theory [51, 52, 53, 54, 55, 56, 57, 58, 59], whereas the latter is addressed by modeling the flow field characteristics in a given CVD system [60, 61, 62, 63, 64, 65]. In order to validate such models, a clear need for experimental kinetic studies of the decomposition processes in the gas-phase exists. Besides the evolving field of theoretical studies of the thermodynamics [66, 67] and kinetics [68, 69, 70, 71, 72], which is up to today on a advanced level, several methods were applied to experimentally analyze thermal decomposition pathways in the gas-phase. In particular, flow reactors with well defined flow fields, usually operated in the

[1] Commonly abbreviated as $Al(acac)_3$, which will be primarily used within this thesis.
[2] Commonly abbreviated as $Zr(acac)_4$, which will be primarily used within this thesis.
[3] Commonly abbreviated as $Fe(Cp)_2$, which will be primarily used within this thesis.

idealized plug-flow regime, are used to elucidate the gas-phase chemical kinetics of various organometallic precursors by applying *in-situ* and *ex-situ* analytical methods, such as Fourier-transform infrared spectroscopy (FTIR) [73, 74, 75, 76], molecular beam mass spectrometry (MBMS) [73, 75] or gas chromatography-mass spectrometry (GC-MS) [77, 78].

In most cases, combinations of these techniques are used to tackle questions on the analysis of thermal decomposition pathways in the gas-phase. The flow field, for which analytical solutions exist, is well-characterized. Therefore, the evaluation of kinetic rate data for elementary reactions to stable product species is easy to perform. Besides the well described flow field, the main disadvantage of these analytical methods lies within their sensitivity to sample highly complex initial reactive intermediates and primary pyrolysis products with lifetimes of a few hundreds of microseconds. Often, using the aforementioned setups, the unimolecular decomposition pathways could not be easily assessed due to the interference of intramolecular secondary reactions or collisions with the wall and therefore a termination of reactive species formed in the early stages of precursor decomposition. For instance, in the CVD of $Al(acac)_3$ and $Zr(acac)_4$ only stable species were found and the complex high temperature kinetics were not possible to reveal. This leads to rather superficial models and therefore the observation and characterization of these early products is of fundamental interest for the optimization of a CVD process.

1.1.2.1 Decomposition Mechanism of $Al(acac)_3$

In the past, considerable efforts were made to study the reaction kinetics [79, 80] and to characterize the involved primary gaseous reaction products [80, 81, 82] of the thermal decomposition of $Al(acac)_3$, which is frequently used in the synthesis of Al_2O_3 thin films by CVD at temperatures of 623-1223 K [83, 84, 85, 86]. In the first systematic investigation of the decomposition mechanism, Hoene and coworkers [81] identified several decomposition products, such as carbon dioxide (CO_2), acetone (C_3H_6O) and acetylacetone ($C_5H_8O_2$) at temperatures of 423-673 K, using electron ionization molecular beam mass spectrometry (EI-MBMS) [80, 81]. These findings were complemented by low-pressure pyrolysis studies using the manometric method[4] by Minkina [79] ranging from 653-723 K, where she additionally verified methane (CH_4), ketene (C_2H_2O), butene (C_4H_8) and carbon monoxide (CO) as the most abundant species. In a later study, Bykov and colleagues [80] covered a wider temperature range from 423-923 K using EI-MBMS. Based on their findings, a few newly detected volatile oxygenated hydrocarbons, such as $C_{10}H_{12}O_2$ and C_5H_6O, were detected. Furthermore, they proposed the first reaction scheme for the thermal decomposition of $Al(acac)_3$ in the gas-phase[5]:

[4] Measurement of pressure rises due to a thermal decomposition of the precursor.

[5] Species marked with an asterisk are postulated species. The arrows indicate, if the species is desorbed (↑) from, or adsorbed (↓) on the surface.

$$\mathrm{Al(C_5H_7O_2)_3} \longrightarrow \mathrm{Al(C_5H_7O_2)_2(OH)^* + C_5H_6O\uparrow}, \tag{R 1.1}$$

$$\mathrm{Al(C_5H_7O_2)_3} \longrightarrow \mathrm{Al(C_5H_7O_2)(OH)_2{}^* + C_{10}H_{12}O_2\uparrow}, \tag{R 1.2}$$

$$\mathrm{Al(C_5H_7O_2)_3} \longrightarrow \mathrm{C_5H_8O_2\uparrow + C_3H_6O\uparrow + C_2H_2O\uparrow} + \text{condensed phase (Al, C-residuum, O-residuum)}^*\downarrow . \tag{R 1.3}$$

This mechanism was later extended by adding subsequent heterogeneous surface reactions of the volatile metal-containing species suggested in Reac. R 1.1 to Reac. R 1.3, but also surface reactions directly from $Al(acac)_3$ were considered. Those surface reactions would lead to the formation of volatile reaction by-products and metal-containing surface intermediates, where the latter may form Al_2O_3 layers in subsequent surface reactions [82, 87, 88]:

$$\mathrm{Al(C_5H_7O_2)_2(OH)^*\downarrow \longrightarrow Al(OH)_3{}^* + C_{10}H_{12}O_2\uparrow}, \tag{R 1.4}$$

$$\mathrm{Al(C_5H_7O_2)(OH)_2{}^*\downarrow \longrightarrow Al(OH)_3{}^* + C_5H_6O\uparrow}, \tag{R 1.5}$$

$$\mathrm{Al(C_5H_7O_2)_3\downarrow \longrightarrow Al(C_5H_7O_2)O^* + C_5H_8O_2\uparrow + C_5H_6O\uparrow}, \tag{R 1.6}$$

$$\mathrm{Al(C_5H_7O_2)_3\downarrow \longrightarrow Al(C_5H_7O_2)O^* + C_5H_6O\uparrow + C_3H_6O\uparrow + C_2H_2O\uparrow}, \tag{R 1.7}$$

$$\mathrm{Al(C_5H_7O_2)_3\downarrow \longrightarrow Al(C_5H_7O_2)O^* + C_5H_8O\uparrow + C_3H_6O\uparrow + CO\uparrow + C}, \tag{R 1.8}$$

$$\mathrm{Al(C_5H_7O_2)_3\downarrow \longrightarrow Al(C_5H_7O_2)O^* + C_5H_6O\uparrow + C_4H_4O_2\uparrow + CH_4\uparrow}, \tag{R 1.9}$$

$$\mathrm{Al(C_5H_7O_2)O^* \longrightarrow AlO(OH)^* + C_5H_6O\uparrow}. \tag{R 1.10}$$

If we evaluate the above written mechanism and consider the main takeaways from previous literature, two statements can be made. First, although the metal-containing intermediates seem to play a central role in the mechanism, they have not been experimentally validated, yet, rendering the current mechanism speculative. Second, gas-phase chemistry plays an important role in the decomposition of $Al(acac)_3$, since the detected decomposition products hint to an initial destruction of the ligands in the gas-phase. These reactions lead to an unfavorable carbon contamination in the film, as indicated in Reac. R 1.8. Its extent can reach considerable amounts of up to 25% [89]. Efforts to reduce these detrimental impurities were made in the past, by adding water vapor to the reaction mixture, leading to a complete removal of the splitted-off ligand parts, which results in carbon

free films that grow at lower temperatures [89, 90]. These insights additionally demonstrate that major challenges, such as an incomplete decomposition of the ligands, but also tools to solve these challenges, are deeply rooted in the gas-phase chemistry. However, despite its importance, the gas-phase mechanism and kinetics of $Al(acac)_3$ were, up to this point, not understood sufficiently.

1.1.2.2 Decomposition Mechanism of $Zr(acac)_4$

Since $Zr(acac)_4$ is an important precursor for the formation of ZrO_2 thin films at temperatures of 573-1073 K [91, 92, 93, 94], many attempts have been made to characterize the reaction products and pathways involved. It was found that $Zr(acac)_4$ decomposes by a series of steps, which was rationalized by the detection of various organic hydrocarbons and oxygenated species in the gas-phase. Among others, acetylacetone ($C_5H_8O_2$), acetic acid ($C_2H_3O_2$) and propyne (C_3H_4) were found at temperatures up to 523 K. Carbon dioxide (CO_2), water (H_2O) and methane (CH_4) were revealed as secondary decomposition products at temperatures higher than 623 K [95, 96, 97].

Responsible for their formation are reactions occurring in the gas-phase or on the surface that afford the formation of metal acetates ($Zr(acac)_2(CH_3COO)_2$, $ZrOH(CH_3COO)_3$, $ZrO(CH_3COO)_2$), metal carbonates ($ZrOCO_3$), as well as other intermediate species on the surface [95]. In this context, a critic of the aforementioned findings by Ismail [95] is done by Schlupp et al. [96], who argued that their measurements indicate an incomplete conversion of the precursor and a considerable carbon residue, which they contributed to a possible oxygen contamination in Ismail's system. As for the decomposition of $Al(acac)_3$, the detection of volatile hydrocarbons and oxygenated species and the proof of carbon residuals in the deposited film [96, 97] demonstrates that gas-phase chemistry plays an important role here. Although some insights were gained by the assignment of surface reaction products, based on the associated weight loss [95, 96], a complete reaction mechanism, including the gas-phase intermediates proposed, has not been formulated. So far, only a global reaction has been suggested [95, 98]:

$$Zr(C_5H_7O_2)_4 \longrightarrow ZrO_2 + C{-}residual + gas{-}phase\uparrow . \qquad \text{(R 1.11)}$$

To overcome parasitic side reactions and carbon impurities enclosed in the film, similar strategies as for $Al(acac)_3$, for instance adding reagents such as oxygen or water vapor, were successfully established and can be described by the following global reactions [98]:

$$Zr(C_5H_7O_2)_4 + 24\,O_2 \longrightarrow ZrO_2 + 20\,CO_2\uparrow + 14\,H_2O\uparrow , \qquad \text{(R 1.12)}$$

$$Zr(C_5H_7O_2)_4 + 2\,H_2O \longrightarrow ZrO_2 + 4\,C_5H_8O_2\uparrow . \qquad \text{(R 1.13)}$$

Besides oxidation of ZrO by molecular oxygen on the surface, beneficial effects of reagents such as oxygen and water can likely be assigned to the gas-phase. Here,

a destruction of ligands can be avoided and stable products are formed by the reaction of oxygen and water with metal-containing intermediates or carbonaceous by-products, which ultimately leads to carbon-free ZrO_2 films [96]. However, for the gas-phase neither experimental verification of metal-containing intermediates, whose formation most probably drive the deposition process, nor precise reaction pathways can be found in the literature. Only global reactions as described in Reac. R 1.11 to Reac. R 1.13 were agreed on in the past, clearly leaving some gaps in knowledge on the decomposition of $Zr(acac)_4$.

1.1.2.3 Decomposition Mechanism of $Fe(Cp)_2$

Unlike the aforementioned metal β-diketonate precursors, the organometallic precursor ferrocene is mainly used in the manufacturing of functional nanomaterials, such as carbon nanotubes (CNTs) by the catalytic chemical vapor deposition (CCVD) method [27, 99]. Typical synthesis temperatures range from 923 to 1223 K [100, 101]. From the analysis of the associated synthesis routes, it can be concluded that the morphology, crystallinity and growth kinetics of CNTs are highly influenced by the gas-phase mechanism and kinetics [102]. When used simultaneously as carbon source and catalyst, the following simple pathway for thermal decomposition of ferrocene is suggested:

$$Fe(C_5H_5)_2 \longrightarrow Fe + 2\,C_5H_5\,. \qquad \text{(R 1.14)}$$

This reaction was rationalized by various studies on the decomposition products [103, 104, 105] and kinetics [48, 106] upon the thermal decomposition of ferrocene. Summarizing the findings in those studies shows that the formation of volatile hydrocarbons such as methane (CH_4), ethylene (C_2H_4), the cyclopentadienyl radical (C_5H_5), cyclopentadiene (C_5H_6) and naphtahlene ($C_{10}H_8$) were observed. However, a key issue, especially with earlier literature results in relation to the detection and characterization of those gaseous products, are the pitfalls of the utilized analysis methods. These do often not allow to detect gaseous intermediates and the intermediate reaction pathways, for the most part, remain unclear. Due to highly versatile experimental conditions applied in previous studies, up to today, the gas-phase kinetics are not well understood either [107].

Another important aspect is that ferrocene is often not used as a single source precursor for the synthesis of CNTs, but additionally serves as catalytic agent in combination with further hydrocarbon sources, such as acetylene and xylene [108]. The presence of other reaction partners certainly complicates the mechanism occurring in the gas-phase. This is because possible intermediates act either as promoter for CNT growth or as detrimental impurity that may lower the growth rate and lead to unacceptable product quality by forming parasitic volatile intermediates [109, 110]. Some studies indicate that the by-products may also deactivate the catalytic Fe-particles leading to a slower growth rate or even a termination of the growth [111].

Consequently, methods to improve catalyst lifetime by reduction of ferrocene using hydrogen were established and rationalized [112, 113], which, as a positive side effect, significantly lower the decomposition temperature [114, 115, 116]. Again, attention is drawn to the gas-phase chemistry, since some of the additional reactions are likely to take place in the gas-phase and it is widely accepted that the gas-phase decomposition mechanism, besides the quality, additionally influences the type of product obtained [117]. Therefore, a complete understanding of the decomposition pathways and kinetics of $Fe(Cp)_2$ in inert and reactive atmosphere is important and would enable scientists to control the synthesis process, when applying a wide range of reaction conditions.

1.2 Research Objectives

In sum, the decomposition pathways of all three model precursors are highly complex and are of homogeneous-heterogeneous nature. Despite considerable efforts in the past to tackle gas-phase reaction pathways and explain unwanted side-products and carbon incorporation in the films, complete mechanisms of the initial steps of thermal decomposition in the gas-phase are still unknown. Uncovering the mechanism is especially important since it has a strong influence on the morphology and therefore the quality of the thin film or functional material synthesized.

A key problem with the analysis of CVD reaction systems *in-situ* is the detection and characterization of the chemical species involved. In typical CVD environments, it is difficult to isolate reactive molecules and intermediates and often only secondary, as well as stable decomposition products are detected using conventional spectroscopic methods, such as FTIR, GC-MS and EI-MBMS. In addition, it is difficult to obtain meaningful data by inserted probes. This is because condensation of the precursor on the probe's surface may occur, which falsifies product detection and the derivation of kinetic rate data, where the latter is highly dependent on an accurate quantification of the inlet and outlet composition. This is why kinetic rate data of metal-organic precursors is scarce in the literature, although data is clearly needed to validate and build up models for film growth. The demand for a basic understanding of the processes in the gas-phase should not be underestimated, since well established models bridge the gap between small scale laboratory and industrial scale reactor setups. These often have a wide variety of geometries and flow conditions, which mainly influence the quality and growth rate of film deposition by an interplay between gas flow, heat and mass transfer and chemical reactions close to the deposition surface. This is accounted for by accurate modeling of the deposition mechanism with computational fluid dynamics (CFD) methods and underlines the necessity to deliver satisfactory experimental validation data [118, 119].

When using solid precursors that are transported to the reaction chamber by sublimation in an inert carrier gas, the maintenance of well-defined reaction conditions in the chamber can be another challenge for various classes of compounds

[120]. Precursor decomposition and the exposure to moisture and air in the evaporator prior to chemical reaction in the reactor could falsify and complicate the interpretation of kinetic data. This calls for suitable methods to track and control the incoming gas-phase composition, prior to the analysis of the decomposition upon thermal excitation inside the reactor. In the context of the previously stated insights from the literature and given the importance of gas-phase reactions in CVD processes, the primary aim of the present work is to develop a deep understanding of the elementary processes and fundamentals of the decomposition of $Al(acac)_3$, $Zr(acac)_4$ and $Fe(Cp)_2$ in inert and for the latter in reactive atmosphere. To overcome recent challenges in the detection of reactive intermediates with low lifetime, a novel approach is needed, which is capable to:

- **Reactive intermediates**: Isolate, detect and characterize short-living intermediates, also in trace amounts, in CVD like environments with high sensitivity. The method should have a sufficient resolution to distinguish between various species in complex sample compositions, by separation of similar masses and isomers using a single detection method.
- **Metal-containing intermediates**: Identify metal-containing intermediates that are considered as true precursors for film growth with a lifetime of at least a few microseconds.
- **Kinetic data**: Extract kinetic rate data for the initial decomposition steps by using CFD assistance for a precise description of the complex flow field in the reactor.
- **Proof of concept**: Establish a blueprint study, which, due to the wide variety of CVD precursors used, demonstrates that also other precursors with higher structural complexity, such as $Zr(tmhd)_4$, could be analyzed with the presented method. This is of particular interest, since with higher complexity of the ligand structure, less data is available on the precursors decomposition routes.

1.3 Research Strategy

New developments in the area of reactor design and spectroscopy have led to promising approaches to tackle the questions outlined in the previous section. For instance, Chen et al. [121] developed a microreactor that allows to continuously generate radicals with lifetimes of a few microseconds. These silicon carbide (SiC) pyrolysis tubes have been extensively used in combustion and catalysis science to elucidate reaction mechanisms in the past [122]. Given that the employed CVD precursor has a sufficient volatility, which is the case for the compounds studied in this work, one can benefit from the short residence times that are achievable in a microreactor. Thus, a successful experimental investigation of the reactions of these compounds seems feasible.

The combination of mass spectrometry with photoelectron spectroscopy by methods such as vacuum ultraviolet (VUV)[6], double imaging photoelectron photoion coincidence spectroscopy (i^{2}PEPICO), paves the way to understand gas-phase mechanisms with high sensitivity, selectivity and tunability by using synchrotron radiation (SR). By exploiting the capabilities of i^{2}PEPICO, both the main spectral fingerprint and the ionization energy (IE) are used for species identification, supplemented by velocity map imaging (VMI) of electrons and ions. This allows to unequivocally prove the existence of species in the sample isomer-selectively, which is especially beneficial for large molecules, where the low ionization energies often lie close to each other. Yet, the isomer-selective identification requires tunability of the ionization energy and additional analytical dimensions in form of the momentum of the detected particles [122]. Additionally, information on the kinetic energy of the electrons that originate from a single ionization event, leaving a cation behind, gives orbital specific information, which is unique for each isomer. The detection method ultimately yields a multidimensional dataset consisting of the mass dimension, the ionization energies and the vibrational structure in the cation of each single ionization event [123]. In addition, the tunability of the photon energy from synchrotron sources allows one to obtain fragmentation free mass spectra, when the ionization energy is chosen slightly above the ionization limit of the species of interest. Finally, synchrotron-assisted i^{2}PEPICO does not only provide the opportunity for the detection of short-living metal-containing intermediates in the gas-phase [124], but also enables one to identify and characterize reactive intermediates isomer-selectively and therefore unravel complex chemistry of CVD precursors.

So far, this field of research has been explored less profoundly with respect to CVD precursors and only a few attempts were performed, using a relatively simple approach of tunable photoionization mass spectrometry to investigate the reaction mechanism. Examples are the decomposition of trimethylaluminium in a flow reactor [125], the deposition of transition metal-alloys on glass substrates [126], as well as the investigation of silicon compounds upon thermal excitation using a Chen-type pyrolysis reactor setup [127, 128]. From the previous literature review it becomes clear that the detailed reaction kinetics of $Al(acac)_3$, $Zr(acac)_4$ and $Fe(Cp)_2$ are not well understood. Despite a common agreement that unimolecular gas-phase reactions forming metal-containing intermediates should play an important role in the mechanism of thin film deposition by CVD, only a limited amount of studies show experimental evidence for them. However, as outlined, these results are interfered by possible drawbacks of the employed analysis methods, such that a re-investigation is reasonable. First of all, the question must be answered whether metal-containing gas-phase intermediates for the three precursors can be observed at all, or whether the reactions mainly take place on the surface. Besides the general

[6]The wavelength range from 120-240 nm which is strongly absorbed by the surrounding air. Therefore, a vacuum apparatus is often necessary for its usage. Vacuum ultraviolet radiation is considered as a universal detector in spectroscopy due to its absorption characteristic for many different molecules.

verification of gas-phase chemistry in these systems, the main research questions to be answered are:

- **$Al(acac)_3$**: What is the structure of the proposed metal-containing intermediates outlined in Reac. R 1.1–Reac. R 1.10? What is their role in the reaction mechanism? How do they influence the ligand destruction and result in a possible carbon contamination of the thin film? Do the proposed unimolecular gas-phase reactions obey first-order kinetics? What are the reaction kinetics of the formation of possible metal-containing intermediates? How can the beneficial effects of oxidizing reactions on the film morphology be explained?

- **$Zr(acac)_4$**: Is it possible to investigate this precursor under stable conditions, since a decomposition in the evaporator is expected? Are reactive intermediates, such as metal acetates, solely formed on the surface, or do they initially form in gas-phase reactions? Can the global mechanism in Reac. R 1.11 be extended to reach conclusions about the impact of possible gas-phase intermediates on the film morphology and structure?

- **$Fe(Cp)_2$**: Can the previously proposed intermediate primary $Fe(C_5H_5)$ be experimentally validated? To what extend and in which temperature window do catalytic surface reactions significantly influence the decomposition mechanism? What is the role of hydrogen in the decomposition mechanism?

Important groundwork on metal-containing intermediates, i.e., their generation and spectroscopic characterization, is an essential part of this thesis. By using the capabilities of i^{2}PEPICO, a novel approach is presented to answer the above summarized questions and provide direct experimental evidence on the initial steps of gas-phase chemistry of CVD precursors. This will be helpful to determine thin film synthesis pathways more precisely and may give rise to improvements in the growth rate and film morphology (less C-incorporation) by controlling the critical reaction parameters such as pressure, temperature and gas composition. Finally, the experimental results from the novel method presented can serve as an input to model the complete CVD process and use less time-consuming experiments in future process improvement steps.

If gas-phase reactions are present it must be assured that these originate from gas-phase reaction steps rather than being adsorbed molecules that come from surface reactions of the precursor. Using a microreactor with small residence times and a high dilution of the precursor <0.01% should minimize the contribution of surface reactions to the reaction pathway. Therefore, the present approach covers the gas-phase chemistry and the precise determination and characterization of surface reactions is not within the scope of this thesis. Although not focusing on surface reactions, indirect conclusions on surface reaction residues are occasionally drawn by analyzing the gaseous composition, especially at low reaction temperatures, where surface reactions may play a role in the mechanism.

1.4 Structure of the Thesis

After the preceding introductory part, a discussion of the fundamental principles of the methods used in this thesis is presented in Chap. 2. First, the reader shall be introduced into the topic of synchrotron radiation and its beneficial properties for the analysis of gaseous samples. This is followed by a description of spectroscopic methods suitable for gas-phase investigations, such as photoionization mass spectrometry (PIMS) and photoelectron spectroscopy (PES). This discussion sets the foundation to elaborate on the advanced blended evolution of both aforementioned methods, called i^{2}PEPICO. In this context also interfering phenomena, such as dissociative photoionization (DPI), are explained. Especially the advantages of i^{2}PEPICO in comparison to conventional spectroscopic methods for the analysis of gaseous samples are highlighted.

In the preceding Chap. 3 the experimental aspects of the VUV beamline and endstation at the Swiss Light Source (SLS) synchrotron facility are covered, where all experiments were conducted that are part of this thesis. Details on the construction of the SiC microreactor are summarized and the operation procedures specific to the investigation of CVD precursors are explained. The simulation of the microreactor is challenging because of the large pressure gradient between inlet and outlet and unclear gas flow conditions inside the reactor. These aspects were investigated in cooperation with Dr. Seung-Jin Baik. Results of the simulations by Dr. Baik were used as input for data reduction procedures.

The following Chap. 4 - Chap. 6 present and discuss the main results of the synchrotron-assisted mass spectrometic investigation of the thermal decomposition of three exemplary organometallic precursors: $Al(acac)_3$ in Chap. 4, $Zr(acac)_4$ in Chap. 5 and $Fe(Cp)_2$ in Chap. 6, respectively. The results were already presented and discussed at scientific conferences and published in peer-reviewed journals [129, 130, 131] in the field of materials science and physical chemistry. Therefore, the structure of the chapters is in accordance with the original publications. Each chapter additionally contains a separate introductory paragraph emphasizing the author's contributions to the investigation.

These chapters are followed by highlighting the results obtained in this thesis in Chap. 7, containing a summary of the important findings of this work and discussion of the main insights and conclusions that are derived from the preceding investigations. The chapter closes by pointing out limitations of the presented approach and suggests areas for future investigations to either tackle the outlined weaknesses and challenges or continue the work presented. Finally, additional information on the respective chapters are given in Appendix A to Appendix C.

Chapter 2

Theoretical Background

Starting from the basics of the generation of synchrotron radiation (SR), the structure of elemental storage rings and the associated physics necessary to understand the phenomena of SR are described. The further discussion of the main radiation characteristics explains why SR, especially in the vacuum ultraviolet (VUV) range, is advantageous to analyze gaseous probes and is therefore used in this work. A general discussion on photodissociation and photoionization dynamics is presented thereafter, followed by a brief overview of spectroscopic techniques used to characterize elusive gas-phase intermediates, which exploit the ionization by photons. The chapter will conclude with an introduction to promising approaches to detect molecules with short lifetimes in gaseous samples. The focus of this discussion lies on the flash-pyrolysis technique, which was applied to obtain the main results presented in this thesis. This is complemented by an introduction to the principles of unimolecular gas-phase kinetics.

2.1 Synchrotron Radiation

2.1.1 Definition and Properties

Synchrotron radiation (SR) is generally understood as a specific kind of radiation emitted by accelerated particles. This radiation provides a constant spectrum of intense, collimated electromagnetic radiation with a well defined polarization and a quasi-continuous time structure [132, 133]. For centuries, mankind was in touch with SR by observing stars and galaxies emitting light, from which portions stem from the acceleration of elementary particles in the magnetic fields located around those astronomical objects [134]. James Clerk Maxwell started the theoretical analysis of electromagnetism in 1865, when he predicted in his pioneering study that electromagnetic radiation is emitted by transversely accelerated, charged particles, which move along a trajectory at almost the speed of light [135]. However, it was half a century later, when in 1898 Liénard first pointed out specific emission properties of this kind of radiation by presenting mathematical expressions for the quantification of the rate of energy emitted, whose relation is given by the fourth

power of the energy-mass ratio γ (Lorentz factor) [136]:

$$P \simeq \frac{2e^2c}{3r_{\text{orb}}^2}\beta^4\left(\frac{E}{mc^2}\right)^4 = \frac{2e^2c}{3r_{\text{orb}}^2}.\beta^4\gamma^4. \tag{2.1}$$

Here, P is the radiation power per particle, e is the charge of a particle, c is the speed of light, β the relativistic velocity, r_{orb} the radius of the orbit and m the mass of a particle. This equation implies that the emitted energy can reach high levels. Considering that the radiated power P scales inversely with the fourth power of the particles mass, it becomes apparent that electrons, due to their low mass, are advantageous for the generation of SR with high intensity and are therefore compared to protons predominantly used.

Given these insights and in the context of building larger electron accelerators with substantially higher energies of a few tens of MeV, the amount of energy loss due to emitted radiation is not neglectable. This is because the energy loss, according to Eq. 2.1, scales with the fourth power of the electrons energy. Therefore, the classical theory of the radiation loss of electrons traveling in circular trajectories received attention in the literature. The question arose whether those electron accelerators have an intrinsic energy limit due to radiation losses [137]. In 1944, Ivanenko and Pomeranchuk [138] formulated a mathematical expression of the rate of energy loss due to radiating electrons and hence the first formal description of SR. Shortly thereafter this radiation was firstly observed in a General Electric 70 MeV electron synchrotron [139] and its properties, such as the fourth power relation (see Eq. 2.1), the spectral distribution, geometry, angular collimation and coherence, as well as the polarization, were thoroughly summarized by Schwinger in 1949 [140]. Those insights were later utilized in the 1960s for the construction of the first generation electron storage rings and the parasitic use of SR by beamlines to investigate a wide variety of problems in physics, chemistry and materials science [141].

2.1.2 Generation

Modern synchrotrons of the third generation, as depicted in Fig. 2.1, consist of six main components to accelerate electrons to relativistic speeds of several GeV and exploit the broadband synchrotron radiation [133, 142, 143]:

(1) **Injection system**: First, electrons are produced in the electron gun by using a hot filament. These are then further accelerated in a linear accelerator (LINAC) to about 100 MeV, which forces the electrons to build small discrete packets ("bunches"). These bunches have an elliptical shape with the length of a few centimeters, roughly consisting of 10^{10} electrons that are responsible for the well-defined, pulsed time structure of SR in the hundreds of MHz range, generating photon pulses with a duration of up to 100 ps.

(2) **Booster ring**: This section is used to further accelerate the bunches of electrons after leaving the electron injection unit by forcing them on a circular

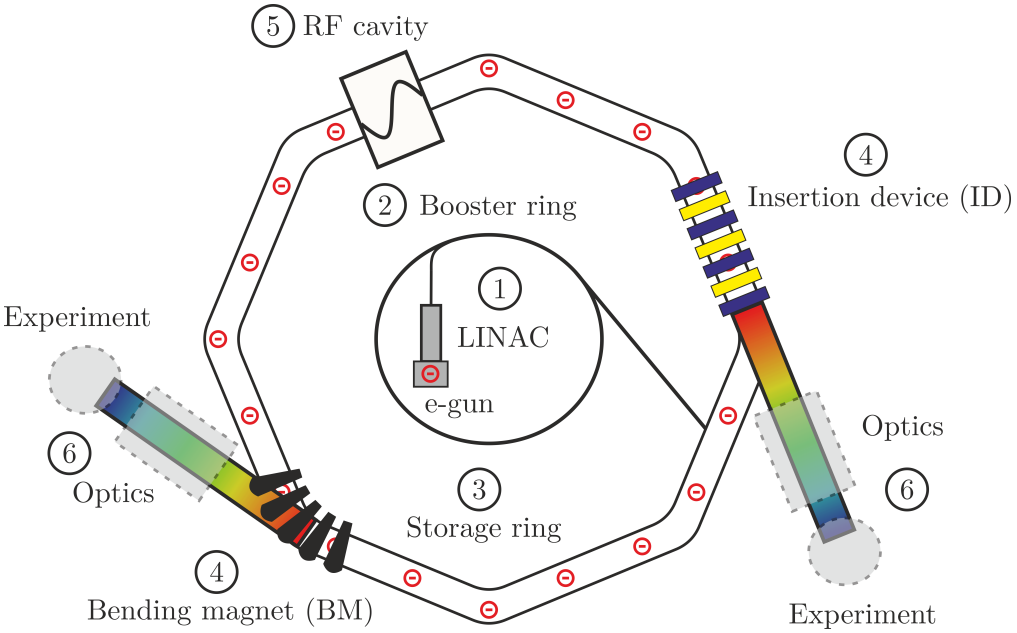

Figure 2.1: Schematic of the most important parts of a third generation synchrotron, based on [142]. The devices numbered from (1) – (6) are further explained in the text.

motion using bending dipole magnets. The stored bunches of electrons are then periodically injected into the storage ring to maintain a constant ring current. Usually this is done in top-up operation mode, where electrons are accelerated to the same energy as they have in the storage ring, which allows an uninterrupted user operation.

(3) **Storage ring**: This part contains the electrons moving in circular paths by using an array of magnets to constitute the ring magnetic lattice. Due to a possible collision with residual gas molecules, and the resulting unwanted electron loss, storage rings are operated under ultra high vacuum, below 10^{-9} mbar. For instance the Swiss Light Source (SLS) storage ring is operated at an electron energy of 2.4 GeV and has a circumference of 288 m.

(4) **Major source components**: These devices are built in specific sections of the storage ring in order to generate synchrotron radiation by passing them. (a) The bending magnets (BM) are dipole magnets working in opposite directions, which are used to deflect the electrons in the arced sections of the storage ring. This generates a broad spectrum and good photon flux. (b) Insertion devices (ID), such as undulators and wigglers, are a series of alternating magnet poles constructed in the straight lines of the storage ring, which force a sinusoidal trajectory to the electrons leading to high photon energy and flux, as well as a brighter and a more focused radiation. Additionally, the radiation is linearly polarized in the plane of the storage ring and elliptical polarized out of plane. Radiation in the monochromatic vacuum

ultraviolet (VUV) spectral range from 6-12 eV is particularly useful for valence shell photoionization experiments. The radiation can therefore serve as a useful source for spectroscopy of valence and even inner shell electrons [141]. To generate photon energy in the VUV range BMs are used because they cover a broad spectral range at narrow vertical angular divergence of $1/\gamma$. This results in collimated light, especially useful for photoelectron experiments that were conducted in this work.

(5) **Radiofrequency cavities (RF)**: For every turn in one cycle the electrons in the storage ring loose energy in form of synchrotron radiation. Integration of Eq. 2.1 over an isomagnetic storage ring with a constant orbital radius of the arc r_{orb} and a ring current j results in an expression for the amount of electron energy loss P_{tot} in one turn in engineering units [142, 143]:

$$P_{\mathrm{tot}}[\mathrm{W}] \cong 88.5 \cdot \frac{E^4[\mathrm{GeV}]}{r_{\mathrm{orb}}[\mathrm{m}]} \cdot j[\mathrm{mA}]. \tag{2.2}$$

For a machine with an electron energy of 2.4 GeV (SLS), using the definition of the orbit radius according to

$$r_{\mathrm{orb}}[\mathrm{m}] = 3.34 \cdot \frac{E[\mathrm{GeV}]}{B[\mathrm{T}]} \tag{2.3}$$

and a magnetic field strength B of 1.4 T, the energy loss per cycle can be calculated to be approximately 205 kW. This energy loss must be replaced by RFs which supply the electrons the extra amount of energy needed to replenish and keep them on a stable trajectory inside the storage ring. The frequency used is typically on the order of a few MHz (SLS: 500 MHz).

(6) **Optics and experimental endstations**: Since the bandwidth of the emitted synchrotron radiation from bending magnets is too broad for high resolution spectroscopic experiments, optical elements must be used in order to tailor the beam, such that only distinct photon energies can be selected. This tunability is especially useful for photoionization experiments because it permits to measure close to the ionization threshold, without fragmentation interference.

In summary, the excellent tunability due to a wide spectral distribution from infrared to X-ray, the low divergence of $1/\gamma$ minimizing the ionization volume, the pulsed nature of the emitted light with an accurate repetition rate, together with a stable photon flux over a long timescale, offer a wide variety of options for spectroscopists. Especially the specific ranges of the BM radiation, such as the radiation in the VUV range, can be exploited for photoionization experiments, and is therefore utilized in this thesis.

2.1.3 VUV Beamline at the SLS

Since most of the results presented in this thesis were obtained at the SLS storage ring in Switzerland, some important facts and features of the VUV beamline attached to it are summarized here. In the storage ring, an electron energy of 2.4 GeV at a ring current of 400 mA is generated by 36 dipole magnets, which are separated in 12 groups of three triple bend achromats, which deflect the electron beam. The magnetic field strength of the dipole magnets is 1.4 T, which are build on a circumference of 288 m. In total 177 quadrupole magnets focus the beam to an equilibrium emittance[1] of 5.5 nm rad^{-1}. The facility contains nine undulator and eight bending magnets in operation giving a total of 18 experimental endstations that are used to tackle a wide variety of problems in chemistry, physics, biology and materials science [144].

One of those endstations is the X04DB VUV beamline which was used to perform the measurements reported in this thesis. An exemplary layout of a system of optical elements used to control the angular acceptance by specific apertures, block hard X-ray radiation by appropriate filters and focus, as well as monochromatize the molecular beam to utilize VUV synchrotron radiation of desired properties in the experiment, is displayed in Fig. 2.2 [145]. As described in the previous section, synchrotron radiation from bending magnets is characterized by a wide energy spread with unequal distribution and is horizontally diverging with an angle of 8 mrad at the SLS. Since the experiments for studying chemical mechanisms and kinetics require precisely tunable monochromatic light at a high resolution, special optical devices (see Fig. 2.2 (6),(8),(9)) are used to tailor the beam, while a ring (4) and a lead shield (7) work to prevent high energetic deflections from the storage ring to the beamline.

The power of the emitted beam from the BM (1) is on the order of 200 W and can be controlled by two entrance slits (2) and (3) in vertical and horizontal direction. By adjusting the photon flux, one can avoid a saturation of the spectroscopic devices in the experimental endstation. While the distribution of BM radiation is independent from the photon energy (i.e., wavelength of the radiation) in horizontal direction, its vertical characteristics are strongly influenced by the photon energy [145]. Having high energy, X-ray radiation is mainly emitted in the plane and the less energetic VUV radiation contains trajectories above and below the plane of the storage ring. This calls for a high vertical acceptance of the beamline optics. Therefore, a water-cooled copper rod (5) is placed centrally to the beam eliminating most of the X-ray photons in the area of ± 0.2 mrad, but allowing most of the VUV photons to pass, while the beam energy is reduced to ≈ 53 W. This measure decreases the heat load on the optical elements (6), (8) and (9) and avoids their deformation during operation, which would otherwise lead to beam instability.

Afterwards, the beam reaches the first optical component of the monochromator, a platinum-coated copper mirror (6). This mirror serves to tremendously decrease

[1] Refers to the area occupied by the beam in a position and momentum phase space. As a rule of thumb one can say that if the emmitance is high, the brightness of the beam is high.

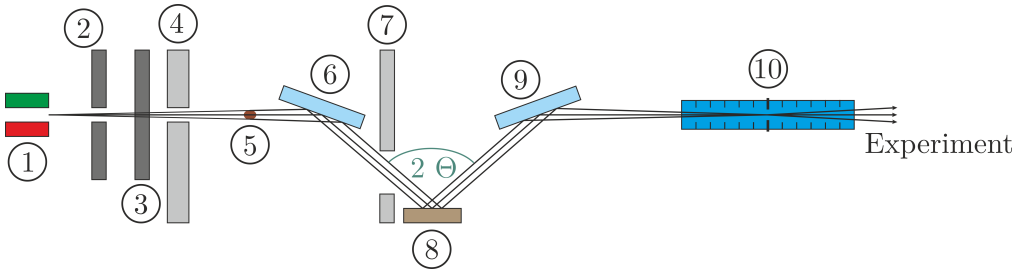

Figure 2.2: Schematic of the VUV beamline at the SLS based on [145]. The purpose of the devices numbered from (1) - (10) is further explained in the text.

the photon beam energy by almost 98% and owns a high reflectivity in the VUV range, blocking radiation with energies >150 eV. In this spectral range, grating monochromators are the first choice to generate a small bandwidth of radiation from a high incoming band, since, depending on the gratings installed, their reflection covers photon energies from a few eV up to 2000 eV [146]. To obtain VUV radiation from 5-30 eV at the SLS endstation, the reflected beam hits a 150, 600 or 1200 lines/mm silicon grating (8), which acts as a dispersive element and is responsible for tuning the wavelength λ and therefore its energy according to:

$$m \cdot \lambda = 2 \cdot d \cdot cos(\Theta) \cdot sin(\phi). \tag{2.4}$$

Here, m is the diffraction order, d the line spacing and Θ and ϕ the constant deviation and scan angle. Depending on the grating used, one can tune the resolution $E/\Delta E$ and photon flux, as well as energy range without breaking vacuum [145]. Higher grid line densities lead to lower photon fluxes, while the resolution increases. As a compromise between flux and resolution and to cover the ionization potentials of most of the expected products, a grating with 150 lines/mm was used in all experiments. Hence, a resolution of $E/\Delta E = 1500$ and a photon flux of $5 \times 10^{11}\,\mathrm{s}^{-1}$ is achieved at 7.882 eV [145].

After being tailored by the dispersive element, the collimated beam is then refocused by a second platinum-coated silica mirror (9) into a rare gas filter (10). Having higher harmonic radiation, this gas filter serves to block these harmonics by using a mixture of noble gases in a differential pumped system. Additionally, a MgF_2 window can also be used to block radiation above 11 eV, which is especially useful for the investigation of molecules having ionization energies below 8.0 eV. After passing a vertical exit slit, which is adjustable between 110 and 1000 µm, the beam can be utilized in the ionization volume of the experimental endstation. Details on the last part of the endstation, including the gas filter, are given in Sec. 3.1.

2.2 Spectroscopic Techniques

In order to reach the listed goals in Chap. 1, a quantitative, highly sensitive, fast and selective detection method to *in-situ* monitor the early stages of thin film deposition in the gas-phase is needed. The method should be able to track the fate of stable and reactive molecules and therefore provide a more profound picture of the associated reaction mechanism. All four criteria are met by a combination of photoionization mass spectrometry (PIMS) and threshold photoelectron spectroscopy (TPES) at imaging conditions, commonly referred to as double imaging photoelectron photoion coincidence spectroscopy (i^{2}PEPICO). The basic approach and principles behind both methods, as well as their combination, are discussed in this section.

2.2.1 Photoionization Mass Spectrometry

A potential energy diagram of a photoionization process of an exemplary diatomic molecule is depicted in Fig. 2.3. Here, on the left side, the transitions from the ground state neutral molecule AB to different excited states of the cation are shown. Upon a gradual increase of the molecules excitation by synchrotron radiation and only if the photon energy is high enough for the electron to be released form the valence shell of the molecule AB, a cation in its ground state $AB^+(X)$ and an electron e^- are formed [147]:

$$AB + h\nu \rightarrow AB^+(X) + e^-. \tag{2.5}$$

This process is called photoionization and the mass-selective detection of the corresponding ions, is denoted photoionization mass spectrometry (PIMS). The minimum photon energy, which is required to ionize the molecule AB in such a process is defined as the adiabatic ionization energy IE_{ad}. Its values are on the order of 8-12 eV for most of the organic molecules, whereas open-shell molecules (radicals) have generally lower ionization energies because the unpaired electron destabilizes the initial state. This holds also for larger compounds, such as metal β-diketonates and metallocenes.

If the photon energy exceeds the ionization energy, also fragmentation can occur, such that a fragment ion is formed from the parent ion. Although this ion is then probed from complex chemical mixtures, it is formed due to ionization and not a real product of the reaction that is under investigation. If one gradually increases the photon energy and tracks the intensity of the parent ion using a mass spectrometer with Wiley-McLaren space focusing optics [149][2], photoionization efficiency curves (PIE) are obtained (see Fig. 2.3, right).

If the excitation energy exceeds the adiabatic ionization energy IE_{ad}, higher vibrational states can be occupied, leading to a stepwise increase in the PIE curves

[2]This technique allows fast and slow ions of the same mass to arrive at the same time on the detector.

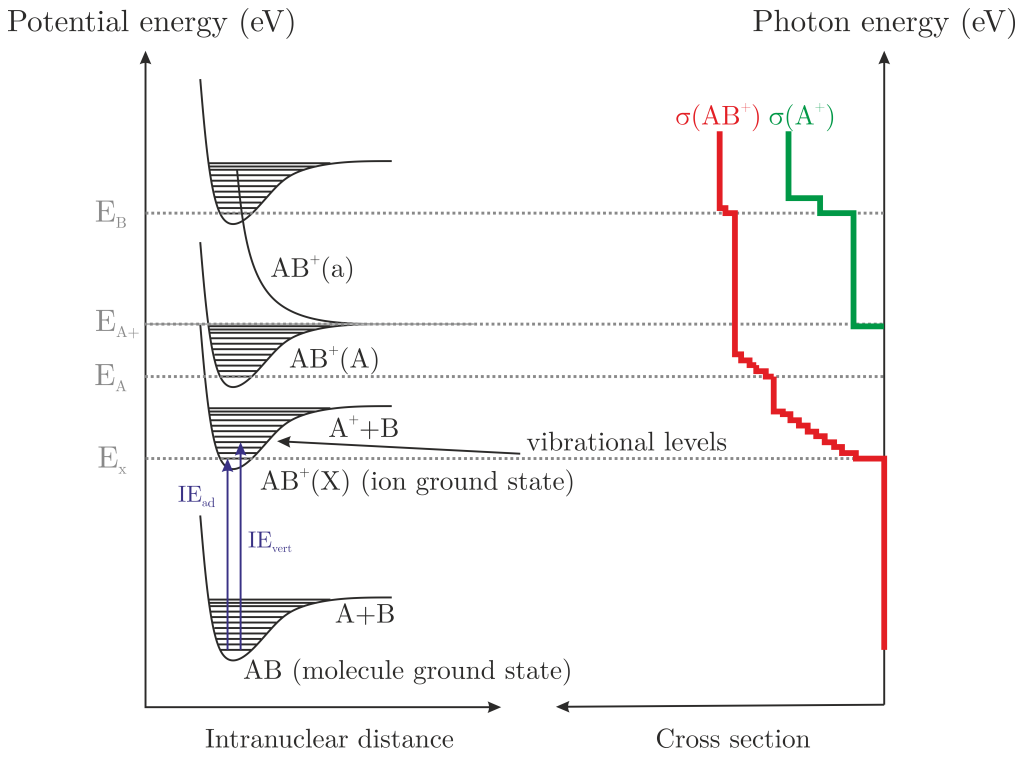

Figure 2.3: Schematic of a typical photoionization process of a diatomic molecule AB. Left: single photon ionization to distinct ion states; right: sketch of an idealized photoion yield curve for those transitions (based on [148]).

(see right side of Fig. 2.3). The most intensive transition of the cationic ground state $AB^+(X)$ to form an ion in a configuration which is the same as that of the equilibrium geometry of the ground state neutral molecule[3] is defined as vertical ionization energy IE_{vert} which is also a distinct parameter given in the literature for various organic and inorganic molecules. After ionization of a specific molecule, the ion signal sharply increases close to the ionization threshold because the probability of ionization, represented by the absolute photoionization cross section σ, increases. For large molecules, having many transitions, the onsets in the associated PIE curves can be used to approximately determine the adiabatic ionization energy IE_{ad} by a simple linear extrapolation method with an exponent of unity, a slope m and the crossing with the y-axis denoted as b [150, 151, 152]:

$$\sigma(h\nu) = m \cdot h\nu^1 + b. \tag{2.6}$$

Given the knowledge of the ionization thresholds, it is possible to identify and characterize specific molecules in a gaseous sample according to their ionization energies [153]. Additionally, if σ is known, for instance from specific databases [154, 155], quantitative measurements of various species in the sample are also possible. However, especially for elusive intermediates, ionization cross sections are

[3]This is the transition with the highest Franck-Condon factors, i.e., those with the greatest overlap integral of the respective vibrational wavefunctions.

often not available, since their generation and detection in sufficient amounts is difficult. Especially photon energy-dependent ionization cross sections $\sigma(h\nu)$ of CVD precursors and their decomposition products are scarce, unlike for stable molecules involved in flame chemistry, for which there are copious data [156, 157, 158].

Three of the criteria discussed in the introductory paragraph of this thesis can be met by PIMS. Given that the cross sections are known, the method is quantitative, as other mass spectroscopic methods, highly sensitive and in part selective because the soft ionization provided by synchrotron radiation as energy source allows for the suppression of fragments by tuning the photon energy close to the specific ionization thresholds, working in part isomer-selective. PIMS also offers the possibility to obtain three-dimensional datasets with variations in temperature, photon energy and mass-to-charge ratio to derive temperature-dependent species profiles and track the evolution of specific species in complex CVD reaction environments. Yet, due to several reasons discussed in the following section, Sec. 2.2.2, the characterization of species from complex reaction mixtures by various types of photoelectron spectroscopy provide a higher accuracy in the exact determination of species molecular fingerprints and therefore deliver isomer-selectivity.

Although the applicability of PIMS is quite versatile, a possible ionization event, called dissociative photoionization (DPI), can occur. This means the fragmentation of the cation and therefore an increased difficulty in the characterization of neutral species that were initially present in the sample. By taking into account the simple diatomic example in Fig. 2.3, dissociative ionization can be observed if the excitation energy is higher than the bond energy of the cation $AB^+(A)$[4]. According to the anharmonic approximation[5], the vibrational bands of the cation converge towards the bond dissociation energy. Therefore the fragment ions A^+ and B are formed:

$$AB^+(A) + h\nu \rightarrow A^+ + B. \tag{2.7}$$

Crossing the energy barrier to the vibrationally excited state $AB^+(A)$ leads to a stepwise increase in the corresponding idealized PIE curve (see Fig. 2.3, right). Here, DPI gives rise to a signal emerging from the newly formed cation A^+, while the neutral fragment B according to Eq. 2.7 is also generated, but not detected. The direct dissociation with photon energies above $E(A^+)$ yields another PIE curve (green) for the fragment ion A^+. Its appearance energy (AE) is defined as the activation barrier for the breakage of the weakest bond in the cation (see Eq. 2.7).

The process of dissociative ionization is often observed in high energy ionization methods with energies higher 20 eV, for example electron impact ionization. This is a common problem in species identification because in conventional electron ionization mass spectrometry one can hardly distinguish from the mass spectra, whether the measured signals correspond to parent ions that emanate from direct ionization, or are in fact induced by daughter ions formed by DPI. This issue occurs because the

[4]This process should not be confused with photodissociation, which occurs when solely UV photons are utilized to trigger a bond break in a neutral molecule.

[5]A concept from classical mechanics assuming that in an oscillator, the restoring force is not linear to the atomic spacing.

precursor can undergo DPI to form fragments which have the same mass-to-charge ratio as possible reactive intermediates formed due to thermal excitation. Also at incomplete conversion of the precursor, while scanning the photon energies beyond the appearance energy (AE) of a specific precursor, dissociative ionization (DPI) cannot be prevented and must be accounted for, when species profiles are evaluated. It is therefore essential to elucidate the precursor cation's fragmentation pattern in detail by at least a determination of its room temperature appearance energies. This is to understand the precursors pathways of dissociative ionization in order to accurately judge on ion signals collected in pyrolysis experiments. As will be discussed later in Sec. 2.2.4, photoelectron spectroscopy combined with imaging techniques can help to address this issue experimentally.

2.2.2 Photoelectron Spectroscopy

Although PIMS is quite sensitive with respect to isomer-specific characterization, mass-selectivity alone cannot provide the full picture of the chemical mechanism in a reactive sample. For instance, in the case of two molecules having the same mass and close ionization energies one cannot successfully resolve their molecular structure by PIMS because the onsets in the PIE curves do not have an idealized staircase structure (see Fig. 2.3). In reality, a continuous increase is observed, which is detrimental for the accuracy of the determined ionization threshold. Therefore, other methods must be combined with PIMS to improve the analysis.

Photoelectron spectroscopy (PES) is an indispensable tool to study the photodynamics of open-shell molecules. Since most of the excess kinetic energy is transported away by the photoelectron, information of the electronic structure of the remaining cation can be obtained. Based on the photoelectric effect, it can be observed that upon excitation by electromagnetic radiation the energy balance is shared between the absorbed adiabatic ionization energy of the molecule IE_{ad}, the internal energy of the cation E_{ion} (vibrational, rotational), as well as the kinetic energies of the ion and electron, respectively. Considering the energy balance one obtains the following relation:

$$\epsilon_{kin} + E_{ion} = h\nu - IE_{ad}. \tag{2.8}$$

In conventional photoelectron spectroscopy lightsources with sufficient intensity at a fixed wavelength, as provided by He discharge lamps (21.22 eV), are used [124]. This energy is sufficient to analyze most of the valence orbitals because the majority of ionization energies is within the energy range applied. The photoelectrons kinetic energy distribution is then captured using an electron energy analyzer which tracks the electron signal by applying a range of electric fields in a hemispherical deflection analyzer. The most recent construction methods achieve a resolution of 10-30 meV [159].

By applying Eq. 2.8 one can obtain information on the ionization energy of the molecule and the vibrational structure of the corresponding cation. As already discussed, the ionization energy is defined as the negative binding energy of the

ejected electron, which is in the case of valence orbitals weekly bound. The most intense transition equals the vertical ionization energy IE_{vert}, whereas the lowest energy corresponds to the previously introduced adiabatic ionization energy IE_{ad}. Although PES can obtain information on both ionization thresholds, no information on the cations mass is obtained, such that the nature of the corresponding molecule remains unclear. This is especially the case when transitions to non-bound electronic states, in other words DPI, occurs. In addition, samples containing a complex mixture of many constituents, as usually probed in thermal decomposition studies of complex precursors, can hardly be interpreted due to the missing mass dimension. This is mainly because of the difficult ion extraction, since electric fields, necessary for ion sampling, are almost always absent in PES systems. In addition, due to the limited resolution, rotational energies in the cation cannot be resolved. However, the missing information can be obtained by adding mass-selectivity to the method which is intrinsic in mass-selective threshold photoionization techniques. This topic will be discussed later in this chapter. In addition, although the photoions from a reaction mixture can, in principle, be collected by their m/z ratio, conventional PES provides only information on the kinetic energy of the photoelectrons. This results in a series of often overlapping photoelectron spectra of neutrals in the reaction mixture whose analysis is tedious [160]. Therefore conventional photoelectron spectroscopy, without any modifications, is not an attractive method to study mixtures of neutral species as found in the thermal decomposition of CVD precursors.

2.2.3 Threshold Photoelectron Spectroscopy

A major disadvantage of PES is the low collection efficiency of electrons, since most of the energetic electrons enter the electron analyzer under a variety of angles and do not reach the final aperture. Thus, the collection efficiency, and therefore the resolution of the instrument mainly depends on the initial energy of the energetic electrons. High energies correspond to low efficiencies and *vice versa*. Therefore, the method of conventional PES leads to very low collection efficiencies below 0.1% [124]. It becomes apparent that the resolution barrier of conventional PES does not allow to resolve vibrational progressions of a molecule. Because of that, some improvements were made to the original technique of PES which are based on the idea to discriminate between energetic and near-zero energy electrons, so called threshold electrons, and obtain threshold photoelectron spectra. This is corroborated by the observation that threshold electrons benefit from intrinsically higher collection efficiencies than energetic electrons, which makes a method, detecting only threshold electrons, more efficient. By definition, threshold electrons are produced at the ionization threshold when the photon source is on-resonance with the electrons. At this point, their yield considerably increases, providing the ionization thresholds of a molecule as a function of photon wavelength. Since this method necessitates to scan the photon energy and scan through the ionization thresholds of a molecule, instead of a continuum light source, one needs a tunable monochromatic light to account for all of the ion states. As has been discussed in the previous subsection

Sec. 2.1, synchrotron radiation can fulfill such a demand and is therefore frequently used in threshold photoelectron experiments [161].

In comparison to PES, not only the energy source but also the collection method of the electrons has to be modified in order to collect only threshold electrons with satisfactory precision and resolution. The first approach was presented by Villarejo et al. [162] who added an electron extraction region by applying a relatively weak constant electric field of $3\,\mathrm{V\,cm^{-1}}$. Electrons were accelerated to a specific energy and refocused onto an entrance slit that only allowed electrons having the same energy to pass, before entering the electrostatic analyzer. This method, however, did not exceed the resolution obtained by photoelectron spectroscopy at that time (50 meV) and the energy spread of the threshold electrons was relatively high (10%). Some inventions followed which improved the resolution by a reduction of the thickness of the ionization region. This lowered the dispersion of electrons leaving the ionization region to 150 meV and therefore improved the resolution to 35 meV, yet they suffered from low signal levels [163, 164].

Other solutions to improve the method of threshold photoelectron spectroscopy (TPES) using an electrostatic analyzer, are either not applicable for coincidence studies [165] or suffer from low collection efficiencies due to electrical fields applied [165, 166] and the low mass resolution of the ions [167]. Besides these approaches, another solution where the electrons are detected by their time-of-flight (ToF) [168] using Wiley-McLaren space focusing conditions was established [149]. This approach does not only erase the aforementioned energy spread due to a high voltage drop in the ionization region but also avoids the collection of energetic electrons whose velocity vector points towards the detector and therefore contributes to the threshold electron signal. These so called “hot electrons” are responsible for asymmetric peaks towards higher energies in the spectra and increase the background signal [124]. Applying the discussed method, coincidence studies [167], i.e., analyzing electrons and ions from the same ionization event at the same time, are possible and the resolution of the photoelectron spectra are only limited by the photon bandwidth of the lightsource used.

2.2.4 Imaging Photoelectron Photoion Coincidence Spectroscopy (iPEPICO & i^{2}PEPICO)

As neither PIMS, nor PES, nor TPES provide the full information on electrons and ions that are formed upon a single ionization event, a blend of those methods is necessary to exclude the detection of any false products. A possible solution is to detect photoelectrons and photoions in coincidence and also measure the kinetic energy distributions of both by appropriate imaging techniques. The possibility to also analyze the ions tackles the basic problem of mass-selectivity inherited to PES and gives possibilities to apply coincidence studies on complex mixtures of neutrals to determine single ionization energies and explore fragmentation patterns.

This is even enhanced when velocity map imaging (VMI) is used for a measurement of the kinetic energy distribution of both electrons and ions. Here, charged

particles are focused according to their velocity at a right angle to their extraction axis, irrespective of their origin within the ionization region. Those particles are then collected on imaging plates, on which rings with specific radii, corresponding to the electron's initial kinetic energies, are displayed [169]. For the electrons, this represents an effective method to extract them, enables one to account for hot electron contributions and is also taking care of the collection efficiency issue of electrons from the relatively large ionization regions. If one combines VMI with the collection of threshold electrons, the electron intensity increases by a factor of ten and the resolution by a factor of two. In addition, more insightful coincidence studies are also possible, as well as narrow ion ToF peaks can be achieved because of the considerable higher electric fields applied compared to conventional PES [170]. However, in earlier setups, hot electron contributions were only minimized but not avoided. A major challenge associated with coincidence studies of threshold electrons and ions after enhancing both the ion collection efficiency and high photoelectron resolution by VMI methods, is the prevention of hot electron detection. This was solved by Sztáray and Baer [171] who established a threshold photoelectron study with velocity map imaging and suppressed hot electron contribution by using a multi-channel plate[6] with two anodes, collecting the center (threshold & hot) and ring (hot) electrons.

As has already been outlined, it is also beneficial to probe the photoions associated to a specific ionization event and examine their kinetic energy distribution. This is because it adds another analytical dimension to the dataset, providing the possibility to distinguish between cold rethermalized background and hot molecular beam ion signals. This additionally provides the ability to characterize a broad kinetic energy release of ions which is associated to fragments rather than directly ionized species. Hereby, DPI patterns can be explored and reaction pathways can unambiguously be identified. Given these advantages, based on an early concept [172], a specific coincidence experiment was developed by Bodi et al. which benefits from a combination of the electron kinetic energy analysis and the ToF analysis of ions, utilizing the imaging of both charged particles on position-sensitive detectors [173, 174]. Such a method, where also the ions are velocity map imaged, is termed double imaging photoelectron photoion coincidence spectroscopy (i^{2}PEPICO). This method allows to study ionization energies and species formation in multi-species mixtures at high ionization rates by collecting both electrons and mass-selected ions in delayed coincidence [173].

Since photoionization mechanisms, especially of bigger molecules such as CVD precursors, are complicated and often include competing parallel pathways that have to be considered, one needs a method to distinguish between the detection of artificial molecules, due to the dissociative photoionization and directly ionized molecules that were present in the sample [127, 129, 130]. Reconsidering the capabilities of i^{2}PEPICO, these criteria are met. By using this method one can distinguish between dissociative and direct ionization with high certainty. The

[6] A device to detect single particles, for instance electrons and ions.

presented i^{2}PEPICO technique therefore allows to execute threshold photoelectron spectroscopy on mass-selected parent ions, which is a great opportunity when problems of thermal decomposition of CVD precursors are addressed. Consequently, this experimental method is mainly used to obtain the results shown in Chap. 4, Chap. 5 and Chap. 6.

2.3 Probing Gas-Phase Intermediates

The main objective of this thesis is to determine the major species formed in the gas-phase. A common approach is to rely on macroscopic system parameters as, for instance, the temperature and pressure in the reactor, as has been done in previous kinetic studies analyzing the growth rate of CVD processes [175, 176, 177, 178]. Due to the experimental techniques applied, for the most part, stable species were probed. As an extension to previous investigations, in this thesis an *in-situ* mass spectrometric analysis coupled to photoionization, is used. The main advantages of this approach, such as the high sensitivity without exhibiting massive fragmentation of the ions, was already explained in the previous section. However, the *in-situ* detection of elusive, highly reactive intermediates, which are a major player in the gas-phase chemistry, are not straightforward. In this section, ways are presented to probe and analyze those molecules with high efficiency, and an experimental environment for their collection and evaluation is discussed.

An essential requirement to investigate chemical reactions in the gas-phase, containing highly reactive intermediates that are ejected from a tubular reactor to perform qualitative and quantitative kinetic investigations, is an appropriate sampling method. The method must not only conserve the chemical composition of the sample leaving the reactor, but also enable to efficiently detect reactive intermediates. In addition, this should be accompanied by a sufficiently high signal intensity of the source signal, even at low concentrations in the gaseous composition to be analyzed. Since radical-radical reactions are mainly driven by molecular collisions, the mean free path λ_{mean}, i.e., the average distance a particle travels before its collision with another particle, is an important factor to be considered. From kinetic gas theory, assuming the ideal gas law, one obtains:

$$\lambda_{\text{mean}} = \frac{k_{\text{B}}T}{\sqrt{2}\pi\sigma^2 p}, \tag{2.9}$$

where k_{B} is the Boltzmann constant, σ is the Lennard-Jones parameter, in other words the particle diameter of a soft sphere, T the temperature and p the pressure. The higher λ_{mean}, the lower is the probability for two particles to collide. A beneficial relative lack of collisional perturbations can be found in so-called free molecular flows where the chemistry is considered as “frozen”, meaning that no further bimolecular reactions occur.

A common way to transform a flow into a free molecular flow is by generating a supersonic, continuum jet expansion from a high-pressure source (here, the reactor

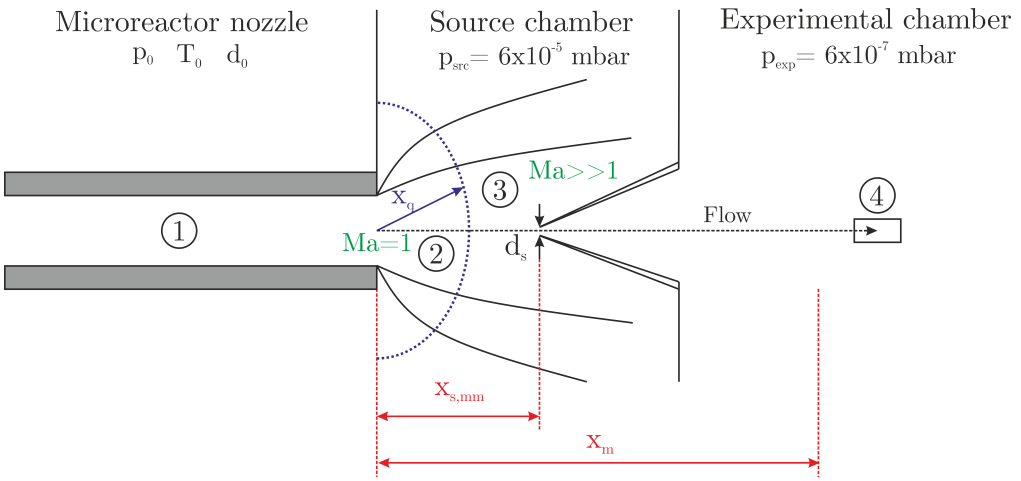

Figure 2.4: Schematic of the molecular beam sampling method. A supersonic expansion (2) is formed by expanding a gas mixture from a nozzle (1) with diameter d_0. Its characteristic shock waves form a free molecular flow region (molecular beam). The transition between continuum and free molecular flow is denoted as "quitting surface" (3). The sampling cone with diameter d_s is sketched to indicate that the analysis of the gaseous composition takes place downstream within the ionization volume (4). The dashed streamline indicates the direction of the flow (in accordance with [182, 183]).

(1) in Fig. 2.4) into a low-pressure background where the flow transits into the desired molecular flow regime. Right in this region, a sampling cone is inserted. For this purpose and since spectroscopic investigations can often only be performed in ultra-high vacuum environments, the gas leaving the reactor being at low vacuum to ambient condition, exhibits a mandatory multi-stage differential pumping, i.e., pressure levels are reduced to ultra-high vacuum at 10^{-7} mbar. Such an expansion in the first stage forms a molecular beam (see Fig. 2.4) after passing a specific threshold area (3) [179, 180] where the randomly oriented motion of the molecules, due to their thermal energy inside the reactor, is almost completely converted into kinetic energy directed towards the beam propagation axis [181]. In terms of energy conservation this reads:

$$h_0 = h + \frac{v^2}{2}. \tag{2.10}$$

According to Eq. 2.9 and assuming for the reactor part (1) of the system in Fig. 2.4 an average pressure $p_0 = 1500\,\mathrm{Pa}$ and a maximum temperature $T_0 = 1200\,\mathrm{K}$ the mean free path can be calculated for an inner diameter $d_0 = 1\,\mathrm{mm}$. One obtains for two typical carrier gases used in spectroscopy, namely helium ($\sigma_{\mathrm{He}} = 2.66 \times 10^{-10}\,\mathrm{m}$) and argon ($\sigma_{\mathrm{Ar}} = 3.33 \times 10^{-10}\,\mathrm{m}$) [182] values for the mean free path of $\lambda_{\mathrm{He}} = 3.51 \times 10^{-5}\,\mathrm{m}$ and $\lambda_{\mathrm{Ar}} = 2.24 \times 10^{-5}\,\mathrm{m}$. Since the aperture of the gas reservoir to the background chamber $d_0 = 1\,\mathrm{mm}$ is a factor of 30 higher, the flow situation at (3) is that of a continuum free jet expanding from a high-pressure source to a

low-pressure background chamber, since $\lambda_{\text{mean}} \ll d_0$.

There are two distinct features of supersonic free jets that are beneficial. First, the velocity increases along the flow axis. Second it even increases faster than the speed of sound. An isentropic region, called "zone of silence" is formed along the centerline of the jet (see Fig. 2.4 (2)). In order to describe the expansion physics of free molecular beam jets, one assumes an isentropic free expansion of the gas while it transits smoothly from continuum to free molecular flow. The latter one is advantageous, most importantly because in a free molecular flow particle collisions are reduced and the molecules do not chemically react. Therefore the composition at the outlet of the reactor is conserved [182]. However, the transition from continuum to free molecular flow (3) is not instantaneous and must be considered when choosing the distance between the reactor outlet and the sampling device, which the gas will pass, before entering the spectroscopic analysis apparatus (4).

2.3.1 Free Jet Physics

The nature of a free jet expansion is that the enthalpy is almost completely converted into directed kinetic energy (see Eq. 2.10). That is an acceleration of the flow to supersonic conditions with $Ma>1$ in the central part of the expansion (see Fig. 2.4). This is a good approximation as long as the flow remains in the continuum region of the expansion (2). In this case, the one-dimensional isentropic relations of an ideal gas with constant heat capacities give the following expressions for the thermodynamic variables T, p, v and ρ [182]:

$$\frac{T}{T_0} = \left(1 + \frac{\gamma - 1}{2} Ma^2\right)^{-1}, \tag{2.11}$$

$$\frac{v}{v_\infty} = Ma \left(\frac{\gamma - 1}{2}\right)^{1/2} \left(1 + \frac{\gamma - 1}{2} Ma^2\right)^{-1/2}, \tag{2.12}$$

$$\frac{p}{p_0} = \left(1 + \frac{\gamma - 1}{2} Ma^2\right)^{-\gamma/(\gamma-1)}, \tag{2.13}$$

$$\frac{\rho}{\rho_0} = \left(1 + \frac{\gamma - 1}{2} Ma^2\right)^{-1/(\gamma-1)}. \tag{2.14}$$

In the above written equations v_∞ is the terminal velocity which is reached in the area, where no further cooling of the molecules in all internal degrees of freedom (translational, rotational, vibrational), occurs [184]. The ratio of heat capacities $\gamma = c_p/c_v$ is equal to 1.667 for an ideal monatomic gas, such as the noble gases used in this study. The expressions for the state variables are given solely as a function

of the Mach number Ma which is defined as the velocity of the gas divided by the propagation of sound in a gas. The speed of sound can be expressed as:

$$a = \sqrt{\frac{\gamma RT}{Ma}}, \tag{2.15}$$

where $R = 8.314\,\mathrm{J\,kg^{-1}\,K^{-1}}$ is the universal gas constant which yields:

$$Ma = \frac{v}{a}. \tag{2.16}$$

Considering the above given relations Eq. 2.11 to Eq. 2.14, it can be stated that the temperature, density and therefore the collision frequency decrease continuously with distance from the expansion source. In contrast, the axial velocity is rapidly increasing and asymptotically approaching its terminal speed v_∞. The velocity distribution is characterized by a Boltzmann distribution of the mean value in both directions, parallel and perpendicular to the streamlines with an almost Gaussian shape for the first one and a superposition of two Gaussians for the latter one. Here, the temperature is the connecting parameter and $T_\parallel = T_\perp$ is valid. Additionally, collisions with walls, clustering or striking events with background gas molecules or the sample device may attenuate the beam intensity and broaden the velocity distribution [182].

The propagation length x_m of the Mach disc in Fig. 2.4 is often much longer than the transition zone x_q which represents the boundary between continuum and free molecular flow region. This location is reached quite fast, due to the strong acceleration of the flow in axial direction. In the transition region of finite size (3), modeled as discrete "quitting surface" [185], the cooling of the internal states terminates. This is represented by the temperature parallel to the streamlines $T_\parallel$ which is, in other words, nothing else than the spread in parallel velocities. At this point, the transition to free molecular flow comes into play, where the description of the flow by continuum mechanics is not appropriate to analytically examine the properties of the flow in the centerline, i.e., where the molecular beam is sampled and analyzed. Its location can be approximated using the correlations for the terminal parallel speed ratio $S_{\parallel,\infty}$ suggested by Miller from a heated source in terms of the dimensionless Knudsen number $\mathrm{Kn}_0 = \lambda_0/d_0$ [182]:

$$S_{\parallel,\infty} = A\left[\sqrt{2}n_0 d_0 \pi\sigma^2\right]^B = A\left[\mathrm{Kn}_0^{-1}\right]^B, \tag{2.17}$$

where n_0 is the number density of molecules in the source, $\pi\sigma^2$ is the cross section of a hard sphere, and the dimensionless parameters A and B were analytically derived by Beijerinck and Verster [185], who suggest to set $A = 0.527$ and $B = 0.545$ for monatomic gases. The Mach number far downstream of the quitting surface boundary (3) is then approximated with:

$$Ma_{\parallel,\infty} = \frac{\sqrt{2}}{\gamma} S_{\parallel,\infty}. \tag{2.18}$$

For the case derived in Sec. 2.3 and following the above described procedure, we obtain values for helium: $Ma_{\parallel,\infty,\mathrm{He}} = 3.58$ and argon: $Ma_{\parallel,\infty,\mathrm{Ar}} = 4.57$. Using these results, the approximate demarcation between the continuum and the free molecular flow regime in the setup used in this thesis is at [182]:

$$\frac{x_q}{d_0} \sim \left(\frac{Ma_{\parallel,\infty}}{C_1}\right)^{1/(\gamma-1)}. \tag{2.19}$$

Inserting $C_1 = 3.26$ [186] yields a quitting surface distance from the tube exit of $x_{\mathrm{q,He}} = 0.12\,\mathrm{cm}$ $x_{\mathrm{q,Ar}} = 0.17\,\mathrm{cm}$. Although the distance between the skimmer and the reactor can be tuned in z-direction in the experimental setup used in this study (see Chap. 3), the position of the sampling cone (skimmer) exceeds the quitting surface boundary in any case.

At this point, it is of interest whether fast reactions in a typical time frame may occur while the gas composition travels from the exit of the reactor until it reaches the transition point x_{q}. This is because conditions should be chosen, such that these reactions are minimized. The speed of sound a represents an upper limit to this time because the flow is considerably faster than the sonic speed [187]. Since most of the recombination reactions, which would be parasitic for the analysis, occur on the microsecond timescale [188], the time for the gas to reach the skimmer

$$\tau_s = \frac{x_q}{a}, \tag{2.20}$$

is with $\tau_{\mathrm{s,He}} \approx 2\,\mu\mathrm{s}$ and $\tau_{\mathrm{s,Ar}} \approx 9\,\mu\mathrm{s}$ on the lower boundary of this microsecond timescale. Therefore, not only a free molecular flow is probed in the experiments presented in this thesis, but it is also ensured that the outlet composition, despite a few very fast reactions that may occur, is predominantly preserved for spectroscopic analysis.

In sum, a correctly adjusted molecular beam sampling apparatus provides a high beam intensity on the order of 10^{18} particles/rad^{-1} s^{-1} leading to a sufficiently high signal-to-noise ratio, as well as a tight focusing of spatial distributions, due to the high velocities in supersonic jets [182]. In this thesis this method is therefore used to probe the gas-phase because the described state is advantageous for the spectroscopic evaluation of gaseous molecules and allows to detect and isolate inorganic and organic reactive intermediates.

2.3.2 Concepts for the Analysis of Elusive Species

In the previous paragraph, when describing the molecular beam physics, the source, from which the expansion occurs, is represented by a simplified concept of a capillary nozzle with a specific radius d_0 (see Fig. 2.4). However, in order to isolate and analyze radicals and elusive intermediates at high number densities and simultaneously avoid bimolecular reactions to examine the reaction pathways and kinetics, special

concepts for the decomposition of a precursor, prior to the spectroscopic analysis in a supersonic jet expansion, are necessary. This is especially the case when one aims on the detailed investigation of the decomposition mechanisms of metal-organic CVD precursors and their associated metal-containing reactive intermediates, since their handling and the isolation of elusive species is not straightforward.

Besides numerical approaches, high effort has been undertaken to unravel gas-phase chemistry using various analysis methods such as optical spectroscopy [189, 190, 191], mass spectrometry [127, 128, 192, 193, 194, 195, 196] and gas-chromatography [78, 197]. Drawbacks of those methods are their limited sensitivity towards the isolation of elusive intermediates and the possible interference of secondary reactions.

A popular method which accounts for the drawbacks of the aforementioned investigation methods is infrared laser powered homogeneous pyrolysis (IR-LPHP). Here, a chemically inert photosensitizer in the infrared region (usually SF_6) absorbs vibrational energy from a CO_2 laser and rapidly converts this energy to translational and rotational energy (i.e., heat) via relaxation processes [198]. The main advantage lies in the direct transformation from the laser's energy to heat in a finite volume of the pyrolysis cell, leading to very high achievable temperatures in the center of the cell (up to 1500 K), whereas the walls remain unheated. Although wall reactions can be minimized, the induced temperature gradient, in conjunction with the unknown temperature field in the flow cell, complicates the extraction of kinetic parameters. Therefore, kinetic data obtained from this method, by taking average values, is only a rough approximation [198]. Despite the complexity of the experiment and the associated drawbacks, valuable insights into the pyrolysis mechanisms of CVD precursors by applying IR-LPHP were obtained by the group of Douglas K. Russell. They subsequently analyzed the pyrolysis products by matrix isolation [199, 200], FTIR and GC-MS [199, 200, 201].

As an alternative, thermal flash-pyrolysis sources such as the famous Chen nozzle [121], a resistively heated silicon carbide (SiC) flow tube used to thermally crack the precursors bonds, are used. When combined with numerical simulations of the flow field, these can be utilized to extract kinetic rate data, as demonstrated previously [129, 130, 202, 203, 204]. The main advantage over the conventional flow reactor method is rooted in the intrinsically low residence time of the molecules in microreactors on the order of a few tenth of microseconds and the high dilution of $<0.01\%$, which minimizes intramolecular reactions [130, 202]. This has led to their successful application as pyrolysis sources in order to obtain mechanistic insights into the chemistry of e.g., organosilicon compounds [127, 205, 206, 207, 208]. Nevertheless, considerable effort must be undertaken because the evaluation of data generated from flash-pyrolysis is not straightforward and requires a careful coupling and interpretation of computational and experimental results. In this thesis, it will be demonstrated, how a microreactor, combined with numerical simulations of the flow field, leads to valuable insights, both mechanistically and kinetically, into the decomposition channels of metal-organic precursors [129, 130, 131]. The topic of the microreactors flow field will be addressed later in this thesis (see Chap. 3).

2.3.3 Unimolecular Decomposition Kinetics

2.3.3.1 Reaction Rate and Rate Laws

Given the initial and final state of an arbitrary chemical reaction, thermodynamics is able to make a statement on the feasibility by calculating the free enthalpy and the concrete equilibrium states of the reaction. However, no information on the reaction rate or reaction path can be obtained. This is where chemical kinetics comes into play which monitors the progress of a chemical reaction, i.e., the change of the concentration of the reactants with time. In order for a reaction to occur, the reacting system cannot easily change to a state of lower free enthalpy, but it has to overcome a certain reaction barrier. For an exemplary unimolecular dissociation reaction of molecule AB the reaction sequence reads:

$$\mathrm{AB} + \mathrm{M} \longrightarrow \mathrm{A} + \mathrm{B} + \mathrm{M}. \tag{R 2.1}$$

Considering the above given reaction, the instantaneous rate of reaction r is defined as the rate of consumption of a reactant or formation of a product, which is the slope of a tangent on the graph of concentration vs. reaction time:

$$r = -\frac{d[\mathrm{AB}]}{dt} = \frac{d[\mathrm{A}]}{dt} = \frac{d[\mathrm{B}]}{dt}. \tag{2.21}$$

It has been found that the rate of a reaction is proportional to the reactants concentrations to a specific power, called the reaction order n, which is the sum of the exponents to which the concentration of a specific reactant is raised in the rate law:

$$r = k_{\mathrm{uni}} \cdot [\mathrm{AB}]^n, \tag{2.22}$$

with the proportionality factor k_{uni} defined as the specific unimolecular reaction rate constant for a reaction order of $n = 1$. This rate is mainly influenced by the temperature, whereas for gas-phase reactions in specific setups also a pressure dependence can be observed.

If, for a given reaction, the associated rate law and the rate constant is known, one can predict the reaction rate from the composition of the sample at a given temperature and pressure. Rate laws can also be utilized to provide evidence to assess the plausibility of an assumed mechanism by checking for the correctness of the initially assumed reaction order. The reaction rate may be obtained, such as has been done in this thesis, by spectroscopic methods that provide information on the gaseous sample composition by quantifying the individual components concentrations. This has been done in this thesis when analyzing the unimolecular decomposition of $\mathrm{Al(acac)_3}$ and $\mathrm{Fe(Cp)_2}$ and the bimolecular decomposition of the latter (see Sec. 4.3.8 and Sec. 6.2.6).

A common approach to obtain the proportionality factor k_{uni} in Eq. 2.22 is to express the dependence of the reaction rate on the concentrations of the reactants with respect to the reaction order n in terms of differential equations, so called rate laws. To finally evaluate the composition of a reaction mixture and determine the reaction order as well as the rate constants of a given reaction, one needs to solve the rate law by integration, which reads for a unimolecular reaction with $n = 1$:

$$\frac{d[\text{AB}]}{dt} = k_{\text{uni}} \cdot [\text{AB}]. \tag{2.23}$$

Integration in the limits of the initial concentration $[\text{A}]_0$ and the final concentration [A] yields:

$$ln\left(\frac{[\text{A}]}{[\text{A}]_0}\right) = -k_{\text{uni}} \cdot t. \tag{2.24}$$

When the left-hand side is plotted against t, for a first order reaction, a linear function with the slope of $-k_{\text{uni}}$ is found. The above given Eq. 2.24 is then used to predict the concentration of any component at any reaction time in the system and to compare it to the measured composition obtained by spectroscopic methods.

Using this approach, temperature-dependent values of the reaction rate k_{uni} can be determined and the order of the reaction n can be confirmed. Note that usually effects of the product concentrations or the influence of surface reactions by changing the surface-to-volume ratio is considered in the analysis. However, in the course of this thesis, surface reactions are minimized in the microreactor setup, and therefore their role on the kinetics is not discussed further at this point.

2.3.3.2 Temperature, Pressure and Concentration Dependence

It has been found and was numerously confirmed experimentally that the rate of a reaction is highly dependent on the temperature. Although first formulated longer than a century ago, the Arrhenius-equation [209, 210], in its traditional from, is able to describe the temperature-dependency of gas-phase chemistry using two parameters, the frequency factor A and the activation energy E_{a}:

$$k_{\text{uni}} = A \cdot \exp^{\frac{-E_{\text{a}}}{RT}}. \tag{2.25}$$

Here, following the collision theory, the first parameter A can be interpreted as a probability of collision in a given volume, whereas the second parameter E_{a} defines the energy required to overcome the reaction barrier necessary for the reaction to occur.

To qualitatively understand the meaning of the latter empirical parameter E_{a}, one must consider the potential energy profile of a chemical reaction. An exemplary profile is shown in Fig. 2.5, where the molecular potential energy change of an exothermic unimolecular decomposition reaction according to Reac. R 2.1 along the reaction coordinate t is displayed. In the initial state, the reactant AB contains

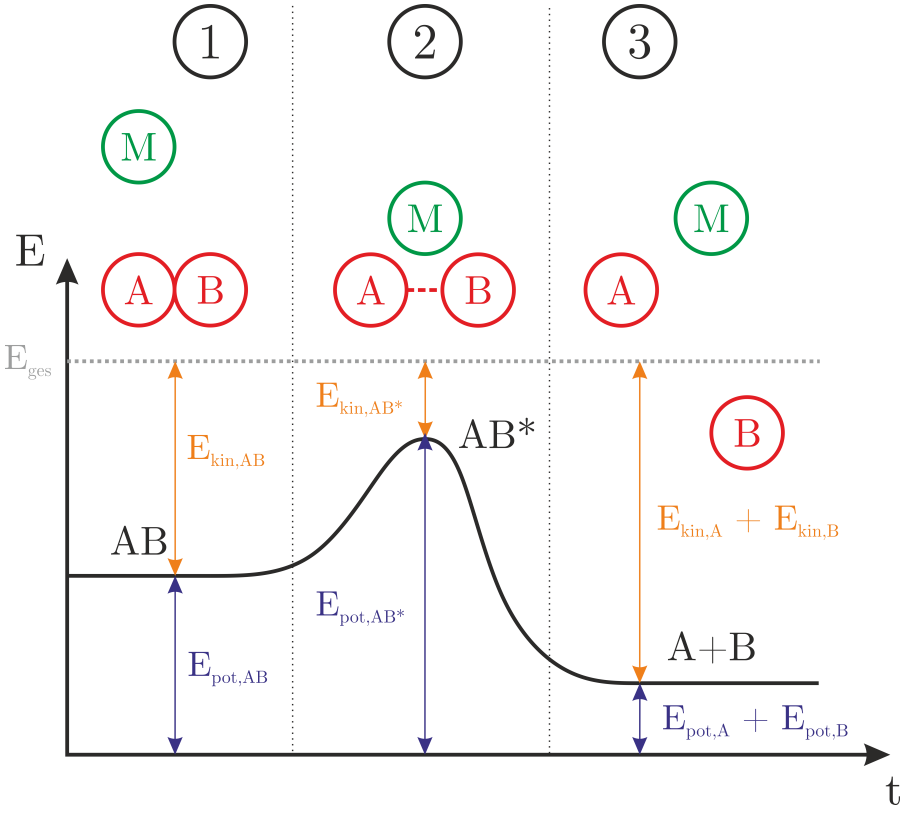

Figure 2.5: Schematic of an energy diagram for a unimolecular decomposition reaction according to Reac. R 2.1 which shows the energy as a function of the progress of the reaction t, adapted from [211].

a specific potential energy $E_{\mathrm{pot,AB}}$. When the reaction event proceeds by e.g., a collision with a background gas molecule M, a specific amount of kinetic energy is added until a maximum in the energy diagram is reached, called the transition state AB*. Here, the molecule AB is distorted by such an extent that a further addition of energy would inevitably lead to the breakage of the weakest bond and the formation of the lower energetic products A and B. The minimal difference between the reactants potential energy and the potential energy of the transition state is defined as the activation energy E_{a} of the forward reaction.

It has been observed that for the reaction rate of a unimolecular decomposition reaction, besides the temperature, also the pressure is an important factor. This is especially valid for CVD precursors where often no reactant is present and the dissociation of the precursor molecule bonds either by excitation or by a collision with surrounding inert gas molecules M drives the process. Although these reactions contain steps that can be attributed to unimolecular, as well as bimolecular chemistry, the overall mechanism turns out to proceed according to first order kinetics.

The first description of a collisional-activation mechanism for a unimolecular reaction was introduced by Lindemann [212] and later refined by Hinshelwood [213]. In this theory, commonly known as Lindemann-Hinshelwood mechanism, it is

assumed that a reactant molecule A[7] collides with a third-body molecule M, which could be A itself, and becomes energetically excited:

$$\mathrm{A} + \mathrm{M} \xrightarrow{\mathrm{k_1}} \mathrm{A}^* + \mathrm{M}. \tag{R 2.2}$$

This step, is by nature, bimolecular. But as we will see in the derivation of the reaction rate for such a mechanism, under specific circumstances, the reaction follows first order kinetics[8]. After the first step, the energized molecule A^* can proceed via two pathways, either following a deactivation step in another collision process

$$\mathrm{A}^* + \mathrm{M} \xrightarrow{\mathrm{k_{-1}}} \mathrm{A} + \mathrm{M}, \tag{R 2.3}$$

or it can undergo a unimolecular decay according to

$$\mathrm{A}^* \xrightarrow{\mathrm{k_2}} \mathrm{P}. \tag{R 2.4}$$

It is further assumed that step Reac. R 2.3 is one hundred percent efficient, such that every molecule A^* is deactivated upon collision with M at the rate k_{-1}. The integrated rate laws for these reactions with respect to A^* read:

$$\frac{d[\mathrm{A}^*]}{dt} = k_1 \cdot [\mathrm{A}][\mathrm{M}], \tag{2.26}$$

$$\frac{d[\mathrm{A}^*]}{dt} = -k_{-1} \cdot [\mathrm{A}^*][\mathrm{M}], \tag{2.27}$$

$$\frac{d[\mathrm{A}^*]}{dt} = -k_2 \cdot [\mathrm{A}^*]. \tag{2.28}$$

Applying the stead-state assumption ($d[\mathrm{A}^*]/dt = 0$) for the net rate of A^* yields:

$$\frac{d[\mathrm{A}^*]}{dt} = k_1 \cdot [\mathrm{A}][\mathrm{M}] - k_{-1} \cdot [\mathrm{A}^*][\mathrm{M}] - k_2 \cdot [\mathrm{A}^*] \approx 0. \tag{2.29}$$

The rate of formation of the product P is expressed as:

$$\frac{d[\mathrm{P}]}{dt} = k_2 \cdot [\mathrm{A}^*]. \tag{2.30}$$

One can now replace the concentration of A^* by rearrangement of Eq. 2.29. In terms of the concentration of A this yields:

$$\frac{d[\mathrm{P}]}{dt} = \frac{k_1 k_2 [\mathrm{A}][\mathrm{M}]}{k_2 + k_{-1}[\mathrm{M}]}. \tag{2.31}$$

[7] Usually the precursor in the framework of this thesis.

[8] This is commonly referred to as pseudo-first order reaction kinetics.

As one can immediately recognize this reaction is not first order since it has a dependence on both the concentration of the reactant A and the third-body molecule M. However, for understanding the pressure influence on a unimolecular reaction, one has to distinguish between two cases for the above given expression. First at high pressure, where $[M] \rightarrow \infty$, k_2 can be neglected in the denominator, whereas for the second case, at low-pressure, where $[M] \rightarrow 0$, k_{-1} can be ignored. After simplifying the rate expression in Eq. 2.31 by combining the rate coefficient k_{uni} with the rate law similar to Eq. 2.23, one can obtain information on the respective reaction order.

When the rate of deactivation is much greater than the rate of unimolecular decomposition (high-pressure), such that $k_{-1} \gg k_2$. Then Eq. 2.31 simplifies to the following first order expression for the rate of decomposition of A to its products P:

$$\frac{d[P]}{dt} = k_{uni} \cdot [A], \tag{2.32}$$

with the rate constant k_{uni} defined as:

$$k_{uni} = \frac{k_1 k_2}{k_{-1}}. \tag{2.33}$$

So, for the first case, at high pressure, a first order reaction and for the second case, at low-pressure, a second order reaction mechanism is obtained. This concept is later taken into account when analyzing the reaction kinetics of $Al(acac)_3$ and $Fe(Cp)_2$ in Chap. 4 and Chap. 6.

Chapter 3

Experimental Methodology

Following the theoretical aspects of synchrotron radiation and its usage in double imaging photoelectron photoion coincidence experiments (i^{2}PEPICO) to unveil decomposition mechanisms and kinetics, this chapter is devoted to describe the technical aspects of the i^{2}PEPICO experiment at the Swiss Light Source (SLS). This is complemented by a description of the silicon carbide (SiC) microreactor and its basic properties, which is useful in the understanding of the analysis presented in the following chapters. Additionally, some aspects of data extraction and analysis is given that are important for the interpretation and evaluation of the obtained data described in the upcoming chapters.

3.1 Overview of the Setup

The most important parts of the reactor setup that was used in this work can be extracted from Fig. 3.1 and its features are discussed in detail in e.g., Sec. 4.2.1 and in the literature [172, 173, 174]. Only a brief overview is given here.

The experimental setup consists of three main elements. The first part is a sample container, embedded in an isothermal copper block (evaporator). Here, small amounts[1] of a solid CVD precursor with low volatility is placed in a heated stainless-steel tube with and inner diameter of 3 mm and a total length of $\approx$ 40 mm. To increase the vapor pressure and therefore obtain higher concentrations of the precursor in the gas mixture, the copper block is heated by up to four temperature controlled heating cartridges mounted inside two drillings at each side of the copper block. The sublimed gas is then transported by a carrier gas[2] and expanded through a 100 µm pinhole and transported into a SiC microreactor whose properties and features are thoroughly described in the next section (Sec. 3.2).

At the reactor outlet, a molecular beam is formed and its central part is cut out by a 1 mm conical skimmer. In order to obtain sufficient vacuum for analysis, both, the source (SRC) and experimental (EXP) chamber are pumped by a turbomolecular

[1] Usually a few grams.
[2] An inert gas, such as argon or helium.

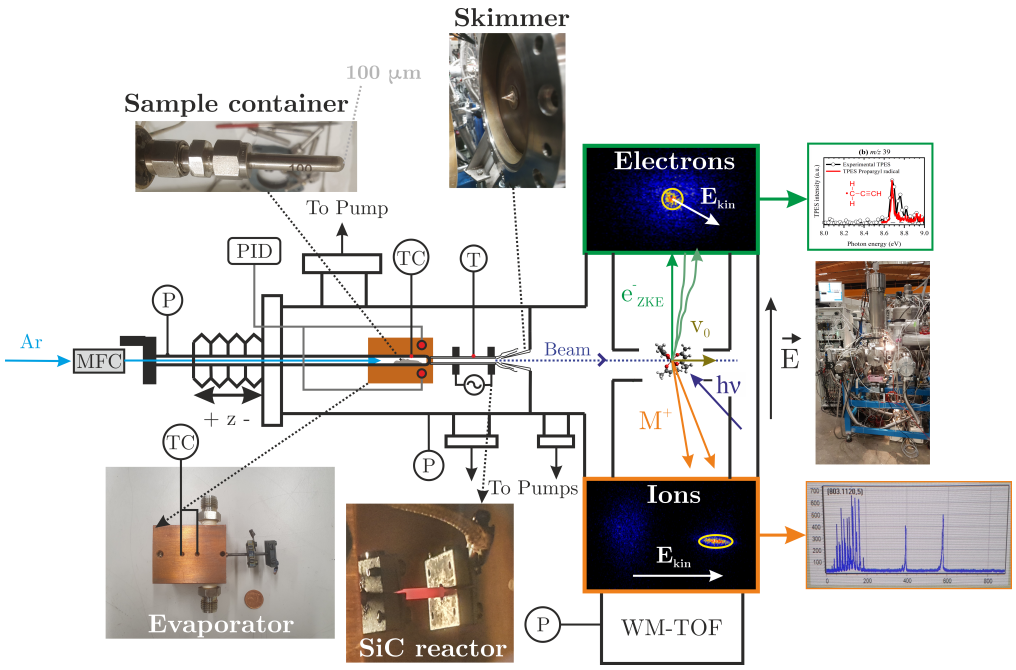

Figure 3.1: Vacuum apparatus of the experimental setup at the X04DB VUV beamline at the SLS synchrotron facility with embedded images of the most important parts of the pyrolysis reactor setup. The schematic in the background is taken from a recent publication [129].

diffusion pump (SRC: Pfeiffer TPH 1201 UP at 1600 l s^{-1}; EXP: Pfeiffer TMH 521 YP at 500 l s^{-1}). Those are accompanied by a single cryopump mounted at each chamber (SRC: Leybold COOLVAC CK at 5000 l s^{-1}; EXP: Leybold COOLVAC 1500 CL at 1500 l s^{-1}) [173]. The gas composition of the molecular beam is then analyzed by the combustion reactions followed by photoelectron photoion coincidence (CRF-PEPICO) endstation currently running at the SLS synchrotron facility in Switzerland. Thanks to its flexible design, various experiments can be performed using laminar flames [214], flow [215], as well as catalytic [122], photolitic [216] and pyrolytic reactor setups [153].

3.2 SiC Microreactor

The following paragraph will highlight key features of the flash-pyrolysis reactor as introduced in Sec. 2.3.2, which was used in this work. Among the known pyrolysis reactors, resistively heated microreactors [217] based on the initial design by Chen et al. [121] are frequently used to generate and isolate reactive organic and inorganic species by forming a supersonic jet at the nozzles exit with the properties and advantages as described in Sec. 2.3.1. The most important physical relations, as well as the setup itself will be explained in the following.

3.2.1 Flow Characteristics

Because of the rapid pressure drop at the exhaust of the microreactor and the high temperature heating, a characterization of the flow field is not straightforward. Usual methods to experimentally sample important flow field parameters fail here, since the microreactor is not optically accessible and probes such as thermocouples would, because of their size, strongly disturb the flow. To anyway accurately interpret and quantify the data and not only obtain mechanistic information on the precursor's chemistry, analytical or computational calculations can be used to characterize the complex flow field and extract values of flow field parameters, especially pressure, velocity and density. Since it is possible to sample the flow conditions at the boundaries of the microreactor, i.e., the temperature and pressure, computational fluid dynamics (CFD) studies of the flow field were performed [129, 130]. A detailed discussion on the results obtained will be made in the corresponding chapters Chap. 4 and Chap. 5 and only basic considerations for the description of the flow field in a microreactor is given here. This is mainly because the numerical simulations were conducted by my project cooperation partner Dr. Seung-Jin Baik at the Chair of Fluid Dynamics and a detailed discussion about the methods applied is therefore not within the scope of this thesis. However, some basic aspects that are important for the interpretation of the experimental results presented in this work are given here.

The Boltzmann equation provides a general description of the time-dependent evolution of a gas flow and represents the motion of gas molecules and their collision at a specific location in a mixture. As has been touched in Sec. 2.3 the type of flow is determined by the Knudsen number, which is defined as the ratio of the mean free path from Eq. 2.9 to the characteristic length l_{charac} of the flow region. Inserting the dimensionless numbers Ma and Re, one obtains:

$$Kn = \sqrt{\frac{\gamma\pi}{2}}\frac{Ma}{Re}. \tag{3.1}$$

For a tube l_{charac} is represented by the tubes inner diameter d_{i}. Having values of Kn below 0.01, the flow is operated in the continuum region and can be treated by continuum mechanics as represented by the Reynolds averaged Navier-Stokes-equations (RANS) for mass and momentum conservation (see Sec. A.1.1 and

Sec. B.1.1). Applying a no-slip boundary condition leads to pressure, temperature and velocity fields and therefore a complete description of the flow field. Hence, the influence of the often very complex field can be analyzed with the aim of a determination of kinetic rate parameters and to obtain information on the residence time distribution of molecules traveling through the microreactor. Despite their importance, those information are scarce in the literature.

Since CVD precursors are investigated here close to their deposition conditions, the question about the extent of the surface reactions in the microreactor arises. From fluid mechanics we known that the extent of wall reactions depend on the Péclet number Pe, a dimensionless relation between residence time $\tau_{\mathrm{res}} = l_{\mathrm{charac}}/u$ and radial diffusion time $\tau_{\mathrm{diff}} = l^2_{\mathrm{charac}}/D_{\mathrm{AB}}$:

$$Pe = \frac{\tau_{\mathrm{res}}}{\tau_{\mathrm{diff}}} = \frac{l_{\mathrm{charac}} \cdot u}{D_{\mathrm{AB}}}, \tag{3.2}$$

where D_{AB} is the diffusion coefficient of species A (the specific precursor) in the bath gas B (argon or helium). The diffusion coefficient is obtained using empirical equations. Depending on the flow rate and carrier gas used, residence times on the order of 14–100 µs are achieved. In the exemplary case of $Al(acac)_3$ in argon (see Sec. A.1.5), for all, but the highest temperature, Pe is <1, meaning that the residence time in the microreactor is in most cases too short for significant radial diffusion. This is valid for all, but the closest molecules to the wall, leading to a minimized impact of wall reactions on the high temperature results obtained in this thesis.

Another major influence factor that could bias probing only unimolecular reaction products from a microreactor experiment are radical recombination reactions. Because of the almost nonexistent reaction barrier, they are expected to occur extremely rapid on timescales that are below the microreactors residence time. As these reactions are of second order, their rate scales quadratic with the radical concentration. To exploit the second benefit of the presented setup, the dilution of the precursor molecule entering the reactor is kept below 0.01%, which keeps the radical concentration low and has proven to be an effective method to suppress bimolecular reactions under pyrolytic conditions and therefore probing only the unimolecular reaction pathways [122].

In line with the general description of molecular beam physics in Sec. 2.3.1 the radial pressure gradient causes a diffusion of light species from the centerline of the jet. This phenomenon is known as mach-number focusing and could influence the results by an enrichment of heavy species in the centerline of the molecular beam. Although the velocity of all species in beam propagation direction is constant, the transverse velocity perpendicular to the beam centerline axis is higher for lighter molecules such as H_2 since the velocity scales with $1/\sqrt{m}$. In the data evaluation, this pressure diffusion is accounted for by an instrument factor called mass discrimination factor, which has been evaluated for the i^{2}PEPICO apparatus by different groups for various setups independently to be close to unity [218, 219].

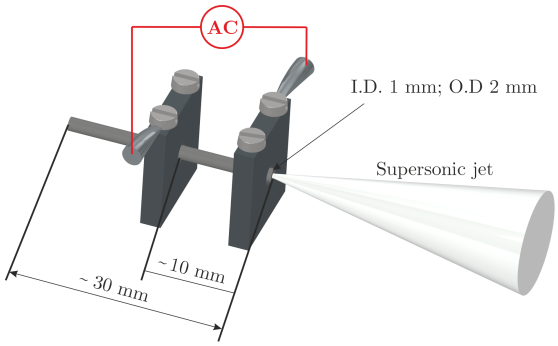

Figure 3.2: Schematic of the silicon carbide (SiC) microreactor used in this thesis to investigate the thermal decomposition of the precursor molecules. At the outlet, a molecular beam is formed by expanding the gas to high-vacuum.

3.2.2 Setup and Calibration

An exemplary sketch of the microreactor setup used in this thesis is shown in Fig. 3.2. The reactor is a tube made out of the refractory semiconductor silicon carbide (SiC) obtained by *Saint-Gobain Ceramics* under the brand Hexoloy©SA. The tube has an inner diameter of about 1 mm and an outer diameter of about 2 mm. The reactor spans a total length of approximately 30 mm, whereas only a short area is resistively heated. Two electrical contacts are mounted on the SiC tube and their distance defines the heated reaction zone of the microreactor. Here, the precursor molecules are thermally cracked. The design principle of this region is that it should be as small as possible in order to keep the residence time low and therefore decrease the chance of formed reactive intermediates to undergo secondary reactions. In the studies presented in this thesis, a constant heated length of 10 mm was chosen which represents a compromise between appropriate resistivity and advantageous short residence times, which are inversely connected.

The resistance of the SiC tube scales inversely with the temperature and has values of 20–150 Ω [217]. Since the thermal conductivity of SiC is relatively low, despite the thick reactor wall of ≈ 1 mm, the temperature gradient between the inner and outer surface is neglectable. Therefore the temperature reading of a type C thermocouple, attached to the central part of the tube, allows for a reliable approximation of the inner surface temperature of the SiC tube under reaction conditions (see Fig. 3.3).

To minimize the temperature reading error, the thermocouple was first attached to the reactor surface with an insulating tape to fix its position and maximize its contact efficiency and second consistency was kept by using the same thermocouple

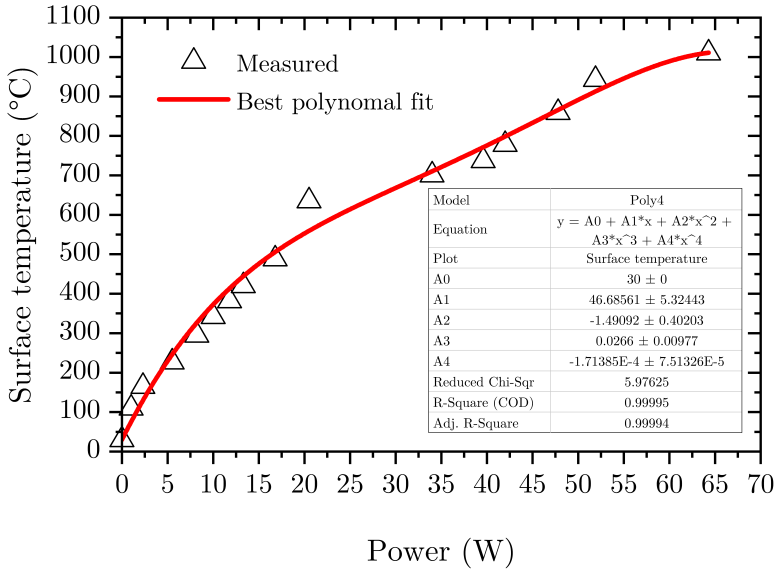

Figure 3.3: Calibration curve of the surface temperature vs. electrical power.

throughout the measurements while keeping the step size of the resistive power source nearly constant. The values so obtained are used as boundary condition in computational fluid dynamics (CFD) simulations of the flow field (see Sec. 4.2.3; Sec. 5.2.1). This procedure is widely accepted and has already successfully provided boundary conditions to perform CFD calculations in similar setups [202, 204]. Most of the studies that utilize such kind of microreactors either rely on those simulation results or on a single surface temperature measurement and quote the overall uncertainty, due to imperfect contact between the reactor surface and the thermocouple, to be ± 50–100 K in the centerline [220, 221]. Temperatures between 300 and 1500 K can be realized in the heated zone which is sufficient to cover primary reaction pathways of the precursor molecule with the highest bond dissociation energy under investigation, ferrocene [48].

3.3 Data Acquisition and Evaluation

As outlined in Sec. 2.2.4 the i^{2}PEPICO spectrometer is capable to detect both photoions and photelectrons generated in the same ionization event. In the present setup, both particles are accelerated in opposite directions from the ionization volume on two position-sensitive delayed-line anode detectors (DLD) connected to a micro-channel plate (MCP) manufactured by *Roentdek*, DLD40. Since strong and curved electric fields are required for ion velocity map imaging (VMI), the voltages can be adjusted to run experiments either at imaging or space focusing operation conditions [174]. The first one is advantageous for the determination of fragment signals and background subtraction which leads to fragmentation free mass spectra. The latter one plays out its strengths when it comes to distinguishing isotopic patterns, since

the mass resolution is improved. To understand the experimental method applied for generating the results presented in this thesis, the data acquisition technique of such a system is shown in Fig. 3.4 and described in detail in the following paragraph.

3.3.1 Ion and Electron Collection Method

As can be depicted from Fig. 3.4, upon ionization, a constant electric field accelerates electrons and ions in opposite directions perpendicular to the ionization region. Both are focused on detector plates using electrostatic lenses. The electric fields can be altered such that either linear fields are used for space focusing conditions or dual curved fields are applied, providing imaging conditions. Depending on the experimental requirements, the electric fields can be tuned to either yield a good mass resolution (space focusing), or focused kinetic energy distributions of the cations (imaging conditions) [174, 222]. Central part of the apparatus are the position-sensitive detectors (PSD), which are two particle delay line detectors (DLD), in principle a lattice of x- and y-filaments, which are mounted at the backside of a multi-channel plate (MCP). The MCP amplifies the impact signal and transmits it to the DLD. Since the electrons, by nature, have a much lower mass then the ions, their time to reach the detector is considerable smaller than that of the corresponding ions. Again, in order to merge both analytical benefits from PES and PIMS, i.e,. the mass analysis of the cations and the kinetic energy of the electrons, one must identify fitting ion-electron pairs that originate from the same ionization event, termed true coincidence and delimit them from false coincidences, where erroneous ion-electron pairs are matched. Since those false coincidences naturally occur in coincidence experiments and they also scale with the ionization rate, which is high when synchrotron radiation is used, special care must be taken to minimize their impact.

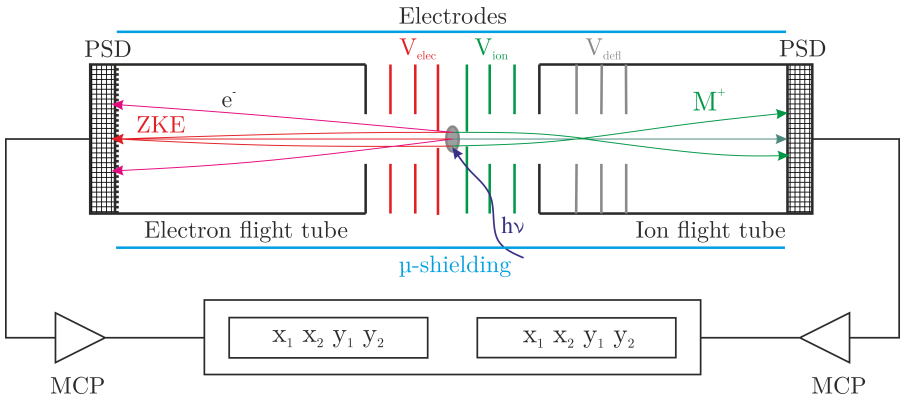

Figure 3.4: Schematic of the data acquisition principle of the CRF-PEPICO apparatus, based on [174, 222].

3.3.2 The Coincidence Principle

An effective method to minimize false coincidence is the multi-start multiple stop (MM) data acquisition approach [223], which is schematically shown in Fig. 3.5. Here, exemplary signals arising from the cations, electrons and possible coincidences are shown. After the first particles impact on the electron detector, a master clock is triggered, representing the start signal of a specific, reasonable time-of-flight (ToF) time window of usually >40 µs, depending on the flight-time of the heaviest molecule in the mixture. The signals of both, electrons and ions, are given a time stamp with respect to the master clock and they are cross correlated within the preselected time window. According to the scheme in Fig. 3.5, 13 false (dashed arrows) and 6 true (colored checkmarks) coincidences can be identified. The false coincidences contribute to the background of the ToF spectrum on the right hand side of Fig. 3.5, whereas true coincidences represent the signal peaks in the ToF spectrum. The cation's ToF of the true coincidences is then calculated by taking the difference between the electron and ion timestamp with respect to the master clock. It becomes apparent that although using the MM method still an inevitable fraction of false coincidences occur, leading to a low dynamic range of the apparatus, which is detrimental for the analysis of highly diluted mixtures. Considering that CVD precursors are seeded in small number densities within the carrier gas stream, the detection of low amounts of radicals and intermediates is only successful, when the dynamic range of the instrument is sufficiently high. By utilizing a position-sensitive detector to record the ion impact coordinates in combination with a time-dependent electric field (see Fig. 3.5 c)), which deflects the ions perpendicular to their flight direction as a function of time, one can judge from combining the cross correlation technique with the time-dependent deflection field, if an electron-ion pair is termed true or false coincidence with a very high efficiency. This is, if the impact position of an ion fits the theoretical position according to the electrical deflection field at the time of ionization. A theoretical impact position of the ion on the position sensitive detector in subfigure d) is calculated based on an instrumental factor and the time of flight of the cation t_{cation} (gray) in subfigure c). The intersections between the field curves for V_{x} (dashed-line) and V_{y} (straight line) determine the predicted position of the ion having the flight time equal to t_{cation}. If the theoretical predicted position (grey circle in subfigure d)) matches the predicted position (crosses), the cross correlation is then counted as a true coincidence (see Fig. 3.5 d), blue cross). Otherwise, the event is termed false coincidence (orange cross). This procedure is done for all electron-ion pairs and the result of this analysis is shown as a mass spectrum in subfigure b). Such a data treatment increases the dynamic range to 10^5 and therefore allows to record mass-selected threshold photoelectron spectra (ms-TPES) at high ionization rates of up to 100 kHz. This is advantageous when using pulsed synchrotron radiation, as provided by the electron accelerator of the SLS [222].

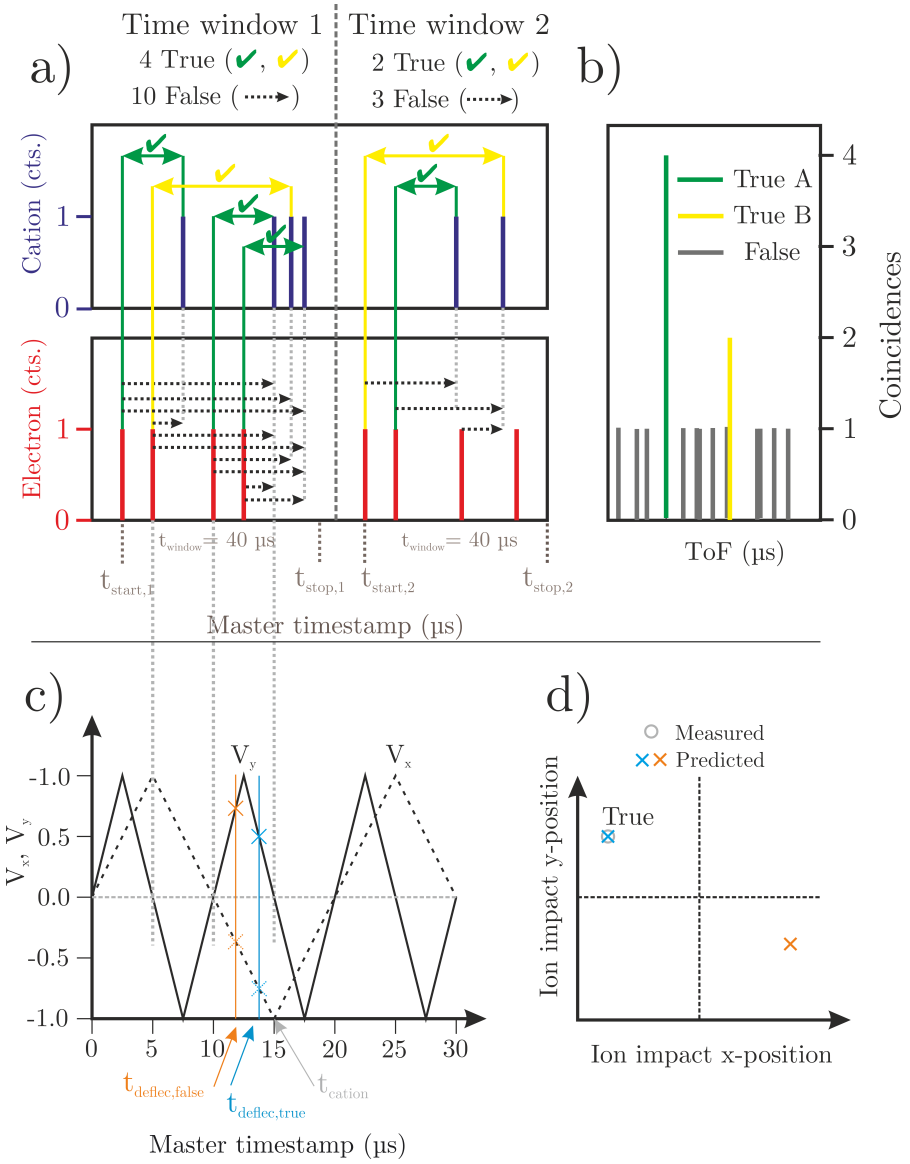

Figure 3.5: Schematic of the multi-start multiple stop (MM) data acquisition approach with exemplary matches of true (green and yellow checkmarks) and false (black dashed arrows) coincidences for the two molecules A (green) and B (yellow), based on [222]. False coincidences are randomly distributed over time while true coincidences have a specific timescale. In subfigure b) on the right hand side, an exemplary mass spectrum derived from the raw data on the left hand side a) is shown, where the coincidences are summed up. A stick spectrum is obtained where true coincidences are colored and false coincidences are shown in gray as a function of their time of flight (ToF). The analytical procedure to distinguish between true and false coincidences is displayed in subfigures c) and d). The method is based on the usage of time-dependent deflection fields V_x and V_y having different frequencies and is further explained in the text.

3.3.3 Data Analysis

3.3.3.1 Identification and Separation of Energetic Ions

The ions that are generated from a single ionization event are mass-analyzed in a conventional time-of-flight (ToF) mass spectrometer with Wiley-McLaren space focusing conditions [149]. In the present setup, the electrons trigger the start signal for the ToF of the ions. These ion are then accelerated in a constant electric field of $>200\,\mathrm{V\,cm^{-1}}$, subsequently pass a field free drift region (see Fig. 3.4), before hitting the position-sensitive detector (PSD). The signal gets then intensified by an MCP and is sent to further analysis.

Applying an energy balance between the potential energy $E_{\mathrm{pot,ion}}$ pertained to the electric field of a plate capacitor with the potential difference U for an ion with the electrical charge $z \cdot e$, $E_{\mathrm{pot,ion}} = z \cdot e \cdot U$, and the kinetic energy of the ion $E_{\mathrm{kin,ion}} = 1/2 \cdot m \cdot (\mathrm{l_{drift}}/\mathrm{ToF})^2$ due to acceleration, results in the following relation to calculate the ToF of a particle having the mass m:

$$\mathrm{ToF} = \sqrt{\frac{m \cdot l_{\mathrm{drift}}^2}{2 \cdot z \cdot e \cdot U}}. \tag{3.3}$$

The above given relation shows that ions can be separated by their mass, because the ToF is proportional to the ions mass m, meaning for higher masses, the ToF is longer than for shorter masses.

In order to distinguish between ions having almost the same mass, as e.g., ketene (C_2H_2O; $m/z = 42.0367$) and propene (C_3H_6; $m/z = 42.0797$), a sufficient mass resolution is necessary. The mass resolution is defined as the smallest difference between masses that can be separated and reads $R = m/\Delta m$. Unfortunately, as pointed out in the previous section, in the present setup a compromise must be made, since the mass resolution is increased by applying a high electric field. Yet this is simultaneously detrimental for the electron collection efficiency. To exploit all the benefits described for the i^{2}PEPICO setup, as a trade-off, a resolution of ≈ 300 is achieved when using imaging conditions, while space focusing conditions would improve the overall mass resolution to about 500. Whenever possible, the results presented in this thesis are measured with both operation modes to obtain the valuable information given by the mapping of ions on the position-sensitive detectors using imaging conditions, but also space focusing conditions were applied to sufficiently resolve neighboring m/z values for isotope characterization of metal-containing intermediates (see Sec. 5.2.4).

The respective photoionization mass spectra (PIMS) are then obtained by averaging over a specific integration time of 60–900 s to achieve sufficient signal-to-noise ratios for even the lowest product concentrations. Additionally, conventional photoionization efficiency (PIE) curves, a summation of the total ion signal over a respective energy range for each m/z channel, can be obtained. These are utilized for the evaluation of ionization energies which hint on the underlying species contributing to the m/z channel, as described in Sec. 2.2.1.

To exploit the major enhancement of the present CRF-PEPICO apparatus and obtain fragmentation free mass spectra, the 2D-images of the kinetic energy distribution of the ions mapped on position-sensitive detectors are evaluated. An example is given in Fig. 3.6. As the photoions are velocity map imaged (Fig. 3.6, left), the molecular beam component (yellow ellipsis) can clearly be separated from the room temperature background, because of its higher kinetic energy [153]. The alignment of the molecular beam prior to each experiment by using the kinetic energy distribution of the ions enhances the sensitivity of the instrument and radical detection is improved [224]. A smart choice of the beam component region-of-interest (ROI) extracts only the energetic ions from the raw data, contributing to background and fragmentation free mass spectra.

3.3.3.2 Mass Calibration & Fitting Procedure

The transformation of ToF raw data to mass dimensions (m/z) is performed by using a polynomial of the second degree and the mass-to-charge ratio is obtained from the following relation:

$$m/z = a \cdot \mathrm{ToF}^2 + b \cdot \mathrm{ToF} + c. \tag{3.4}$$

At least three peaks must be directly allocated spanning the whole ToF range of interest, usually up to the precursors nominal mass. The calibration constants a, b and c are then obtained and can be used to convert the spectra from time to mass scale. The integration of the peaks is done by fitting the specific mass peaks to a Gaussian function using the program "Flammenfit 4.7" [225]. Physically reasonable parameter boundaries for the resolution (i.e., width range of the Gaussian function) and the location of each expected species based on their flight-time can be set in the programs species list. Although the mass resolution in the present system is limited when using imaging conditions, by applying space focusing conditions, convoluted peaks at neighboring masses can be evaluated by a deconvolution of the raw signal and an integration of the respective overlapping Gaussian functions using a customized list of observed peaks. Due to the modification of electric fields, this calibration must be performed separately after each measurement block for both operating conditions, imaging and space focusing. The data is exported in ASCII format and further evaluated using "Origin Pro" in its latest version.

3.3.3.3 Identification of Threshold Electrons

As already discussed in Sec. 2.2.4, collected threshold electrons have negligible off-center momentum and are usually located inside a small spot on the position-sensitive detector (see Fig. 3.7). But in the same area, photoelectrons with significant kinetic energy ("hot electrons") distribute in larger radii around the center and also contribute to the overall electron signal. Using the strategy introduced by Sztáray et al. [171] the contribution of these energetic electrons can be efficiently reduced by subtracting the ring signal, weighted by a constant empirical factor f, from the

center signal (see Fig. 3.7). This factor relates the area of the ROI for the center signal A_{center} to the area of the annular gap representing the ROI for the ring signal A_{ring}:

$$f = \frac{A_{\text{center}}}{A_{\text{ring}}}. \tag{3.5}$$

Usually the empirical factor f is determined to be around 1/3. The raw signals are obtained using the i^{2}PEPICO software tool at version 3.0, which is provided by the beamline staff [226]. The TPES signal is then calculated by the following relation:

$$S_{\text{TPES}} = S_{\text{center}} - f \cdot S_{\text{ring}}. \tag{3.6}$$

In summary, each threshold electron can be assigned to a single ionization event. Together with the mass-selection capability of the photoions that are tracked in coincidence, ms-TPES can be obtained. An advantage over conventional photoelectron spectroscopy is that collecting only the threshold electrons, which follow the Franck-Condon principle allows to directly compare the obtained spectra to literature references from quantum chemical calculations, which is especially useful for reaction intermediates, whose reference spectra are tedious to measure and therefore are scarce in the literature.

3.3.4 Evaluation of Mole Fractions

To take all temperature-dependent expansion effects into account, the influence of gas-expansion on species signal intensity is summed up by introducing the instrument dependent gas-expansion factor $\lambda(T)$ [227]. Measuring the signal intensity of an inert species, here the bath gas argon, gives the gas expansion coefficient (see Fig. 3.8) using the following relation:

$$\lambda(T) = \frac{S_{\text{Ar}}(T, 15.8\,\text{eV})}{S_{\text{Ar}}(T_0, 15.8\,\text{eV})}. \tag{3.7}$$

According to the method introduced by Cool et al. [156], the signal intensity of species i is written as follows:

$$S_{\text{i}}(T, E) = C \cdot x_{\text{i}}(T, E) \cdot \sigma_{\text{i}}(E) \cdot D_{\text{i}} \cdot \Phi_{\text{P}}(E) \cdot \lambda(T). \tag{3.8}$$

In this relation C is an instrument-dependent constant, $x_{\text{i}}(T, E)$ is the mole fraction of species i at the photon energy E and temperature T. At a fixed photon energy, the photon flux $\Phi_{\text{P}}(E)$ is constant and given that the mass discrimination factor D_{i} is close to unity at the SLS apparatus [218, 219] assuming a constant C [227], the mole fraction of the precursor gas can then be calculated by the following relation:

$$x_{\text{pre}}(T) = x_{\text{pre}}(T_0) \cdot \lambda(T) \cdot \frac{S_{\text{pre}}(T)}{S_{\text{pre}}(T_0)}. \tag{3.9}$$

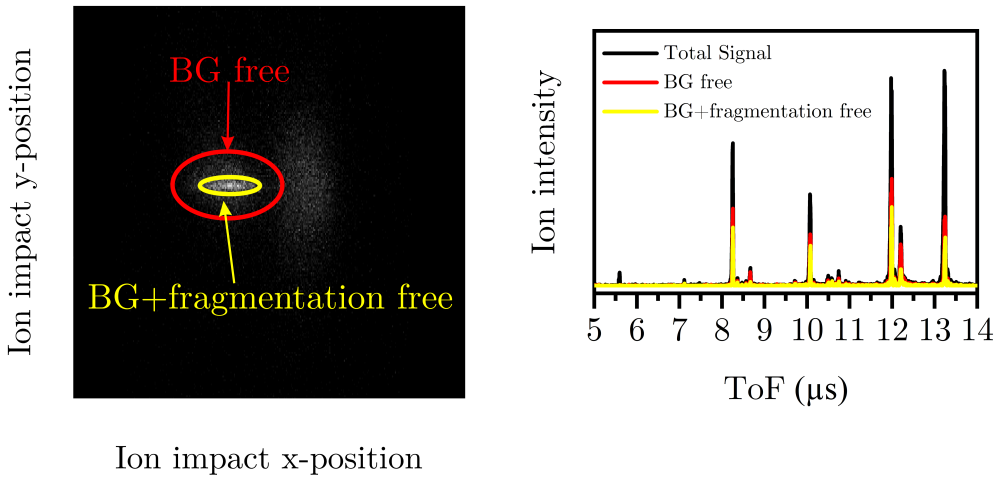

Figure 3.6: Procedure to obtain fragmentation and background free mass spectra from ion image data. Left: Exemplary velocity mapped ion image (VMI) with a specific region-of-interest (ROI) to obtain background (BG) free mass spectra (red) by leaving out the room temperature BG as well as fragmentation free mass spectra (yellow). This is done by only evaluating the ions with narrow kinetic energy distribution, since fragmentation is characterized by a randomly distributed kinetic energy release, which would result in a broader kinetic energy distribution of the ion signal in the VMI.

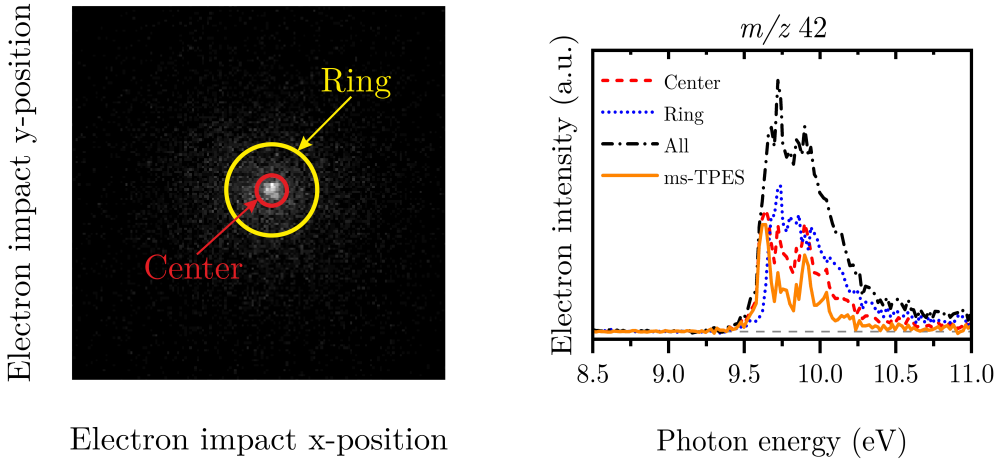

Figure 3.7: Procedure to subtract hot electrons from electron VMI raw data (left) to obtain threshold photoelectron spectra (orange, right) by analyzing only the threshold electrons and subtracting the hot electron contribution using center (dashed) and ring (dotted) electrons according to Eq. 3.6 [171], own representation.

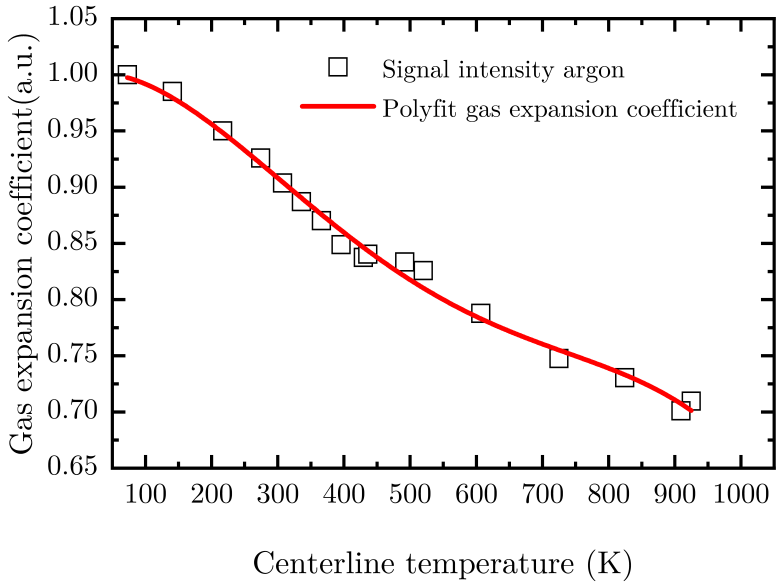

Figure 3.8: Gas expansion coefficient λ as a function of temperature using argon as inert gas.

The initial mole fraction in the evaporator stage is calculated using the vapor pressures relations from the literature for $Al(acac)_3$ [228], $Zr(acac)_4$ [229] and $Fe(Cp)_2$ [230], respectively. Using Eq. 3.9 one can obtain temperature-dependent mole fraction profiles of the precursor and therefore kinetic investigations are possible. Details on the calculations can be found in the respective chapters Chap. 4–Chap. 6.

3.3.5 General Procedures and Settings for the Analysis

When using a synchrotron radiation source coupled to an i^{2}PEPICO apparatus for data collection and analysis, some procedures must be undertaken to obtain satisfactory signal-to-noise ratios and high signal levels. Appropriate settings and calibration are also a prerequisite to obtain a well-resolved molecular beam on the imaging detector which is one of the major benefits of double-imaging setups. Prior to each experiment, the photon energy is calibrated using the 11s', 12s' and 13s' autoionization lines of argon in the first and second order. The mass discrimination factor can be neglected in the experiments and is set to unity (see Sec. 3.2.1). The stark shift of the observed signals to lower photon energies due to the high extraction fields of $>200\,\mathrm{V\,cm^{-1}}$ used was accounted for by correcting the mass-selected photoelectron spectra (ms-TPES) accordingly [231]. At the cost of a slightly lower energy resolution of 8 meV [232], but to optimize the photon flux necessary to detected elusive species, in this study, a 150 lines/mm grating was used (see Sec. 2.1.3).

Further methods to tailor the beam by filtering higher harmonics or unwanted artificial signal fragments were exploited. Those beneficial effects can be achieved by using an optical mirror that is transparent up to a specific wavelength, but opaque

above this threshold. Higher harmonics can also be eliminated by the absorption of energy in a noble gas filter through ionization, where the ionization energy of the noble gas limits the use of each substance to a specific energy range (Sec. 2.1.3). In the present CRF-PEPICO apparatus both methods are used. Hence, three modes of operation can be adjusted to manipulate the refocused monochromatized radiation with the aim to maximize signal intensity in the i^{2}PEPICO apparatus while suppressing artificial signals, e.g., from higher harmonics. First, for energies below 8.0 eV, a magnesium fluoride (MgF_2) window can be screwed into the optical path, having the benefit to only transmit electromagnetic radiation below 11.0 eV. This is especially useful for suppressing artificial signals at energies below 8.0 eV, where the ionization threshold of large metal-containing and organic molecules are often located. Its usage helps to avoid fragmentation of heavy metal-containing molecules and simultaneously achieves a better signal-to-noise ratio for the collected ms-TPES. The second mode of operation is primarily used which utilizes a rare gas filter with nine differentially pumped chambers, operated either with a mixture of Ne/Ar/Kr for energies of 8.0–12.0 eV or in case of the third operation mode pure Ne for energies up to 21 eV. This configuration efficiently suppresses second order radiation [173].

Passing these optical elements through an adjustable exit slit, radiation with the desired properties enters the vacuum apparatus and ionizes the gaseous sample within the ionization volume. In the described experiment, the choice of averaging times depend mainly on the concentration and ionization cross section of the species of interest. Since the costly beamtime[3] is shared among many users in a competitive application process and its total amount is therefore strictly limited, averaging times should be kept to a minimum. Considering this, and given the high dilution of the precursor molecules in the carrier gas stream, acquisition times for the main species of 240–360 s were chosen. Species with lower expected mole fractions need longer averaging times of up to 900 s, especially when using the MgF_2 window. Hereby, for the metal-containing intermediates, satisfactory signal-to-noise ratios of >10 are achieved.

[3]One hour of beamtime costs approx. 1000 Euro.

Chapter 4

Gas-Phase Aluminium Acetylacetonate Decomposition: Revision of the Current Mechanism by VUV Synchrotron Radiation

The content of the following chapter was initially published as part of the themed collection "2021 PCCP HOT articles" in the Journal *Physical Chemistry Chemical Physics (PCCP)*, **23**, 15059-15075, (2021) by S. Grimm, S.-J. Baik, P. Hemberger, A. M. Kempf, T. Kasper and B. Atakan entitled "Gas-phase aluminium acetylacetonate decomposition: revision of the current mechanism by VUV synchrotron radiation".

The article is reprinted, applying minor formal changes to adhere to the style and structure of this thesis, with permission from the Royal Society of Chemistry (RSC) and is available online under the following citation:

DOI: https://doi.org/10.1039/D1CP00720C

Contribution Statement

In the course of this publication **I** chose the experimental conditions, set up and performed all the experiments that are presented. I additionally analyzed and evaluated the data from the i²PEPICO experiment, visualized both, the experimental and numerical results and wrote the original draft.

Dr. Seung-Jin Baik conducted the numerical simulation of the microreactor, provided these results for further analysis and contributed to the interpretation of the numerical results, as well as editing and review of the manuscript. **Dr. Patrick**

Hemberger provided the resources at the Swiss Light Source in Switzerland, performed, evaluated and wrote about the quantum chemical calculations and contributed to the remaining manuscript by review and editing. **Dr. Andras Bodi** helped in performing the experiments, provided the resources at the Swiss Light Source and contributed to the manuscript by review and editing. **Prof. Dr. Andreas M. Kempf** was involved in the conceptual design of the numerical simulation, acquired the research funding and was responsible for the project administration. **Prof. Dr. Tina Kasper** and **Prof. Dr. Burak Atakan** were also involved in the conceptual design, acquired the research funding and were responsible for the project administration, as well as contributed to the interpretation of the results. All authors were engaged in the correction and later proof-reading of the manuscript.

CRediT (Contributor Roles Taxonomy author statement):

S. Grimm: investigation, formal analysis, visualization, writing – original draft; **S.-J. Baik**: methodology, investigation, software, writing – review & editing; **P. Hemberger**: investigation, resources, writing – review & editing; **A. Bodi**: investigation, resources, writing – review & editing; **A. Kempf**: methodology, supervision, writing – review & editing, project administration, funding acquisition. **T. Kasper**: conceptualization, methodology, supervision, project administration, funding acquisition; **B. Atakan**: conceptualization, methodology, supervision, writing – review & editing, project administration, funding acquisition.

Abstract

Although aluminium acetylacetonate, is a common precursor for chemical vapor deposition (CVD) of aluminium oxide, its gas-phase decomposition is not well-known. Here, we studied its thermal decomposition in a microreactor by double imaging photoelectron photoion coincidence spectroscopy (i^{2}PEPICO) between 325 and 1273 K. The reactor flow field was characterized by computational fluid dynamics (CFD). Quantum chemical calculations were used for the assignment of certain species. The dissociative ionization of the room temperature precursor molecule starts at a photon energy of 8.5 eV by the rupture of the bond to an acetylacetonate ligand leading to the formation of the $Al(C_5H_7O_2)_2^+$ ion. In pyrolysis experiments, up to 49 species were detected and identified in the gas-phase, including reactive intermediates and isomeric/ isobaric hydrocarbons, oxygenated species as well as aluminium-containing molecules. We detected aluminium bis(diketo)acetylacetonate-H, $Al(C_5H_7O_2)(C_5H_6O_2)$, at m/z 224 together with acetylacetone ($C_5H_8O_2$) as the major initial products formed at temperatures above 600 K. A second decomposition channel affords $Al(OH)_2(C_5H_7O_2)$ along with the formation of a substituted pentalene ring species ($C_{10}H_{12}O_2$), as assigned by Franck–Condon simulations and quantum chemical calculations. Acetylallene

(C_5H_6O), acetone (C_3H_6O) and ketene (C_2H_2O) were major secondary decomposition products, formed upon decomposition of the primary products. Three gas-phase aromatic hydrocarbons were also detected and partially assigned for the first time: *m/z* 210, *m/z* 186 ($C_{14}H_{18}$ or $C_{12}H_{10}O_2$) and *m/z* 146 ($C_{11}H_{14}$ or $C_9H_6O_2$) and their formation mechanism is discussed. Finally, Arrhenius parameters are presented on the gas-phase decomposition kinetics of $Al(C_5H_7O_2)_3$, aided by numerical simulation of the flow field.

4.1 Introduction

Due to its wear and corrosion resistance, high band gap and beneficial refractive index, aluminium oxide (Al_2O_3) is a popular coating, widely used in a variety of applications, for instance, in protective coatings, microelectronics, and optical devices. In particular, Al_2O_3 can act as a passivating layer, as an alternative gate dielectric oxide [233, 234], anti-corrosion and permeation barrier coating [235, 236, 237, 238], as well as surface enhancement coating in the cutting tool industry [236, 239]. Thanks to high growth rates and comprehensive surface coverage, Al_2O_3 layers are frequently synthesized by metal–organic chemical vapor deposition (MOCVD), a widely used technique for the preparation of functional coatings [240]. In MOCVD processes, a volatile, metal-containing precursor is used for the deposition of thin films.

Metal β-diketonates are advantageous, due to their relatively high vapor pressure at moderate temperatures and their thermal stability [241], which explains the increased use of the non-toxic and inexpensive aluminium tris(acetylacetonate) $Al(C_5H_7O_2)_3$[1] as a precursor in MOCVD [83, 86, 241, 242, 243, 244, 245, 246, 247, 248]. It is well-known that gas-phase reactions play an important role in the determination of the film composition, purity, and growth rate [240]. Due to the high activation energy of the unimolecular dissociation of metal β-diketonates, the homogeneous decomposition of the gaseous precursor is considered as the rate-limiting step for film growth [241]. Unwanted particle formation and nucleation processes may also occur in the gas-phase which reduce the growth rate significantly [240]. Consequently, the characterization of the gas-phase chemistry is of particular interest. This explains efforts to study the reaction kinetics [79, 80] and attempts to characterize [80, 81, 82] primary gaseous reaction products of the thermal decomposition of $Al(C_5H_7O_2)_3$, although the definitive reaction mechanism has remained elusive so far.

In an early work, von Hoene and coworkers [81] used *ex situ* mass spectrometry to identify the primary decomposition products of the thermal degradation of $Al(C_5H_7O_2)_3$ in vacuum at temperatures of 423–673 K. They identified carbon dioxide (CO_2) and acetone (C_3H_6O) as the major decomposition products and found traces of acetylacetone ($C_5H_8O_2$), too. A drawback of this study was the possible interaction between the condensed and the gas-phase which may lead to side reactions. Tackling this, Minkina [79] investigated the gas-phase pyrolysis at a low pressure of 1 kPa under static conditions by the manometric method between 653 and 723 K. Besides methane (CH_4) and ketene (C_2H_2O), acetone, carbon dioxide, butene (C_4H_8), and carbon monoxide (CO) were the most abundant species detected. Because of the large excess of acetone and carbon dioxide, she concluded that these products originated from the sequential decomposition of acetylacetone. Therefore, only secondary decomposition products of $Al(C_5H_7O_2)_3$ were identified. Covering a wider temperature range from 423 to 923 K, Bykov and colleagues [80] determined the onset of the thermal decomposition of $Al(C_5H_7O_2)_3$ in a heated

[1] Commonly abbreviated as $Al(acac)_3$.

reactor to be around 563 K by electron ionization mass spectrometry. Additionally, they recorded temperature-dependent species profiles, which showed three distinct temperature regimes, and proposed reaction schemes for each. According to their findings, the first decomposition step proceeds via the loss of acetylacetone and the subsequent formation of acetone and ketene. A second decomposition pathway involves the cleavage of the enolic C–O bond combined with an intramolecular rearrangement of the central H-atom, followed by loss of an uncharacterized C_5H_6O isomer at m/z 82. The formation of a cyclic diketone at m/z 164, which further decomposes upon ketene loss to yield 3,5-dimethylphenol at m/z 122, represents the third proposed decomposition pathway. It has been stated that this mechanism can be explained by an Al–O bond breakage and a transformation of bidentate $C_5H_7O_2$ ligand into a monodentate one [82].

However, standard 70 eV electron ionization mass spectra suffer from fragmentation, which complicates the assignment of the detected m/z peaks to their neutral parent species. To address this, Rhoten and DeVore [90] conducted an *in situ* study of the thermal decomposition of $Al(C_5H_7O_2)_3$ in a low-pressure stationary flow reactor in the 500–900 K temperature range by Fourier-transform infrared spectroscopy (FTIR) and subsequent gas chromatography-mass spectrometry (GC-MS) analysis of the sample residue. They identified at least ten volatile organic products. In addition to a confirmation of the findings by Bykov et al. [80], they could assign C_5H_6O to 3-pentyn-2-one and emphasized the role of H-atom migration with intramolecular rearrangement in the reaction mechanism. However, they did not detect aluminium-containing intermediates or products besides the precursor itself and indicated that the species characterization using GC-MS can be biased by the reaction of $Al(C_5H_7O_2)_3$ in the column.

Previous studies probing the gas-phase of CVD processes using $Al(C_5H_7O_2)_3$ show that the experimental results under CVD process conditions are often too complex to be exploitable, because mostly secondary decomposition products were detected and the real nature of the mechanism remained elusive so far. As the deposition temperature increases, gas-phase chemistry may initiate complex sequential reactions leading to the production of surface-active reaction products that facilitate or even allow the desired film growth. This means that relying exclusively on such methods may result in major reaction pathways being overlooked. This motivated us to identify aluminium-containing decomposition products of $Al(C_5H_7O_2)_3$ definitely and isomer-selectively to provide comprehensive insight into the reaction mechanism.

Recently, tuneable vacuum ultraviolet (VUV) synchrotron radiation has been used as a soft ionization technique to probe harsh environments, such as flames [158, 249, 250], flow reactors [122, 251, 252], and MOCVD processes [125, 126], to characterize reactive intermediates and products unambiguously. Combining the tunability of the photon energy and velocity map imaging (VMI) kinetic energy analysis of the photoelectrons, double imaging photoelectron photoion coincidence spectroscopy (i^{2}PEPICO) [253], has been shown to be a promising tool for the isomer-selective identification and characterization of reactive intermediates upon

pyrolysis [254]. These sophisticated techniques to detect short-lived gas-phase species have proven to be useful not only to determine and characterize elusive reactive intermediates but also to delimit surface-bound and gas-phase chemistry. An accurate description of the gas-phase kinetics is of great importance to model and understand film growth processes. This holds especially true for modeling the whole deposition process, where a complete set of reactions in necessary.

The present work reports on the photolysis and thermal decomposition of highly diluted $Al(C_5H_7O_2)_3$ in inert carrier gas in a silicon carbide (SiC) flow tube microreactor at reduced pressure and temperatures between 325 and 1273 K. To model the flow field inside the SiC reactor, we applied computational fluid dynamics (CFD). Products leaving the reactor expand into high vacuum and form a molecular beam, in which reactive molecules are preserved. The intermediates and products are subsequently ionized by tuneable VUV synchrotron radiation and detected by imaging photoelectron photoion coincidence spectroscopy (i^2PEPICO). Temperature-dependent photoionization mass spectra offer insights into the decomposition steps. Photoionization mass spectra (PIMS) and photoion mass-selected threshold photoelectron spectra (ms-TPES) were recorded in the 7.0–11.5 eV photon energy range to assign the reactive intermediates and the products formed. In contrast to previous studies, we are able to detect metal-containing intermediates when their lifetime is at least a few microseconds.

4.2 Methods

4.2.1 Experimental Setup

The experiments were performed at the VUV beamline [145] at the Swiss Light Source (SLS) of the Paul Scherrer Institute in Switzerland. A detailed description of the experimental apparatus [173, 174] as well as the reactor setup pioneered by Chen et al. [121] can be found elsewhere [217]. A schematic sketch of the experimental setup is shown in Fig. 4.1. Aluminium tris(acetylacetonate) (>99%, *Sigma-Aldrich Inc.*) is sublimed in a stainless steel tube, heated within a copper block (reddish brown in Fig. 4.1), to ensure isothermal sublimation conditions. The temperature and pressure of the sublimation chamber are monitored and kept constant during each measurement. Unimolecular reaction conditions are achieved by a relatively low pressure and a highly diluted sample stream to minimize the likelihood of reactive collisions. Argon (99.9999%) was delivered by calibrated mass flow controllers (*MKS Instruments*) at a constant flow rate of 22 sccm. To reveal potential bimolecular chemistry in the reactor we conducted six separate experimental sets operating at evaporator pressures of 550 and 1600 mbar and sublimation temperatures of 395/405/420 K. Assuming thermal equilibrium, the precursor mole fractions at the reactor inlet ranged between $6.8 \times 10^{-5} < x_{Al(acac)_3} < 4.8 \times 10^{-4}$. After sublimation, the mixture is expanded through a 100 µm pinhole into a resistively heated SiC flow microreactor [217] with an inner diameter of 1 mm and a heated length of 10 mm. To measure the decomposition temperature, a type C thermocouple, with

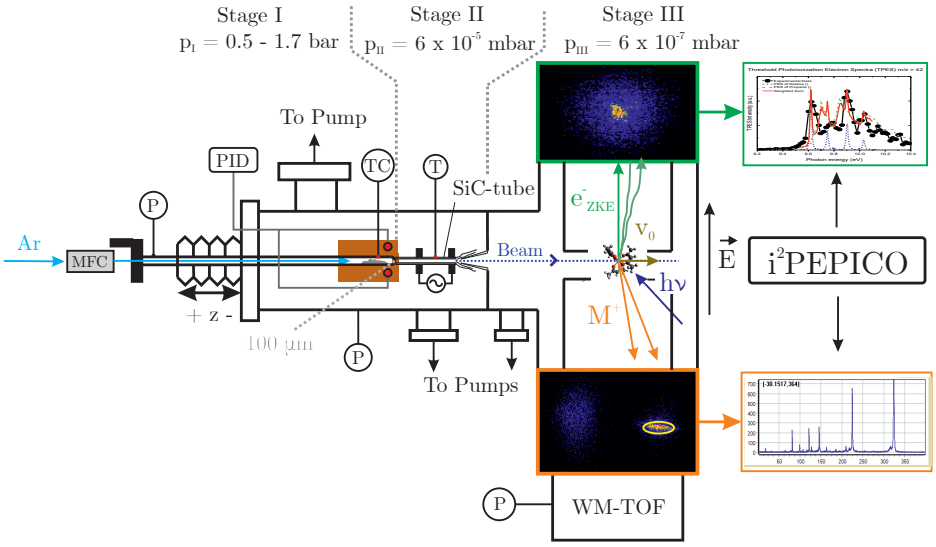

Figure 4.1: Schematic drawing of the pyrolysis reactor coupled to the i²PEPICO experimental apparatus. The working principle of velocity map imaging (VMI) and the raw data are shown on the right hand side; the yellow circle in the ion (bottom) image displays the region of interest chosen to sample the translationally cold molecular beam directly, suppressing the background and the dissociative photoionization signal.

an estimated uncertainty in the examined temperature range of 1%, was attached centrally to the outer surface of the pyrolysis reactor in the middle of the heated range. Earlier studies quote the overall uncertainty of the centerline temperature to be ± 100 K [220, 221]. The temperature readings were used as boundary condition in the numerical simulation of the flow field and will be given in the results part. This procedure has been already established in previous studies [202, 204].

After passing the reaction zone, the reactive mixture is rapidly expanded to high vacuum at 6.8×10^{-5} mbar and forms an effusive molecular beam. The rapid drop in collision frequency preserves the gas composition, including highly reactive species. After expansion from the reactor, a nickel skimmer with a 2 mm orifice cuts out the central part of the gas mixture, letting a fraction of the pyrolyzed gas sample proceed towards the ionization chamber, which is kept at a background pressure of less than 10^{-6} mbar. In the ionization region, the sample beam is crossed by the monochromatized VUV radiation at an energy resolution of 6 meV. The resulting cations and photoelectrons are separated by a constant extraction field of 243 V cm^{-1}, which accelerates them in opposite directions. After passing the

respective flight tubes, electrons and ions are detected by two *Roentdek* DLD40 fast position-sensitive delay-line anode detectors in delayed coincidence in velocity map imaging (VMI) conditions. This means that the impact radius is proportional to the species' initial kinetic energy corresponding to its momentum perpendicular to the extraction axis [124]. VMI allows us to spatially separate the parent ions from the room temperature background in the chamber and also from ions formed in dissociative ionization, which is often accompanied by large kinetic energy release perpendicular to the beam propagation direction (see region-of-interest (ROI) highlighted in Fig. 4.1) [173].

In all experiments the photon energy was either kept constant at near-threshold photoionization energies of the decomposition species of interest or was scanned with a step size of 0.025 eV in the 7.0–11.5 eV range. To minimize fragmentation and to be above the ionization threshold for various molecules, we recorded mass spectra of the reaction mixtures at 7.8, 8.0, 8.5, 9.0, 9.5, 10.0, 10.5, and 11.5 eV within a temperature range of 325 K to 938 K. Single measurements were carried out at higher temperatures up to 1273 K to investigate secondary and tertiary decomposition products. The spectra were corrected by the known photon flux at the respective photon energies and were used to derive temperature-dependent species profiles. In order to account for the higher internal energies of the pyrolyzed species and the corresponding red shift of the ionization onset, we shifted the literature spectra for better comparison by less than 0.1 eV. Species were assigned based on their molecular mass, photoionization mass spectrum (PIMS) or their mass-selected threshold photoelectron spectrum (ms-TPES). The latter are based on the center signal of the electron detector, where threshold electrons are detected, from which the hot electron contribution has been subtracted according to the procedure by Sztáray and Baer [171]. The photoelectron spectra allow for an unambiguous identification of most of the primary decomposition products by comparing them to reference spectra [253]. Additionally, quantum chemistry can help in species identification, as shown below.

4.2.2 Quantum Chemical Calculations

The Gaussian 16 A03 [255] suite of programs has been utilized to calculate the adiabatic ionization energies of some of the detected species. Geometries were optimized on the B3LYP/6-311++G(d,p) level of theory and the vibrational frequencies of both neutral and ionic species have been calculated. Adiabatic ionization energies were calculated using composite methods, such as CBS-QB3 [256] or G4 [257]. The hydrogen transfer reaction of the initial decomposition reaction of aluminium tris(acetylacetonate) was explored using constrained geometry scans applying B3LYP/6-311++G(d,p) and further refined by utilizing the synchronous transit-guided quasi-Newton method [258] to locate the transition state. We have refined the energetics of this reaction applying CBS-QB3 computations [259].

Franck–Condon (FC) simulations have been carried out in the double harmonic approximation, based on frequency analysis at the optimized geometries of the

neutral and cation utilizing eZspectrum [260]. The stick spectra were convoluted with a 20–40 meV full width at half maximum Gaussian function to account for the rotational envelope and the energy resolution and the adiabatic ionization energy was shifted to fit the experimental threshold photoelectron spectra (TPES). Time-dependent density functional theory (TD-DFT) calculations were carried out to identify excited-state bands in the photoelectron spectrum, at the B3LYP/6-311++G(d,p) level of theory [261].

4.2.3 CFD Simulation of the Microreactor

Reactive intermediates are not detectable at long residence times, because they are converted to more stable products. Thus, the reactor is designed such that secondary reactions are minimized by ensuring short residence times <100 µs [202]. This requires small reactor geometries, whose characterization is not straightforward. For instance, the microreactor surface temperature is measured at one point on the outer surface, while the whole temperature profile is of interest. To interpret and quantify the experimental observations, the flow field in the microreactor must be known, as well as residence times, pressure, and temperature fields. As the conditions in the microreactor are hardly measurable directly [262], modeling was used to estimate them.

The Boltzmann equation provides a general description of the evolution of a gas and represents the motion of gas molecules at each location in the gas and the change with time due to collisions between molecules [263]. When the fluid's molecules have a short mean free path, the fluid can be treated by continuum mechanics, for instance with the Navier–Stokes equations (see Eq. A.1 and Eq. A.2). The Knudsen number (Kn) represents the ratio of the mean free path to the characteristic length of the flow region (see Eq. A.3 and Eq. A.4), and determines whether the continuum mechanics formulation can be used. Depending on Kn the flow region can be divided into a continuous flow region (Kn<0.01), a slip flow region (0.01≤Kn<0.1), a transition flow region (0.1≤Kn<10), and a free-molecular flow region (Kn≥10). The flow in the slip region can be predicted by considering a slip (boundary) condition with the Navier–Stokes equations when Kn deviates from the continuum regime just slightly (0.01≤Kn<0.1). Since Kn is between 0.005 and 0.02 in the microreactor it is in the slip condition range as shown in Fig. A.3. Thus, to investigate the flow field the Navier–Stokes equations with a slip (boundary) condition (see Eq. A.5 and Eq. A.6) are solved using ANSYS Fluent 19.1 [264]. Furthermore, gaseous flows should be considered as compressible when the pressure changes are more than approximately 20% of the mean pressure [265]. The microreactor flow must be considered compressible since its outlet is connected to high vacuum at 6×10^{-5} mbar. Compressibility is accounted for using the second-order upwind Roe-flux difference splitting scheme [266].

The simulation was performed with pure argon flow because the concentration of the precursor is negligible. The viscosity and thermal conductivity of argon were determined by Bich et al. [267]. To obtain simulation results for different operating

conditions efficiently the computational domain was set up as axisymmetric two-dimensional geometry (see Fig. A.1). A single simulation took approximately 300 core hours with 1.09 M nodes and 1.08 M cells with 10 µm grid size. This grid size is small enough to resolve the flow field (see Fig. A.2 and Fig. A.3). Due to the lack of experimental data for such systems, as for instance pressure and temperature readings inside the reactor, we validated our approach on a similar numerical microreactor study utilizing the boundary-layer model by Weddle et al. [203]. The flow field of our approach correlated fairly well with the reference data (see Fig. A.4) which shows its feasibility under the present experimental conditions. Results of our CFD calculations are taken into account when the effective pyrolysis temperature as well as the kinetics are determined based on the measured surface temperature and the modeled flow field temperatures. The findings (see Sec. 4.3.7) show that the reactor geometry and experimental conditions should allow radicals to survive up to the reactor outlet so that they can be probed after expansion into high vacuum.

4.2.4 Kinetics

Studies that use a microreactor to investigate the thermal decomposition processes rarely quantify the reaction kinetics because the conditions inside the reactor are poorly known. We overcame this by modeling the flow field inside the SiC reactor, which includes detailed temperature fields and residence times for various reaction conditions (see Sec. 4.3.7). This information, combined with the measured species profiles, enabled us to carry out a kinetic analysis of the primary decomposition step. The steps to determine the temperature dependence of the $Al(C_5H_7O_2)_3$ mole fraction proceed according to Zhang et al. [227]. In our case, argon is used as reference species for the determination of the gas expansion coefficient $\lambda(T)$, which summarizes temperature-dependent signal variations of argon (m/z 40), representing the variation in sampling efficiency due to changing expansion behavior as a function of temperature. The mass-dependency is not further investigated in our case, because it only affects light species such as H_2 significantly [227]. The gas expansion coefficient has been determined by recording temperature-dependent mass spectra at a fixed photon energy of 15.8 eV in the 346–909 K range and is shown as Fig. A.6. For an incident photon energy of 8.0 eV and fixed photon flux, the mole fraction of $Al(C_5H_7O_2)_3$ at temperature T can be calculated by Eq. 4.1

$$x_{\mathrm{Al(acac)_3}}(T) = x_{\mathrm{Al(acac)_3}}(T_0) \cdot \lambda(T) \cdot \frac{S_{\mathrm{Al(acac)_3}}(T)}{S_{\mathrm{Al(acac)_3}}(T_0)}, \tag{4.1}$$

where $S_i(T)$ represents the ion signal intensity measured at temperature T and $x_{\mathrm{Al(acac)_3}}$ is defined as the precursor mole fraction measured at temperature T. The inlet mole fraction was calculated assuming saturated conditions inside the evaporator; for an evaporation temperature of 405 K this results in $x_{\mathrm{Al(acac)_3}}(T_0) = 4.15 \times 10^{-4}$ from vapor pressure data [228]. Arrhenius plots were derived using the integral method for the unimolecular dissociation reaction

$$\mathrm{Al(C_5H_7O_2)_3} \xrightarrow{k_{\mathrm{uni}}} \text{Products}\,. \tag{R 4.1}$$

Unimolecular gas-phase dissociation reactions of organometallic precursors often follow first order kinetics as shown in Eq. 4.2:

$$k_{\mathrm{uni}}(T) = A_0 \cdot \exp(E_a/RT), \tag{4.2}$$

with the respective Arrhenius behavior, representing A_0 as the pre-exponential factor and E_a as the molar activation energy in $\mathrm{kJ\,mol^{-1}}$. Previous experiments demonstrated that this is also the case for surface reactions following the Langmuir–Hinshelwood mechanism, which is first order at low partial pressures of $\mathrm{Al(C_5H_7O_2)_3}$ [82]. Surface and gas-phase reactions may take place concurrently in our microreactor, thus the total rate constant is the sum of both contributions. Both were derived simultaneously and the kinetic constants for each follows the Arrhenius expression given in Eq. 4.2, where:

$$k_{\mathrm{tot}}(T) = k_{\mathrm{g}}(T) + k_{\mathrm{s}}(T). \tag{4.3}$$

The time-dependent concentration change for a unimolecular reaction is given by:

$$\frac{\mathrm{d}c}{\mathrm{d}t} = -k_{\mathrm{tot}}(T) \cdot c, \tag{4.4}$$

leading to

$$c = c_0 \cdot \exp(-k_{\mathrm{tot}}(T) \cdot t), \tag{4.5}$$

combined with Eq. 4.2 and Eq. 4.3 the following expression results:

$$c = c_0 \cdot \exp(-\left[A_{0,\mathrm{g}} \cdot \exp(E_{\mathrm{a,g}}/RT) + A_{0,\mathrm{s}} \cdot \exp(E_{\mathrm{a,s}}/RT)\right] \cdot t). \tag{4.6}$$

This expression was used to fit the four unknowns $A_{0,\mathrm{g}}$, $A_{0,\mathrm{s}}$, $E_{\mathrm{a,g}}$ and $E_{\mathrm{a,s}}$ to the experimental data $c(c_0, T, t)$.

4.3 Results and Discussion

In the following, first the photoionization of room temperature $Al(C_5H_7O_2)_3$ is shown in order to properly distinguish pyrolysis from dissociative ionization leading to the same m/z species. Next, the identification of the pyrolysis products is described, which is rationalized by photoionization and mass-selected threshold photoelectron spectra ms-TPES, compared with reference spectra or Franck–Condon simulations. These results are subsequently used to obtain temperature-dependent species profiles, from which a reaction scheme is derived. By invoking the known reactor conditions given by the CFD simulations, we finally investigate the reaction kinetics of the primary $Al(C_5H_7O_2)_3$ decomposition step.

4.3.1 Dissociative Photoionization of $Al(C_5H_7O_2)_3$

Since the incident photon beam can, depending on the energy, dissociatively photoionize the sample, it is often difficult to distinguish directly ionized thermal decomposition products from those stemming from dissociative photoionization (DPI) of the neutral precursor surviving the pyrolysis reactor. To address this, we analyzed the room temperature dissociative ionization of $Al(C_5H_7O_2)_3$ in the 7.5–11.5 eV energy range.

Mass-selected threshold photoelectron spectra (Fig. 4.2 (a)) were recorded to shed light on the dissociative ionization mechanism of $Al(C_5H_7O_2)_3$. The first band of the parent m/z 324 ms-TPES (red curve) is centered at 8.14 eV and its maximum agrees with the literature value of $IE_{vert} = 8.17$ eV [268], as well as with the calculated adiabatic ionization energy $IE_{ad} = 7.81$ eV.

Trivalent cations produce even-electron fragment ions upon dissociation by losing a $C_5H_7O_2$ radical and consecutive dissociation have rarely been observed, because of the energetically favored 3+ valence state of the fragment ion [269]. This explains the main dissociation channel, the loss of a $C_5H_7O_2$ ligand, leading to the formation of $Al(C_5H_7O_2)_2^+$ at m/z 225 (blue curve, Fig. 4.2 (b)). The daughter ion signal starts to rise at around 8.5 eV. However, with increasing photon energy, m/z 100 also appears in the spectra. It can clearly be stated that m/z 100 and its fragment m/z 85 is due to enolone- and diketo-acetylacetone, since Antonov et al. [270] ascertained that the ionization energy of enolone-acetylacetone is 8.9 eV, which fits the onset of our m/z 100 ms-TPE spectrum (see Fig. A.5: 300 K). Given the narrow lateral kinetic energy distribution of the m/z 100 ions, traces of acetylacetone are indeed in the sample at room temperature. Consequently, the room temperature m/z 100 signal is due to sample impurities. We can rely on these insights to derive the temperature-dependent species profiles.

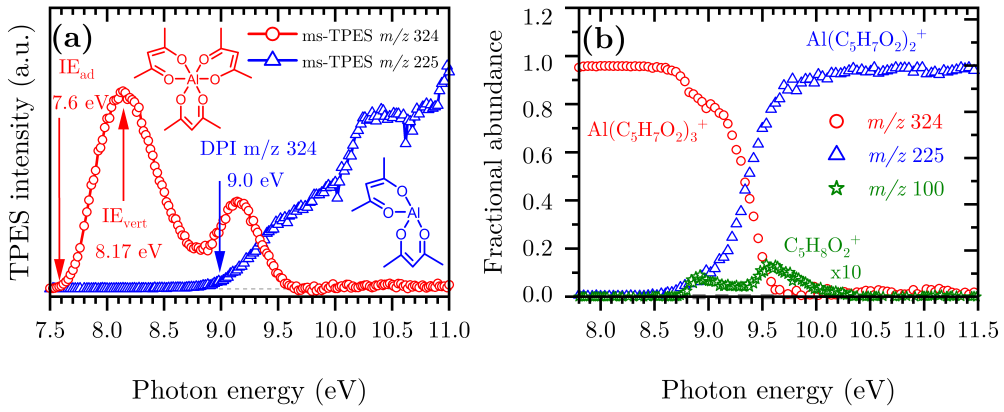

Figure 4.2: (a) Mass-selected threshold photoelectron spectra (ms-TPES) recorded at room temperature in the 7.5–11.0 eV photon energy range. The main dissociative ionization product at m/z 225 is denoted in blue, whereas the parent molecule $Al(C_5H_7O_2)_3$ is displayed in red along with literature ionization energies [268]. (b) Breakdown diagram of $Al(C_5H_7O_2)_3$ at room temperature without considering the m/z 100 signal (see text for discussion).

4.3.2 Photoionization Mass Spectra of the Pyrolysis Products

After insights in the dissociative ionization of the precursor have been gained, $Al(C_5H_7O_2)_3$ was pyrolyzed in the temperature range of 325–973 K. Photoionization mass spectra were recorded and evaluated at fixed photon energies. Representative photoionization mass spectra at fixed photon energies of 8.0 and 9.5 eV are shown in Fig. 4.3. When the SiC reactor is heated above 525 K, we clearly see a depletion of the precursor signal and product peaks at m/z 122, 164, and 224–225 are observed (Fig. 4.3 (a)). This threshold value agrees well with the 523 K pyrolysis onset observed by Rhoten and coworkers [90]. Since we only evaluate the ion signal intensities that emerge from the molecular beam at low ionization energies, these ions are almost exclusively assigned to the primary decomposition products of $Al(C_5H_7O_2)_3$ with small contributions of dissociative ionization. Increasing the reactor temperature to 655 K, the intensity of the m/z 224–225 peak increases by a factor of 10, while the precursor molecule signal decreases. Additionally, new product peaks arise in the spectrum at m/z 82 and 146. To assess product species with lower masses, mass spectra at higher photon energies were recorded (Fig. 4.3 (b)). At temperatures above 700 K, several peaks appear below m/z 100, while the primary decomposition product signal at m/z 224–225, is reduced markedly. In addition to the previously reported species in the literature, our mass spectra show species with m/z 146, 186, and 210 rising in concert with the depletion of the primary gas-phase decomposition product m/z 224.

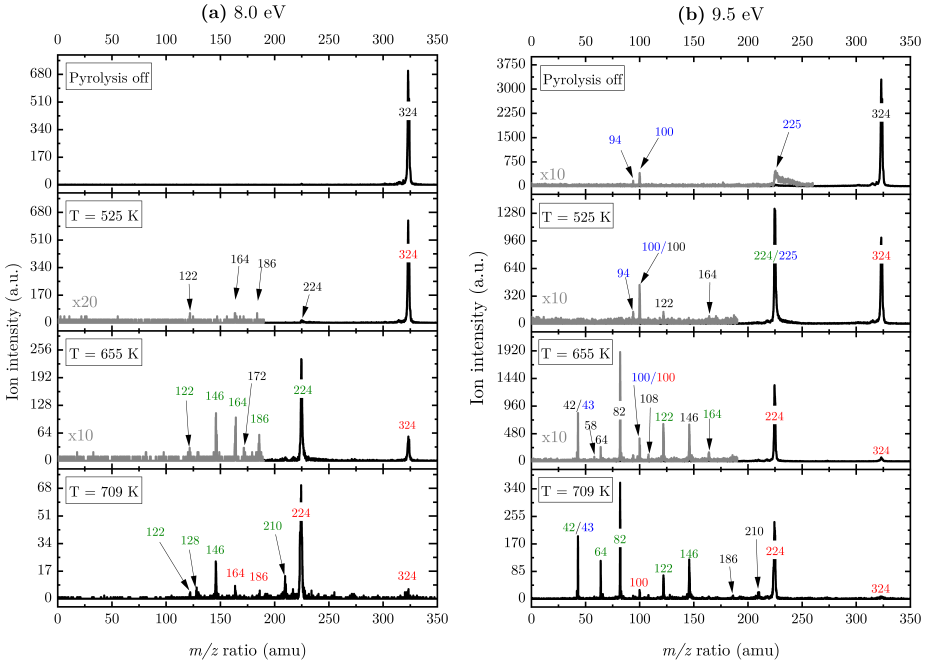

Figure 4.3: Temperature-dependent mass spectra of $Al(C_5H_7O_2)_3$ pyrolysis recorded at a photon energy of 8.0 (a) and 9.5 eV (b) and an inlet mole fraction of 4.15×10^{-4} (0.05%). The major peaks are labeled by their m/z ratio and with respect to their absolute decay (red) or increase (green) in comparison to the previous spectrum at lower decomposition temperature. Species that emerge for the first time are marked in black, whereas the blue numbers indicate that the species are due to dissociative ionization or impurities. For better comparison, the gray spectra are multiplied by a factor of 10 or 20.

4.3.3 Identification of the Primary Decomposition Product

Regarding the temperature-dependent mass spectra in Fig. 4.3, the question arises whether and to which extent the peak at m/z 224/225 is a pyrolysis product or formed by DPI of the parent molecule. Figure 4.4 (a) shows temperature-dependent mass-selected threshold photoelectron spectra (ms-TPES) of the precursor molecule as well as its primary decomposition and DPI product convoluted in the m/z 224 and 225 range. The ionization energy of the $Al(C_5H_7O_2)_2$ radical to form the singlet and triplet cation state at m/z 225 are calculated to be 4.76 and 7.81 eV at the CBS-QB3 level of theory, respectively. Therefore, we conclude that m/z 225 is formed exclusively by DPI. This is also substantiated by the broad kinetic energy distribution of the beam component of m/z 225 in the VMI images displayed in Fig. 4.4 (b-d) at 9.5 eV. In contrast, at 633 K, the m/z 224/225 channel follows the shape of the parent molecule m/z 324 and further increases above 9.0 eV, when dissociative ionization is observed at room temperature leading to the assumption that at higher temperatures a convolution of DPI and pyrolysis species is present.

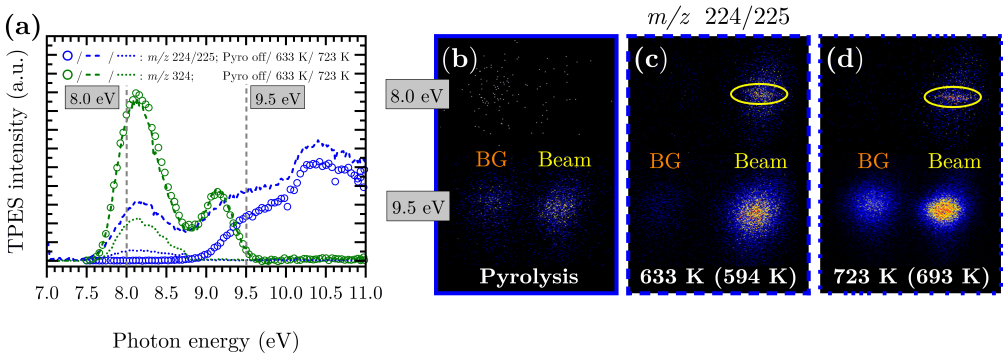

Figure 4.4: (a) Temperature-dependent ms-TPES of m/z 224/225 (blue) and m/z 324 (green) at photon energies from 7.0 to 11.0 eV at the pyrolysis temperatures of 303 K (circle), 633 K (dashed), and 723 K (dotted). The decay of the signal intensity of m/z 324 due to thermal decomposition can clearly be observed. Representative VMI images of m/z 224/225 at photon energies of 8.0 and 9.5 eV are shown at temperatures of (b) 303 K, (c) 633 K, and (d) 723 K. The estimated centerline temperature by CFD is given in brackets. The ROI for the molecular beam signal is marked in yellow. The kinetic energy distributions enable us to identify pyrolysis and dissociative ionization products.

For an unambiguous verification of the temperature onset and nature of the primary decomposition product observed, representative VMIs of the m/z 224 ion channel at 8.0 eV photon energy are displayed in Fig. 4.4 (b-d). We can clearly differentiate between the room temperature velocity distribution (denoted as "BG ") and those ions that have a large velocity perpendicular to the incident photon beam (denoted as "Beam"). Unlike in the lower part of Fig. 4.4 (c), where the beam component exhibits a broad kinetic energy distribution, typical for kinetic energy release in dissociative ionization, the former VMI shows a narrow distribution inside the molecular beam region. The ratio of m/z 224 to m/z 225 increases at higher temperatures, as seen in the increasing contribution of the cold molecular beam component of the band, which is substantiated by the m/z 224 kinetic energy distribution at 723 K (Fig. 4.4 (d)). At this point, the parent molecule m/z 324 is almost fully pyrolyzed, and only the first ms-TPES band is seen for the fragment channel, centered at around 8.2 eV. This indicates that the primary decomposition product m/z 224 contributes almost exclusively to this signal, as opposed to DPI delivering ions at m/z 225. Our assignment of $Al(C_5H_7O_2)(C_5H_6O_2)$ is corroborated by adiabatic ionization energy calculations, which find a value of 6.64 eV at the CBS-QB3 level of theory. The Franck-Condon (FC) simulation of the ground state (see Fig. A.3) predicts a broad band centered at 6.8 eV. At 7.0 eV, the lowest photon energy studied herein, the ms-TPES shows signal which overlaps with the simulation but drops quickly. Time-dependent density functional theory (TD-DFT) excited ion state calculations revealed vertical IEs to the $\tilde{A}^+$, $\tilde{B}^+$, and $\tilde{C}^+$ states of $Al(C_5H_7O_2)(C_5H_6O_2)^+$ at 8.2, 8.8 and 9.2 eV using B3LYP/6-311++G(d,p), which agrees with the observed features in the 723 K ms-TPE spectrum. Thus, we tentatively assign the m/z 224 peak to the $Al(C_5H_7O_2)(C_5H_6O_2)$ aluminium

species. Following this argumentation, near-threshold photon energies of 8.0 eV will be used for the detection of $Al(C_5H_7O_2)_3$ and the primary decomposition product $Al(C_5H_7O_2)(C_5H_6O_2)$, respectively. This allows us to suppress the DPI interference with the pyrolysis products at higher temperatures.

4.3.4 Assignment of Further Pyrolysis Products

Besides the mass-selective identification of the ions from the photoionization mass spectra (Fig. 4.3), we rely on photoionization mass spectra (PIMS) and mass-selected photoelectron spectra (ms-TPES) to assign further pyrolysis products. Following the approach of Hemberger et al. [271] we analyzed the threshold photoionization matrix (TPM), i.e., the threshold photoionization signal as a function of ion m/z and photon energy, of $Al(C_5H_7O_2)_3$ under pyrolysis at reactor temperatures of 633 K, 738 K and 824 K, at which we observe ca. 25, 50 and 100% depletion of the precursor signal and progressively larger product signals. In total, we observed 31 temperature-resolved ion peaks (see Tab. 4.1) which we assigned to 49 unique pyrolysis and dissociative ionization products of the precursor molecule. It is generally known that the dissociative ionization onset is shifted to lower ionization energies if the sample temperature is increased, as the initial thermal energy is also available for the dissociation of the parent ion [272]. As discussed above, these DPI contributions could be established with the help of ion VMI. The experimental spectra generally correlated well with the reference data for the assigned species. Experimental ionization energies are listed for better comparison in Tab. 4.1.

The peaks at m/z 18 and 32 were assigned to H_2O^+ and $O_2{}^+$, identified by a single photon energy measurement at 12.8 eV, close to their ionization energies. In similar manner, we recorded spectra at 14.2 eV and assigned the signal at m/z 28 exclusively to CO^+, as the peak was absent at lower photon energies. A series of C_1-C_{16} hydrocarbons was identified in the pyrolyzed sample. Representative examples of the species identification for the most relevant pyrolysis products are shown in Fig. 4.5 and Fig. 4.6, which are addressed in this paragraph. Additional PIMS and ms-TPES with the corresponding assignments can be found in Sec. A.4.

Table 4.1: Species assignment in $Al(C_5H_7O_2)_3$ pyrolysis by VUV i^{2}PEPICO using adiabatic and vertical ionization energies. Reference spectra and energies have been taken from the literature and are denoted at the respective value.

m/z	**Formula**	**Name**	**IE (eV)**	
			Ref.	This work
15	CH_3	Methyl radical	9.84 [273]	9.82
18	H_2O	Water	12.62 [155]	–
26	C_2H_2	Acetylene	11.40 [156]	11.42
28	CO	Carbon monoxide	14.01 [274]	–
30	CH_2O	Formaldehyde	10.89 [275]	10.90
32	O_2	Oxygen	12.33 [276]	–
39	C_3H_3	Propargyl radical	8.71 [277]	8.72
40	C_3H_4	Allene	9.69 [278]	9.70

		Propyne	10.38 [279]	10.38
42	C_2H_2O	Ketene	9.62 [280]	9.60
	C_3H_6	Propyne	9.73 [281]	9.72
43	C_2H_3O	DI-acetone	10.30 [270]	–
		DI-diketo AcAc	10.42 [282]	–
44	C_2H_4O	Vinyl alcohol (anti-)	9.17 [282]	–
		Vinyl alcohol (syn-)	9.30 [282]	–
		Acetaldehyde	10.23 [283]	9.82
52	C_4H_4	1-Buten-3-yne (vinylacetylene)	9.58 [284]	9.59
54	C_4H_6	1,3-Butadiene	9.07 [285]	–
		1,2-Butadiene	9.33 [155]	–
		2-Butyne	9.59 [284]	–
		1-Butyne	10.18 [155]	–
58	C_3H_6O	Acetone	9.71 [281]	9.68
64	C_5H_4	Pentatetraene	8.99 [286]††	8.98
		Ethynylallene	9.22 [287]	9.20
		Methyldiacetylene	9.50 [288, 289]	9.48
65	C_5H_5	Cyclopentadienyl radical	8.41 [290]	8.42
66	C_5H_6	1,3-Cyclopentadiene	8.58 [291]	8.56
		1,2,4-Pentatriene	8.88 [292]	8.86
		1-Penten-3-yne	9.10 [284]	8.96
82	C_5H_6O	2-Methylfuran	8.38 [293]	8.40
		Acetylallene	9.44 [270]	9.42
86	$C_5H_{10}O$	2-Pentanone	9.38 [155]	9.39
94	C_6H_6O	Phenol	8.49 [155]	–
100	$C_5H_8O_2$	Acetylacetone (enol)	8.90 [270]	8.90
	$C_5H_{10}O$	Acetylacetone (diketo)	9.50 [270]	9.51
108	C_7H_8O	Phenol, 2-methyl	8.39 [294]	8.40
122	$C_8H_{10}O$	2,6-Dimethylphenol	8.05 [295]	–
128	$C_{10}H_8$	Azulene	7.42 [296]	–
146	$C_{11}H_{14}$	2,4,6-Trimethylstyrene	8.33 [297]	–
		Benzocycloheptene	8.44 [298]	–
	$C_9H_6O_2$	1,2-Indenedione	8.80 [299]	–
164	$C_{10}H_{12}O_2$	Dimethyl-dihydroxo-dihydropentalene	7.29†	–
		Dimethyl-hydroxo-keto-tetrahydropentalene	7.55†	–
186	$C_{14}H_{18}$	Octahydroanthracene	7.86 [300]	–
	$C_{12}H_{10}O_2$	Naphthaleneacetic acid	8.05 [294]	–
210	$C_{16}H_{18}$*/$C_{14}H_{10}O_2$*	Aromatic hydrocarbon*	–	–
224	$Al(C_5H_7O_2)(C_5H_6O_2)$	Aluminium bis(acetylacetonate)-H*	6.64†	–
225	$Al(C_5H_7O_2)_2{}^+$	DI of $AlC_5H_7O_2)_3$	9.10 [268]††††	8.60†††
324	$Al(C_5H_7O_2)_3$	Aluminium tris(acetylacetonate)	7.60 [268]†††	7.81†††
			8.17 [268]††	–

†This work
††Vertical ionization energy (IE_{vert})
†††Adiabatic ionization energy (IE_{ad})
††††Electron impact ionization energy

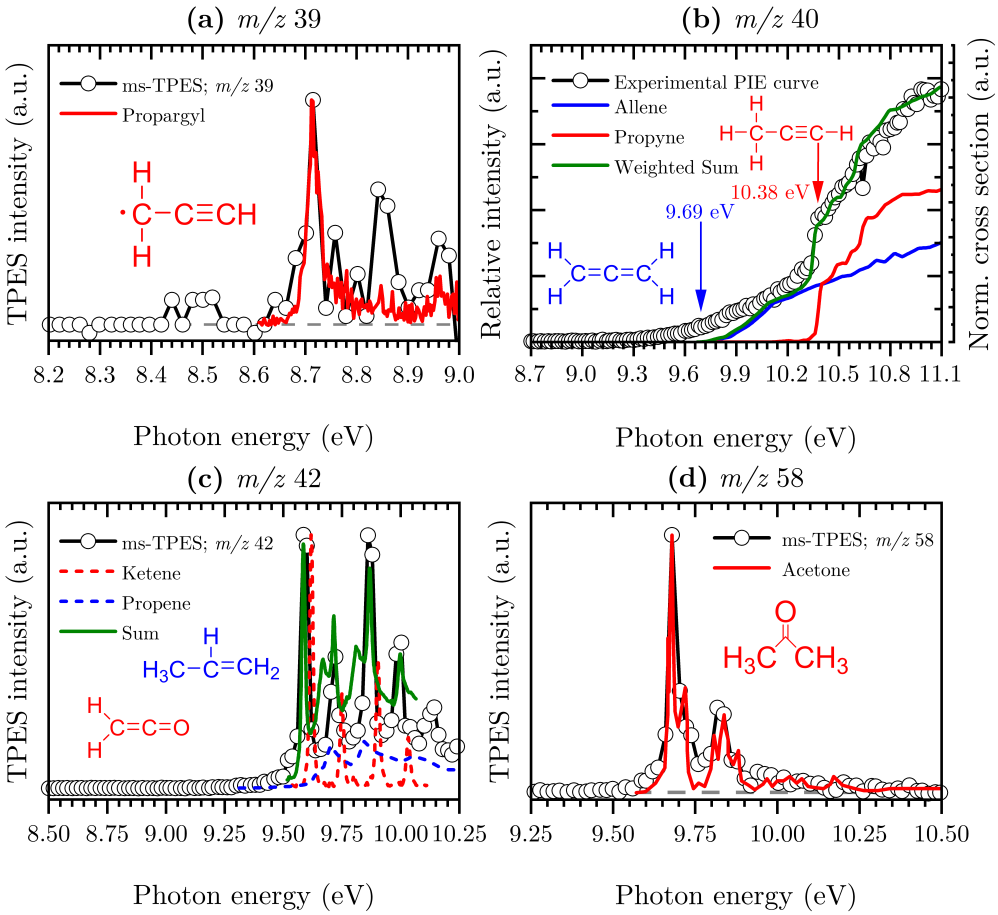

Figure 4.5: Representative examples of product species identification and assignment for C_2-C_3 hydrocarbons and oxygenated species generated by pyrolysis of $Al(C_5H_7O_2)_3$ using ms-TPES (a, c and d) and PIE curves (b) (black lines with circles); literature reference spectra (red) and cross sections (blue, red) are as follows: (a) m/z 39 (C_3H_3) [277] and (b) m/z 40 (C_3H_4) [278, 279], (c) m/z 42 (C_2H_2O) [280] (C_3H_6) [284] and (d) m/z 58 (C_3H_6O) [281].

At 8.70 eV, a clear peak emerges in the ms-TPES of m/z 39 which corresponds to the published ionization potential of the propargyl radical (IE = 8.70 eV) [277], see Fig. 4.5 (a). The analysis of the m/z 42 ms-TPES in Fig. 4.5 (c) shows a clear onset at 9.60 eV and confirmed that ketene (C_2H_2O) is the most abundant product that contributes to the m/z 42 channel (IE = 9.62 eV) [80, 90, 280]. Interestingly, propane (C_3H_6) [284] was also observed in the spectrum. Strong evidence of a mixture of allene and propyne was found for the m/z 40 channel by comparing their photoionization spectra to reference cross sections [278], revealing a relative ratio of 1.4:1.0 (Fig. 4.5 (b)). As will be seen a number of times later, hot and sequence bands are responsible for the red shift of the ionization onset of allene to below 9.69 eV [279], due to the inefficient cooling in the molecular beam. Acetone (C_3H_6O) has been identified as a major pyrolysis product by its ionization energy threshold in the ms-TPES shown in Fig. 4.5 (d) with an onset at 9.69 eV [281].

The most interesting result was observed for the m/z 64 channel in Fig. 4.6 (a), where pentatetraene (IE = 8.99 eV) [286] is unambiguously confirmed using a reference PES [286], in addition with the formation of its isomers ethynylallene (IE = 9.22 eV) [287] and methyldiacetylene (IE = 9.50 eV) [288]. These pyrolysis products were not observed in previous studies [79, 80, 90], although their formation plays a significant role in the gas-phase decomposition of $Al(C_5H_7O_2)_3$. The existence of C_5H_6O among the pyrolysis products has been reported by others [80, 90], whereas no unambiguous assignment has been proposed yet. Clear onsets in the ms-TPES in Fig. 4.6 (b) revealed that this channel can indeed be assigned to 2-methylfuran [293] and acetylallene [270]. Rhoten and DeVore [90] proposed the formation of $CH_3C(O)CCCH_3$ based on FTIR data, which differs from our conclusion that acetylallene is the dominant product at this mass channel.

In contrast to earlier studies [80, 88, 90], we were able to detect hydrocarbon intermediates in the gas-phase, as well as the aluminium-containing intermediate at m/z 224, thanks to the low residence time, the soft ionization method and molecular beam sampling preserving these intermediates. We found clear evidence for aromatic compounds among the pyrolysis products in the ms-TPES. The most abundant was 2,6-dimethylphenol ($C_{10}H_8O$), identified by its clear onset at IE = 8.26 eV that fits the literature value [295] well (see Fig. 4.6 (c)). The second most abundant species has been detected in the m/z 164 channel and attributed to $C_{10}H_{12}O_2$, which was proposed to be a 8-membered ring cyclic diketone in previous studies [80, 82]. By using FC simulations and G4 ionization energy calculations of possible isomers, we identified dimethyl-dihydroxo-dihydropentalene $IE_{ad(calc.)}$ = 7.29 eV and its tautomer dimethyl-hydroxo-keto-tetrahydropentalene $IE_{ad(calc.)}$ = 7.55 eV to be the major carrier of the ms-TPES in Fig. 4.6 (d).

Additionally, we newly found compounds at m/z 146, 186 and 210 as important pyrolysis products (see Fig. A.11). Since they have not been reported by others, the question arises whether these heavy species are gas-phase aluminium-containing intermediates or can be assigned to the group of aromatic compounds. To review the question, we first calculated ionization energies for possible aluminium intermediates, namely $Al(C_4H_5O_2)(OH)_2$ (m/z 146), $Al(C_5H_7O_2)(C_2H_3O_2)$ (m/z 186) and $Al(C_5H_7O_2)Al(C_5H_7O_2)(C_4H_4O_2)$ (m/z 210) with IE's of 9.15 eV, 5.25 eV and 5.25 eV, respectively. These do not match the recorded ms-TPES in Fig. A.11. Although the spectra for m/z 186 and 210 are rather weak, we can still identify a broad band in the 7.0–9.0 eV range, representative of a large molecular geometry change upon ionization. This in turn leads to unfavourable FC factors at the adiabatic ionization energy and a broad band in the threshold photoelectron spectrum. This is often the case for larger aromatic compounds studied in the literature [155]. Possible matches were found for m/z 146, where at least three possible species, 2,4,6-trimethylstyrene, IE = 8.33 eV [297], benzocycloheptene, IE = 8.44 eV [298] ($C_{11}H_{14}$), and 1,2-indanedione, IE = 8.80 eV [299] ($C_9H_6O_2$), may contribute to the spectrum (Fig. A.11, top). Additionally, octahydroanthracene, IE = 7.86 eV [300] ($C_{14}H_{18}$), and naphthaleneacetic acid, IE = 8.05 eV [294] ($C_{12}H_{10}O_2$), were identified in the m/z 186 channel, whereas other contributions remain unclear (see

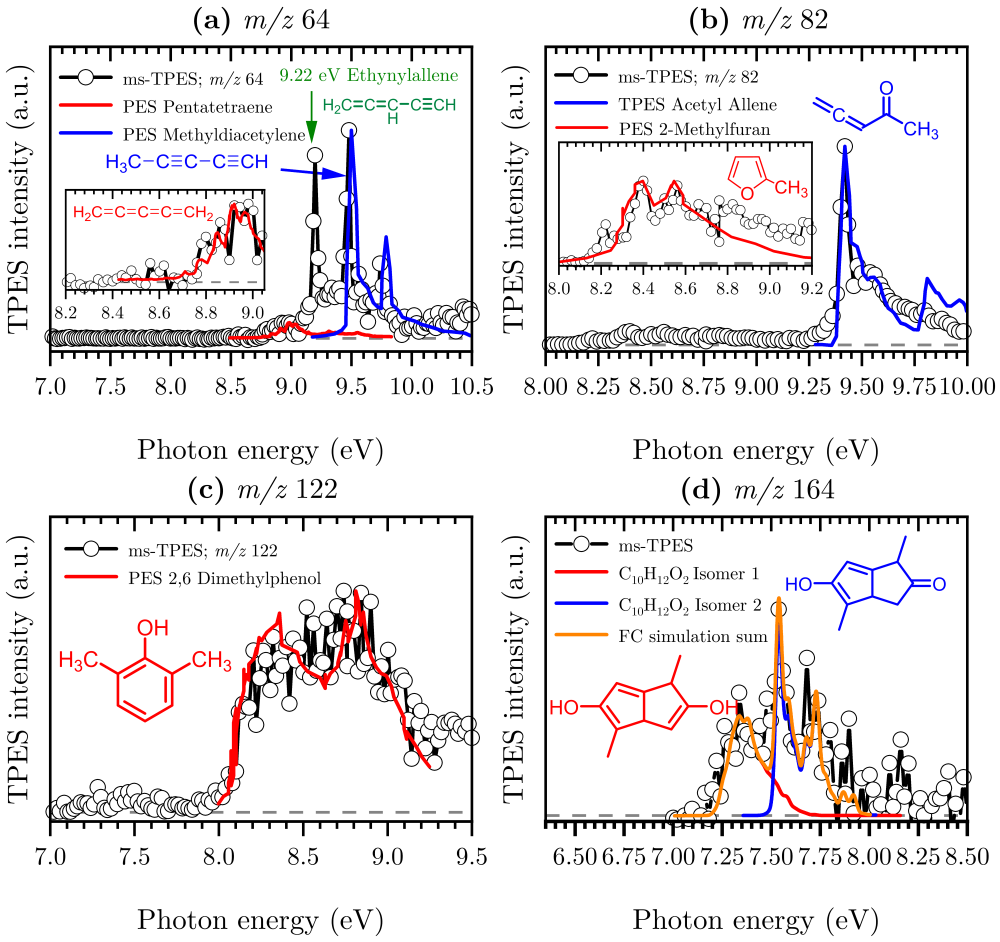

Figure 4.6: Product species identification and assignment for C_5-C_{10} hydrocarbons and oxygenated hydrocarbons formed by pyrolysis of $Al(C_5H_7O_2)_3$ using ms-TPES (black lines with circles); literature reference spectra (red and blue) as well as our FC simulations are as follows: (a) m/z 64 (C_5H_4) [286, 287, 288] and (b) m/z 82 (C_5H_6O) [270, 293], (c) m/z 122 ($C_8H_{10}O$) [295] and (d) m/z 164 ($C_{10}H_{12}O_2$) [this work].

Fig. A.11, middle). Thus, it is most likely that m/z 186 and 210 (Fig. A.11, bottom) can also be assigned to aromatic hydrocarbons rather than to aluminium-containing intermediates.

4.3.5 DPI of Pyrolysis Products

Earlier studies reported m/z 100 to be a primary decomposition product upon thermal decomposition of $Al(C_5H_7O_2)_3$ [80, 90]. In contrast, we observe just small quantities of acetylacetone in the gas-phase. As we already pointed out, most of the signal attributed to m/z 100 at room temperature (300 K) is due to impurities in the sample. At higher temperatures, acetylacetone tends to shift its equilibrium to the diketo side, having m/z 43 as major fragment upon photoionization (see

Fig. A.5) [270]. Nevertheless this does not explain the majority of the large ion signal at m/z 43 upon pyrolysis that we observe in this study, since the abundance of $C_5H_8O_2$ is relatively low at pyrolysis temperatures. As can be seen in Fig. A.12 (right), most of this channel indeed corresponds to a DPI product according to its broad velocity distribution perpendicular to the molecular beam propagation axis in the VMI at 738 K. The major dissociative photoionization product of acetone, another expected pyrolysis product [80], at energies higher than 10.3 eV is m/z 43 by the loss of a methyl radical to form $C_2H_3O^+$ [281, 301]. Because of the hot pyrolysis products, a significant red shift in the appearance of the m/z 43 fragment ion is to be expected [272]. These findings are considered in the temperature-dependent species profiles discussed later in this study.

4.3.6 Primary Decomposition Pathways

We now compare relative product signal intensities upon pyrolysis as a function of temperature, to understand the reaction mechanism. Now, the ionization photon energy for each temperature scan is selected to rule out or minimize possible DPI contributions and capture pyrolysis products close to their ionization thresholds. We calculated the centerline temperature by CFD calculations of the flow field (see Sec. 4.3.7). Temperature-dependent species profiles from the pyrolysis of $Al(C_5H_7O_2)_3$ between 325 and 923 K are shown in Fig. 4.7 and Fig. 4.8. The precursor signal, as well as its primary gas-phase decomposition product m/z 224, $Al(C_5H_7O_2)(C_5H_6O_2)$, are shown on the top, to better understand the decomposition steps. Note that the fractional abundances may not reflect the absolute mole fractions, as the underlying intensities are not scaled by the absolute ionization cross sections, which are unknown for most of the detected species. This especially holds true for reactive intermediates in the gas-phase, as for instance Al-containing species. Nevertheless, the apparent trends provide hints regarding the decomposition mechanism, summarized in Scheme 1.

Considering the temperature dependence of the dissociative ionization, no signals other than the ones belonging to the precursor were observed up to ca. 450 K, indicating thermal stability of the sample. In the view of the isomer-resolved species characterization and the temperature-dependent mass spectra, three major thermal dissociation channels can be established for $Al(C_5H_7O_2)_3$ at temperatures >450 K (see Scheme 1).

(i) Direct decomposition Unimolecular decomposition to yield aluminium bis(diketo)acetylacetonate-H, $Al(C_5H_7O_2)(C_5H_6O_2)$, and acetylacetone, $C_5H_8O_2$, according to:

$$Al(C_5H_7O_2)_3 \longrightarrow Al(C_5H_7O_2)(C_5H_6O_2) + C_5H_8O_2\,. \qquad \text{(R 4.2)}$$

The temperature-dependent species profiles in Fig. 4.7 and Fig. 4.8 confirm this to be the major decomposition pathway in the gas-phase, at least for temperatures

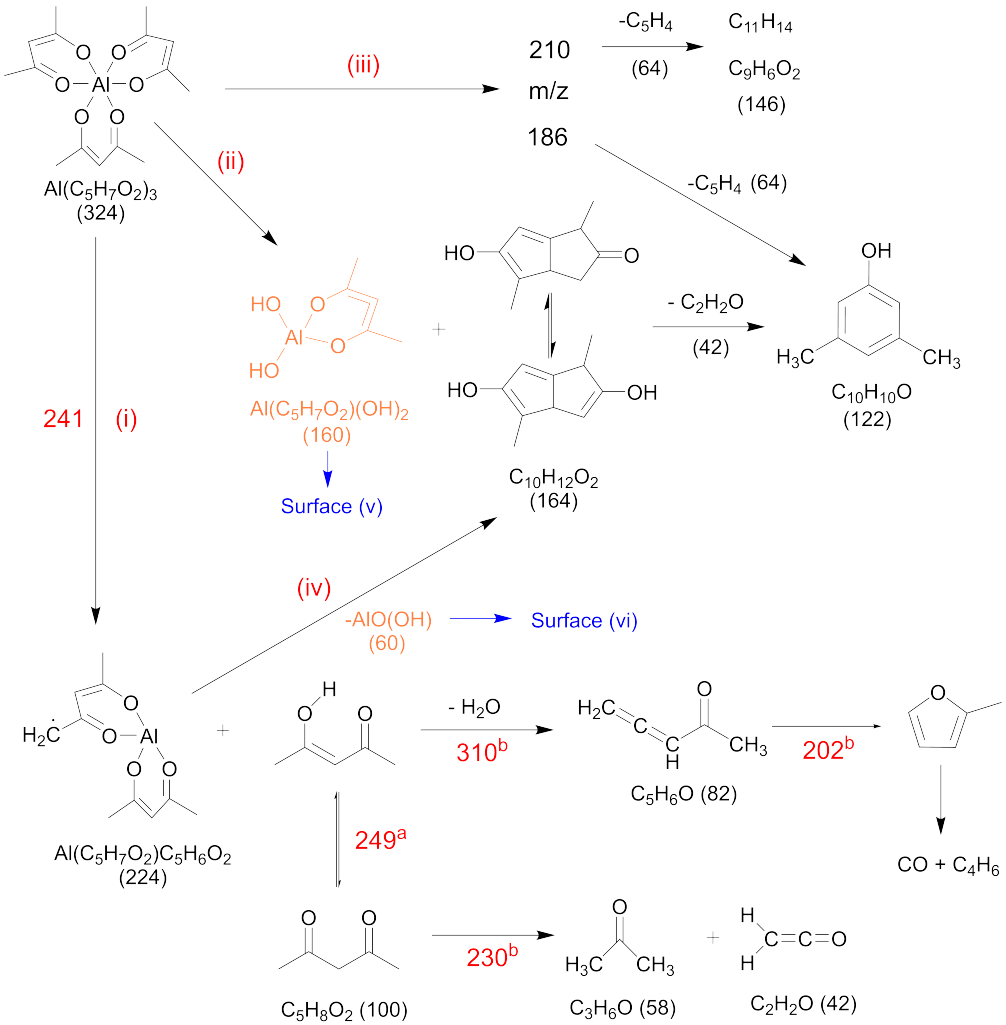

Scheme 1: Proposed primary thermal dissociation mechanism of $Al(C_5H_7O_2)_3$ in the gas-phase on the basis of the i^{2}PEPICO analysis. Calculated values for the activation energies in kJ mol^{-1} are denoted in red and are partially taken from [a]Antonov et al. [270] and [b]Russell et al. [200].

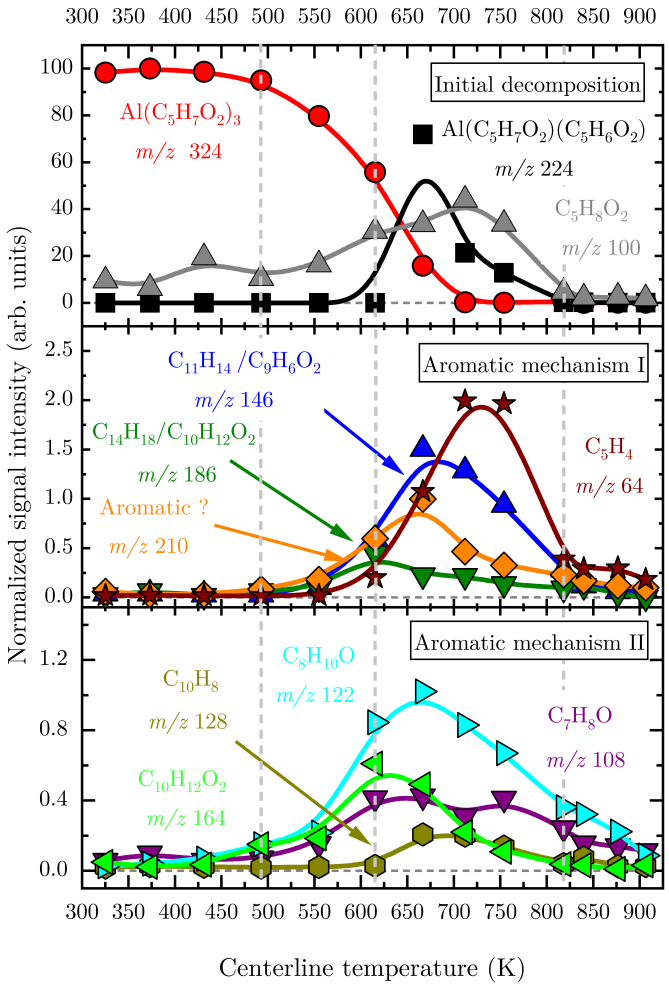

Figure 4.7: Temperature-dependent species profile of aromatic hydrocarbons and oxygenated species detected as products of $Al(C_5H_7O_2)_3$ pyrolysis, which are labeled by their assignment based on ms-TPES.

above 600 K, where m/z 224 is detectable. Due to its major contribution to the mass spectra (see Fig. 4.3), TD-DFT calculations were carried out to rationalize the reaction pathway (see Fig. 4.9). A hydrogen transfer (**TS1** at 2.50 eV) from the CH_3 group of the axial/ equatorial acetylacetonate ligand to the second axial/ equatorial one initiates the reaction, while a metal–oxygen bond is cleaved. This leads to a bound intermediate at 2.08 eV relative to the precursor with five Al–O bonds (**INT1**). **INT1** is only shallowly bound and breaking the second Al–O bond leads to m/z 224 aluminium bis(diketo)acetylacetonate-H, $Al(C_5H_7O_2)(C_5H_6O_2)$ and m/z 100 acetylacetone. Our calculations show that the unimolecular decomposition is endothermic with a computed energy of 2.28 eV (**FS**). In contrast, the direct loss of an acetylacetonate ($C_5H_7O_2$) radical would require an activation energy of 4.82 eV and is thus deemed unlikely to occur. The H-transfer mechanism is further supported by the steady rise in the acetylacetone signal, which was obtained by summing the ion signals at m/z 100, 72, and 85, the latter two being the dissociative

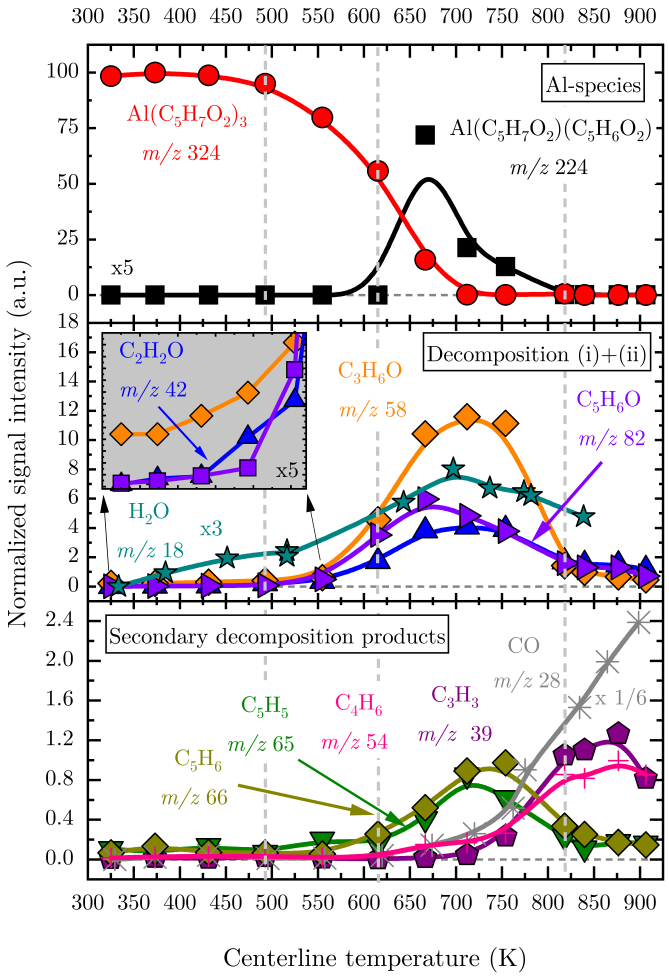

Figure 4.8: Temperature-dependent species profiles of primary and secondary decomposition products, labeled by their assigned species based on ms-TPES and mechanistic analysis.

photoionization signals belonging to its diketo and enol-tautomers. Thus, channel (i) is the dominant primary decomposition step.

Two pathways may produce m/z 82 acetylallene ($CH_2CCHC(O)CH_3$). First, a dehydration of $Al(C_5H_7O_2)_3$ with C−O bond cleavage in one ligand yielding aluminium bis(diketo)acetylacetonate-H and acetylallene. Second, water elimination from the enol-tautomer of acetylacetone produces acetylallene, which may also contribute to the m/z 82 signal. This was computed by Antonov et al. to require a barrier of 3.82 or 4.05 eV [270]. According to an infrared laser pyrolysis study of acetylacetone by Russell et al. [200], acetylallene may react further at 202 kJ mol^{-1} by a 1,2-hydrogen shift and simultaneous cyclization reaction to produce 2-methylfuran. This leads to the assumption that both products are due to sequential reactions of acetylacetone at higher temperatures, as also observed in our study, rather than being primary decomposition products of aluminium acetylacetonate.

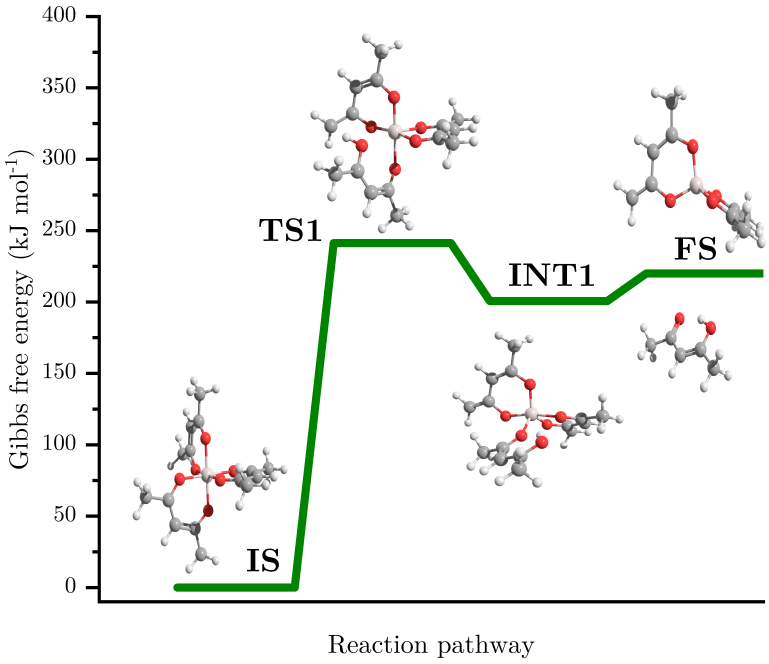

Figure 4.9: Potential energy surface of the unimolecular decomposition of $Al(C_5H_7O_2)_3$ at CBS-QB3 level of theory.

This observation most likely also applies to the formation of ketene (C_2H_2O) and acetone (C_3H_6O) at higher temperatures, which may be formed in an intramolecular process by further unimolecular decomposition of the liberated ligand through C−C bond cleavage and H-atom transfer with a calculated activation barrier of 230 kJ mol^{-1} [200]. Both products are also observed at relatively low temperatures starting from a centerline temperature of 450 K, where we observe a decrease in precursor signal intensity. In this temperature regime, they may be formed by surface rather than gas-phase reactions. Therefore, we conclude that this channel corresponds to a sequential decomposition step at high temperatures above 600 K, since we observe acetylacetone represented by its fragments m/z 72 and m/z 85 at those temperatures in the gas-phase.

(ii) Aromatic pathway I The species profile of m/z 164 shows that the signal intensity of the cyclic diketone, $C_{10}H_{12}O_2$, is non-zero even when the precursor exhibits full conversion. Indeed, we found evidence that, in contrast to previous findings by Bykov et al. [80], the formation of a cyclic diketone cannot be solely attributed to the decomposition of the trivalent Al-precursor to form m/z 164 ($C_{10}H_{12}O_2$) [80] and possible surface reactions of the precursor [88]. Additionally, Bykov and colleagues proposed a second channel for the formation of m/z 164 by a dimerization reaction of m/z 82 (C_5H_6O) [80]. Since the precursor is heavily diluted (<0.1%) in our experiment, we consider it as rather unlikely that bimolecular chemistry plays a major role in the decomposition mechanism under the prevailing conditions. Furthermore, we did not find a connection between the gas-phase

concentration of the precursor and the peak intensity at m/z 164. We also tested the influence of possible surface reactions of two adjacent $Al(C_5H_7O_2)_3$ molecules as proposed by Igumenov et al. [88] that may also lead to a formation of m/z 164 (see Fig. A.6). Since surface reactions may play a role in the investigated system, we evaluated the diffusion length, i.e., the root mean square displacement along the radial direction of an arbitrary $Al(C_5H_7O_2)_3$ molecule inside the reactor to be below 0.04 mm in the whole temperature range. Considering that the reactor diameter is 1.0 mm, thus much larger, we assume that wall reactions will play at most a minor role but they cannot be completely ruled out (see also Fig. A.5). We estimate that ca. 8–20% of the gas-phase molecules will get in contact with the surface, and larger conversions must be due to gas-phase reactions, as observed starting at approx. 550–600 K. For temperatures below this threshold, our findings substantiate the proposed mechanism by Bykov et al. [80], shown as channel (ii) in Scheme 1:

$$Al(C_5H_7O_2)_3 \longrightarrow Al(C_5H_7O_2)(OH)_2 + C_{10}H_{12}O_2\,. \qquad \text{(R 4.3)}$$

Only traces of the gas-phase intermediate m/z 160 were detected in our study, likely corresponding to $Al(C_5H_7O_2)(OH)_2$ [80]. This supports the proposition of Igumenov et al. [88] that this species is almost completely adsorbed on the surface (i.e., in our microreactor) and subsequently reacts at higher temperatures according to:

$$2\,Al(C_5H_7O_2)(OH)_2 \longrightarrow Al_2O_3 + C_5H_6O + 3\,H_2O + CO\,, \qquad \text{(R 4.4)}$$

leading to various organic products and radicals, as also observed here. Since CO is only detected at temperatures above 700 K in significant amounts, the activation barrier for the surface reaction (v) (Reac. R 4.4) appears to be higher than that of the decomposition reaction to form m/z 164. Our data reveal that this species may additionally be formed during the thermally activated decomposition of $Al(C_5H_7O_2)(C_5H_6O_2)$, m/z 224, at temperatures higher than 675 K according to channel (iv) in Scheme 1. This is supported by the increasing H_2O signal correlating with depleting m/z 224 signal because water is a product of the surface reaction (vi) in Scheme 1:

$$2\,AlO(OH) \longrightarrow Al_2O_3 + H_2O\,, \qquad \text{(R 4.5)}$$

(iii) Aromatic pathway II At temperatures above 500 K, where the decomposition of the parent molecule becomes evident, the signal at m/z 210 exhibits a small increase (see Fig. 4.8). By further heating the reactor to temperatures above 550 K, the signal intensity increases further, while the precursor signal at m/z 324 has its steepest descent. This may identify m/z 324 as possible source of m/z 210. For further clarification, we tracked the ion intensity as a function of

temperature and saw that, in a secondary decomposition step, *m/z* 210 may lose *m/z* 64 (C_5H_4) to form $C_{11}H_{14}$ or $C_9H_6O_2$ (*m/z* 146), assigned in Fig. A.11. This correlates with the simultaneous increase of *m/z* 15, 64, and 146 signal intensities while *m/z* 210 attenuates. We therefore assume that *m/z* 210 is likely a $C_{16}H_{18}$ or $C_{14}H_{10}O_2$ isomer. In contrast to the aforementioned species, the convoluted signal of at least two species in the *m/z* 186 channel, $C_{12}H_{10}O_2$ and $C_{14}H_{18}$ (see Fig. A.8) exhibits an earlier maximum at approximately 650 K. This supports the idea that this gas-phase product may predominantly be formed from the parent molecule. Nevertheless, its intensity is non-zero at complete conversion of $Al(C_5H_7O_2)_3$. At temperatures higher than 650 K, $C_{14}H_{18}$ may further decompose and contribute to the *m/z* 146 channel by the loss of C_3H_4 to form $C_{11}H_{14}$ (*m/z* 146). The species profiles in Fig. 4.7 also show evidence for an alternative reaction pathway upon the loss of ketene (C_2H_2O) to form *m/z* 144, $C_{10}H_8O$. This pathway seems to have a higher activation barrier, since it is mainly observed at temperatures higher than 600 K. In addition, an oxygenated hydrocarbon at *m/z* 146 ($C_{10}H_{10}O$) may additionally be formed by the dehydration of *m/z* 164, $C_{10}H_{12}O_2$. This is supported by the increase of the H_2O signal intensity at temperatures around 650 K, whereas the amount of *m/z* 164 decreases simultaneously.

4.3.7 Flow Conditions in the Microreactor

Since the flow inside the microreactor is accelerated by the large pressure difference, the temperature profile differs from the ideal "plug-flow" characteristics. The upper part of Fig. 4.10 shows three contour plots of the temperature profile along the reactor centerline, as modeled by CFD. Starting at low temperatures of 423 K, where heat transfer is fast enough, we observe a relatively small temperature difference across the reactor length. Nevertheless, even at such low surface temperatures, the centerline temperature at $x = 8.5$ mm differs by ca. 43 K (10.3%) from the recorded surface temperature. This effect becomes more apparent, when the surface temperature is increased to 553 K (54 K, 9.8%) and 673 K (65 K, 9.7%) (see bottom of Fig. 4.10). The temperature gradient becomes smaller closer to the exit of the reactor starting at a reactor length of ca. 5.0 mm. This spot, where most of the chemical reactions occur, has also been reported by Guan et al. [202]. The temperature deviation within this area is only about 6–10% depending on the applied surface temperature. Since this area is relatively small and, as seen in Fig. 4.11, the temperature-dependent axial velocity is relatively high at 225–400 $m\,s^{-1}$, a small residence time of 25–46 µs is achieved in the heated section of the reactor. This is beneficial for the suppression of bimolecular reactions and helps to isolate reactive intermediates.

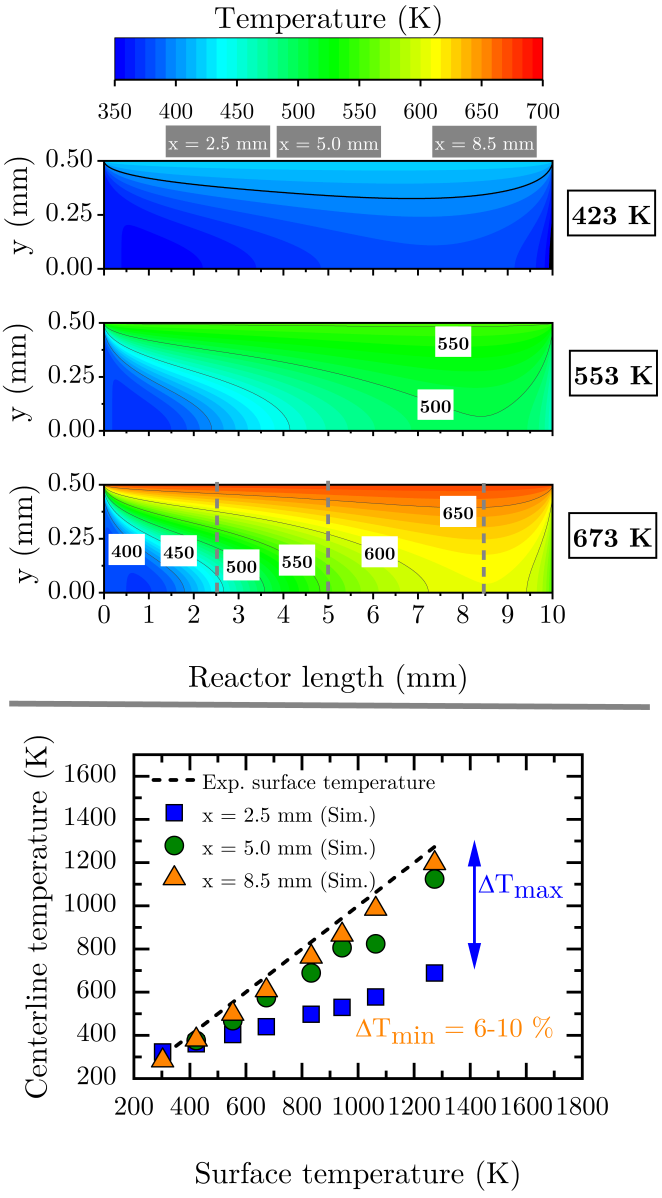

Figure 4.10: Top: Contour plots of the reactor temperature obtained from the numerical calculations; bottom: centerline temperature as a function of the measured surface temperature 2.5 mm (blue squares), 5.0 mm (green dots) and 8.5 mm (orange triangles) from the beginning of the heated part. The maximum deviation between the centerline and the surface temperature is >500 K at the inlet of the reactor.

4.3.8 Kinetics of the Primary Dissociation Step

Supported by the modeling of the flow field, we were able to determine the residence times, temperatures, and pressure more accurately inside the microreactor (see Fig. 4.11). This enabled us to relate the mole fraction profile (see Fig. 4.12; left) for m/z 324, $Al(C_5H_7O_2)_3$ to the centerline temperature. Invoking the information from CFD, a reasonable Arrhenius plot was derived for the pyrolysis of $Al(C_5H_7O_2)_3$ as presented in Fig. 4.12 (right). The data evaluation was described above, the measured mole fractions at different temperatures and reaction times were used to fit the parameters of Eq. 4.6, in order to derive both activation energies and pre-exponential factors. We also included the scaled signals at mass 224 as primary product from the gas-phase (gray dots, Fig. 4.12). At temperatures below 650 K, the signal stems, as discussed above, from contributions at m/z 224 and 225, which could not be deconvoluted. Thus, for the lower temperatures only an upper limit can be given; they are marked as gray error bars. The Arrhenius plot can be understood as a sum of two reaction rates with different activation energies; both have an equivalent rate at 492 K. The fit to the data for the whole temperature range (green curve), with an activation energy of $E_{a,s} = 14 \pm 9\,\mathrm{kJ\,mol^{-1}}$ and a pre-exponential factor of $A_{0,s} = 3.7 \times 10^{-3}\,\mathrm{s^{-1}}$ is obtained for the low temperature region (red curve). One should note that the variance of the kinetic constants is quite high, because of the limited number of points that could be measured at the low temperature range, where the reaction rate is low. At higher conversion and higher temperature, a larger activation energy is observed with $E_{a,g} = 57 \pm 4\,\mathrm{kJ\,mol^{-1}}$ and a pre-exponential factor of $A_{0,g} = 2.48 \times 10^{-8}\,\mathrm{s^{-1}}$ (blue curve), respectively. This is also the temperature regime where aluminium-containing intermediates are detected. At these high temperatures, the depletion of $Al(C_5H_7O_2)_3$ is dominated by gas-phase reactions, because they get faster, and dominate k_{tot} as seen on the right side of Fig. 4.12. It is further very unlikely that alumina, formed at the surface, evaporates again, thus, aluminium products detected at higher temperatures are expected to be formed directly in the gas-phase rather than in surface reactions.

Earlier experimental determinations of the kinetic rate constants range between 68.6–100 $\mathrm{kJ\,mol^{-1}}$ from EI-MBMS [82] as well as FTIR [90] and static very low pressure pyrolysis studies [79]. The activation energy of the high temperature regime is close to the value of ca. 68.1 $\mathrm{kJ\,mol^{-1}}$, as obtained by Tsyganova et al. [82]. They quoted the existence of a surface reaction regime and reported Langmuir-surface catalyzed kinetics for $Al(C_5H_7O_2)_3$ which is, *per se*, first order at low partial pressures of the precursor [82]. This is additionally indicating that surface reactions may have been of some importance here. Our interpretation is that surface reactions dominate the low temperature regime up to 492 K, where the conversion is low, as is the activation energy with $14 \pm 9\,\mathrm{kJ\,mol^{-1}}$. The value by Tsyganova et al. agrees well with our higher temperature result of $57 \pm 4\,\mathrm{kJ\,mol^{-1}}$, which we attribute to gas-phase kinetics. In contrast, earlier works by Rhoten and DeVore [90] and Minkina [79] quote values of ca. 100 $\mathrm{kJ\,mol^{-1}}$ using a static system and mass spectrometry. Bykov et al. also reported a lower value, 83.4 $\mathrm{kJ\,mol^{-1}}$,

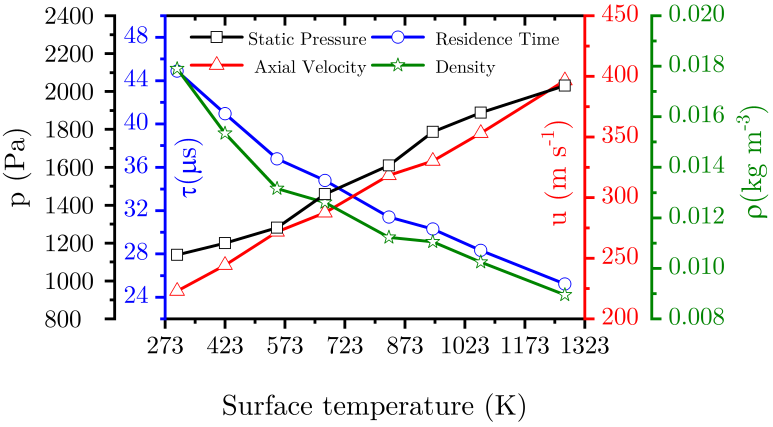

Figure 4.11: Calculated pressure, velocity, and density at the midpoint (x = 5.0 mm) of the reactor as a function of pyrolysis temperature, along with the residence time in the pyrolysis zone from x = 5 to 10 mm at an inlet nozzle pressure of 1.6 bar.

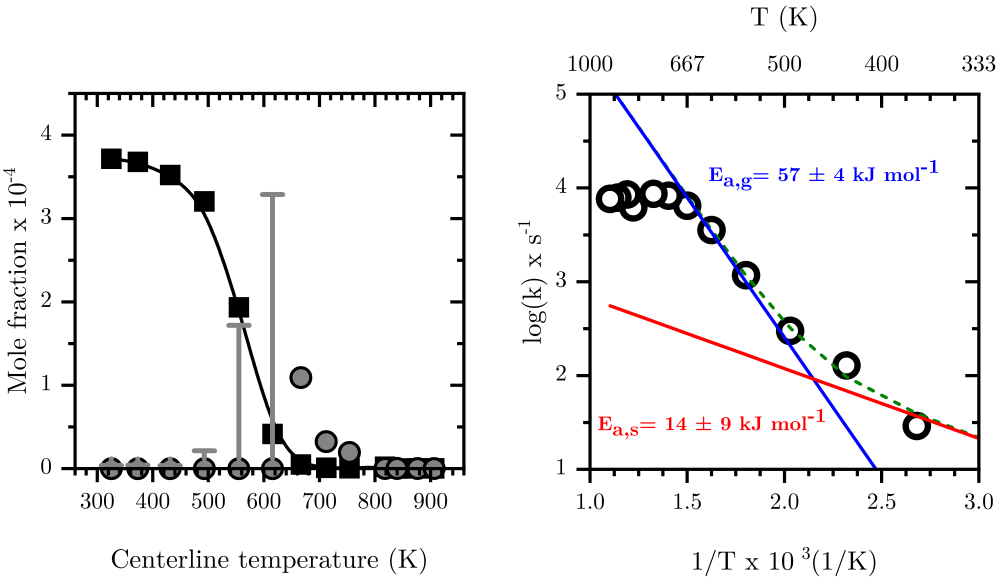

Figure 4.12: Left: Mole fraction profile (b-spline: black curve, data: squares) of $Al(C_5H_7O_2)_3$ and a scaled relative profile of m/z 224 (gray dots) together with a convoluted profile of m/z 224/225 at temperatures below 650 K (gray error bars), obtained with aid of CFD modeling at a computed average pressure of 1600 Pa and residence times from 25 to 45 µs. Right: Arrhenius plot (fit: colored curves, data: circles) derived for the decomposition of $Al(C_5H_7O_2)_3$. The apparent activation energy for each temperature region is given next to the plot.

[80] utilizing EI-MBMS. However, those previous studies only consider the global reaction pathway because none of them detected all of the intermediates observed herein, including the major gas-phase intermediate at m/z 224. Additionally, they suffered from a high degree of fragmentation due to hard ionization, precursor loss in the analysis column, or product loss in the reactor. This may have led to a convolution of fragment and product ion signals or signal loss and therefore a possible bias in the determination of the kinetic constants. Notwithstanding the limitations of the kinetic analyses reported previously as well as in our approach herein, the good agreement with literature results, albeit contingent on a few reasonable assumptions, illustrates that the process of CFD flow field modeling of microreactors to derive reaction kinetics data, is reasonable.

4.4 Conclusion

We have investigated the pyrolysis of $Al(C_5H_7O_2)_3$ in the temperature range of 325–1278 K by flash-vacuum pyrolysis using tuneable VUV photoionization and double imaging photoelectron photoion coincidence (i^2PEPICO) spectroscopy to detect and unambiguously identify pyrolysis intermediates and products. Studying the decomposition mechanism with a combined experimental and numerical approach provided unique insights into the decomposition mechanism of $Al(C_5H_7O_2)_3$. Temperature-dependent photoionization and ms-TPES of the precursor enabled us to distinguish between soft, fragmentation free ionization of neutrals and dissociative ionization of heavier species yielding fragments at the same m/z in the temperature-dependent species profiles. Our investigations of the photoion mass-selected threshold photoelectron spectra provided new mechanistic insights, while confirming some conclusions of previous studies.

First, considerable progress has been made in the detection and characterization of aluminium-containing gas-phase intermediates. The primary decomposition pathway is revised, because the loss of H_2O and C_5H_6O is energetically unfavorable. Indeed, we found that the formation of a major aluminium-containing intermediate, $Al(C_5H_7O_2)(C_5H_6O_2)$ and acetylacetone is the primary decomposition step in the gas-phase. Possible pathways for its initial formation (i) and further secondary decomposition were proposed, based on the temperature-dependent species profiles. Especially the proposed surface reaction pathways (v) and (vi) (Reac. R 4.4 and Reac. R 4.5) characterize the inherited intermediate species as the true precursors, directly responsible for the desired film growth in thin film applications.

Second, we confirmed the first aromatic decomposition step (ii), already proposed in the literature [80]. Additionally, besides the formation of already detected aromatic hydrocarbons, e.g., dimethylphenol and m/z 164, we point out that a third pathway (iii) may lead to the formation of additional aromatic hydrocarbons, notably at m/z 146, 186 and 210. At low temperatures, these may be formed in surface reactions but we could also identify a homogeneous gas-phase reaction as a likely source of m/z 164 ($C_{10}H_{12}O_2$) at higher temperatures.

In contrast to previous studies, we were able to identify various species and isomers for the first time, such as C_5H_4, C_3H_3 and C_3H_4, which are considered secondary reaction products. We were also able to assign m/z 82 acetylallene, facilitating the development of a complete reaction mechanism. Additionally, this mechanism may help understand possible nucleation and particle formation temperature thresholds and pathways, leading to unwanted particle contamination and, consequently, a decrease in film growth rate [240].

By utilizing the gas expansion factor, it was possible to calculate mole fraction profiles, based on the vapor pressure derived inlet concentration of the precursor molecule. With the aid of a numerical simulation of the microreactor, we obtained residence times and temperature profiles, opening the way to estimate kinetic parameters, such as the activation energy. For the unimolecular decomposition, our experimental data predicts the overall rate constant in quite good agreement with the literature values. This shows the feasibility of numerical flow field modeling to aid the interpretation of experimental results in complex environments. Nevertheless, there is still some discrepancy between the experimental and calculated values for the newly proposed aluminium intermediate pathway (i) (see Reac. R 4.2). A major source of uncertainty is the inlet mole fraction, which was only calculated based on literature vapor pressure data and not measured directly. Second, we were not able to record smaller temperature increments to better resolve the linear regions, especially the one at low temperature in Fig. 4.12. Third, although the loss of precursor through wall reactions is expected to be small, it still contributes at lower temperatures, below 492 K, to the conversion of $Al(C_5H_7O_2)_3$. The importance of surface reactions at these temperatures is mainly concluded from the absence of Al-containing intermediates and from the low activation energy. At higher temperatures, gas-phase reactions clearly dominate and an Al-containing intermediate is detected, together with an increase of the observed activation energy to $57 \pm 4\,\mathrm{kJ\,mol^{-1}}$. The contribution of surface reactions may explain some of the difference between the experimental and calculated values.

The combination of state-of-the-art mass spectrometric detection methods with mild photoionization as well as quantum chemical and CFD calculations represents a promising way to tackle the kinetics of organometallic compounds in the gas-phase, as demonstrated here for one archetypal aluminium precursor.

Chapter 5

Insights Into the Decomposition of Zirconium Acetylacetonate using Synchrotron Radiation: Routes to the Formation of Volatile Zr-Intermediates

The content of the following chapter was presented on the *MRS Symposium Spring 2022* and initally published as an invited paper in the *Journal of Materials Research*, **37**, 1558-1575, (2022) by S. Grimm, S.-J. Baik, P. Hemberger, T. Kasper, A. M. Kempf and B. Atakan, entitled "Insights into the decomposition of zirconium acetylacetonate using synchrotron radiation: Routes to the formation of volatile Zr-intermediates".

The article is reprinted with permission from Springer Nature, applying minor formal changes to adhere to the style and structure of this thesis. The original publication is available online under the following citation:

DOI: https://doi.org/10.1557/s43578-022-00566-6

Contribution Statement

My own contribution included choosing the experimental conditions, and performing all the experiments presented here. Subsequently, I analyzed and evaluated the data from the remote i^{2}PEPICO experiment and visualized both the experimental as well as the numerical results. In addition, I coordinated the assembling of the manuscript and wrote the whole original draft.

Dr. Seung-Jin Baik conducted the numerical simulation of the microreactor and provided the results for further analysis. He contributed to the interpreta-

tion of the numerical results, as well as editing and review of Sec. 5.2.1 of the manuscript. **Dr. Patrick Hemberger** provided the resources at the Swiss Light Source in Switzerland, and helped in setting up the experimental setup during the remote-experiment by refilling the precursor. He performed the quantum chemical calculations and provided the simulated spectra. Additionally, he contributed to the remaining manuscript by review and editing. **Prof. Dr. Andreas M. Kempf** was involved in the conceptual design of the numerical simulation, acquired the research funding and was responsible for the project administration. **Prof. Dr. Tina Kasper** and **Prof. Dr. Burak Atakan** were also involved in the conceptual design, and acquired the research funding. They additionally were responsible for the project administration, as well as contributed to the interpretation of the results. All authors were engaged in the correction and later proof-reading of the manuscript.

CRediT (Contributor Roles Taxonomy author statement):

S. Grimm: investigation, formal analysis, visualization, writing-original draft; **S.-J. Baik**: methodology, investigation, sofware, writing-review & editing; **P. Hemberger**: investigation, resources, writing—review & editing; T. Kasper: conceptualization, methodology, supervision, project administration, funding acquisition; **A. Kempf**: methodology, supervision, writing—review & editing, project administration, funding acquisition; **B. Atakan**: conceptualization, methodology, supervision, writing—review & editing, project administration, funding acquisition.

Abstract

The thermal decomposition of $Zr(C_5H_7O_2)_4$ is studied in a silicon carbide (SiC) microreactor on the microsecond time scale. By utilizing synchrotron radiation and photoelectron photoion coincidence spectroscopy, six important zirconium intermediates, as for instance $Zr(C_5H_7O_2)_2(C_5H_6O_2)$, and $Zr(C_5H_6O_2)_2$, are identified in the gas-phase for the first time. The adiabatic ionization thresholds of intermediately formed zirconium species are estimated and the main products of their thermal decomposition, acetylacetone, acetylallene and acetone are characterized unambiguously and isomer-selectively. Based on all detected intermediates, we deduce the predominant pyrolysis pathways of the precursor in the temperature range from 400 to 900 K. Our findings are complemented by numerical simulations of the flow field in the microreactor, which show that the choice of dilution gas significantly influences the temperature profile and residence times in the microreactor, such that helium provides a more uniform flow field than argon and should preferentially be used.

5.1 Introduction

Solid zirconia layers have interesting thermophysical properties, are inert, have a wide band gap and a high-κ dielectric constant. Consequently, these ceramic layers are used i.e., as thermal barrier coatings [302, 303], anti-corrosion layers [304], high-κ dielectric layers [305, 306], anti-reflective coatings [307], dielectric capacitors [308], or for energy storage applications [309]. Film preparation by chemical vapor deposition (CVD) allows high growth rates and uniform film thicknesses. In CVD processes, a metal-containing precursor is evaporated and forms a thin film in a surface reaction, but often the formation mechanisms are not fully uncovered. Until now, many studies have been published on the CVD of ZrO_2 layers, where various types of zirconium based derivatives, such as organo-zirconium complexes, zirconium aminoalkoxide-substituted precursors [310], alkoxides [311, 312] and β-diketonates [91, 92, 94] were used as precursor for thin film formation.

Metal β-diketonates, as for instance zirconium acetylacetonate, $Zr(C_5H_7O_2)_4$[1], are frequently used as precursors due to their high volatility, stability in air and commercial availability. The homogeneous decomposition of the gaseous precursor is considered as the rate-limiting step for film growth, because of the intrinsically high bond dissociation energies of these complexes. At higher temperatures, competing processes like particle formation and nucleation may also occur in the gas-phase, and reduce the growth rate significantly. The reactivity of metal-containing intermediates determines if the desired film structure and morphology is obtained or undesired side reactions occur. Clearly, gas-phase reactions play an important role in the *a-priori* determination of film composition, purity and the total yield of CVD processes [240].

Consequently, attempts to characterize the reaction products and pathways were undertaken by thermogravimetric analysis [313, 314] coupled to infrared spectroscopy [95, 315, 316] and mass spectrometry [96, 97, 317], respectively. The main conclusion drawn in previous work on $Zr(acac)_4$ was that the precursor undergoes a series of decomposition steps rationalized by the detection of various organic by-products in the gas-phase. While acetylacetone (m/z 100; $C_5H_8O_2$), acetic acid (m/z 60; $C_2H_3O_2$) and propyne (m/z 40; C_3H_4) were found at temperatures up to 523 K, carbon dioxide (m/z 44; CO_2), water (m/z 18; H_2O) and methane (m/z 16; CH_4) are the main products at temperatures higher than 623 K [95, 96, 97]. These by-products are formed from the initial precursor and lead to the formation of metal acetates ($Zr(acac)_2(CH_3COO)_2$; $ZrOH(CH_3COO)_3$; $ZrO(CH_3COO)_2$), metal carbonates ($ZrOCO_3$), as well as other intermediate species, which were detected on the surface [95]. Finally, at high temperatures a ZrO_2 film, with a substantial amount of carbon contamination from unreleased ligand fragments, is formed [96].

Concerning the gas-phase chemistry, so far experimental limitations precluded the detection of most of the postulated intermediate zirconium species [96], and thus reaction mechanisms are incomplete [95, 97]. However, an analysis of these early stages of growth initiated in the gas-phase, requires fast and sensitive and

[1] Commonly abbreviated as $Zr(acac)_4$.

multiplexed analytical techniques with sufficiently low detection limits for short-living gaseous species, which are usually difficult to detect and characterize with conventional thermogravimetric and spectroscopic methods [122].

Here, we present a combined numerical and experimental study to elucidate the gas-phase chemistry of zirconium acetylacetonate using a microreactor, which is characterized by short residence times of <50 µs, coupled to a double imaging photoelectron photoion coincidence spectrometer (i^{2}PEPICO) combined with vacuum ultraviolet (VUV) radiation provided from the Swiss Light Source (SLS) synchrotron. The wide tunability of the photon energy emitted from a synchrotron facility combined with velocity map imaging (VMI) enables us to distinguish fragmentation from direct ionization, commonly observed in standard electron ionization mass spectrometry. This feature allows us to characterize and identify important organometallic and organic reactive intermediates isomer-selectively. This experimental strategy was demonstrated previously, to be an effective way to detect and characterize metal-containing intermediates and radicals with short lifetime in comparable systems [125, 129, 318]. By computational fluid dynamic (CFD) methods, the temperature and flow field in the microreactor is characterized. This is because the reaction area is hard to access experimentally, due to the small size (I.D. = 1 mm) of the reactor.

In this context, the influence of two different inert gases, argon and helium, with strongly differing thermal conductivity is investigated. We report the results of our successful approach to use VUV and i^{2}PEPICO for the *in-situ* detection of gas-phase radicals and zirconium-containing intermediates in the vacuum pyrolysis of $Zr(acac)_4$ at temperatures between 400 and 900 K under conditions relevant to thin film growth by CVD. Our results provide direct experimental evidence for the initial steps of the gas-phase chemistry and can be used to improve the modeling of thin film synthesis pathways, ultimately, as the work contributes to a more efficient materials synthesis.

5.2 Results and Discussion

In the upcoming section we will first present and discuss the findings of the CFD simulations to interpret the decomposition mechanism, especially the temperature onsets, more accurately. Since it has been reported that $Zr(acac)_4$ may be unstable in the evaporator [92, 319], prior to its desired thermal decomposition in the microreactor, in the following paragraph the influence of this effect on the products sampled at the outlet of the reactor is discussed. These insights are considered for the correct interpretation of mass spectra upon pyrolysis of $Zr(acac)_4$. The identification of the corresponding pyrolysis products proceeds mainly via mass-selective threshold photoelectron spectra (ms-TPES) and an analysis of the photoionization efficiency curves (PIE). However, in the case of the identification of important zirconium intermediates that were formed by thermal decomposition, their isotopic patterns are taken into account and a chemical structure is suggested. With aid of the flow

field information provided by CFD, temperature-dependent species profiles and possible formation pathways for the zirconium-intermediates are discussed.

5.2.1 Flow Field of the Microreactor

In this section, we report on the pressure, temperature, and velocity fields, as well as residence time in the microreactor, modeled by CFD, using both argon and helium as dilution gas. In the left part of Fig. 5.1, an axial temperature profile of the microreactor is shown. It can be stated that a relatively small temperature difference in axial, as well as radial direction is observed, indicated by exemplary sampled streamlines at $y = 0\,\text{mm}$, $0.25\,\text{mm}$ and $0.4\,\text{mm}$ (dashed gray lines, Fig. 5.1 (b)). The helium gas temperature reaches its target value of $671\,\text{K}$ with a deviation of less than 1% at an axial distance from the reactor inlet of $x = 1\,\text{mm}$, which results in an almost isothermal zone of $9\,\text{mm}$. This length is considerably longer in comparison to the results with argon, where at almost $2.1\,\text{mm}$ a maximum deviation of 1% is reached, with respect to the target temperature. This difference becomes more evident in radial direction, where the centerline temperature of helium shows a deviation of $21\,\text{K}$ (3.1%) from the measured surface temperature, see Fig. 5.1 (b), whereas for argon the deviations in the inlet region are considerably higher with $66\,\text{K}$ (9.8%) at $x = 1\,\text{mm}$. The deviations are much smaller inside the isothermal zone, for instance at $x = 2.5\,\text{mm}$ the temperature deviation is $15\,\text{K}$ (2.2%) using argon and $6\,\text{K}$ (0.9%) for helium, respectively.

Considering the extraction of kinetic data from microreactor experiments, from CFD calculations it was deduced that most of the precursor conversion occurs within a specific spatial interval of the microreactor [129, 202]. Here we observe a small variation in both, pressure and temperature, which allow to extract kinetic data for unimolecular dissociation reactions, as demonstrated before for another organometallic precursor [129]. Using these insights, we can relate the ion intensity profiles, e.g. in Fig. 5.8, to the centerline temperature of the reactor. Therefore, we conclude that under the given experimental conditions, the experimental data obtained is suitable to develop a mechanistic understanding of chemical reactions that occur in the microreactor, since in both cases, the temperature profile is known with small uncertainties of about $10\,\text{K}$ and $30\,\text{K}$ between the measured surface and the calculated centerline temperature for helium and argon, respectively. Moreover, if we combine the information on the local residence time of a molecule in each computational cell of a dimension of $10\,\mu\text{m}$ which has a specific local temperature, these uncertainties decrease up to $5\,\text{K}$ to $10\,\text{K}$ in the case of helium (see Fig. B.1 in Appendix B). Additionally, it is important to note that the temperature profile is more uniform for helium than for argon using the same boundary conditions (see Fig. B.2 in Appendix B).

Besides the temperature profiles, we also investigated other important flow parameters and found an average pressure in the heated zone between $3.5\,\text{mbar}$ and $6.0\,\text{mbar}$ and residence times of $5\,\mu\text{s}$ to $30\,\mu\text{s}$ for wall temperatures ranging from $400\,\text{K}$ to $900\,\text{K}$ (see Fig. B.3 in Appendix B). Since the flow field in the microreactor

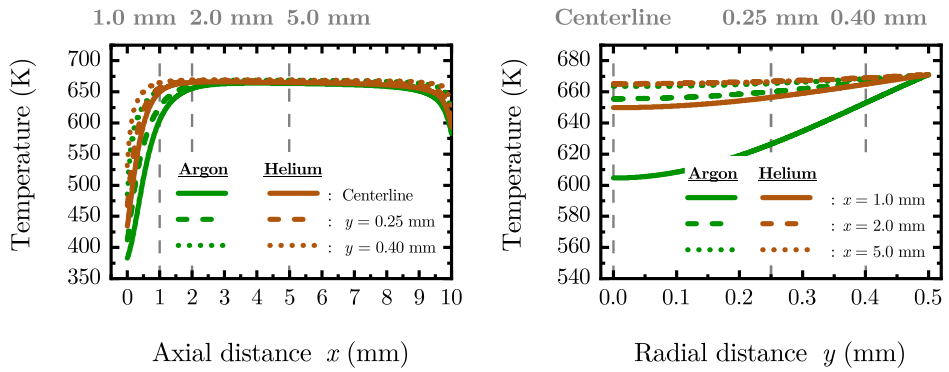

Figure 5.1: Temperature profiles calculated by CFD for an initial pressure of 215 mbar and a wall temperature of 671 K, a value, where most of the reactions occur. (a): Axial temperature profile extracted at $y = 0$ mm (straight), 0.25 mm (dashed), and 0.4 mm (dotted) from the reactor centerline inside the heated zone; (b): Radial temperature profile along a vertical line at $x = 1.0$ mm (straight), 2.0 mm (dashed), and 5.0 mm (dotted) measured from the inlet of the heated zone. The vertical dashed gray lines in each plot represent the exemplary sampled lines in the respective other graph marked at their position.

is characterized by an almost uniform temperature profile, and the residence time distribution is narrow, the experimentally determined temperature profiles are comparable to other studies using conventional flow reactors. The CFD results are in accordance to previous findings with different boundary conditions [202, 203, 204] and allow to probe mainly the initial unimolecular decomposition products, provided they occur on a timescale of the order of a few microseconds. Further details on the flow field under the given experimental conditions are presented in Sec. B.1 of Appendix B.

5.2.2 Precursor Stability: On the Degradation Products in the Evaporator

As outlined in the introduction, our main goal was to determine the pyrolysis products of $Zr(acac)_4$. Recent studies, however, propose that the precursor may already be unstable in the evaporator at temperatures of 423 K or higher, as typically used in CVD applications, but possible decomposition products have not been detected yet [92]. To distinguish between products that are due to pyrolysis in the reactor and those that are already formed in the evaporator, we kept the reactor temperature at the level of the evaporator and gradually increased both temperatures from 393 K to 443 K. Because the residence time is increased by the time that the precursor spends in the reactor, giving it additional time for possible decomposition reactions, it can be safely assumed that if no decomposition products can be detected, the precursor will also stably evaporate at this temperature in the sample container.

By recording mass spectra at 8.0 eV, 9.0 eV, 10.0 eV, 11.0 eV and 11.5 eV, relevant

decomposition products were identified, based on their unique ionization onsets. It is evident from the mass spectra in Fig. 5.2 (a) that m/z 486 $Zr(acac)_4$ ionizes dissociatively by losing one ligand (m/z 99) to yield m/z 387 $Zr(acac)_3^+$, as pointed out in the literature [320]. A comparison of the ms-TPE spectra of the parent ion m/z 486 and its major fragment at m/z 387 proves this behavior of $Zr(acac)_4$ (see Fig. B.4 (a) in Appendix B). Additionally, the analysis of the ion kinetic energy available from the VMI ion image shows a considerable momentum distribution (see Fig. B.5 in Appendix B) perpendicular to the molecular beam propagation direction. This fact let us conclude that at photon energies higher than 8.0 eV, we almost exclusively detect the major fragment of $Zr(acac)_4$. In the following analysis, when showing data recorded at higher photon energies, we ascribe the signal at m/z 387 to the precursor.

As can be seen in the recorded mass spectra of Fig. 5.2 (a), the signal of the main precursor fragment at 8.0 eV with m/z 387 increases up to an evaporation temperature of 423 K. This occurs at lower temperature than expected, since others determined a first weight loss of the precursor at around 423 K–463 K by coupled thermogravimetric and spectroscopic measurements [95, 97]. However, such an onset is mainly a question of experimental detection limits and reaction times. They found volatile hydrocarbons such as C_3H_4 (m/z 40) and acetic acid (m/z 60) that are released to the gas-phase upon precursor degradation. In agreement with these studies, we found traces of acetic acid formed in the evaporator, in a slow, but continuous decomposition process, which takes place prior to pyrolysis in the sample container. This interpretation of the mass spectra is substantiated by room-temperature VMI ion images as well as characteristic features for acetic acid in the ms-TPES profile (see Fig. B.6 in Appendix B). Since the signal intensities at m/z 60 are relatively low and remain almost constant upon pyrolysis, we attribute them to a degradation product in the evaporator. Slow degradation may be a possible explanation why others observed acetic acid by spectroscopic methods but ascribed this species to a major gaseous decomposition product [95, 97]. In contrast to the observations in the literature, neither the room-temperature mass spectra, nor the ion image or the experimental ms-TPES provides evidence that C_3H_4 forms in considerable amounts in the evaporator under the conditions used in this study.

In contrast, we detected significant amounts of other decomposition products, which are partially shown in Fig. 5.2 (b)-(e). The mass spectra (a) and the velocity map images (b) and (c), as well as ms-TPE spectra in (d) and (e) provide strong evidence that the precursor partially decomposes in the evaporator even at temperatures below 443 K. Still a significant amount of $Zr(acac)_4$ reaches the analytical chamber at the outlet of the microreactor which is represented by a steep increase of the major fragment signal at m/z 387 (M^+-L). Its signal reaches a maximum at a temperature of 423 K. Major degradation products are identified at m/z 58, 100, 122 and 164, leaving a zirconium-containing residue in the evaporator, which we did not characterize further.

We assigned the oxygenated and hydrocarbon products in the gas-phase based on their spectroscopic fingerprint and ion VMI image, exemplary shown in Fig. 5.2

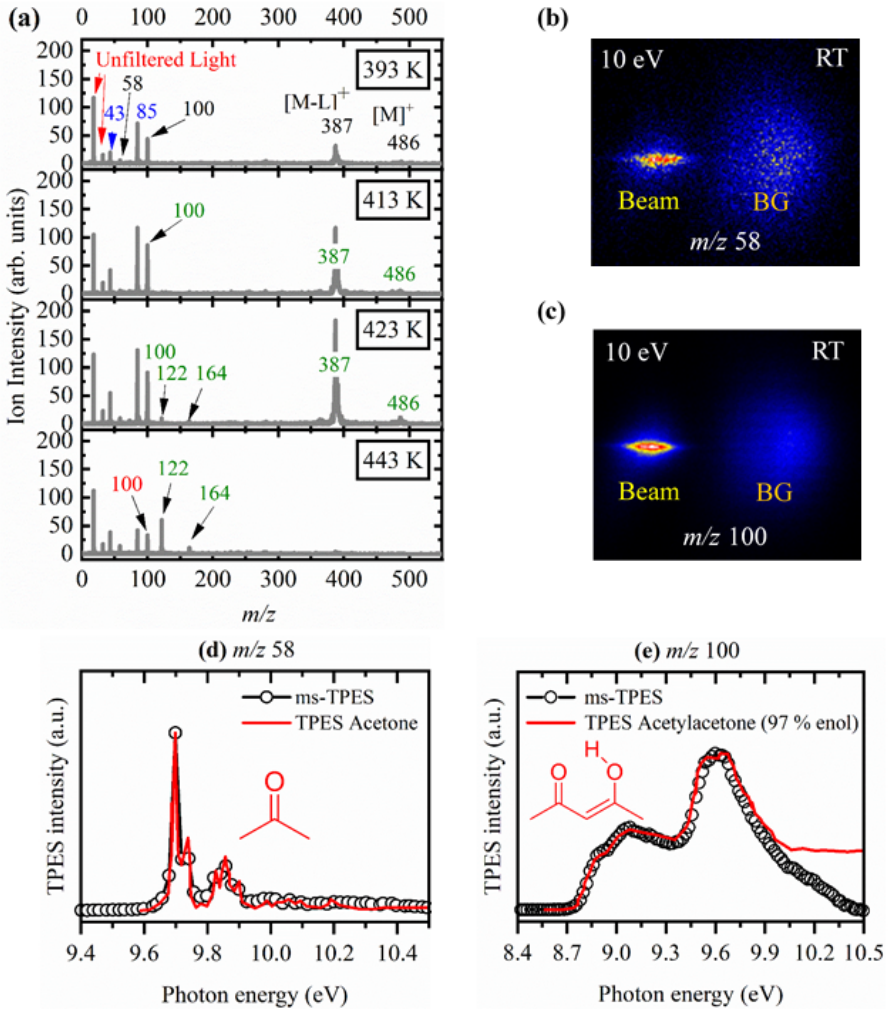

Figure 5.2: (a) Temperature-dependent mass spectra at 8.0 eV for various evaporation temperatures, which show a decrease in $Zr(acac)_4$ signal at temperatures higher than 423 K together with a simultaneous increase of the peaks denoted in green, whereas the red signals decrease in comparison to their intensity in the spectra above. Blue indicates signals that rise from small amounts of unfiltered light (i.e., light >8.0 eV); (b) and (c) show VMI images of the most abundant degradation products at a photon energy of 10.0 eV which is slightly higher than their respective ionization thresholds. The VMI images prove that the species with m/z of 58 and 100 are indeed attributed to decomposition in the sample container and do not come from dissociative ionization of $Zr(acac)_4$. The threshold photoelectron spectra (black dots) in (d) and (e) rationalize our assignment by comparison to literature reference spectra (red curves) as acetone (IE = 9.71 eV) [321] and acetylacetone (IE = 8.9 eV) [270].

(b), (d) and (c), (e), to acetone (C_3H_6O) (IE = 9.71 eV) [321] and acetylacetone ($C_5H_8O_2$) (IE = 8.9 eV) [270], as the most abundant species. Considerable amounts of 2,6-dimethylphenol ($C_8H_{10}O$) and two isomers of $C_{10}H_{12}O_2$, namely dimethyl-dihydroxo-dihydropentalene and dimethyl-hydroxo-keto-tetrahydropentalene were also found and characterized in the same manner (see Sec. 5.2.3). Our findings let us conclude that an evaporation temperature of <413 K is sufficient to minimize thermal degradation in the evaporator and allows probing the pyrolysis products in the flow reactor on a reasonable timescale. The subsequent pyrolysis experiments were carried out at a sufficiently low evaporation temperature of 403 K minimizing precursor decomposition before the reactor is reached.

5.2.3 Photoionization Mass Spectra upon Pyrolysis

To investigate the pyrolysis of $Zr(acac)_4$, photoionization mass spectra were evaluated at fixed photon energies of 8.0 to 11.5 eV in 0.5 eV increments over a temperature range of 400–900 K. The top trace of Fig. 5.3 illustrates an exemplary mass spectrum of $Zr(acac)_4$ without pyrolysis. As discussed in the previous paragraph, small contributions from the degradation in the evaporator can already be identified on the left hand side in the m/z range from 0 to 175. With pyrolysis turned on that is at higher reactor temperature, some species emerge in the mass spectra, which are shown on the bottom graphs in Fig. 5.3 (b), (c), (d). At the highest temperature of 761 K the precursors ion signal at m/z 387 is absent (purple spectrum) (a) and product peaks at m/z 82, 100 (b), 122, 128, 146 164 (c), as well as 204, 222, 286 and 304 (d) are observed in the mass spectra.

5.2.4 Identification of Elusive Species

The species assignment by conventional mass spectrometric methods is influenced, by fragmentation and is therefore often insufficient for the unambiguous assignment of reactive open-shell species, such as radicals in reactive mixtures. To identify zirconium-containing molecules, we utilize the distinct isotope distribution of zirconium, with its four stable isotopes at ^{90}Zr, ^{91}Zr, ^{92}Zr and ^{94}Zr and compare the natural distribution with our mass spectra. Additionally, we do not solely rely on the mass dimension alone, but also rely on further analytical features by scanning the photon energy. Given that each molecule has characteristic bands in its threshold photoelectron spectrum (ms-TPES), we assign the most abundant species by comparing them to literature reference spectra or Franck–Condon simulations obtained from quantum chemical calculations. This procedure has been proven to be an efficient analytical tool to monitor chemical reactions in complex environments, such as the one investigated here [122, 322].

5.2.4.1 Characterization of Hydrocarbons and Oxygenated Species

Spectra of the most abundant species obtained at 776 K are shown in Fig. 5.4. Because of the large internal energy of the neutrals obtained in the heated reactor,

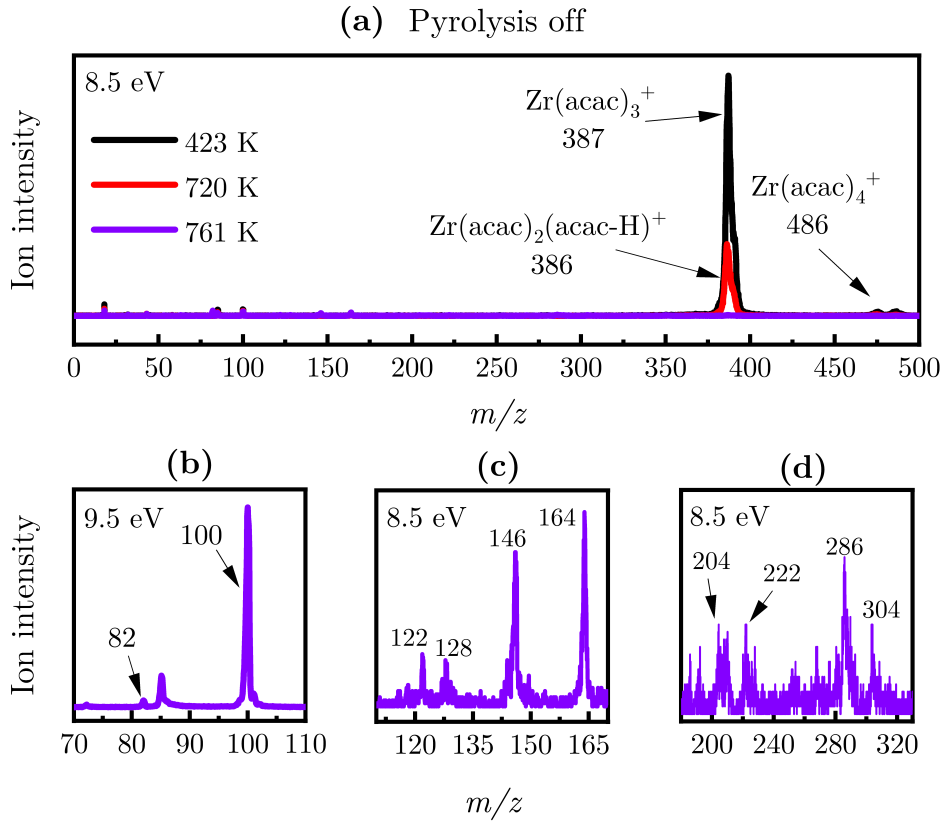

Figure 5.3: (a): Mass spectra obtained upon the pyrolysis of $Zr(acac)_4$ recorded at 423 K (black), 720 K (red) and 761 K (purple) at a photon energy of 8.5 eV. Selected parts of the mass spectrum at 761 K are enlarged in (b) at a photon energy of 9.5 eV and in (c) and (d) at a photon energy of 8.5 eV. The respective peaks are labeled by their assigned ions (a) and/or mass-to-charge ratio (a-d).

hot bands are responsible for non-zero signal levels below the adiabatic ionization onset in all the spectra observed here. We can clearly identify strong signals of hydrocarbons and oxygenated species at m/z 42, 58, 64, 82. In Fig. 5.4 (a) we observe strong bands at m/z 42 between 9.6 and 10.2 eV. The spectrum shows clear vibrational features of ketene (9.62 eV) [280], but we cannot exclude minor contributions of propene (9.73 eV) [284], which both have the same nominal mass. We observe a clear band at 9.74 eV in the ms-TPES of m/z 58 which aligns well with the published spectrum of acetone (9.70 eV) [321] in Fig. 5.4 (b). The analysis of the spectrum in Fig. 5.4 (c) shows that we can distinguish between three isomers at m/z 64, whereas 1,3-pentadiyne (9.50 eV [288]) and ethynylallene (FC simulation: 9.22 eV) are the spectral carriers. Traces of pentatetraene (8.99 eV) [284] could also be identified by a weak signal increase at around 8.9 eV. Because of the vibrational progression of the ground state band of 1,3-pentadiyne and the limited signal-to-noise ratio traces of other isomers with m/z 64 with higher ionization energies are, if present, difficult to characterize. The majority of the ms-TPE signal at m/z 82 with a strong band at 9.50 eV fits to the published Franck–Condon simulated spectrum

of acetylallene (9.44 eV) [270]. Minor contributions below 9.0 eV are assigned to its cyclic isomer 2-methylfuran (8.38 eV) [293].

As already indicated in Fig. 5.3 a few larger hydrocarbons with masses >100 could also be identified in the mass spectra and we characterize these by using both their PIE and ms-TPE signals and compare these to literature references (see Fig. 5.5). The low energy part of the ms-TPES at *m/z* 122 can be assigned to dimethyl-substituted hydroxyfulvenes. We have calculated four isomers which possess appearance energies AEs of 7.57, 7.34, 7.26 and 7.35 eV (G4), respectively. A linear combination of the two isomers in the 7.34–7.35 eV energy range reproduce the ms-TPE spectrum well, but we cannot exclude contributions from the other isomers. Despite the matching (AEs) and FC simulations such species make also chemically sense as fulvene (c-C_5H_5=CH_2) is a well-known precursors for benzene [323, 324]. In analogy to our substitution pattern we expect the fulvene moiety, probably produced as intermediate after a ketene (H_2C=C=O) loss from *m/z* 166, to rearrange to dimethylphenol (also *m/z* 122). Based on the sharp increase of the PIE curve at energies >8.0 eV on the *m/z* 122 channel in Fig. 5.5 (a), contributions of 2,6-dimethylphenol with an adiabatic IE of 8.05 eV [298] were detected. The comparison with Franck–Condon simulations of the spectrum at *m/z* 164 revealed two isomers of a cyclic hydrocarbons with the formula $C_{10}H_{12}O_2$ which are the main contributors to the overall signal in our ms-TPE spectrum of *m/z* 164 in Fig. 5.5 (b). Dimethyl-dihydroxo-dihydropentalene [129] is identified by a sharp signal increase at its IE of 7.29 eV [129] whereas its isomer dimethyl-hydroxo-keto-tetrahydropentalene (IE = 7.55 eV) [129] is the spectral carrier at energies >7.55 eV.

Besides the assignments that were discussed so far, other minor products and intermediates were identified and characterized in the same manner. Their assignments, together with the major products, are shown in Tab. 5.1 and some of the spectra are included in Fig. B.7 of Appendix B. Since the sample is highly diluted and only small amounts of the minor products were identified these minor species are not considered in the major thermal decomposition pathways discussed later in the text.

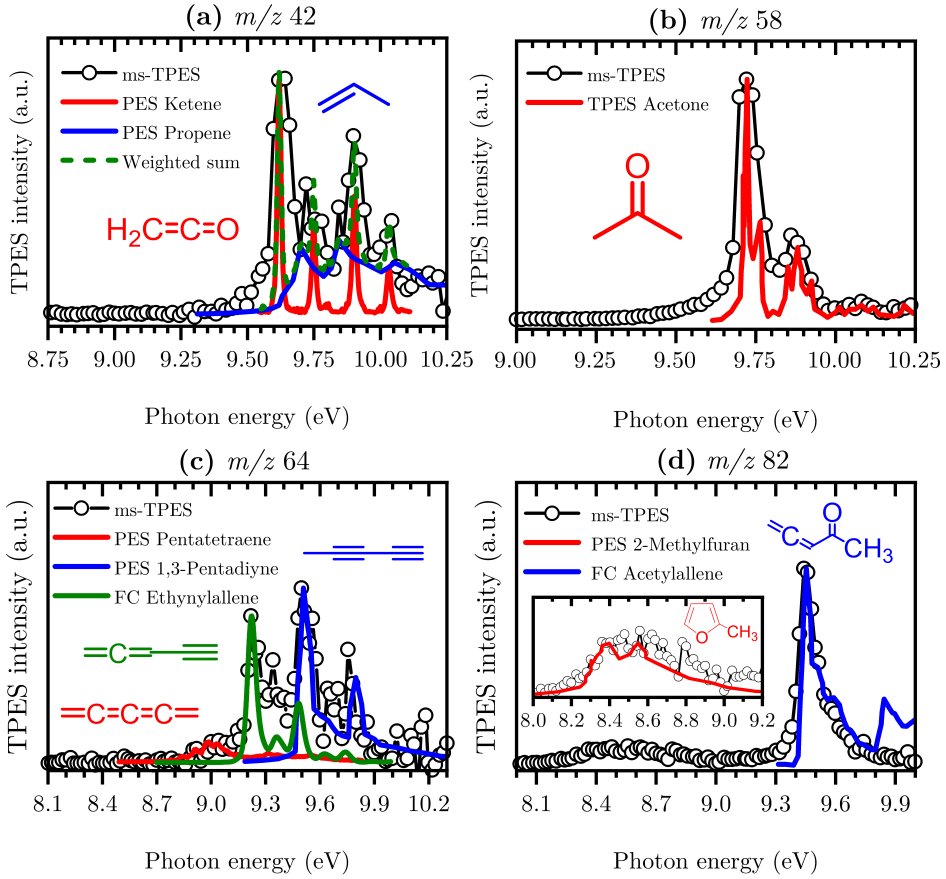

Figure 5.4: Representative examples for species identification and assignment of the major decomposition by-products using experimentally obtained ms-TPE spectra (black dots and lines) recorded at 776 K. Species are either characterized by literature reference spectra in (a)-(d), by specific ionization onsets in (c) or Franck–Condon simulations (FC) in (d). References are as follows: (a) m/z 42 red: ketene (C_2H_2O) [280], blue: propene (C_3H_6) [284]; (b) m/z 58 red: acetone (C_3H_6O) [321]; (c) m/z 64 C_5H_4 red: pentatetraene [284], blue: 1,3-pentadiyne [288] and green: ethynylallene [this work]; (d) m/z 82 C_5H_6O red: 2-methylfuran [293], blue: acetylallene [270].

Table 5.1: List of identified species upon pyrolysis of $Zr(acac)_4$ by VUV i^{2}PEPICO using their adiabatic and vertical ionization energies and, when necessary their distinct isotopic pattern. Reference spectra and energies have been taken from the literature and are denoted at the respective value. The identification of the compounds in bold are discussed further in the paper. Species marked with an asterisk are tentatively assigned, based on mechanistic evidence.

m/z	Formula	Name	IE (eV) References
15	CH_3	Methyl radical	9.84 [273]
39	C_3H_3	Propargyl radical	8.71 [277]
42	$\mathbf{C_2H_2O}$	**Ketene**	9.62 [280]
	$\mathbf{C_3H_6}$	**Propyne**	9.73 [284]
43	C_2H_3O	DPI Acetone	9.50††
		DPI Acetylactone	10.20††
58	C_3H_6O	Acetone	9.70 [321]
60	$C_2H_4O_2$	Acetic Acid	10.69 [325]
64	$\mathbf{C_5H_4}$	**Pentatetraene**	8.99 [284]
		Ethynylallene	9.22
		1,3-Pentadiyne (Methyldiacetylene)	9.50 [288]
82	$\mathbf{C_5H_6O}$	**2-Methylfuran**	8.38 [293]
		Acetylallene	9.44 [270]
100	$\mathbf{C_5H_8O_2}$	**Acetylacetone (enol)**	8.90 [270]
		Acetylacetone (diketo)	9.50[270]
122	$\mathbf{C_8H_{10}O}$	**2,6-Dimethylphenol**	8.05 [298]
		2-Dimethylhydroxo-fulvene	7.34†
		4-Dimethylhydroxo-fulvene	7.35†
146	$C_{11}H_{14}$	2,4,6-Trimethylstyrene	7.72 [326]
164	$\mathbf{C_{10}H_{12}O_2}$	**Dimethyl-dihydroxo-dihydropentalene**	7.29 [129]
		Dimethyl-hydroxo-keto-tetrahydropentalene	7.55 [129]
204	$\mathbf{ZrO(C_5H_6O_2)}$	**Zr-intermediate**	7.4 ± 0.2†
222	$\mathbf{Zr(OH)_2(C_5H_6O_2)}$	**Zr-intermediate**	7.6 ± 0.2†
286	$\mathbf{Zr(C_5H_6O_2)_2}$	**Zr-intermediate**	7.6 ± 0.2†
304	$\mathbf{Zr(OH)(C_5H_7O_2)(C_5H_6O_2)}$	**Zr-intermediate**	7.5 ± 0.2†
322*	$Zr(OH)_2(C_5H_7O_2)_2$*	Possible surface product*	Not detected*
344	$\mathbf{Zr(C_5H_7O_2)(C_5H_6O_2)(C_3H_5O)}$	**Zr-intermediate**	7.7 ± 0.2†
386	$\mathbf{Zr(C_5H_7O_2)_2(C_5H_6O_2)}$	**Zr-intermediate**	7.5 ± 0.2†
387	$\mathbf{Zr(C_5H_7O_2)_3}$	**Zr-intermediate**	7.95††
486	$\mathbf{Zr(C_5H_7O_2)_4}$	**Zr-intermediate**	7.95 [327]

†This work
††Appearance energy (AE)

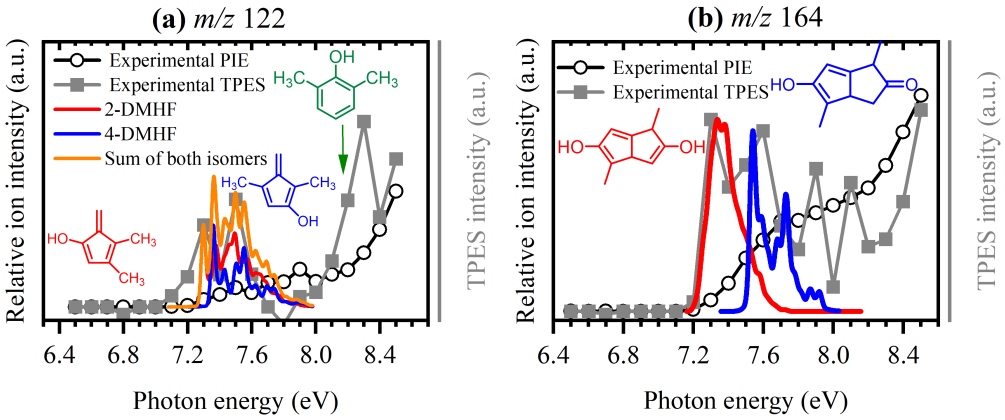

Figure 5.5: Representative examples of species identification and assignment of major species at a temperature of 676 K at masses >100 using experimental obtained ms-TPE spectra (gray squares and lines) and PIE curves (black dots and lines). The species are either characterized by literature reference values (red label) in (a) or spectra obtained from FC-simulations (red and blue lines) in (b). References are as follows: (a) m/z 122 $C_8H_{10}O$: 2- and 4-dimethylhydroxyfulvene (red) [this work] and (blue) [this work]; 2,6-dimethylphenol (green) [298], (b) m/z 164 $C_{10}H_{12}O_2$ [129].

5.2.4.2 Identification and Assignment of Volatile Zirconium Species

Experimental data of the ionization onset, ionization cross sections and photoelectron spectra of metal-containing intermediates are, due to their high reactivity, scarce in the literature. For this reason, we utilized the isotopic pattern to identify which intermediates contain zirconium. Additionally, we measured the ionization onsets of the most abundant zirconium-containing intermediates in the gas-phase, which will be useful in future studies. Figure 5.6 shows a compendium of the most abundant Zr species detected upon pyrolysis. The distribution of the zirconium isotopes is indicated by blue sticks in the respective spectra, with a focus on the four most intense isotopes at ^{90}Zr, ^{91}Zr, ^{92}Zr and ^{94}Zr. Here, by comparing the isotopic pattern to our mass spectra, it can be easily recognized that zirconium species are present, hinting that these species have the general formula (m/z 286, $Zr(C_5H_6O_2)_2$; m/z 304, $Zr(OH)(C_5H_7O_2)(C_5H_6O_2)$; m/z 344, $Zr(C_5H_7O_2)(C_5H_6O_2)(C_3H_5O)$ and m/z 386, $Zr(C_5H_7O_2)_2(C_5H_6O_2)$), respectively. The respective ion VMI images of these species confirm that they originate from pyrolysis and are no dissociative ionization products (see Fig. 5.6 (d), middle and Fig. B.8 in Appendix B). We also determined the ionization onsets of these species and recorded spectroscopic fingerprints (ms-TPES and PIE spectra) of those volatile intermediates of zirconium for the first time (see Fig. 5.7). The ionization onsets of the zirconium intermediates have been determined by a Wannier-type linear fit [150, 151, 152] to be 7.4 ± 0.2 eV; 7.6 ± 0.2 eV; 7.6 ± 0.2 eV, 7.5 ± 0.2 eV, 7.7 ± 0.2 eV and 7.5 ± 0.2 eV for m/z 204, 222, 286, 304, 344 and 386, respectively (see Fig. 5.6 (d), left and Fig. 5.7). It is evident from Fig. 5.7 that the ionization onsets of the zirconium intermediates are close to the adiabatic ionization energy of the precursor, however only a tentative

isomeric structure can be given here, as open-shell heavy atom calculations are outside the scope of the current study. All ionization potentials determined in this study are summarized in Tab. 5.1 and indicated by a dagger symbol. Possible mechanisms to the formation of these intermediates are discussed in the following paragraph. All these characterized species may lead to the formation of ZrO_2 thin films, whereas additional oxygen is needed for its formation [96].

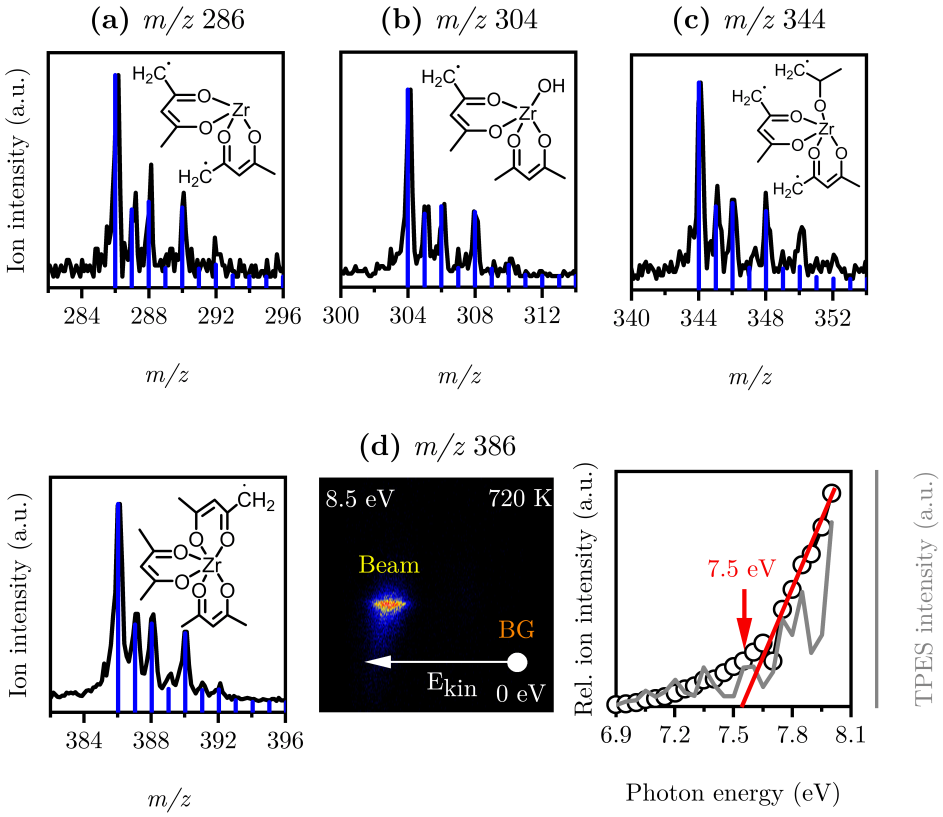

Figure 5.6: Identification of the most abundant gaseous zirconium-containing intermediates detected in the pyrolysis of $Zr(acac)_4$ at a surface temperature of 775 K in helium (a)-(c) and at a temperature of 720 K. (d), left: Blue sticks indicate the isotopic pattern of the zirconium-containing species. (d), middle: Ion velocity map image (VMI) for the m/z 386 channel. The narrow kinetic energy distributions approve that the species is formed in the reactor rather than a product of dissociative ionization (fragmentation). (d), right: Photoion intensity curve (PIE) (black) and threshold photoelectron spectrum (ms-TPES) (red) of m/z 386, where a clear ionization onset at 7.5 ± 0.2 eV was identified.

5.2.5 Pyrolysis Pathways of Zirconium Acetylacetonate

After a successful identification of the relevant hydrocarbons and zirconium intermediates formed in the pyrolysis of $Zr(acac)_4$, their temperature-dependence is investigated. The centerline temperatures given are deduced from the CFD simulations (see Sec. 5.2.1). The temperature dependencies of the most important

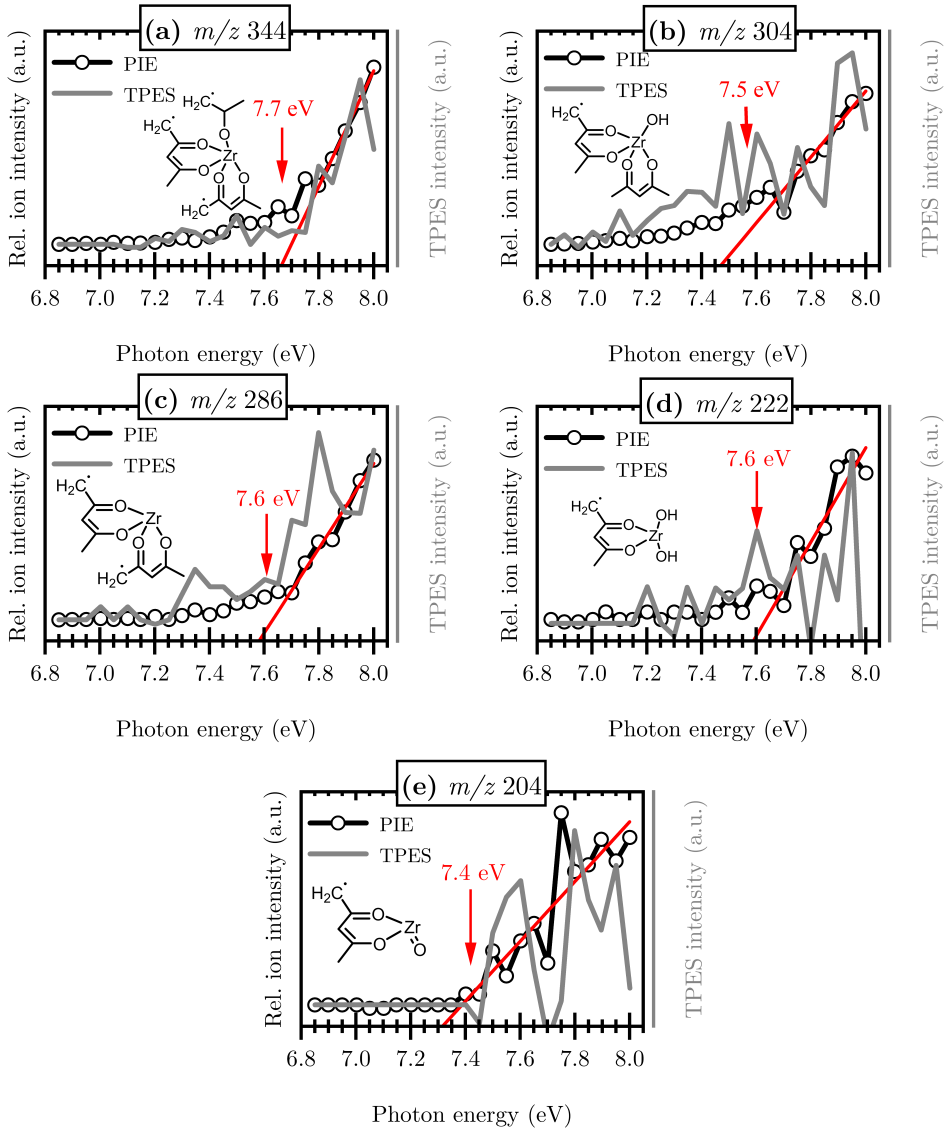

Figure 5.7: Recorded PIE curves (black lines, symbols) and ms-TPES (gray lines) of secondary zirconium species detected upon pyrolysis of $Zr(acac)_4$ at 775 K. The adiabatic ionization onsets were determined by evaluating the intersection between the slope of the red line with the x-axis according to a Wannier-type linear fit. The isomeric structures are tentative ones.

intermediate species are displayed on the middle and lower trace of Fig. 5.8. These species are either formed by a possible surface-mediated decomposition step or by secondary zirconium intermediates that are generated from the primary decomposition products. We note that the type of dilution gas changes the branching ratio of the products, for example the amount of acetylacetone, represented by its major fragment m/z 85, increases considerably by a factor of three when argon is used as carrier gas compared to helium. This phenomenon can be explained by shorter residence times and a more uniform temperature distribution in the microreactor with a larger high-temperature zone, which is the case when helium is used as dilution gas. The same observation is made for other zirconium species as well, whose signal intensity is five times higher in the helium case, pointing to rapid formation and decomposition reactions of these intermediates. These fast reactions explain why these intermediates were not observed in previous experiments using reactors with longer residence times. However, the difference in the decomposition mechanism between the two dilution gases is gradual and mainly due to different time-temperature history. Consequently, the mechanistic findings that are described in the following are valid for both dilution gases.

Combining the species assignments from the previous paragraphs, together with the species profiles in Fig. 5.8, enables us to describe the dominant decomposition pathways in the temperature range from 400 K to 900 K (see Scheme 2). Although the temperature onset of decomposition at around 450 K found in this study is in accordance to the observation of others who determined the onset of thermal decomposition to be around 450 K to 550 K [82, 95, 315], the thermal decomposition pathways of $Zr(acac)_4$ suggested here differ from previously published ones. It was stated in the literature that zirconium acetylacetonate either decomposes by a coordination polymerization step of its, yet unknown, initial decomposition product [82], or $Zr(OH)(CH_3COO)_3$ forms. The latter one was rationalized by the corresponding weight loss and the detection of C_3H_4 and $C_2H_3O_2$ at temperatures from 438 K to 563 K by thermogravimetric and spectroscopic measurements [95, 314, 315], which mainly observe condensed phase chemistry. Another possible reaction path was observed, in which cyclic diketones are formed by an intramolecular interaction of two neighboring ligands [82].

However, the results obtained in this study only partially agree with previous findings. We found a single heavier species than $Zr(acac)_4$ at m/z 691 in our mass spectra. Yet, ion VMI images verified that the detected species at m/z 691 is rather a cluster ion or a fragmentation product and can therefore not be ascribed as thermal decomposition product. This observation disagrees with the literature, where a dimerization product was found [82]. When compared to earlier studies, its absence may be owed to the much higher dilution and an order of magnitude shorter residence times in our microreactor. Furthermore, different temperature windows are recognized in the species profiles of Fig. 5.8 which indicate three separate mechanisms. A surface-mediated mechanism that forms oxygenated cyclic hydrocarbons by a cyclic dimerization reaction of two neighboring ligands starting at temperatures >500 K, leading to zirconium species which may be attached to

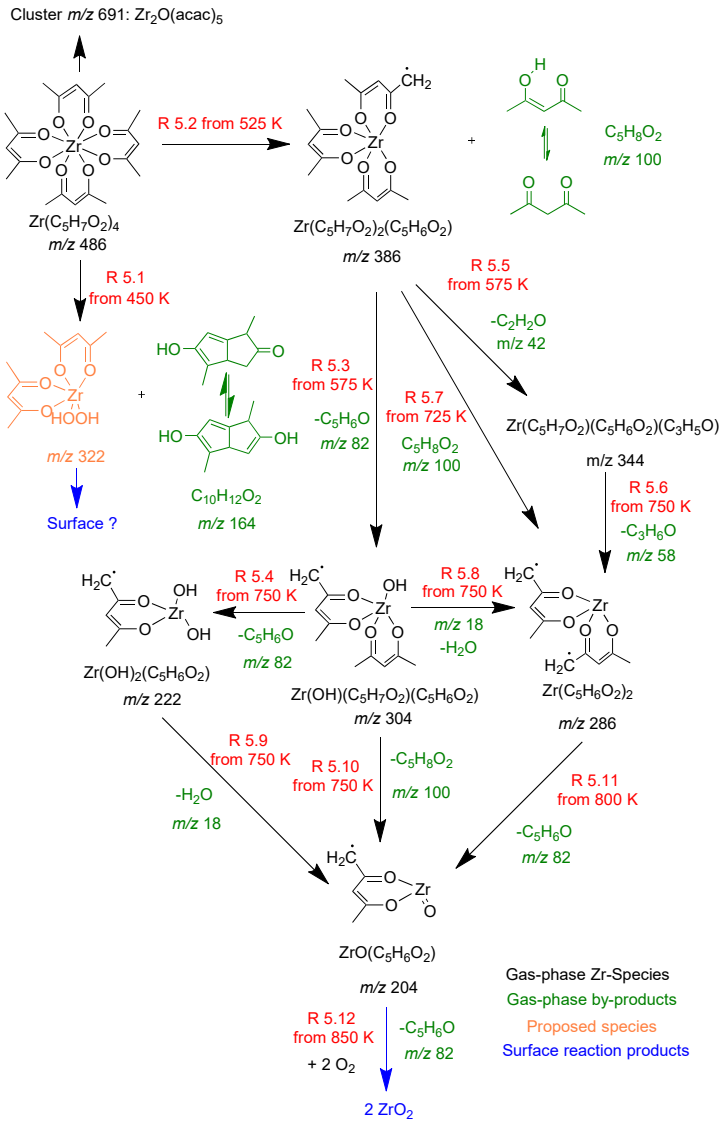

Scheme 2: Schematic representation of the major decomposition pathways of $Zr(C_5H_7O_2)_4$ in the gas-phase which has been rationalized by ms-TPES and temperature-dependent species profiles. Species are colored according to their role in the mechanism; green: gaseous by-products; black: zirconium intermediates; blue: surface reaction products; orange: hypothetical intermediates which were not detected by the i^{2}PEPICO experiment.

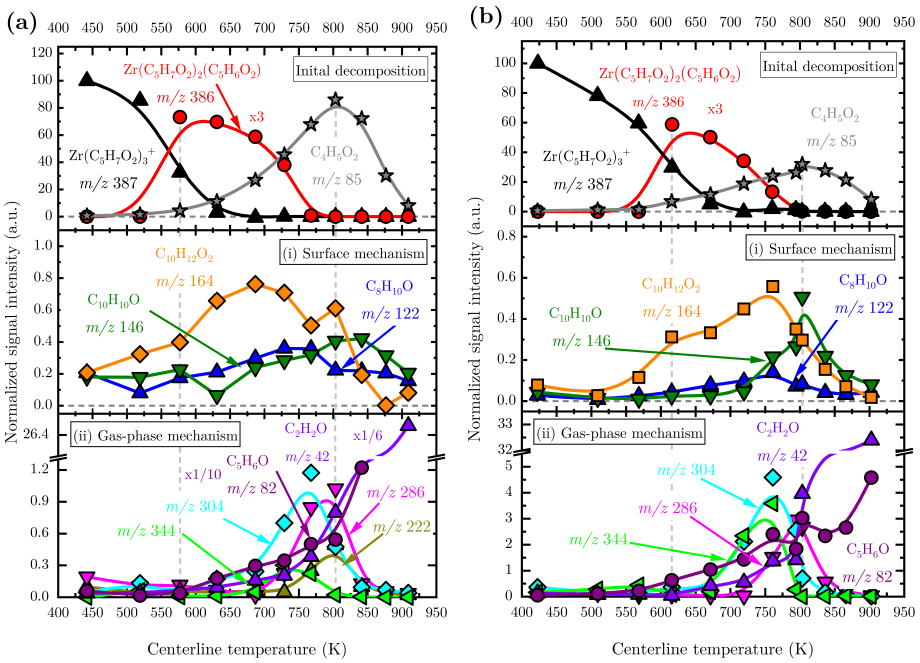

Figure 5.8: Temperature-dependent species profiles of intermediates and products upon the thermal decomposition of $Zr(acac)_4$ at T_{vap} = 403 K (0.0048%) in argon (a) and helium (b), probed by i^{2}PEPICO VUV mass spectrometry in the microreactor. The respective species that were characterized according to Sec. 5.2.4 are labeled by their formula and all signals are normalized to the initial zirconium main fragment signal at m/z 387 at a photon energy of 8.5 eV. Note that the axis in the bottom trace of both graphs contain a break in order to display all signals that belong to the secondary decomposition of the zirconium intermediates.

the surface and thus were not detected in the gas-phase:

$$Zr(C_5H_7O_2)_4 \longrightarrow Zr(OH)_2(C_5H_7O_2)_2 + C_{10}H_{12}O_2. \qquad \text{(R 5.1)}$$

This pathway has been verified for similar group III and IV metal β-diketonates and the formation of the three isomers detected at m/z 122 can be explained by a loss of ketene (C_2H_2O) which we found in our mass spectra starting from temperatures at 575 K (see Fig. 5.8, bottom trace) [82, 129].

In contrast to other work, we neither found evidence for the formation of C_3H_4, nor considerable amounts of acetic acid upon pyrolysis at low temperatures which would lead to metal acetate species as primary decomposition products on the surface [95]. Instead, we detected zirconium tris(diketo)acetylacetonate-H, $Zr(C_5H_7O_2)_2(C_5H_6O_2)$ and acetylacetone ($C_5H_8O_2$) as primary decomposition products which are formed in a unimolecular decomposition step according to:

$$Zr(C_5H_7O_2)_4 \longrightarrow Zr(C_5H_7O_2)_2(C_5H_6O_2) + C_5H_8O_2. \qquad \text{(R 5.2)}$$

We interpret these findings similar as in our previous study on the decomposition of $Al(acac)_3$ [129], where an H-transfer from the CH_3 group of a neighboring acetylactonate ligand to the second equatorial ligand initiates this reaction sequence, in which at first, one of the metal–oxygen bonds is cleaved. This step produces a weakly bound intermediate from which the second Zr−O bond breaks readily, yielding *m/z* 386 $Zr(C_5H_7O_2)_2(C_5H_6O_2)$ and acetylacetone. This pathway is in line with the temperature-dependent species profiles, where the trace of *m/z* 387 (major fragment of $Zr(acac)_4$) exhibits a steep decrease, while *m/z* 386 and 100 are increasing simultaneously. Given the absolute intensities we can plausibly state that this H-transfer mechanism is the dominant primary decomposition step in pyrolysis of $Zr(acac)_4$. All preceding steps that were observed can be traced back to a thermal fragmentation of the primary decomposition product *m/z* 386 $Zr(C_5H_7O_2)_2(C_5H_6O_2)$, resulting in further zirconium intermediates, whose existences were suspected by others [96], but until now, has not been experimentally validated.

The following gas-phase decomposition mechanism at temperatures above 575 K follows two branches where *m/z* 386 first undergoes a series of C_5H_6O loss reactions leading to the stepwise formation of *m/z* 304, $Zr(OH)(C_5H_7O_2)(C_5H_6O_2)$, and *m/z* 222 $Zr(OH)_2(C_5H_6O_2)$, respectively:

$$Zr(C_5H_7O_2)_2(C_5H_6O_2) \longrightarrow Zr(OH)(C_5H_7O_2)(C_5H_6O_2) + C_5H_6O, \quad \text{(R 5.3)}$$

$$Zr(OH)(C_5H_7O_2)(C_5H_6O_2) \longrightarrow Zr(OH)_2(C_5H_6O_2) + C_5H_6O. \quad \text{(R 5.4)}$$

These steps are corroborated by identifying *m/z* 82 as acetylallene at temperatures above 575 K and a simultaneous formation and decomposition of *m/z* 304 (see Fig. 5.8, bottom trace). Another decomposition pathway of *m/z* 386 was identified in the same temperature window. After a loss of ketene (C_2H_2O) followed by a subsequent acetone (C_3H_6O) loss at temperatures higher than 750 K, *m/z* 286, $Zr(C_5H_6O_2)_2$, is formed in the gas-phase according to:

$$Zr(C_5H_7O_2)_2(C_5H_6O_2) \longrightarrow Zr(C_5H_7O_2)(C_5H_6O_2)(C_3H_5O) + C_2H_2O, \quad \text{(R 5.5)}$$

$$Zr(C_5H_7O_2)(C_5H_6O_2)(C_3H_5O) \longrightarrow Zr(C_5H_6O_2)_2 + C_3H_6O. \quad \text{(R 5.6)}$$

Similarly, ketene, acetone as well as *m/z* 286, $Zr(C_5H_6O_2)_2$ were unambiguously identified in this temperature regime by their spectroscopic fingerprints, ion images and species profiles. The primary decomposition product *m/z* 386 may also lose another ligand at temperatures above 725 K leading to the direct formation of *m/z* 286, following a similar mechanism as proposed for the initial cleavage of one ligand from $Zr(acac)_4$ in reaction Reac. R 5.1:

$$Zr(C_5H_7O_2)_2(C_5H_6O_2) \longrightarrow Zr(C_5H_6O_2)_2 + C_5H_8O_2. \quad \text{(R 5.7)}$$

Further decomposition of zirconium intermediates in the gas-phase was observed, starting at temperatures above 750 K. Here, the secondary zirconium intermediates *m/z* 304, *m/z* 286 and *m/z* 222 decompose in probably unimolecular reactions yielding *m/z* 204 which is evidenced by the Zr-isotopic pattern in our mass spectra (see Fig. 5.3 (d)). We propose four possible pathways that are in line with our findings:

$$Zr(OH)(C_5H_7O_2)(C_5H_6O_2) \longrightarrow Zr(C_5H_6O_2)_2 + H_2O, \quad \text{(R 5.8)}$$

$$Zr(OH)_2(C_5H_6O_2) \longrightarrow ZrO(C_5H_6O_2) + H_2O, \quad \text{(R 5.9)}$$

$$Zr(OH)(C_5H_7O_2)(C_5H_6O_2) \longrightarrow ZrO(C_5H_6O_2) + C_5H_8O_2, \quad \text{(R 5.10)}$$

$$Zr(C_5H_6O_2)_2 \longrightarrow ZrO(C_5H_6O_2) + C_5H_6O. \quad \text{(R 5.11)}$$

The species with *m/z* 286 and 204 are probably formed in reaction Reac. R 5.8 and Reac. R 5.9 after water abstraction. Note that the latter is not observed in the mass spectra in Fig. 5.3, due to its high ionization energy. Both reaction sequences Reac. R 5.8 and Reac. R 5.9 are attributed to gas-phase reactions because the detected zirconium intermediates are expected to have very small vapor pressures and condense on the surface of the reactor. While acetylacetone can be formed from *m/z* 304 in reaction Reac. R 5.10, acetylallene may be formed in reaction Reac. R 5.11 from *m/z* 286. The occurrence of these reactions is substantiated by the steep increase of the ion signal intensity of *m/z* 100 acetylacetone between 750 and 800 K and the increase of *m/z* 82 at temperatures above 800 K. Given the absolute intensities of each of the oxygenated hydrocarbon products formed in these reactions, it appears that the loss of acetylallene from *m/z* 286 is the dominant pathway.

The reason for the small quantities of *m/z* 204 found in the gas-phase in our study may be due to an immediate subsequent decomposition of this intermediate forming acetylallene resulting in the formation of the final product *m/z* 122 ZrO_2 on the surface of the microreactor:

$$ZrO(C_5H_6O_2) \longrightarrow ZrO(C_5H_6O_2)(ads) \longrightarrow ZrO_2(ads) + C_5H_6O. \quad \text{(R 5.12)}$$

Since we found a steep increase in *m/z* 82 at high temperatures >800 K in the mass spectra, we think that such processes starting from reaction Reac. R 5.11 are dominant. However, other zirconium intermediates may also adsorb on the surface and may reside there until oxidation to ZrO_2 occurs at temperatures above 1073 K in oxygen rich atmosphere [95], or an incomplete oxidation to ZrO_xC_y might occur leaving a considerable carbon deposit on the reactor walls [96].

As expected from previous studies on the high-temperature pyrolysis of acetylacetone [200, 270], the observation of large amounts of ketene and acetone most likely stem from an unimolecular decomposition of acetylacetone through a C–C bond cleavage followed by a subsequent H-atom transfer. As indicated by the decrease in acetylacetone signal at temperatures above 800 K, we attribute the main fraction of these products to the decomposition of the liberated ligands rather than to additional surface or gas-phase decomposition products in the high-temperature region.

5.3 Conclusion

We have investigated the pyrolysis of $Zr(acac)_4$, a common precursor used in the synthesis of ZrO_2 thin films, by VUV soft ionization from a synchrotron light source coupled to double imaging photoelectron photoion coincidence spectroscopy (i^2PEPICO). The accompanying numerical simulation of the microreactor's flow field by CFD confirmed that helium is the preferable inert gas ensuring low average residence times of <15 µs and uniform temperature fields as compared to argon. For helium dilution, the experimental flow field approaches a plug-flow and the temperature of intermediate formation is close to the experimentally accessible wall temperatures. Additionally, the low residence times and much higher signal levels are advantageous for the detection of elusive zirconium intermediates.

We have identified the main gas-phase degradation products formed in the evaporator prior to decomposition of the precursor in the microreactor. Interestingly, we cannot confirm previous observations that acetic acid and C_3H_4 are the major products formed, instead acetylacetone and acetone are the major gas-phase species evolving from degradation in the evaporator. At our conditions, we could ensure stable evaporation conditions for several hours using an evaporation temperature of 403 K.

We showed that the pyrolysis of $Zr(acac)_4$ can be divided into three major steps, which take place in distinct temperature regimes starting from 525, 750 and 850 K. For the first time important zirconium intermediates formed in the gas-phase were identified by analyzing the isotopic pattern of zirconium, the momentum distribution of the ions (VMI), as well as the PIE and ms-TPE spectra. In addition, we determined adiabatic ionization energies of these species for the first time which may be of interest for subsequent kinetic investigations and theoretical studies. Besides minor amounts of possible surface reactions, which form aromatic hydrocarbons with masses > 100, in particular 2,6-dimethylphenol ($C_8H_{10}O$), two dimethyl-hydroxo-fulvene isomers, as well as two isomers of $C_{10}H_{12}O_2$, we found strong evidence that the majority of the thermal decomposition of $Zr(acac)_4$ occurs in the gas-phase. Here, $Zr(C_5H_7O_2)_2(C_5H_6O_2)$ m/z 386 together with acetylacetone was identified as primary decomposition product at temperature above 525 K. In a further sequential decomposition of this intermediate at temperatures 550-750 K, mainly zirconium complexes like $Zr(OH)(C_5H_7O_2)(C_5H_6O_2)$ m/z 304, and $Zr(C_5H_6O_2)_2$ m/z 286,

are formed in the gas-phase and their reaction pathways are discussed. Several hydrocarbons are formed as by-products, such as acetylallene, acetone and ketene, which were all identified unambiguously by their spectroscopic fingerprint in the gas-phase. Probably the Zr-species are then adsorbed on the surface of the reactor. By subsequent surface reactions they may produce ZrO_xC_y films which, under excess oxygen, may be oxidized to form ZrO_2 layers at temperatures higher than 1000 K.

The present findings help to solve open questions in the mechanism of similar CVD precursors to model the growth of thin films as well as the particle formation and growth processes and thus contribute to an increase in the yield of the desired product.

5.4 Materials & Methods

5.4.1 Experimental Setup

The experiments were conducted at the vacuum ultraviolet (VUV), X04DB beamline of the Swiss Light Source (SLS) synchrotron facility located at the Paul Scherrer Institute (PSI) in Switzerland. The working principle of the Chen-type pyrolysis microreactor [121, 129], coupled to the imaging i^{2}PEPICO spectrometer [173, 253], as well as the VUV beamline characteristics [145] have been described in detail before [129]. Only a brief explanation of the most important parts is given here.

A schematic sketch of the setup is shown in Fig. 5.9. The $Zr(acac)_4$ powder was purchased from *TCI Chemicals* and was used without further purification. Approximately 2 g of the precursor were placed inside a stainless-steel tube with a 100 µm pinhole at the tip. In order to sublime the solid precursor, the sample was heated by two temperature-controlled cartridge heaters placed centrally inside two drillings of an isothermal copper block. The sublimation temperature was continuously monitored by two type K thermocouples with an accuracy of ± 0.75% and the pressure was held at approximately 200–250 mbar. To entrain the gaseous precursor molecules and carry them into the reactor either argon (99.999%) or helium (99.999%) was passed by calibrated mass flow controllers (*MKS Instruments Inc.*) to the evaporator with a constant flow rate of 22 sccm. Assuming thermal equilibrium in the evaporator and using the measured vapor pressure data from Morozova et al. [229], precursor concentrations of 17–1925 ppm entering the reactor were adjusted. In a first set of experiments the temperature T_{vap} of the evaporator was varied from 393 to 443 K to investigate the possible degradation of the precursor, prior to entering the microreactor. Based on these findings, the precursor concentration is kept constant at 48 ppm (T_{vap} = 403 K) in the seed (argon or helium) for the pyrolysis experiments. This low concentration largely suppresses bimolecular reactions [129, 202, 204] and ensures stable evaporation conditions in our reactor.

The saturated gas-phase was then expanded to a SiC microtubular reactor (L = 15 mm; I.D. = 1 mm; O.D. = 2 mm) which was resistively heated, and its outer

surface temperature was measured by a centrally fixed type C thermocouple with a maximum deviation of reading of ± 1%. As pointed out by others, residence times of <100 µs and pressures of a few tens of mbar can be expected in these Chen-type reactors [202]. A detailed examination of the flow field characteristics in the microreactor under the experimental conditions applied in this study is discussed in the course of the numerical simulation in the following section which we conducted in a similar way as in our recent publication [129] (see Chap. 4).

After passing the reaction zone, the products are expanded into high vacuum at 5×10^{-5} mbar to form a molecular beam which suppresses further chemical reactions. The central part of the beam is cut out by a 2 mm conical nickel-skimmer and the remaining gas sample flows towards the ionization region at a background pressure $<6 \times 10^{-6}$ mbar. For VUV soft ionization, synchrotron radiation is collimated, dispersed by a grazing incidence monochromator with a 150 lines/mm laminar grating, and focused at the exit slit in a differentially pumped gas filter at a photon energy resolution of 5 meV[2]. To suppress potential artificial signals due to higher-order radiation, diffracted by the grating, either a differentially pumped gas filter was filled with a mixture of argon, neon and krypton or a MgF_2 mirror was used. The incoming photon energy was calibrated before the experiments using the auto ionization lines (s' Rydberg series) of argon in both the first and second order [171].

In the ionization volume, the molecular beam intersects with the VUV light at a given energy, leading to photoions and photoelectrons, respectively. Both are separated in a constant electrical field of 213 V cm^{-1}, velocity map imaged (VMI) and detected using position sensitive delay-line anode detectors (*Roentdek*, DLD40) in a multi-start multiple stop approach [124]. In contrast to conventional mass spectrometry, VMI allows to evaluate the kinetic energy distribution of the molecules as additional analytical dimension (see Fig. 5.9, "Ion Image"). By reducing the region-of-interest (ROI) to only the molecular beam component and choosing ionization energies close to the threshold of the specific molecules of interest, background free mass spectra can be recorded, and dissociative ionization can be suppressed. Plotting the threshold photoelectron signal in coincidence with the cation mass-to-charge ratio as a function of the photon energy yields the photoion mass-selected threshold photoelectron spectrum (ms-TPES) which enables isomer-selective assignment of intermediates and stable products by comparing to reference data or to Franck–Condon (FC) simulations [153]. During post-processing, these spectra are corrected for hot-electron contributions as outlined by Sztáray and Baer [171] and normalized by the corresponding photon energy specific photon flux. Franck–Condon simulations were performed with the program ezSpectrum [328] while geometries and Hessian matrices were calculated at the B3LYP/GTBas3 level of theory with Gaussian16 [255]. Adiabatic ionization energies were determined using the G4 composite method.

The i[2]PEPICO experimental apparatus can register the molecular mass as well as the photoionization and threshold photoelectron spectrum of the species of

[2]Characterized at an incident photon energy of 8.0 eV

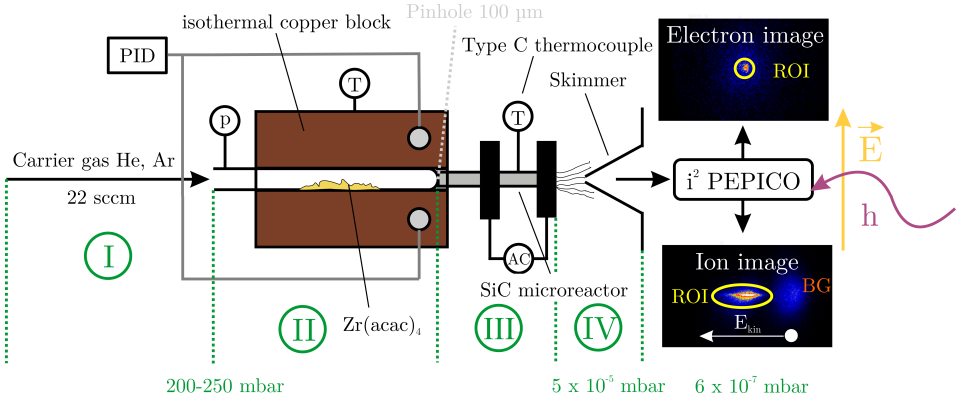

Figure 5.9: Schematic sketch of the experimental setup, based on [129]. The boundary conditions applied for the numerical simulation are displayed in green Roman numerals and are summarized in Tab. B.1 in Appendix B.

interest. These data can be compared to literature data, i.e., photoelectron spectra and used in this way for an unambiguous and isomer-selective characterization of most of the primary decomposition products [253]. In all experiments, we either kept the photon energy constant at near-threshold photoionization energies of the decomposition species of interest, or scanned the energy incrementally at constant temperatures of 676, 776 and 803 K with averaging times of 240 s. With the aim to detect most of the expected hydrocarbon and oxygenated decomposition products, we scanned with a step size of 0.025 eV in the 8.0–11.5 eV range and used a neon/ argon/ krypton gas mixture in the gas filter. Volatile zirconium species are expected to ionize at relatively low energies of <8.0 eV. To detect these species the MgF_2 window was used. Photon losses at the window lead to much longer averaging times of up to 1800 s but also to a better filtering of the higher harmonic radiation. To economize on beam time, the larger averaging times were in part compensated by a larger step width of 0.1 eV. Unfortunately, the signal-to-noise ratios of the ms-TPES were not sufficient to determine accurate ionization thresholds for intermediate species from these datasets, because these species are only present in small quantities. Additionally, Franck–Condon factors are hard to determine numerically. To overcome this issue we estimated the values of the adiabatic ionization energies (IE_{ad}) of the unknown intermediate species by a Wannier-type linear fit, with an exponent of unity, to the photoionization spectra [150, 151, 152]:

$$\mathrm{PIE}(h\nu) = m \cdot (h\nu)^1 + b, \tag{5.1}$$

where m is the slope of the fit and b represents the intersection with the y-axis. By finding the intersection between the fit and the photon energy on the x-axis, adiabatic ionization energies can be determined with an estimated accuracy of ± 0.2 eV [151, 152].

We were able to record a series of temperature-dependent mass spectra at 8.0–11.5 eV with an 0.5 eV increment and an averaging time of 240 s in the tem-

perature range from 400 to 900 K, where most reactions should occur. Isolated reproduction measurements of room-temperature mass spectra using velocity map imaging and space focusing conditions for an evaporation temperature of 423 K showed a maximum deviation of the peak intensities of less than 3%. Additionally, a substantial change of the microreactor's resistivity was not observed which would indicate a serious change in surface area due to high surface deposition. Given this, the recorded spectra enable us to derive temperature-dependent species profiles and evaluate the reaction mechanism with sufficient accuracy.

5.4.2 Numerical Setup

The characterization of the flow field in the microreactor is important in order to accurately determine reaction conditions and extract reliable mechanistic and kinetic data. As demonstrated in previous works, given that the inlet and outlet pressure as well as the exterior wall temperature are measured and the mass flow rate is constant, numerical simulations of these kind of microreactors are possible [129, 202, 204]. It has been shown, both experimentally and numerically that such resistively heated flow tubes have a non-uniform temperature and pressure distribution which strongly depends on the dilution gas used [202, 203, 329]. Recent studies with similar microreactors state that using helium as carrier gas instead of argon not only yields better signal intensities and therefore smaller averaging times but also a more plug-flow like flow field in the microreactor, which is beneficial for the interpretation of chemical kinetics. These benefits will most likely maximize the detection of short-living intermediates upon thermal decomposition of $Zr(acac)_4$ in the microreactor [202, 203]. Since the geometries and the experimental conditions such as pressure and temperature examined by previous studies differ from ours, we decided to conduct a computational fluid dynamics (CFD) study using ANSYS Fluent 19.1 [264] with both helium and argon as dilution gas. Since the precursor is highly diluted, its contribution is negligible for the flow field calculations, and the simulations were performed with pure argon and helium, respectively.

Previous studies on flow fields in microreactors [129, 202, 203, 204] have also demonstrated that the gas velocity strongly accelerates up to the sonic condition near the outlet of the reactor. Therefore, the flow in the microreactor should be modeled with the slip regime corresponding to the range of the Knudsen number ($0.01 \leq Kn \leq 0.1$). In the present study, we solved the Navier–Stokes equations combined with a slip (boundary) condition at the wall, in order to account for these effects and accurately model the flow in the slip region. Because the microreactor was directly connected to a high vacuum chamber, the compressibility of the flow was taken into account in the simulation. The viscosity and thermal conductivity of the dilution gases were implemented with the parameters introduced by Bich et al. [267]. The numerical domain was set up as an axisymmetric two-dimensional geometry and resolved by roughly 106 cells and a respective cell size of 10 µm, leading to approximately 300 cpu core hours per simulation case. Further details on the numerical domain and all relevant equations and boundary conditions (see

Fig. 5.9) used in this study are summarized in Sec. B.1 of Appendix B.

Chapter 6

Mechanism and Kinetics of the Thermal Decomposition of $Fe(C_5H_5)_2$ in Inert and Reductive Atmosphere: A Synchrotron-Assisted Investigation in a Microreactor

The content of the following chapter was initially published in *Advanced Materials Interfaces*, **9**(22), 2200192, (2022) by S. Grimm, P. Hemberger, T. Kasper and B. Atakan entitled "Mechanism and Kinetics of the Thermal Decomposition of $Fe(C_5H_5)_2$ in Inert and Reductive Atmosphere: A Synchrotron-Assisted Investigation in A Microreactor".

The article is reprinted, applying minor formal changes to adhere to the style and structure of this thesis, with permission from the Wiley, and is available online under the following citation:

DOI: https://doi.org/10.1002/admi.202200192

Contribution Statement

In the course of this publication **I** chose the experimental conditions, set up and performed all the experiments that are presented. I additionally analyzed and evaluated the data from the i^{2}PEPICO experiment, visualized the results and wrote the original draft.

Dr. Patrick Hemberger provided the resources at the Swiss Light Source in Switzerland. He performed the ionization energy calculations and additionally

contributed to the manuscript by review and editing. **Prof. Dr. Tina Kasper** and **Prof. Dr. Burak Atakan** were involved in the conceptual design, acquired the research funding and were responsible for the project administration. Additionally, both contributed to the interpretation of the results. All authors were engaged in the correction and later proof-reading of the manuscript

CRediT (Contributor Roles Taxonomy author statement):

S. Grimm: investigation, formal analysis, visualization, writing – original draft; **P. Hemberger**: investigation, resources, writing – review & editing; **T. Kasper**: conceptualization, methodology, supervision, writing – review & editing, project administration, funding acquisition; **B. Atakan**: conceptualization, methodology, supervision, writing – review & editing, project administration, funding acquisition.

Abstract

The decomposition and reduction of ferrocene, an important precursor for iron chemical vapor deposition and catalyst for nanotube synthesis, is investigated in the gas-phase. Reactive intermediates are detected to understand the underlying chemistry by using a microreactor coupled to a synchrotron light source. Utilizing soft photoionization coupled with photoelectron-photoion coincidence detection enables us to characterize exclusive intermediates isomer-selectively. A reaction mechanism for the ferrocene decomposition is proposed, which proceeds as a two-step process. Initially, the molecule decomposes in a homogeneous surface reaction at temperatures <900 K, leading to products such as cyclopentadiene and cyclopentadienyl radicals that are immediately released to the gas-phase. At higher temperatures, ferrocene rapidly decomposes in the gas-phase, losing two cyclopentadienyl radicals in conjunction with iron. The addition of hydrogen to the reaction mixture reduces the decomposition temperature, and changes the branching ratio of the products. This change is mainly attributed to the H-addition of cyclopentadienyl radicals on the surface, which leads to a release of cyclopentadiene into the gas-phase. On the surface, ligand fragments may also undergo a series of catalytic H-losses leading most probably to a high carbon content in the film. Finally, Arrhenius parameters for both global reactions are presented.

6.1 Introduction

Since its discovery in the 1950s [330, 331] the metallocene ferrocene, $Fe(Cp)_2$ is, due to its remarkable stability [332], an extensively studied compound [333]. It is a classical sandwich complex, where two cyclopentadienyl ligands are attached to a central iron core. Ferrocene is characterized by a relatively high vapor pressure at moderate temperatures, it is nontoxic and stable in air and therefore an easy to handle precursor for the synthesis of functional materials [230]. In particular, the use of ferrocene has been successfully established in the preparation of iron-containing thin films for optoelectronic devices [114, 334] or iron thin films in an oxidative atmosphere in metallurgical applications [111]. Upon thermal decomposition of $Fe(Cp)_2$, iron nanoparticles can be formed which may subsequently act as functional nanomaterials for energy conversion and storage systems [335, 336]. Those nanoparticles have additionally shown excellent performance and emission characteristics in biodiesel engines [337, 338] and as a burning catalyst in rocket propellants [339], since hydrocarbon radicals, responsible for soot formation, are quenched [337]. Nowadays, ferrocene is among the most widely used precursors in the synthesis of carbon nanotubes (CNTs) [340], either as a feedstock to produce catalytic sites necessary for their growth [117, 341, 342, 343, 344, 345, 346, 347], or as both carbon and catalyst precursor [100, 101, 105, 348].

Functional nanomaterials such as CNTs are often manufactured by high yield, low-temperature methods [340], as for instance by catalytic chemical vapor deposition (CCVD). The underlying synthesis routes and processes were extensively studied experimentally [117, 341, 342, 344, 345, 349, 350] and numerically [112, 116, 351, 352, 353, 354]. It can be concluded that the hydrocarbon source has a major influence on the morphology, crystallinity, and growth kinetics of CNTs, mediated through its gas-phase decomposition products pertaining to its initial structure [102], as well as the catalyst activity. The control of product quality requires understanding the gas-phase decomposition mechanism of ferrocene at various reaction conditions. The intermediates act either as a promoter of CNT growth by serving as carbon feedstock or as a detrimental impurity, lowering the growth rate by forming unwanted volatile and polyaromatic hydrocarbons [109, 110], deactivating the iron catalyst particles by forming Fe_3C (cementite), or by carbon incorporation or encapsulation [111].

Consequently, vast research has been conducted on the decomposition products [103, 104, 105] and kinetics [106] experimentally and by molecular dynamic simulations [355]. The latter suggests that the bonds in the ferrocene molecule break above 1073 K sequentially according to their bond strength: C–H>C–C>Fe–C. The formation of cyclopentadienyl radicals (C_5H_5) was observed experimentally by mass spectrometry [103, 106] and infrared laser pyrolysis at a pressure of 4×10^3 Pa [104]. Dyagileva et al. [106] conducted a kinetic study on the pyrolysis of ferrocene in closed glass vessels under vacuum by the manometric method at pressures of 1.3–2.4 $\times$ 10^4 Pa and concluded that the solid decomposition products, namely carbon and iron, catalyze the decomposition by a factor of almost 3000, lowering

the decomposition onset temperature to 823 K. They proposed first-order reaction conditions with a rate constant of $1.6 \times 10^{-5}\,s^{-1}$ at 823 K. Main products formed were H_2, CH_4, C_2H_6 and C_2H_4 in the static system, analyzed by electron ionization mass spectrometry, whereas no radicals or elusive species were observed in a continuous flow reactor. This may be due to the rather long residence times on the order of minutes. Gas-phase iron nanoparticles were also not observed in this study [106]. In a later study, also cyclopentadiene and ethylene (C_2H_4) were detected at temperatures starting from 823 K, which may also originate from reactions catalyzed by chemisorbed iron atoms on the surface, which explains the low decomposition temperature [356]. These studies come to the conclusion that most of the species detected are either formed in the secondary decomposition of cyclopentadiene (C_5H_6) to methane and hydrogen, or in catalytic reactions on the wall [106]. Ensuring homogeneous conditions by infrared laser pyrolysis, Russell et al. [104] studied the gas-phase pyrolysis of ferrocene and observed C_5H_6, C_5H_5, and naphthalene ($C_{10}H_8$) among the decomposition products and proposed reaction schemes for their formation. Nevertheless, those products are partially secondary products and owing to the detection method used, no short-lived iron species could be detected either, rendering the decomposition mechanism to be still elusive [104].

In earlier investigations, it was observed that adding hydrogen to the carrier gas stream has a beneficial outcome regarding catalyst lifetime because H_2 acts as a reductive agent [112, 113], and allows control of the amount of desired carbon product formed [357]. Hydrogen is also reported to lead to a significantly lower decomposition temperature of ferrocene [114, 115, 116].

Recently, we demonstrated that vacuum ultraviolet (VUV) synchrotron radiation coupled with a vacuum flash-pyrolysis microreactor and photoelectron photoion coincidence (i^{2}PEPICO) [253] detection can be used to unravel the gas-phase decomposition of CVD precursors [129]. Thanks to the tunability of the photon energy together with velocity map imaging (VMI), we were able to distinguish fragmentation and direct ionization and thus identify important organometallic and organic reactive intermediates isomer-selectively to elucidate the underlying chemistry. Here, we report a detailed VUV i^{2}PEPICO study for the *in-situ* detection of gas-phase radicals and molecular iron during pyrolysis of $Fe(C_5H_5)_2$ at conditions relevant to CCVD and CNT growth. To investigate the influence of hydrogen on the reaction mechanism of $Fe(C_5H_5)_2$, 10% H_2 was added to the mixture before entering the reaction zone. Our results provide direct experimental evidence for the initial steps of the $Fe(C_5H_5)_2$ decomposition through a detailed analysis of the gas-phase composition. It can be used to improve simulation efforts of CNT as well as thin film growth and hence contribute to a more efficient material synthesis.

6.2 Results and Discussion

A pyrolysis microreactor coupled to a molecular beam source, where reactive species are not quenched, is attached to a photoelectron-photoion coincidence spectrometer.

Intermediates and products are detected by mass spectrometry and mass-selective threshold photoelectron spectra (ms-TPES). Furthermore, dissociative photoionization (DPI) is distinguished from direct ionization of reactive species, which allows to extract unimolecular decomposition pathways of ferrocene in an inert as well as in hydrogen atmosphere. Finally, we investigate the reaction kinetics in terms of activation energy and rate coefficients for the global reactions observed in the experiment, based on a numerical simulation of the flow field.

6.2.1 Dissociative Photoionization of Ferrocene: Does $Fe(C_5H_5)^+$ (m/z 121) Form in the Gas-Phase?

As outlined in the introduction, many published reaction schemes propose the formation of $Fe(C_5H_5)$ as an initial product in the gas-phase, whereas none of these studies detected the molecule experimentally. A possible reason could be that, experimental limitations or fragmentation interfered with the results. Since our system is capable of detecting elusive species, as for instance $Fe(C_5H_5)$, its detection appears feasible [129, 358].

When dealing with the detection of reactive radicals in ionization processes, fragment ions from DPI of the precursor need to be distinguished from direct ionization of the radical in the hot reactor. Considering the DPI mechanism, it is known [359] that ferrocene (m/z 186) loses a cyclopentadienyl radial (C_5H_5) according to:

$$Fe(C_5H_5)_2 + h\nu \longrightarrow Fe(C_5H_5)^+ + C_5H_5 + e^-. \qquad \text{(R 6.1)}$$

The literature offers a wide range of bond dissociation energies (BDE) of $Fe(C_5H_5)_2$ either experimentally, or by quantum chemistry that ranges from 2.6 to 6.7 eV [359, 360, 361, 362, 363]. This wide range of reported BDEs is largely attributed to the deficiencies in the methods used to extract those energies [363]. The calculated values range from 3.67 eV (B3LYP) to 4.86 eV (BP86), depending on the basis set used, whereas it has been stated that the first one systematically underestimates and the latter one overestimates experimental values and can therefore be considered as a numerical upper limit to the BDE [363]. In terms of the experimental determination of the appearance energy of $Fe(C_5H_5)^+$ in this work, the BDE reported by Opitz and Härtner of 4.61 ± 0.43 eV [360] using electron-ionization mass spectrometry and the most recent value obtained by threshold collision-induced photodissociation mass spectrometry of 4.26 ± 0.15 eV [363], which additionally considers the kinetic shift that is usually observed in gas samples from hot sources, such as from our microreactor, are comparable to the method used in the approach here.

In order to understand the influence of dissociative ionization in our process using i^{2}PEPICO, we heated up the reactor to 1079 K and followed the m/z 121 signal as a function of the photon energy. The obtained threshold photoelectron spectrum (ms-TPES) and the photoion efficiency curve (PIE) of m/z 121 are depicted in Fig. 6.1 (a). We clearly observe an increase in the relative intensity

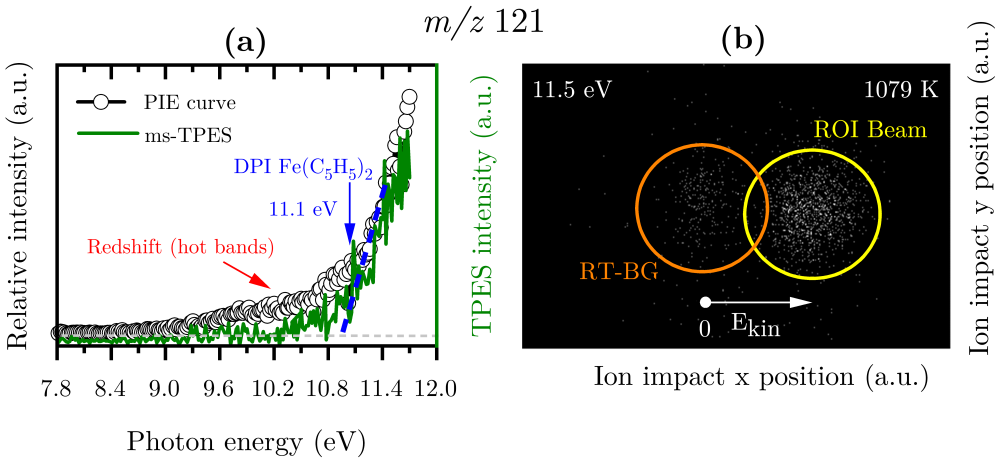

Figure 6.1: (a) Experimental PIE curve (black curve, dots) and mass-selected threshold photoelectron spectrum (ms-TPES) (green curve) of m/z 121 at 1079 K. The contribution of thermal energy to the internal energy of the ion leads to a red shift in ionization energy to lower values (red label); the appearance energy of $Fe(C_5H_5)^+$ has been determined by a linear fit to be 11.1 eV (blue curve). (b) Ion momentum image (VMI) of m/z 121 at 1079 K, which shows the kinetic energy distribution of the ions that reach the ion detector. A part of the excess energy of photoionization is released as kinetic energy, which results in a broad velocity distribution of the room-temperature background ("RT-BG", orange) and the beam component ("ROI Beam", yellow). The number of ions detected increase from black to white. Using those images enables us to distinguish between direct and dissociative photoionization of the neutral molecule. For comparison, a focused molecular beam of direct ionization is shown in Fig. C.1, of the Appendix C.

of the signal at 10.8 eV, but find some signal already at around 9.2 eV. Ionization energy calculations at different levels of theory for the $Fe(C_5H_5)$ find values of 6.45 (B3LYP/6-311+G++(d,p)), 6.66 (ωB987xd/6-311+G++(d,p)) and 6.13 eV (M06L/6-311+G++(d,p)), respectively, which are much lower than the observed ionization onset. The signal increase at 9.2 eV in the PIE/ms-TPES can thus not be rationalized with direct ionization, as we would expect to see a signal above zero already when the calculated ionization energy is reached.

Instead, the reason for the signal increase at lower photon energy is attributed to dissociative ionization [272]. The hot pyrolysis microreactor can shift the onset of the dissociative ionization to 2–3 eV below the 0 K onset, as the neutrals' internal energy is transferred to the cations surface and leads to a fragmentation to $Fe(C_5H_5)^+$, as observed in Fig. 6.1 (a) (green curve). This temperature-dependent red-shift was observed in the literature before, using similar reactors and was recently evaluated in detail [224, 272, 364]. While this fact leads to the appearance of the signal already at 9.2 eV, the majority of the ferrocene fragments appear only above 11.1 eV, which is shown by fitting a line to the linear increase of the signal. When adding the literature bond dissociation energy of the cation $(Fe(C_5H_5)_2{}^+ \longrightarrow Fe(C_5H_5)^+ + C_5H_5)$ to the reported ionization threshold of ferrocene at 6.9 eV [365], the appearance energy of the major fragment, $Fe(C_5H_5)^+$ from ferrocene can be calculated to be 11.51 $\pm$ 0.43 eV (BDE: 4.61 $\pm$ 0.43 eV), using the values of Opitz and Härtner [360], or

from Rowland et al. (11.16 ± 0.15 eV), which agrees slightly better [363]. We have strong evidence that $Fe(C_5H_5)$ is a DPI product, since first, we find an asymmetric peak shape of the time-of-flight (ToF) distribution in the mass spectra, caused by a slow unimolecular dissociation, which takes place upon acceleration of the ion in the mass spectrometer and was also observed for the peak at m/z 121 [361]. Second, thanks to VMI, fragmentation can be clearly distinguished from direct ionization. While a directly ionized sample in a molecular beam shows a narrow velocity distribution along the molecular beam expansion direction (see Fig. C.1, Appendix C), a fragment from dissociative ionization possesses a perpendicular contribution to the molecular beam direction, due to the release of kinetic energy as presented in Fig. 6.1 (b) [122, 366].

Due to the above mentioned analysis, we conclude that the signal of $Fe(C_5H_5)$ is purely caused by dissociative rather than direct ionization. As a consequence, we cannot confirm the gas-phase formation of this species, which contradicts the literature mechanisms, which propose $Fe(C_5H_5)$ to be the major initial decomposition product in the gas-phase [104, 105, 354]. However, we cannot exclude that $Fe(C_5H_5)$ is formed and decomposes further or immediately adsorbs on the reactor wall, where it reacts at higher temperatures due to homogeneous or heterogeneous surface reactions. This possibility will be discussed later in this manuscript.

6.2.2 Photoionization Mass Spectra

After we successfully distinguished signals associated with dissociative from direct ionization of pyrolysis products, only product signals that emanate from pyrolysis are discussed in the following. Photoionization mass spectra were recorded and evaluated at fixed photon energies of 9.0, 10.5, and 11.5 eV over a temperature range of 333–1250 K. Figure 6.2 illustrates mass spectra of the pyrolysis products at fixed photon energies of 9.0, and 11.5 eV with and without (top trace) pyrolysis.

When the SiC reactor is heated, we clearly see a depletion of the precursor's ion signal at m/z 186. Product peaks at m/z 65, 66, 80, and 128 are observed in the mass spectra at temperatures above 781 K (Fig. 6.2 (a)), which is a slightly lower temperature threshold than reported in the literature, where under catalytic conditions, the ferrocene decomposition already starts at 673 K [106, 356], but our value is way below the one reported for the low-pressure pyrolysis, where no decomposition was observed in the gas-phase up to 1178 K [48]. These peaks grow in intensity when the temperature is further increased up to 1087 K, together with a decline of the m/z 186 parent ion signal, which fits the latter temperature onset. The first iron-containing signal at m/z 56 is detected at temperatures >1087 K. Additionally, some new product peaks arise in the spectrum at m/z 39, 52, and 64, which are most likely secondary decomposition products of the initially observed hydrocarbons at lower temperatures. To assess the product species with lower masses or larger ionization energy onsets, mass spectra at higher photon energies were recorded (Fig. 6.2 (b)). At temperatures above 1200 K, several peaks appear at m/z ratio <70, while the primary decomposition product signal at m/z 65

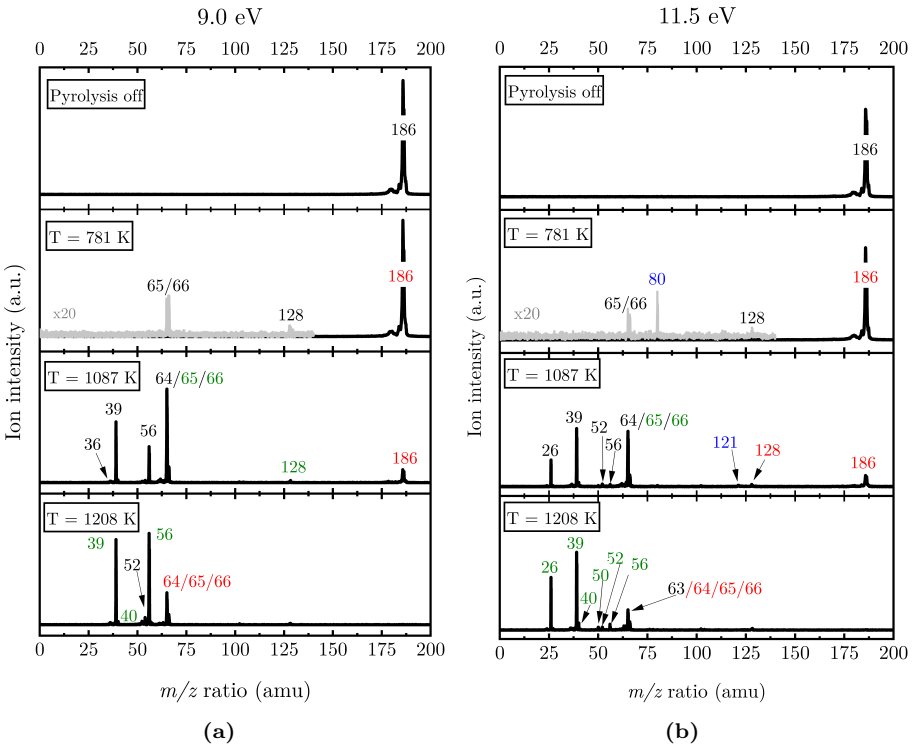

Figure 6.2: Temperature-dependent mass spectra of $Fe(C_5H_5)_2$ pyrolysis were recorded at a photon energy of 9.0 (a) and 11.5 eV (b) and an inlet mole fraction of 8.2×10^{-4} (0.08%). The major peaks are assigned by their m/z ratio and with respect to their absolute decay (red) or increase (green) in comparison to the previous spectrum at lower decomposition temperatures. Species that emerge for the first time are marked in black color, whereas the blue numbers indicate that the species are due to dissociative ionization or impurities. For better comparison, the gray spectra are multiplied by a factor of 20.

decreases markedly. In addition to the previously noticed peaks in the literature [48, 104, 106], our mass spectra show evidence of species with m/z 26, 39, 40, and 52 upon depletion of the primary decomposition product m/z 65, whose origin will be clarified in the next section.

The peak at m/z 80 is assigned to cyclopentadienone (see Fig. 6.2), which may result from traces of oxygen in the reaction mixtures. Because no oxygen flow was intentionally added in our experiments, it is considered an impurity, as will be discussed briefly in the Fig. C.2, in Appendix C.

6.2.3 Identification of Elusive Species

Photoion mass-selected threshold photoelectron spectroscopy (ms-TPES) is an indispensable tool for the isomer-selective detection of reactive species in pyrolysis, combustion, and catalysis, if experimental data is compared to literature or Franck–Condon simulated spectra [122, 153]. To understand the underlying chemistry of $Fe(C_5H_5)_2$ pyrolysis we plotted a threshold photoionization matrix

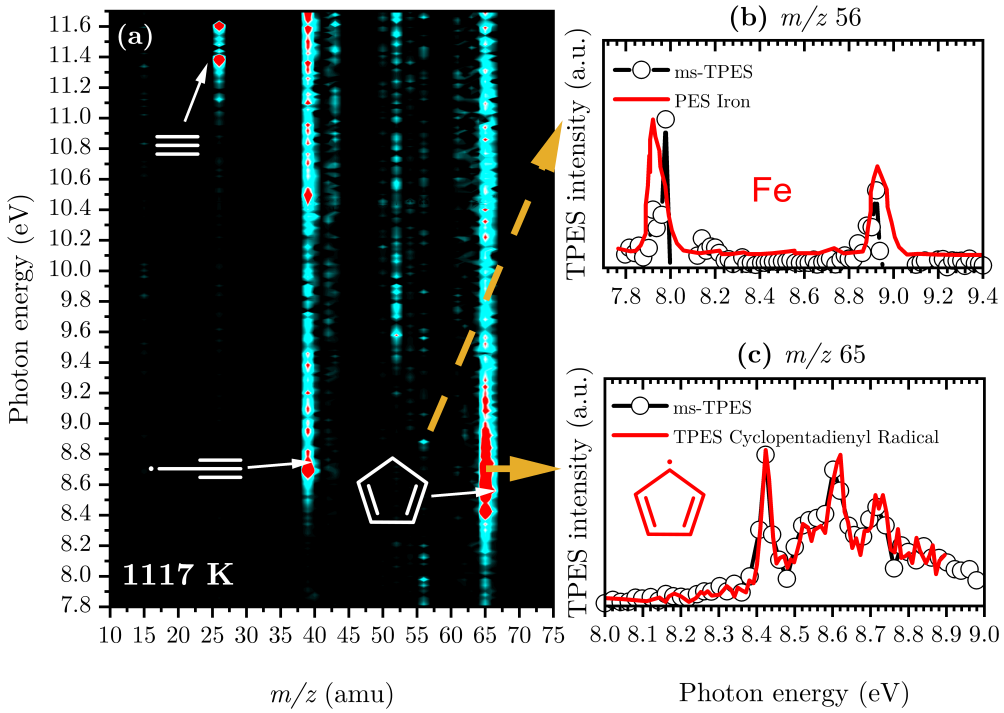

Figure 6.3: (a) Threshold photoionization matrix (TPM) for the identification of the major decomposition products at 1117 K. The subgraphs are representative vertical samples from the TPM at (b) m/z 56 and (c) m/z 65. Iron [367] and the cyclopentadienyl radical [368] were unambiguously identified by literature reference spectra (red). Other than that, additional identified products (acetylene, propargyl radical, cyclopentadiene) are denoted by their chemical structure in white and their characterization is further discussed in the text.

(TPM) at a reactor temperature of 1117 K, as partially shown in Fig. 6.3 (a) [271]. In this presentation, our multidimensional data set is reduced to a photon energy and mass spectrometric axis, while the threshold photoelectron signal intensities correspond to a change in color from light blue to red. By analyzing this illustration, the mass channels, where the main pyrolysis products reside, can be identified. If we extract the data along a vertical line for a given mass ms-TPES can be derived and it is possible to characterize the major pyrolysis species for each m/z ratio. The ms-TPES of the most abundant species are shown in subfigures (b), (c), and in Fig. 6.4.

We can clearly identify strong signals at m/z 26, 39, 56, 65, 66. Up till now, the coexistence of Fe and C_5H_5 as the most abundant products upon pyrolysis was hypothesized [48]. Clear onsets at 7.98 and 8.88 eV in the ms-TPES of m/z 56, which corresponds to the published $^6D \leftarrow ^5D$ and $^4D \leftarrow ^5D$ transition of iron at 7.90 and 8.89 eV [367], see Fig. 6.3 (b), confirm the formation of Fe atoms during the pyrolysis of ferrocene. The analysis of the spectrum in Fig. 6.3 (c) additionally shows that the cyclopentadienyl radical is the most abundant pyrolysis product which contributes to the m/z 65 signal (IE = 8.42 eV) [368]. The onset of the ms-TPE spectrum of

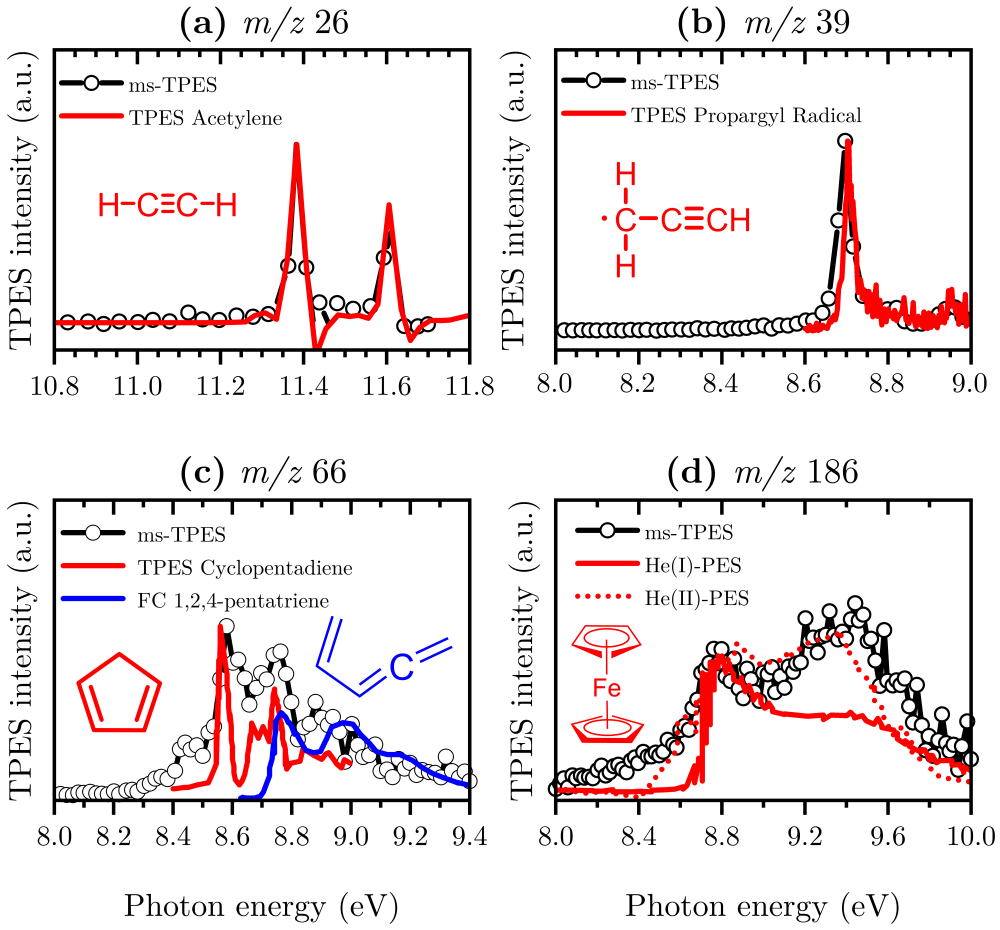

Figure 6.4: Representative examples of species identification and assignment of major species using experimental obtained ms-TPES (black dots and lines) at 1117 K; species are either characterized by literature reference spectra (red), or by computed spectra (blue) in (a)-(d). References are as follows: (a) m/z 26 acetylene (C_2H_2) [156], (b) m/z 39 propargyl radical (C_3H_3) [277], (c) m/z 66 c-C_5H_6 [290] and 1,2,4-pentatriene [291], (d) m/z 186 ferrocene ($Fe(C_5H_5)_2$) dotted line: He(I) [365] straight line: He(II) [369].

m/z 26 at 11.39 eV in Fig. 6.4 (a) fits the literature spectrum of acetylene (C_2H_2) (IE = 11.4 eV) [156] well. At 8.7 eV a peak in the ms-TPE spectrum of m/z 39 emerges and can clearly be assigned to the propargyl radical (C_3H_3) with a vertical IE = 8.71 eV [277] (see Fig. 6.4 (b)). The majority of the ms-TPE signal at m/z 66 in Fig. 6.4 (c) matches a strong transition of cyclopentadiene (c-C_5H_6) with an ionization energy of 8.57 eV [290]. Small contributions of the acyclic isomer 1,2,4-pentatriene at 8.70 eV [291] may also be present but are hidden below the band of c-C_5H_6. The small peak at around 8.4 eV can be explained by the ^{13}C isomer contribution (5.7%) of the of C_5H_5 radical (m/z 65) but does not influence our conclusions drawn from Fig. 6.4 (c) since the literature spectrum of cyclopentadiene matches our observed spectrum well. Due to the vibrational progression of the ground state band of cyclopentadiene and the limited signal-to-noise ratio, traces of other isomers with m/z 66 with higher ionization energies are, if present, difficult

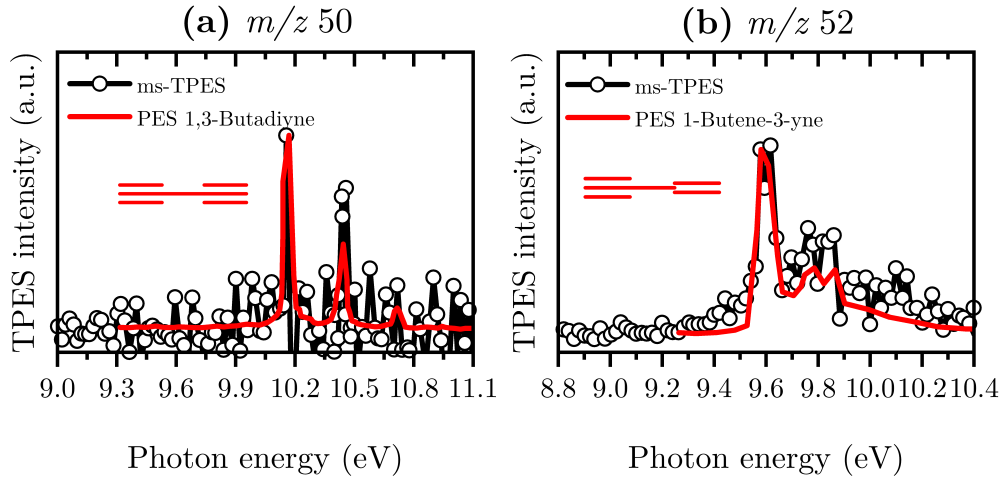

Figure 6.5: Representative examples of species identification and assignment of the minor decomposition products using experimental obtained ms-TPE spectra (black dots and lines) at 1117 K; species are characterized by literature reference spectra (red) in (a) and (b), References are as follows: (a) m/z 50 1,3-butadiyne (C_4H_2) [370], (b) m/z 52 1-butene-3-yne (C_4H_4) [371].

to characterize. In Fig. 6.4 (d) we have also plotted the excited state spectrum of ferrocene between 8 and 10 eV. Note that the ionization energy is 6.9 eV [155]. The steady signal increase is associated with hot bands, while the difference in the He(I) [365] and He(II) [369], especially for the band at 9.3 eV in the literature spectra, stem from the difference in cross-section of ferrocene at the energy used to record them. Nevertheless, the features in Fig. 6.4 (d) can be attributed to ferrocene.

In Fig. 6.5 a collection of the most important minor product species is shown. The ms-TPE spectrum with m/z 50 in Fig. 6.5 (a) fits the literature photoelectron spectrum of 1,3-butadiyne at IE = 10.17 eV [370] well and is solely assigned to this isomer of C_4H_2. The majority of the signal at m/z 52 in panel (Fig. 6.5 (b)) is ascribed to 1-butene-3-yne by a strong band at its IE = 9.58 eV [371]. Besides these assignments, four other products were identified by comparison between the ms-TPES and literature data whenever accessible and are shown in the Appendix C and summarized in Tab. 6.1. Noting that the sample is highly diluted and only small amounts of the minor products were identified, they are not considered in the major thermal decomposition pathways as discussed later in the text.

6.2.4 Pyrolysis Pathways of Ferrocene

The pyrolysis reaction pathways are temperature-dependent so that a measurement of all decomposition products and intermediates at different temperatures is needed to deduce the overall reaction scheme. The temperature-dependent ion signals of the most important intermediates are shown in Fig. 6.6. Based on the unambiguous species assignments in Fig. 6.3, Fig. 6.4, and Fig. 6.5 and mechanistic considerations from the species profiles in Fig. 6.6, we describe the predominant pathways for the

pyrolysis of ferrocene in the temperature range of 333–1200 K (see Scheme 3). The reactions are assigned to Roman numbers which will be used throughout the text to refer to the respective reaction. The colors of the intermediates correspond to the data in Fig. 6.6. Gray species are hypothetical intermediates, which were not detected by the i²PEPICO experiment. The asterisk denotes products which are probably adsorbed on the surface.

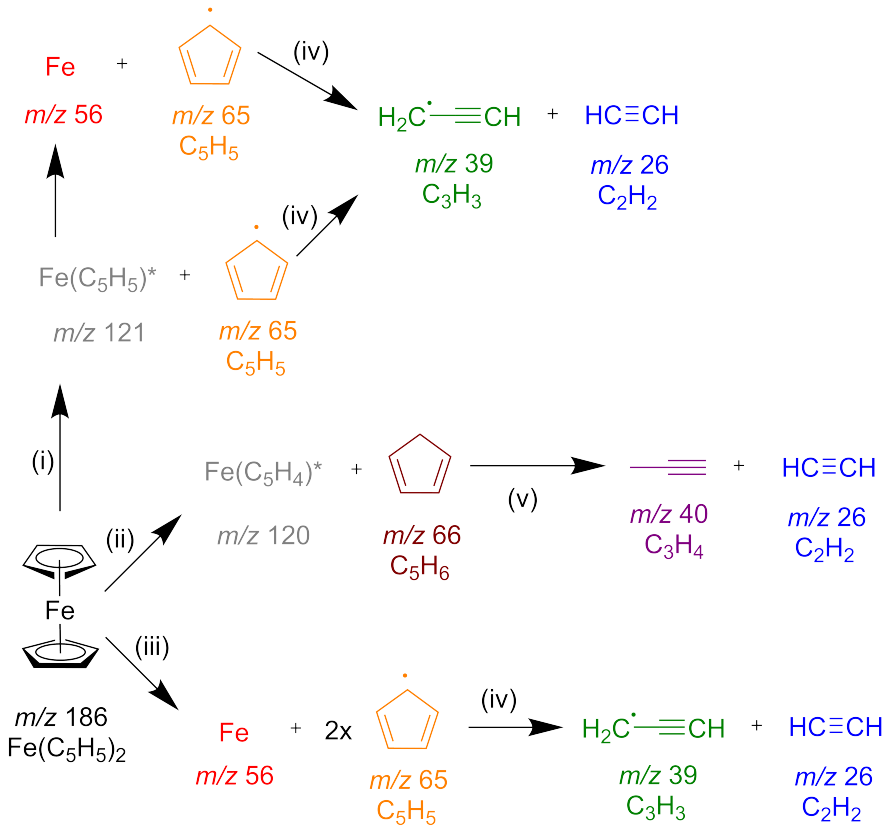

Scheme 3: Schematic reaction mechanism of the decomposition of $Fe(C_5H_5)_2$ in the gas-phase which is rationalized by ms-TPES and temperature-dependent species profiles. The colors of the species in the scheme correspond to their label in Fig. 6.6. Gray species marked by an asterisk are hypothetical intermediates which were not detected in the gas-phase by the i²PEPICO experiment.

Ferrocene already starts to decompose at 600 K but only above 900 K iron and hydrocarbon intermediates appear in significant amounts in the gas-phase. Consequently, three regimes can be distinguished in this experiment, for T<600 K no reaction is observed, for T = 600–900 K ferrocene decomposition is initiated, while above 900 K gas-phase intermediates and atomic iron are formed. This behavior was not expected from the literature data which reports ferrocene to decompose in very low-pressure pyrolysis in the gas-phase at around 1100–1200 K [48, 103]. However, the temperature onset of ferrocene decomposition in this study agrees with the onset reported by Dyagileva et al. [106] at around 673 K, initiated by surface-catalysis.

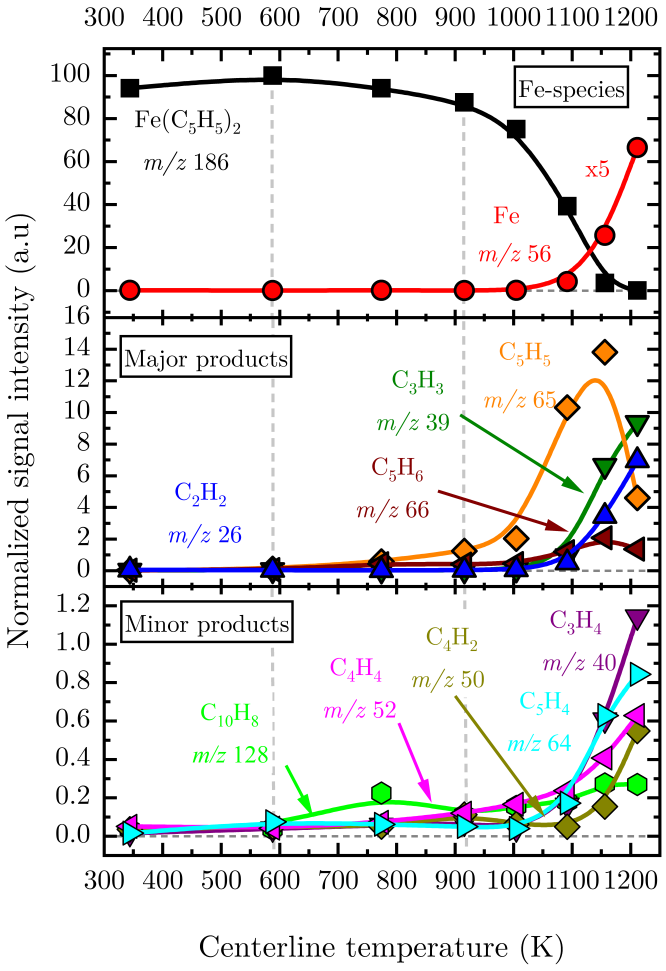

Figure 6.6: Temperature-dependent species profiles of products of thermal decomposition of $Fe(Cp)_2$ at $T_{vap} = 353\,K$ (820 ppm), probed by i^{2}PEPICO vacuum ultraviolet (VUV) mass spectrometry in our microreactor. The respective species that were characterized according to Sec. 6.2.3 are labeled by their formula and all signals are normalized to the initial ferrocene signal.

Since their reactor is operated in batch mode (residence time on the order of minutes), they reported that a considerable number of catalytic Fe-particles are produced which reduced the decomposition temperature in their study. In contrast, in our study the high dilution in argon leads to a low number density of catalytic Fe-particles, which reduces the probability of catalytic surface reactions. Nevertheless, surface reactions cannot be fully ruled out, since we observe a small fraction of ferrocene to be decomposed at a temperature below 900 K.

The species profiles in Fig. 6.6 reveal that for temperatures up to 900 K, $Fe(C_5H_5)_2$ decomposes primarily via the loss of a cyclopentadienyl radical (m/z 65) leaving $Fe(C_5H_5)$ (m/z 121), see Scheme 3 reaction (i). The absence of any $Fe(C_5H_5)$ radicals may be rationalized by the lower bond energy of the second cyclopentadienyl radicals as compared to the first one [372, 373]. Often such fleeting intermediates are difficult to be observed in microreactors, due to very efficient rethermalization and comparable long residence times [259, 368, 374].

We postulate a second pathway of ferrocene decomposition which may yield $Fe(C_5H_4)$ (m/z 120) and C_5H_6 based on the observation of cyclopentadiene in minor amounts below 900 K, whereas major amounts can be observed at temperatures above 900 K (Scheme 3: reaction (ii)). Neither atomic iron, nor other iron-containing intermediates were detected in the gas-phase at temperatures below 900 K. If these species were formed in gas-phase reactions, we expect to be able to detect them based on previous experimental experience [129]. Additionally, previous studies of other investigators by quadrupole mass spectrometry also did not observe their formation at temperatures below 1173 K [105]. It is evident from the findings by Dyagileva et al. [356] that the activation energy for the thermolysis of the Fe−Cp bond on a surface is much lower than in the gas-phase. A similar behavior is observed in our study because a significant amount of Fe is only detected in the gas-phase after heating the reactor above 900 K, although ferrocene already decomposes at lower temperatures.

We suggest that at temperatures <900 K, ferrocene undergoes decomposition on the surface, forming cyclopentadienyl m/z 65 and cyclopentadiene m/z 66, followed by a very fast desorption of these products. The iron-containing species m/z 121 $Fe(C_5H_5)$ and m/z 120 $Fe(C_5H_4)$ remain on the surface of the reactor (see Scheme 3 (i) and (ii)). Alternatively, ferrocene molecules react, e.g., with other ferrocene molecules or iron-containing reaction products from ferrocene on the surface under the liberation of cyclopentadiene which could explain the minor amounts of cyclopentadiene observed at temperatures below 900 K. Previous studies presented evidence that this is a possible pathway for similar π-complexes of transition metals under CVD conditions [104, 375] and that the unstable $Fe(C_5H_5)(C_5H_4)^*$ radical or $Fe(C_5H_4)^*$ decomposes on the surface to form the C_5H_4 species, which are also detected in our study (see Fig. C.3, Appendix C) in trace amounts.

The interpretation that surface reactions occur in the low-temperature regime is further supported by the detection of $C_{10}H_8$ species such as 3-butene-1-ynylbenzene at m/z 128, while the naphthalene contributions were negligible (see Fig. C.3, Appendix C). This was also suggested by Pan et al. for the reaction of cyclopentadiene

over a H-ZSM 5 catalyst, previously [376]. Additionally, the low number density of C_5H_5 radicals in the sample precludes the recombination reaction in the gas-phase [377], as also the dimer $C_{10}H_{10}$ is absent at any reactor temperature which was found to be an intermediate to yield $C_{10}H_8$ species recently [376].

Compared to the low-temperature decomposition pathways of ferrocene the mechanism changes significantly at higher temperatures >900 K (see Fig. 6.6). Following the species profiles in Fig. 6.6 it is evident and commonly accepted in the literature [48] that at T>900 K ferrocene decomposes in the gas-phase leading to the formation of two cyclopentadienyl radicals m/z 65 and atomic iron m/z 56 (Scheme 3: reaction (iii)) [117]. In addition, the formation of cyclopentadiene is enhanced since the amount of C_5H_6 that we found in the gas-phase significantly increases at temperatures >900 K (see Fig. 6.6). A possible explanation for this is that at higher temperatures, either a hydrogenation of the C_5H_5 ligands occurs, leading to the formation of cyclopentadiene, or $Fe(C_5H_4)$ is formed in the gas-phase. The latter immediately adsorbs on the surface which is facilitated by the high temperatures, where we observe high amounts of cyclopentadiene.

Both acetylene (C_2H_2) and the propargyl radicals (C_3H_3) are clearly observed in the ms-TPES at temperatures above 1117 K (Fig. 6.4 (a), (b)). The decrease in the m/z 65 signal intensity and a simultaneous increase of m/z 26 and 39 explains that these organic products are formed in secondary reactions in the gas-phase (Scheme 3: reaction (iv)). Likewise, it has been reported that cyclopentadiene, with m/z 66, decomposes to form propyne (m/z 40) and acetylene (m/z 26) (Scheme 3: reaction (v)) [378] which were identified by their characteristic fingerprints utilizing ms-TPES. Other experiments [104, 111] revealed that the pyrolysis of ferrocene at high temperatures yields cementite (Fe_3C) and iron surrounded by graphite layers (FeC). Given these observations, the formation of FeC or Fe_3C is expected in the microreactor by further decomposition of ligand fragments on the surface which is supported by the existence of a black residuum in our reactor after the experiments. Additionally, the presence of acetylene in the gas-phase accelerates the formation of carbon-coated iron nanoparticles or carbon nanotubes [117, 348] at particle forming conditions [354]. However, the characterization of this residuum and the adsorbed ligand fragments as $Fe(C_5H_4)^*$ requires advanced surface characterization techniques as well as an optically accessible microreactor and is therefore beyond the scope of this study.

6.2.5 Influence of H_2 Addition

In comparison to the pyrolysis of pure ferrocene, higher signals for the masses m/z 26, 42, 43, and 44 were detected at temperatures below 1000 K if hydrogen is added to the reaction mixture (see Fig. 6.7 (a)). We were able to identify the latter three signals as C_3 hydrocarbons according to their ionization onsets in the literature in comparison to our recorded threshold photoelectron spectra or PIE curves. The shape of the ms-TPES in Fig. 6.7 (a) is in agreement with the photoelectron spectrum of propene (C_3H_6) with a vertical ionization energy of

Table 6.1: List of identified species upon pyrolysis of $Fe(C_5H_5)_2$ and the reduction with H_2 (marked with an asterisk) by VUV i^{2}PEPICO using their adiabatic and vertical ionization energies. Reference spectra and energies have been taken from the literature and are denoted at the respective value. The identification of the compounds in bold are discussed further in the paper.

m/z	Formula	Name	IE (eV) References
15	CH_3	Methyl radical	9.84 [273]
26	**C_2H_2**	**Acetylene**	11.40 [156]
39	**C_3H_3**	**Propargyl radical**	8.71 [277]
40	C_3H_4	Allene	9.69 [379]
		Propyne	10.38 [279]
42*	**C_3H_6**	**Propene**	9.73 [284]
43*	**C_3H_7**	**i-Propyl radical$^+$**	–
		n-Propyl radical$^+$	–
44*	**C_3H_8**	**Propane**	10.90 [284]
50	**C_4H_2**	**1,3-Butadiyne**	10.17 [370]
52	**C_4H_4**	**1-Buten-3-yne**	9.58 [371]
54*	C_4H_6	1,3-Butadiene	9.07 [380]
		2-Butyne	9.59 [285]
		1-Butyne	10.18 [155]
56	Fe	**Atomic iron ^{6}D←^{5}D; ^{4}D←^{5}D**	7.90; 8.89 [367]
64	**C_5H_4**	**Ethynylallene**	9.22 [287]
		1,3-Pentadiyne	9.50 [288]
65	**C_5H_5**	**Cyclopentadienyl radical**	8.41 [368]
66	**C_5H_6**	**1,3-Cyclopentadiene**	9.58 [290]
		1,2,4-Pentatriene	8.70 [291]
80	C_5H_4O	2,4-Cyclopentadiene-1-one (impurity), see Fig. C.2, Appendix C	9.42 [381]
128	$C_{10}H_8$	1-Butene-3-ynylbenzene	8.53 [376]
		3-Butene-1-ynylbenzene	8.74 [376]
186	**$Fe(C_5H_5)_2$**	**Ferrocene; excited state band**	6.90, (8.4–8.7) [365]

9.73 eV [284]. Based on the ionization onset at 10.9 eV, we assign the signal at *m/z* 44 to propane [284], and also VMI images at low temperatures show that this species is detected by direct ionization. Unfortunately, we did not record spectra at photon energies higher than 11 eV which would give a much clearer identification of this species being the most abundant one at temperatures of 600–900 K (see Fig. 6.8 (a)). The identity of *m/z* 43 is not determined here because we did not record ms-TPES at such low temperatures, where the formation of *m/z* 43 can be observed. At a higher temperature the dehydrogenation to propene dominates. Yet, we tentatively assign this species to C_3H_7 according to a possible H-abstraction reaction of *m/z* 44 at temperatures higher than 600 K [382] which is rationalized in the species profile on the lower part of Fig. 6.8. Given the ionization energies of 8.42 eV and 8.67 eV for c-C_5H_4 [287], it is tempting to assign the signal to the cyclopentadienylidene carbenes, however, the peaks coincide with transitions of the cyclopentadienyl radical. Due to the large abundance of the cyclopentadienyl radical

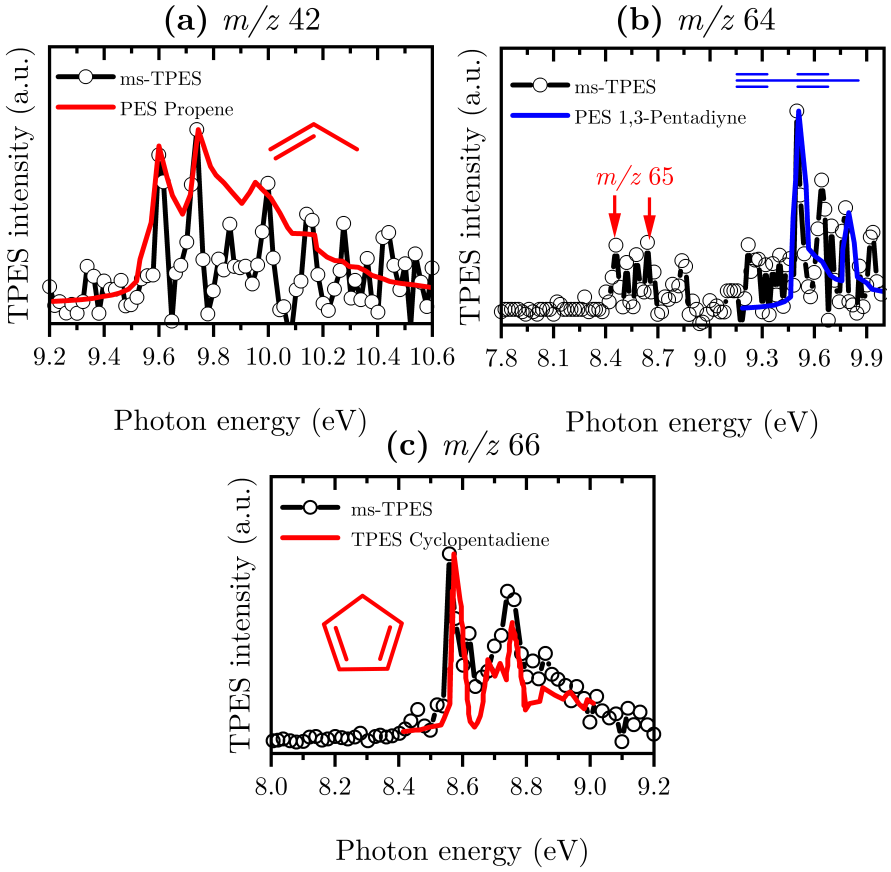

Figure 6.7: Representative examples of species identification and assignment of important decomposition products after adding 10% H_2 to the carrier gas flow, using experimentally obtained ms-TPE spectra (black dots and lines) recorded at 1079 K (a)-(c). The species are characterized by literature reference spectra (colored). References are as follows: (a) m/z 42 C_3H_6 (propene) [284], (b) m/z 64 red: contribution from c-C_5H_5 (see main text for further explanation), blue: 1,3-pentadiyne [287], (c) m/z 66 c-C_5H_6 (cyclopentadiene) [290].

(C_5H_5, m/z 65) a small neighboring signal interference cannot fully be avoided. This is also a result of mass separation observed in the ms-TPES. We can however also find small contributions of the acyclic isomer 1,3-pentadiyne represented by its onset at 9.50 eV [288]. The abundances in the ms-TPES of the channel m/z 64 do change as compared to pure pyrolysis but the signal is still assigned to the same product, 1,3-pentadiyne (see Fig. C.3 in Appendix C). We observe a change in the mechanism here since the signal of m/z 66 significantly increases in the presence of hydrogen. We checked this mass for additional isomers but found exclusively cyclopentadiene, as can be seen in Fig. 6.7 (c).

It is evident from the data in Fig. 6.8 (a) and (b) that the addition of H_2 leads to a decomposition of ferrocene at lower temperatures as compared to our measurements in argon (see Fig. 6.6) and more hydrocarbon intermediates are observed. The decomposition temperature is shifted under these experimental

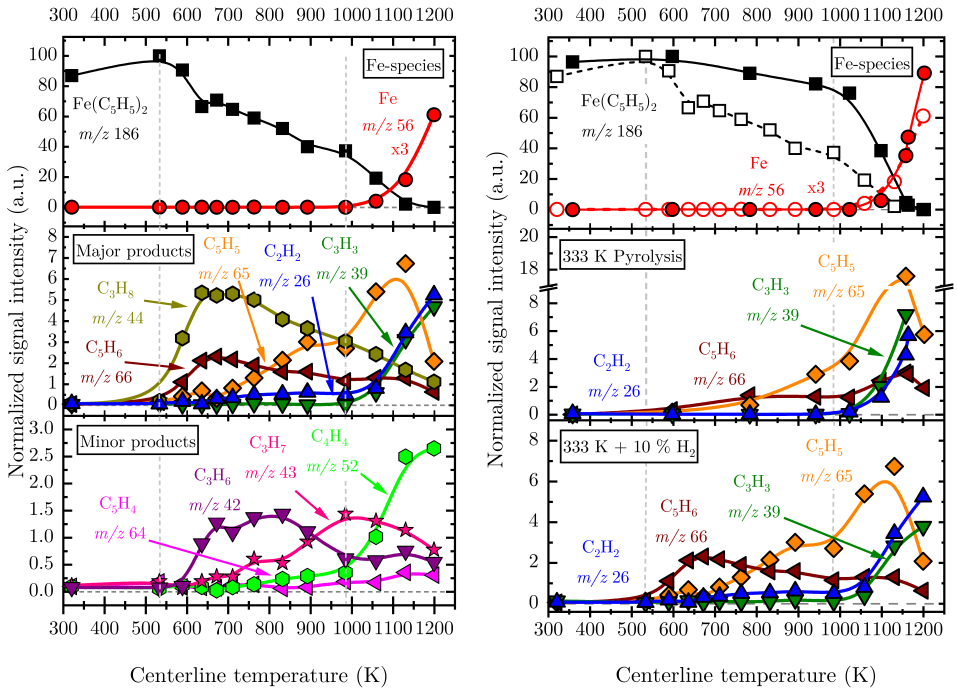

Figure 6.8: (a) Temperature-dependent species profiles of the most important intermediates and products observed during the reduction of 158 ppm ferrocene (T_{vap} = 333 K) with 10% hydrogen. (b) Top trace: Comparison of the ion signal intensities with a temperature of the iron species upon pyrolysis (filled symbols, straight lines) and the course of decomposition of ferrocene in the reductive atmosphere (open symbols, dashed lines); Middle trace: Major pyrolysis products with an inlet concentration of 158 ppm ferrocene as a function of reactor temperature (Note: The y-axis contains a breakpoint from 8 to 18 in order to ensure comparability with the graph on the bottom trace). Bottom trace: Major species upon addition of 10% H_2. All curves are labeled by their assigned species.

conditions to a lower value of around 550 K in agreement with trends reported in the literature [114]. The exact temperature of the onset depends on the different reactor geometries and experimental conditions applied in both studies but the general trend remains the same. Numerical simulations of the deployed microreactor in a previous study [129] revealed that the average temperature is at least 6% higher at the wall than on the centerline of the reactor which may explain the temperature difference between our study and the literature values.

Figure 6.8 (a) shows the temperature-dependent profiles of the intermediates formed during the decomposition of ferrocene in the presence of hydrogen. Below 1000 K the main hydrocarbon intermediates are 1,3-cyclopentadiene (c-C_5H_6), propene (C_3H_6), and propane (C_3H_8) as well as acetylene (C_2H_2), indicating that the underlying decomposition mechanism changes. In contrast to the measurement without H_2 addition, the amount of C_5H_4 is reduced in the high-temperature window. This observation is further rationalized by the steep signal increase of m/z 42, 44, and 65 in Fig. 6.8 (b) starting at around 550 K. Here, direct reactions with

hydrogen explain this behavior of ferrocene and its decomposition products.

The reaction sequence of ferrocene reduction in the temperature window from 550 to 650 K is likely initiated by a subsequent reaction starting from reaction (i) of Scheme 3 in the absence of H_2, which may take place in the gas-phase or on the surface by the following pathway[1]:

$$Fe(C_5H_5)_2 \longrightarrow Fe(C_5H_5)^* + C_5H_5\,, \tag{R 6.2}$$

$$Fe(C_5H_5)^* \longrightarrow Fe(C_5H_5)^*(ads)\,, \tag{R 6.3}$$

$$C_5H_5 + H_2 \longrightarrow C_5H_6 + H\,. \tag{R 6.4}$$

The C_5H_5 ligands are hydrogenated to form C_5H_6, which remains or subsequently desorbs into the gas-phase (Reac. R 6.2). This interpretation is supported by the increase of the C_5H_6 signal in Fig. 6.8 (b) relative to C_5H_5, as compared to the pyrolysis without H_2 (see Fig. 6.6). In addition to the H-radicals formed by reaction (Reac. R 6.4), hydrogen molecules are expected to dissociatively adsorb over iron on the surface of the reactor which leads to a lower dissociation barrier of ferrocene upon hydrogen addition compared to the pure pyrolysis [115].

Previous experimental studies agree that the decomposition of c-C_5H_6 is initiated by C–H bond fission, leading to the formation of the cyclopentadienyl radical [383]. As already discussed in the light of reaction (v) in Scheme 3, cyclopentadiene can additionally isomerize by hydrogen shifts and ring-opening and later breakdown to form C_2H_2 and C_3H_4 at higher temperatures [291, 378]. This is in agreement with the development of the C_2H_2 and C_5H_6 signal at temperatures above 1000 K in the bottom trace of Fig. 6.8 (b). However, these reaction channels do not explain the small acetylene signal below 1000 K, observed in the species profiles upon H_2 addition, in Fig. 6.8 (b) which must have a different origin, though. It has been pointed out that the reduction of similar metallocenes undergoes a competitive reaction mechanism between the hydrogenation of the ligands followed by metal bond cleavage and the decomposition of the ligands on the surface leading to carbon incorporation in the solid films and the formation of particles [384]. It is likely that a similar mechanism takes place here, while hydrogen is present, as proposed by Russell et al. for the pure pyrolysis of ferrocene [104].

A surface hydrogenation followed by desorption of the hydrogenated ligands should be dominant. But we found no evidence for C_5H_x (x = 8, 10) species in the gas-phase which were proposed and observed by others for the hydrogenation of ligand radicals in ferrocene decomposition [102, 114]. Possible reaction products from surface reactions of the postulated hydrogenated species may come from a rapid decomposition of C_5H_8 and C_5H_{10} on the surface or in the gas-phase followed by the formation of the products m/z 26 acetylene (C_2H_2), m/z 42 propene (C_3H_6) and m/z 44 propane (C_3H_8) for n = 1,2 respectively[2]:

[1] Species marked with an asterisk are located on the surface.

[2] Species marked with an asterisk are located on the surface.

$$C_5H_6{}^* + n\,H_2 \longrightarrow C_5H_{6+2n}^*\,, \tag{R 6.5}$$

$$C_5H_{6+2n}^* \longrightarrow C_3H_{8-2n}^* + C_2H_2{}^*\,, \tag{R 6.6}$$

$$C_3H_{10-2n}^* \longrightarrow C_3H_{10-2n}\,, \tag{R 6.7}$$

$$C_2H_2{}^* \longrightarrow C_2H_2\,. \tag{R 6.8}$$

This explains, why we already observed acetylene in the sample in the initial stages of ferrocene decomposition. Since we only observe traces of ligand fragments and significant amounts of hydrogenated ligands we conclude that with the addition of 10% H_2 the hydrogenation reaction of C_5H_5 on the surface is dominant due to active H radicals in comparison to the destruction of the C_5H_5 ligand radicals to smaller hydrocarbons. This should promote the formation of iron films with less carbon content since the destruction of the ligands is necessary for the formation of pure carbon on the surface [104]. Instead, H_2 purges the surface leading to less carbon coverage, and suppressing the formation of FeC and Fe_3C. This will lead to more active catalytic iron sites, which in turn enhances the decomposition of ferrocene by generating H-radicals from the decomposition of ferrocene and a possible contribution of hydrogen to the radical pool as proposed by Luo and coworkers [115].

If compared to the thermal decomposition in argon, significant amounts of C_4 hydrocarbons were also detected. Since the characterization of *m/z* 52 C_4H_4, as 1-buten-3-yne remains the same as in pyrolysis and is formed at higher temperatures, we conclude that this species is considered as a secondary decomposition product of ferrocene fragments. The detection of C_4H_2 can be attributed to either a methyl loss from cyclopentadiene to form C_4H_2 at higher temperatures and also a hydrogen loss of vinylacetylene since we only observe 1,3-butadiene at temperatures higher than 1000 K (see Fig. C.4, Appendix C).

6.2.6 Kinetics of the Thermal Decomposition of Ferrocene

Although the reaction conditions inside a microreactor are difficult to characterize and the pressure and temperature fields are rather complex, various studies, both experimentally [262, 329] and by computational fluid dynamics (CFD) [129, 202, 204] were conducted and demonstrated that kinetic interpretations, to a certain extent, are reasonable. Since the flow field of our microreactor has been investigated numerically by CFD simulations in a previous study [129], we are able to determine the residence time, temperature, and pressure fields more precisely than it could be done using an analytical approach for various experimental boundary conditions. In the temperature window that applies to this study, an average pressure in the reactor of 1500 Pa and residence times between 26 and 44 µs were determined. Considering the extraction of kinetic rate data for microreactor experiments, main takeaway from previous CFD calculations was that most of the precursor conversion occurs

within a specific area at $x = 5$–$8.5\,\mathrm{mm}$ [129, 202]. Here we observe a small variation in both, pressure and temperature, which makes kinetic interpretations of simple unimolecular dissociation reactions, to some extent, possible, as demonstrated before for another organometallic precursors [129].

Although the kinetic parameters such as activation energy E_a and frequency factor A can be pressure-dependent, it should be noted that the pressure drop of about 2200 Pa along the microreactors flow axis mainly influences the frequency factor A that we derive in our kinetic analysis. This is because, assuming the validity of the ideal gas law and considering the reaction order of one, the difference in activation energy is on the order of the experimental uncertainties. Additionally, the influence of the total pressure on A is relatively small, due to the small pressure variation within the sweet spot of the reactor for a first approximation of the kinetic constants

We compared our simple approach to use the average centerline temperature at 8.5 mm with the more sophisticated approach of a volume-weighted temperature in the whole reactor. Simulations show here a deviation of <7% of the centerline temperature at the sweet spot to a volume-weighted temperature for the highest surface temperature of 1273 K which, thanks to CFD, is a more precise approximation of the uncertainty than the one usually claimed in mechanistic studies using microreactors of >10%. We obtained average residence times in our reactor in the same manner, although this approach seems rather simplistic. However, to check its feasibility, we determined the residence time distribution in the microreactor using the flow profile obtained by CFD calculations. We obtained the residence time distribution by seeding 1000 particles in our simulation domain and track their residence time while traveling through the microreactor. The results show that the maximum deviation of the first moment of this distribution (average residence time) differs by 2.6 µs which shows that our simple approach has an uncertainty in the residence time of <10%. In sum, given the uncertainties in temperature, pressure, and residence time, we consider our simple approach to be feasible for extracting kinetic rate data with the stated uncertainty of each parameter. Since especially for the system ferrocene + H_2 limited data is available in the literature, albeit contingent on a few assumptions, our approach is reasonable. Using these insights, we can relate the mole fraction profiles (see Fig. 6.9 (a)) of m/z 186, $Fe(C_5H_5)_2$ to the average centerline temperature of the reactor.

Taking a closer look at Fig. 6.9 (a) and considering the discussion about the reaction mechanism in the previous sections Sec. 6.2.4 and Sec. 6.2.5, we think that the ferrocene decomposition can be divided into two main channels. First, at low temperatures, we observe the surface reaction of ferrocene or its initial decomposition product, probably after adsorption, with first-order kinetics according to:

$$Fe(C_5H_5)_2\,(g) \longrightarrow Fe(C_5H_5)^*\,(ads) + \text{Products}\,. \qquad \text{(R 6.9)}$$

This is responsible for the decrease of the ferrocene mole fraction from ca. 300–950 K in Fig. 6.9 (a). Following the course of the mole fraction profiles, one recognizes a

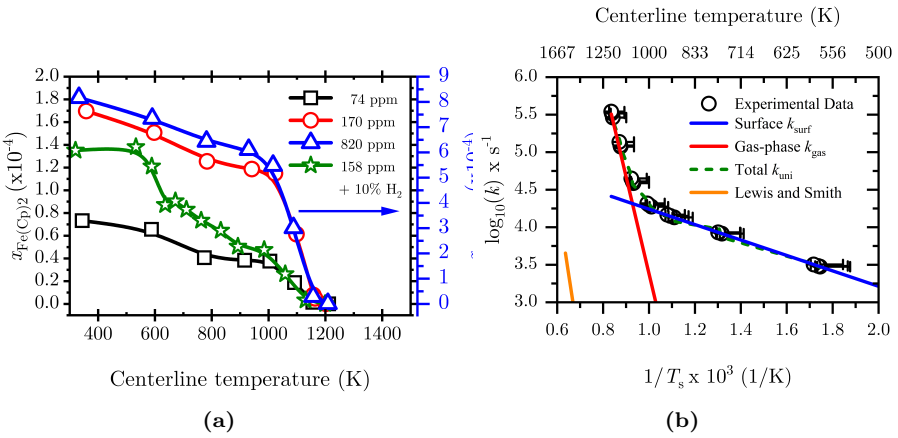

Figure 6.9: (a) Mole fraction profiles of $Fe(C_5H_5)_2$ (b-spline: curve, data: symbols) obtained with the aid of CFD modeling at a computed average pressure of 1500 Pa and residence times from 26 to 44 µs for four initial ferrocene concentrations (74 ppm: black squares; 170 ppm: red circles; 820 ppm: blue triangles; 158 ppm + 10% H_2: green stars). (b) Arrhenius plot (fit: colored curves, data: symbols) derived for the decomposition of $Fe(C_5H_5)_2$ at temperatures from ≈ 300 to 1230 K. The range of activation energy of $Fe(C_5H_5)_2$ decomposition is given next to the plots. The error bars given in the right plot are based on the uncertainty in the determination of the decomposition temperature from surface temperature readings and CFD simulations.

steep decrease in mole fraction between 900 and 1000 K hinting at a change in the dominant decomposition process in this temperature regime. Since we observe the formation of cyclopentadienyl radicals, as well as atomic iron in the gas-phase at these temperatures (see Fig. 6.6), they are formed in the gas-phase according to the following reaction initially proposed by Lewis and Smith [48]:

$$Fe(C_5H_5)_2\,(g) \longrightarrow Fe + 2\,C_5H_5\,. \qquad \text{(R 6.10)}$$

Reasonable Arrhenius plots were derived for the pyrolysis of $Fe(C_5H_5)_2$, with and without 10% H_2 as shown in Fig. 6.9 (b) and Fig. 6.10, respectively. The process of data evaluation is described in Sec. 6.4 in detail. Briefly, the measured mole fractions at different temperatures and reaction times were used to fit the parameters of Eq. 6.5 by the linear least squares method, in order to derive both activation energies and pre-exponential factors. All single fitting results combined with their validities, due to uncertainties of the fit, are summarized in Tab. 6.2. To quantify the goodness of the fit of the activation energy, uncertainties are given next to the respective energies. Additionally, the sum of squared residuals (SSR) of the fits are registered in the last column. It has become apparent that the goodness of the fit is sensitive to the initial ferrocene concentration since the signal intensities that underlie the mole fraction profiles are more concise.

We interpret the data as follows: Adsorption and subsequent surface reactions as Reac. R 6.9 dominate the temperature regime up to 900 K, where the conversion is relatively low. The activation energy in this regime is 19.7 ± 1.4 kJ mol^{-1}. The

Table 6.2: Kinetic parameters for the thermal decomposition on the surface (top) and in the gas-phase (bottom) of $Fe(Cp)_2$ in inert and reductive (10% H_2) atmosphere. Note that the quoted uncertainties are derived from the linear least-squares analysis.

Conditions T_{range} [K]	A_0 [s^{-1}]	E_a [kJ mol^{-1}]	**SSR** [a.u.]
$Fe(C_5H_5)_2$ (g) $\longrightarrow$ $Fe(C_5H_5)$*(ads) + Products			
320–900	$1.9 \pm 0.4 \times 10^5$	19.7 ± 1.4	0.997
650–900 (10% H_2)	$3.0 \pm 0.9 \times 10^5$	17.0 ± 1.8	0.990
$Fe(C_5H_5)_2$ (g) $\longrightarrow$ Fe + 2 C_5H_5			
>900	$2.1 \pm 4.7 \times 10^{16}$	247.6 ± 20.7	0.997
>900 (10% H_2)	$0.2 \pm 1.8 \times 10^{18}$	260.0 ± 107.0	0.990

kinetic parameters estimated by Hirasawa et al. [338] ($A_0 = 1 \times 10^7\,s^{-1}$; $E_a = 12.54\,kJ\,mol^{-1}$) using thermochemistry and quantum chemistry is on the order of our low-temperature activation energy which we attribute to the existence of radicals and loosely bound H-atoms on the surface. Also the pre-exponential factor for the surface reaction is on the order of 10^5 which is in line with the physical understanding that the probability of a molecule to be adsorbed on the surface and react is relatively low in comparison to gas-phase reactions in our microreactor. The Arrhenius plots for the decomposition according to Reac. R 6.10 in the temperature range from 330 to 1230 K are displayed in Fig. 6.9 (b). It should be noted that the temperature regime where atomic iron and cyclopentadienyl radicals were detected as major primary decomposition products is starting at around 900 K (see Sec. 6.2.3). Since at these high temperatures the depletion of $Fe(C_5H_5)_2$ is dominated by gas-phase reactions, we also derived kinetic rate constants for the gas-phase reaction written in the bottom part of Tab. 6.2. Satisfactory fits to the data representing the high-temperature gas-phase reaction lead to an activation energy range of $E_{a,g} = 247.6 \pm 20.7\,kJ\,mol^{-1}$, whereas the pre-exponential factor is determined to be $2.1 \pm 4.7 \times 10^{16}\,s^{-1}$. The value of the pre-exponential factor of approximately 10^{16} is reasonable for high-temperature gas-phase reactions, where collisions of molecules are very frequent. Additionally, others also stated a pre-exponential factor on the same order of magnitude in comparable systems ($2.19 \pm 1.56 \times 10^{16}\,s^{-1}$) [48].

Earlier experimental determinations of the kinetic rate coefficients differ largely from each other due to differences in experimental conditions and techniques to extract them. The reported activation energies range from $171\,kJ\,mol^{-1}$ in surface-catalyzed closed systems probed by electron ionization mass spectrometry (EI-MBMS) at $1.3–2.4 \times 10^4$ Pa [106], over $209\,kJ\,mol^{-1}$ under the impact of radicals in flames at 10^5 Pa [385] to an activation energy of $382\,kJ\,mol^{-1}$ attributed to the gas-phase reaction under very low-pressure pyrolysis (a few hundred Pa) determined by EI-MBMS in a Knudsen cell [48].

In our previous work we discussed the presence of surface reactions which follow, as also valid for other organometallic precursors such as ferrocene, the mechanism of

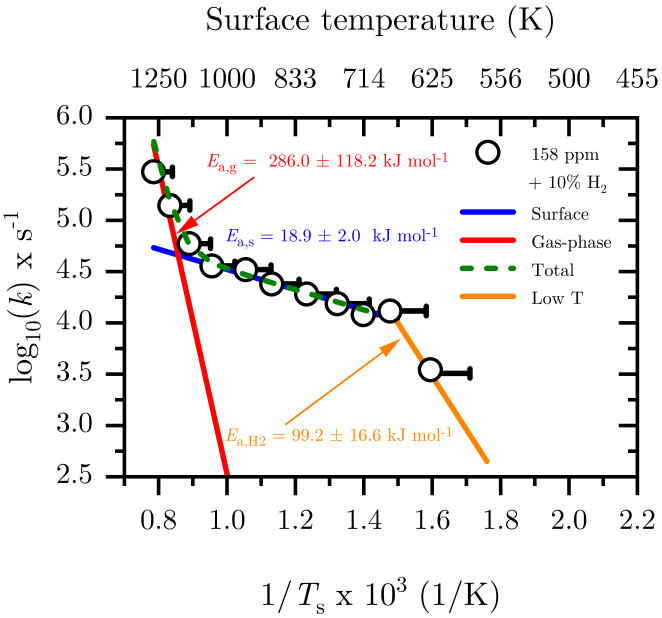

Figure 6.10: Arrhenius plot (fit: colored curves, data: symbols) derived for the decomposition of $Fe(Cp)_2$ adding 10% H_2 at an initial concentration of 1.58×10^{-4} (158 ppm) at temperatures from ≈ 500 to 1250 K. The activation energy for the three reaction regimes are given next to the best fit plot (red: gas-phase, blue: surface, orange: reaction with H_2 on the surface). The influence of H_2 addition does play a large role at lower temperatures shown by the orange plot, where a reaction leads to the formation of C_3-species in the gas-phase (see Sec. 6.2.5).

Langmuir surface-catalyzed kinetics [106]. As discussed in the previous paragraph, the influence of H-radicals emanating from the initial stages of the decomposition of ferrocene, as well as those that are produced surface-catalyzed, explain the range in which the activation energy has been determined. The values obtained in this work are on the order of the ones measured for the radical interaction of 209 kJ mol^{-1} and the 171 kJ mol^{-1} which take the influence of surface-catalyzed kinetics in closed vessels into account. This is especially the case for the decomposition of ferrocene in the presence of hydrogen since H_2 is present in excess and contributes significantly to the H-radical pool in our reactor. In contrast, earlier work by Lewis and Smith quote an activation energy of 382 kJ mol^{-1} which is significantly higher than the value obtained in our study. We attribute this discrepancy to the influence of surface reactions and H-radical formation on the surface as well as bimolecular reactions in the gas-phase of ferrocene with H_2, as in part already suggested by others for metallocenes under the presence of hydrogen [106, 356, 375]. The uncertainty in the temperature determination is also a possible impact factor that let us underestimate the activation energy. The influence of H_2 addition on the kinetics can be seen in the green curve of Fig. 6.9 (a), where the mole fraction of ferrocene in the hydrogen-rich atmosphere exhibits an earlier decrease at around 500 K compared to the pure pyrolysis. As already discussed in the previous paragraph, we attribute this observation to a hydrogenation of the ligands on the surface and a subsequent

desorption of these hydrogenated species. From the Arrhenius plot in Fig. 6.10, we can distinguish between two reaction regimes. First, we obtain a pre-exponential factor of $3.9 \times 10^{14}\,\mathrm{l\,mol^{-1}\,s^{-1}}$ and an activation energy of $88.0 \pm 14.6\,\mathrm{kJ\,mol^{-1}}$ which is valid in the low-temperature regime from 500–625 K. Second, we observe an overlap between a dominant surface reaction according to the one discussed in the previous paragraph (Scheme 3: reaction (i)) and a gas-phase reaction (Scheme 3: reaction (iii)) starting at temperatures >900 K. We derived an activation energy of $17.0 \pm 1.8\,\mathrm{kJ\,mol^{-1}}$ which is similar to the one obtained for pure pyrolysis, hinting that the same reaction is responsible for the consumption of ferrocene at temperatures from 625–900 K. However, one should note that considering the pyrolysis data in the temperature range from 500–900 K, we must consider that there is an overlap between both surface reactions, leading to an additional error in the reaction rate constants obtained in this study. Additionally, it is clear from Fig. 6.10 that our fit overestimates the gas-phase activation energy with a value of $260.0\,\mathrm{kJ\,mol^{-1}}$ compared to the value proposed by Kuwana and Saito [112] of $218\,\mathrm{kJ\,mol^{-1}}$ for the global reaction:

$$\mathrm{Fe(C_5H_5)_2 + H_2 \longrightarrow Fe + 2\,C_5H_6\,.} \qquad \text{(R 6.11)}$$

6.3 Conclusion

Sensitive, selective, and multiplexed i^{2}PEPICO spectroscopy was utilized with VUV synchrotron radiation to investigate the thermal decomposition of ferrocene in a hot microreactor with residence times <50 µs in an inert or hydrogen atmosphere. It was demonstrated that the thermal decomposition under these conditions can be mainly divided in two temperature regimes. At temperatures up to 900 K, surface reactions dominate, while at higher temperatures gas-phase reactions are faster. The first one involves the surface-mediated decomposition and adsorption of ferrocene or fragments as $\mathrm{Fe(C_5H_5)}$ and $\mathrm{Fe(C_5H_4)}$ on the surface which are corroborated by the findings of cyclopentadienyl radicals and cyclopentadiene. The latter one includes the direct formation of atomic iron and cyclopentadienyl radicals in the gas-phase.

We showed that other organic decomposition products could be detected such as *m/z* 26, 39, 50, 52 64, and 128. These were identified as acetylene, the propargyl radical, acyclic isomers of $\mathrm{C_5H_4}$, as well as 1-butene-3-ynylbenzene. The roles of these species in the reaction mechanism have been discussed. In the case of $\mathrm{H_2}$ the reaction mechanism changes significantly such that the decomposition products of ferrocene are either hydrogenated on the surface or directly react with hydrogen to form cyclopentadiene at temperatures <900 K. At higher temperatures, the hydrogenation of ligand in the gas-phase to form cyclopentadiene becomes dominant. In sum, new dissociation channels could be identified from ferrocene which were not fully uncovered in previous studies.

The kinetics of the two main decomposition channels were analyzed at an average pressure of 1500 Pa in the microreactor. Both reactions follow first-order

kinetics with a low activation energy of 19.7 ± 1.4 kJ mol^{-1} for the surface reaction, dominating the decomposition at low temperatures and 247.6 ± 20.7 kJ mol^{-1} for the gas-phase decomposition, dominating the mechanism above 900 K. Upon addition of H_2, the kinetics, as well as the decomposition temperature change. At temperatures between 600 and 700 K, a probably bimolecular reaction of ferrocene with hydrogen is observed in parallel to the above stated ferrocene decomposition mechanism. The kinetics for the reaction with hydrogen were determined to have an activation energy of 88.0 ± 14.6 kJ mol^{-1} at low temperatures. The latter should lead to reduced temperatures in iron CVD with hydrogen addition.

Nevertheless, although there are several deficiencies of the high-temperature microreactor that complicates the interpretation of experimental data, given the circumstances that only limited data is available and that our kinetic parameters are on the order of the ones measured in other systems, we think that our approach marks a good starting point here to exploit microreactor data for kinetic rate measurements of simple unimolecular dissociation reactions. We have shown that our method is very versatile, due to its capability of detecting highly reactive and elusive radicals and can be utilized to investigate the kinetics of CVD precursors.

However, the kinetic studies should be complemented by investigations with traditional mass-spectrometric detection behind larger flow reactors since the temperature profiles are easier to characterize, and the measurement times are less restricted. Since the decomposition of ferrocene is a homogeneous-heterogeneous process, studies to detect and characterize species that are formed on or attached to the surface are absolutely needed in order to explore the fate of reaction products adsorbed on the surface and further develop the proposed decomposition mechanism given in Scheme 3. Hence, a combination of those methods should give an even deeper insight to the reactions of such organometallic precursors used for the synthesis of functional materials, which remain rare so far.

6.4 Experimental Section

6.4.1 Setup

The experiments were conducted at the vacuum ultraviolet (VUV) beamline [145] at the Swiss Light Source (SLS) of the Paul Scherrer Institute (PSI) in Switzerland. A detailed description of the experimental apparatus [173, 174], as well as the microreactor setup [121] can be found elsewhere [129] and only a brief explanation is given here (see Fig. 6.11). Ferrocene (>98% pure, *Sigma Aldrich Inc.*) is sublimed in a stainless-steel tube, jacketed by a copper block, to ensure isothermal sublimation conditions. Temperature and pressure of the sublimation source are continuously monitored and are constant during each measurement. Special attention was paid to reactor conditions that ensure primarily unimolecular dissociation. This is achieved by using a highly diluted sample stream, which minimizes the potential of bimolecular reactions. For this purpose, the precursor gas is diluted in a large excess of argon (99.9999% purity) which is delivered by mass flow controllers

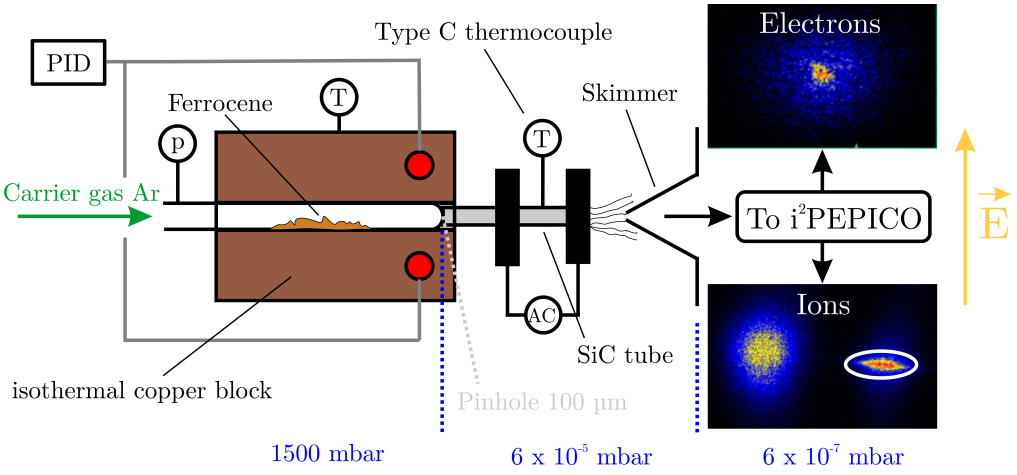

Figure 6.11: Schematic sketch of the evaporation source (brown) and the SiC pyrolysis reactor (gray) coupled to the i²PEPICO system. Exemplary electron (top) and ion (bottom) images are shown on the right-hand side. The white ellipse on the velocity mapped ion image (VMI) represents the region-of-interest (ROI) chosen to sample the translationally cold molecular beam directly, suppressing the background and minimizing the dissociative photoionization signal.

(*MKS Instruments*) at a constant flow rate of 22 sccm. Three separate experiments operating at an evaporator pressure of 1500 mbar and sublimation temperatures of 323/333/353 K were conducted. Assuming thermal equilibrium, the precursor mole fractions at the reactor inlet are calculated from the vapor pressure data [230] to be between $x_{Fe(C_5H_5)_2} = 7.4 \times 10^{-5}$–$8.2 \times 10^{-4}$. After sublimation, the mixture is expanded through a 100 µm pinhole into a resistively heated silicon carbide (SiC) [217] flow reactor with an inner diameter of 1.0 mm and a heated length of 10 mm. To measure the decomposition temperature, a C Type thermocouple is attached to the reactor, with an estimated uncertainty in the examined temperature range between the centerline and surface temperature of ± 100 K.

Under the conditions used here, residence times of 26–44 µs and an average pressure of 1500 Pa in the microreactor were calculated [129]. A computational fluid dynamics (CFD) simulation of the temperature field provided more realistic centerline temperatures which were used in this study for the derivation of temperature-dependent species profiles. Since it is expected that after a while, a considerable amount of deposit may be formed on the reactor surface, the SiC microreactor tube was replaced before conducting the experiments in reductive atmosphere. After the heated reaction zone the decomposition products are rapidly expanded to a high vacuum at $\approx 6 \times 10^{-5}$ mbar, leading to the formation of an effusive molecular beam that minimizes contact time, and preserves the actual gas composition including highly reactive species. The ejected gas is sampled by a nickel skimmer with a 2 mm orifice at the tip which cuts the central part of the gas mixture. A fractional part of the pyrolyzed gas is emitted towards the ionization chamber with a background pressure of $<10^{-6}$ mbar. Once the skimmer is passed the molecules are irradiated with tunable synchrotron radiation, dispersed by a

VUV grating. The radiation perpendicularly hits the ionization chamber with an energy resolution of 6 meV leading, when absorbed, to the formation of photoions and photoelectrons. The cations and electrons are separated by applying a constant electric extraction field of 243 V cm^{-1} which accelerates both in opposite directions. Incoming electrons and ions are subsequently detected in coincidence by two Roentdek DLD40 fast delay-line anode position-sensitive detectors at different impact radii that are proportional to their respective initial kinetic energy perpendicular to the extraction axis and the square root of the ion mass [124]. This double imaging photoelectron photoion coincidence (i^{2}PEPICO) setup allows for the selection of a region-of-interest (ROI) in the velocity map image (VMI) to distinguish direct ionization from dissociative ionization (see Fig. 6.11, ion image).

In all experiments, the photon energy was either kept constant at near-threshold photoionization energies of the decomposition species of interest or scanned incrementally with a step size of 0.025 eV in the 7.8–11.7 eV range. Mass spectra for the decomposition products at 9.0, 10.5, 11.5, 14.2, and 15.8 eV were recorded within a temperature range from 333 K to 1250 K. For each species, fragmentation was suppressed by either staying below the threshold or selecting the ROI in the VMI. The recorded spectra allowed to derive temperature-dependent species profiles. During post-processing, all recorded threshold photoelectron spectra were corrected by the corresponding photon energy specific photon flux. Using these techniques allows to assign species by their molecular mass, photoionization energy or their threshold photoelectron spectrum (TPES) with a resolution of $\leq$ 20 meV, which are corrected for hot electron contribution according to Sztáray et al. [171]. If compared to Franck–Condon (FC) simulations or reference spectra, reactive intermediates (radicals, carbenes) and stable molecules can be isomer-selectively detected [122, 153]. Adiabatic ionization energies and bond dissociation energies were calculated using different density functional theory methods (B3LYP, M06L, ωb97xd) at the 6–311++G(d,p) basis set, as implemented in the Gaussian 16 suite of programs [255]. The given values for the appearance ionization energy are corrected for the respective zero-point energies.

6.4.2 Kinetics

As it was demonstrated in a previous study for aluminum acetylacetonate [129], the utilization of comprehensive numerical simulations of the flow field in the microreactor enabled us to determine the kinetic parameters of the primary decomposition step. For the sake of clarity, the reader is referred to our work on the numerical simulation of the microreactor which is described in detail elsewhere [129] or in Chap. 4.

In brief, to determine the temperature dependence of the $Fe(C_5H_5)_2$ mole fraction the procedure proposed by Zhang et al. [227] was followed, where the influence of temperature-dependent signal variations of argon (m/z 40) due to a change in expansion behavior and therefore the sampling efficiency is characterized by the gas expansion coefficient $\lambda(T)$. This expansion coefficient was determined by recording

temperature-dependent mass spectra at a fixed photon energy of 15.8 eV in the 300–1300 K range (Fig. C.4, Appendix C). The correlation between the concentration of ferrocene at temperature T to the concentration at T_0 at an incident photon energy of 9.0 eV and a fixed photon flux is given as follows:

$$c_{\mathrm{Fe(C_5H_5)_2}}(T) = c_{\mathrm{Fe(C_5H_5)_2}}(T_0) \cdot \lambda(T) \cdot \frac{S_{\mathrm{Fe(C_5H_5)_2}}(T)}{S_{\mathrm{Fe(C_5H_5)_2}}(T_0)}, \tag{6.1}$$

where $\mathrm{S_i}(T)$ represents the ion signal intensity measured at temperature T and is defined as the precursor concentration measured at temperature T. The gas expansion factor is unity at room temperature. As a starting point, the inlet mole fraction was calculated assuming saturated conditions inside the evaporator. For evaporation temperatures of 323/333 and 353 K, respectively. This results in $\mathrm{x_{Fe(C_5H_5)_2}}(T_0) = 7.4 \times 10^{-5}$ to 8.2×10^{-4} from previously measured vapor pressure data by our group [230]. Given this, reasonable Arrhenius plots were derived using the integral method for the unimolecular dissociation reaction of ferrocene (see Sec. 6.2.6). Since unimolecular gas-phase dissociation reactions of metal-organic precursors often follow first-order kinetics, which was also determined here experimentally, the rate constant was approximated using the Arrhenius law shown in Eq. 6.2:

$$k_{\mathrm{uni}}(T) = A_0 \cdot \exp(E_{\mathrm{a}}/RT), \tag{6.2}$$

where A_0 represents the collision frequency in $\mathrm{s^{-1}}$ and E_{a} is the molar activation energy in $\mathrm{kJ\,mol^{-1}}$. This holds for gas-phase and for surface reactions, but the pre-exponential factor and the activation energies differ. The time-dependent concentration change for a unimolecular reaction is given by:

$$\frac{\mathrm{d}c}{\mathrm{d}\tau} = -k_{\mathrm{uni}}(T) \cdot c, \tag{6.3}$$

where τ is the residence time obtained by CFD at temperature T. Separation of variables, integration of Eq. 6.3 and combination with Eq. 6.2 yields:

$$c(\tau) = c(\tau_0) \cdot \exp(-A_0 \cdot \exp\left(E_{\mathrm{a}}/RT\right) \cdot (\tau - \tau_0)). \tag{6.4}$$

Taking the natural logarithm gives:

$$\ln\left(\frac{c(\tau)}{c(\tau_0)}\right) = -\mathrm{k_{uni}}(\tau - \tau_0). \tag{6.5}$$

Surface and gas-phase reactions take place concurrently in the microreactor. Therefore, the total rate constant was the sum of both contributions. Since both rate constants follow the Arrhenius expression given in Eq. 6.2 we derived them simultaneously according to Eq. 6.6:

$$\mathrm{k_{uni}}(T) = \mathrm{k_{gas}}(T) + \mathrm{k_{surf}}(T). \tag{6.6}$$

The experimental data $c(c_0, T, \tau)$ was then fitted by the linear least-squares method applied to Eq. 6.5, with k_{uni} replaced by the sum of the two Arrhenius expressions according to Eq. 6.2, which results in the unknown kinetic parameters A_0 and E_a for the homogeneous and the heterogeneous reaction, respectively. Earlier experiments using metallocenes by others conclude that this is also the case for surface reactions following the Langmuir–Hinshelwood mechanism which is first order at low partial pressures of $Fe(C_5H_5)_2$ [106]. The uncertainties of the kinetic parameters given in Tab. 6.2 only relate to the linear least-squares fitting process.
In the case of ferrocene mixed with H_2, one might expect a bimolecular reaction with its kinetics being second-order. Since hydrogen is present in excess in the reaction mixture and the concentration of ferrocene does not exceed 820 ppm, the reaction of ferrocene with hydrogen can be approximated as pseudo first-order leading to a similar Arrhenius expression as in Eq. 6.2:

$$k_{eff}(T) = A_{0,H_2} \cdot \exp\left(E_a/RT\right). \tag{6.7}$$

Following the procedure described above, also pseudo first-order rate constants for ferrocene in 10% hydrogen have been determined that are discussed in Sec. 6.2.6 in more detail.

Chapter 7

Concluding Remarks

7.1 Summary

The targeted crafting of functional materials is a critical component for most areas of sustainable technologies, making thin film techniques, such as chemical vapor deposition (CVD), instrumental for a sustainable future. It is, therefore, of great importance to investigate the manufacturing aspects of CVD processes used to synthesize thin films. Especially, a comprehensive understanding of the initial steps of the synthesis process is required in order model and control the process to tailor functional materials and thin films with the desired properties.

Thin film deposition often has its origin in a gas-phase decomposition of the precursor and any reactants involved, forming the "true" precursors, responsible for film growth, by subsequent mass transport, surface adsorption and reaction steps. The initial decomposition products are often open-shell species whose characterization, owing to their elusive nature and low barrier for consuming reactions, is not straightforward. Due to the limited experimental insights for the gas-phase decomposition of metal-organic compounds from previous studies, it was the intention of this work to understand the structure, origin and reaction pathways of the occurring reactive intermediates in the gas-phase. This calls for a sensitive approach where commonly used methods such as gas-chromatography or electron-ionization mass spectrometry fail in many cases, since most of the open-shell molecules would not survive the analytical separation or sampling process. For the investigated precursors, gas-phase reactions were expected, but were only partially verified in the literature so far. In the beginning of the project it was even unclear, whether gas-phase metal-containing intermediates that were proposed in the literature can be detected at all, or if the decomposition reactions mainly occur on the surface.

To answer this question, the present thesis has developed a procedure to investigate the gas phase reactions of complex metal-organic CVD precursors in the gas-phase using a microreactor, which is characterized by low residence times of $<50\,\mu s$. This feature turns out to be especially useful to detect highly reactive decomposition products. Although the flow-field in the microreactor is quite complex,

computational fluid dynamics (CFD) simulations of the microreactor helped to describe the conditions within the reactor more accurately than using only general analytical solutions based on many idealizing approximations. The simulation insights allowed to determine reasonable kinetic rate data from microreactor experiments. The reactive intermediates leaving the microreactor were examined experimentally by sampling from a continuous molecular beam with advantageous properties to freeze the underlying chemistry by internal and translational cooling. The highly complex blend of species were analyzed in multiple dimensions, namely the mass, the ion momentum and the electron kinetic energy dimension to resolve the complex composition and enlight the gas-phase chemistry of the selected CVD precursors.

In the course of this thesis, gas-phase VUV photoionization experiments using the i^{2}PEPICO analysis technique were used to obtain information on the intermediates and stable products formed. In particular, the unimolecular and in part bimolecular gas-phase reactions of three metal-organic precursors, namely $Al(acac)_3$, $Zr(acac)_4$ and $Fe(Cp)_2$ were investigated and important reaction intermediates were presented. Based on the experimental results, the reaction pathways were rationalized in mechanistic reaction schemes. For some reactions kinetic parameters could be obtained. As a main result of this work it can be affirmed that indeed at high temperature, gas-phase reactions are a central part of the decomposition mechanism of all three precursors investigated. However, at low temperature, surface reactions significantly influence the reaction mechanism. Several important reaction steps were identified in the gas-phase. First, it can be stated that metal β-diketonates having the same ligand structure show a similar decomposition behavior. In this context it was demonstrated that for both acetylacetonate precursors, the release of a free ligand ($C_5H_8O_2$) is the first decomposition step that is observed at high temperatures in the gas-phase. Its formation is accompanied by the detection of a metal-containing intermediate with the general formula $M(C_5H_7O_2)_{n-2}(C_5H_6O)$[1].

All three precursors show evidence for low temperature surface reaction steps which are overlapped by gas-phase reactions reaching a certain temperature threshold unique for each precursor. In particular, it was found for both metal-acetylacetonates investigated here that not only the first gas-phase decomposition steps, but also the low temperature surface chemistry is similar. They form $M(C_5H_7O_2)_n(OH)_2$ at low temperature leading to the release of cyclic diketones in the gas-phase. Several subsequent reaction steps, especially for the gas-phase reaction pathways were identified and the first step towards a process description by qualitative modeling of the CVD process for the precursors investigated here has been made. Besides the aforementioned overarching results, details of the findings obtained in the course of this work are summarized and discussed in the following.

[1]Here n describes the number of ligands in the molecule and M can be replaced by Al or Zr as the metal center.

7.1.1 Hydrocarbon and Oxygenated Pyrolysis Products

The first objective of this thesis was to isolate, detect and characterize reactive intermediates in CVD like environments. The findings of this work support the idea that the low-temperature decomposition of metal β-diketonates, such as $Al(acac)_3$ and $Zr(acac)_4$, leads to aromatic hydrocarbons with the sum formulas $C_{10}H_{12}O_2$ and $C_8H_{10}O$. These were unambiguously assigned as a blend of dimethyl-dihydroxo-dihydropentalene and dimethyl-hydroxo-keto-tetrahydropentalene as well as dimethylphenol by the mass-resolved threshold photoelectron spectra obtained by the i^{2}PEPICO diagnostic technique. They provide further evidence that at low-temperature surface reactions play a significant role in the decomposition process. Considerable progress has been made in the detection and characterization of further hydrocarbons of higher masses at m/z 146, 186, 210, which implies that parallel minor decomposition pathways are also present. However, these are of homogeneous-heterogeneous nature and highly complex. The extensive analysis of surface reactions was not in the scope of this study, leaving some open questions in the low-temperature decomposition pathways. Nevertheless, the findings add substantially to the understanding of low-temperature decomposition pathways.

At higher temperatures gas-phase reactions become more important. Considerable insight has been gained with regard to the clear identification of the organic decomposition products of all three precursors at temperatures where gas-phase reactions play a major role in the mechanism. Thanks to the collected ms-TPES, it was demonstrated that besides acetylacetone, acetone and ketene, acetylallene (C_5H_6O) is a major decomposition product of $Al(acac)_3$. This work has also highlighted that $Zr(acac)_4$ already decomposes in the evaporator having acetylacetone and acetone as the main gaseous decomposition products, which is in contrast to previous studies proposing acetic acid and C_3H_4. This intimates that investigations of the evaporation stability using various evaporator setups could be necessary to accurately determine mechanisms and kinetic rate data from solid precursors. In the gas-phase satisfactory results were obtained using the moleculare fingerprints from ms-TPES to identify acetylallene, acetone and ketene as major hydrocarbon decomposition products upon pyrolysis of $Zr(acac)_4$.

For the decomposition of $Fe(Cp)_2$ the major organic decomposition products at m/z 26, 39, 50, 52, 64 and 128 as acetylene, the propagyl radical, acyclic isomer of C_5H_4, as well as 1-butene-3-ynylbenzene were identified and characterized, demonstrating the capability of the setup to detect radicals isomer-selectively. The research results have highlighted that adding 10% of the reactive gas H_2 produces more cyclopentadiene and lighter hydrocarbons, which supports the idea that direct reactions of C_5H_5 and/ or the surface hydrogenation of ligand fragments play a major role here. This would lead to a clean removal of ligand fragments from the reaction chamber and therefore a better quality of the obtained product.

7.1.2 Metal-Containing Pyrolysis Products

A second aim of this work was to detect and identify the important metal-containing intermediates that act as true precursors for film growth. The impact of the presented studies clearly lies in the detection and identification of these yet unknown metal-containing intermediates. It has been demonstrated that the microreactor i^{2}PEPICO experiment provides a powerful tool because the strengths of the setup, i.e., low residence time and radical conservation by molecular beam sampling, made the identification of intermediates with low lifetimes possible for all of the three investigated systems. This thesis presented accurate experimental results proving that aluminium bis(diketo)acetylacetonate-H, *m/z* 224 $Al(C_5H_7O_2)(C_5H_6O_2)$ is the primary decomposition product upon the pyrolysis of $Al(acac)_3$ at temperatures above 600 K. Typical Al-CVD is performed at temperatures from 623–1223 K [83, 84, 85, 86]. This emphasizes the importance of gas-phase reactions in Al-CVD from $Al(acac)_3$ and the previously proposed decomposition pathway was revised (see Scheme 1), since quantum chemical calculations showed that the loss of H_2O and C_5H_6O is energetically unfavorable in comparison to a direct loss of acetylacetone to form *m/z* 224.

The value of the current experimental configuration was especially demonstrated in the investigation of the pyrolysis of $Zr(acac)_4$, as discussed in Chap. 5. Here, six zirconium intermediates are identified by their isotopic pattern using both imaging and space focusing conditions. The species assignments were confirmed by the associated velocity map images (VMI). Photoionization efficiency (PIE) curves additionally allowed us to determine the adiabatic ionization thresholds of the zirconium intermediates, which is useful for the determination of ionization cross sections in future investigations. The calculated cross sections could then help to quantify the metal-containing intermediates in the gas-phase in follow up studies. Based on the assignments, this work has revealed that there are three major steps of $Zr(acac)_4$ decomposition at 525, 750 and 850 K. The first step affords acetylacetone together with $Zr(C_5H_7O_2)_2(C_5H_6O_2)$ and is also similar as the one detected for the pyrolysis of the other metal β-diketonate, $Al(acac)_3$. It is further shown that the preceding decomposition steps involve *m/z* 304 $Zr(OH)(C_5H_7O_2)(C_5H_6O_2)$ and *m/z* 286 $Zr(C_5H_6O_2)$. The insights gained are merged in a complete decomposition mechanism which is presented in Scheme 2 and whose derivation is discussed in Chap. 5.

The data on the pyrolysis of $Fe(Cp)_2$ suggest that below 900 K no metal-containing intermediates, especially no *m/z* 121 $Fe(C_5H_5)$, are formed in the gas-phase, which was confirmed by using velocity map imaging. The evidence obtained from threshold photoelectron specta implies that cyclopentadienyl radicals and cyclopentadiene are formed in considerable amounts in this low-temperature regime. Therefore, the present thesis enhanced the understanding of the low-temperature decomposition of ferrocene at residence times of a few microseconds. However, because of the possible fast adsorption of iron containing intermediates and subsequent reaction steps on the surface, further investigations need to follow to elucidate

this aspect. At higher temperatures, the data confirm the previously proposed spontaneous decomposition of ferrocene in the gas-phase to form two cyclopentadienyl radicals. In addition, further hydrocarbon molecules that play a role in the mechanism were detected and characterized (see Scheme 3).

In the case of ferrocene reduction it was shown that by adding 10% H_2 the reaction mechanism changes significantly. In minor amounts, the decomposition products of ferrocene are hydrogenated on the surface and form volatile hydrocarbon products, such as C_5H_{10} that desorb into the gas-phase. However, it was demonstrated that in most cases cyclopentadiene (C_5H_6) is formed by a bimolecular reaction of a cyclopentadienyl radical with hydrogen. This is advantageous, because the detected low amounts of ligand fragments most probably lead to carbon free films in iron CVD. From the process perspective the addition of hydrogen is beneficial because the decomposition temperature could be considerably lowered to 550 K.

7.1.3 Kinetics of the Thermal Decomposition of $Al(acac)_3$ and $Fe(Cp)_2$

Unlike many previous studies, this thesis did not solely investigate mechanistic aspects of the gas-phase chemistry, but also provided a blueprint for a novel procedure to obtain kinetic rate data for the unimolecular decomposition of CVD precursors using a microreactor coupled to the i^{2}PEPICO apparatus. By utilizing the gas expansion coefficient $\lambda(T)$ combined with vapor pressure data of the particular precursor, it was shown that the precursor concentration can be quantified. This was done for two of the three precursors obtaining kinetic rate data, for the primary decomposition steps. As for $Al(acac)_3$, it was demonstrated that the decomposition of the precursor follows first-order kinetics. The reaction rate was defined as a sum of both low-temperature surface and high-temperature gas-phase rates and kinetic parameters for both were derived. Although there are limitations to the obtained kinetic rate, such as a limited number of data points that could be considered in the low-temperature regime and the highly complex flow field, the derived activation energy in the gas-phase of $57 \pm 4\,\mathrm{kJ\,mol^{-1}}$ compares well to the published activation energies of 68.6–100 $\mathrm{kJ\,mol^{-1}}$ from the literature for the decomposition of $Al(acac)_3$ [79, 82, 90]. These were obtained using various reactor concepts and detection techniques. Yet, when compared to previous data, the pre-exponential factors are on a reasonable order of magnitude.

The results for the unimolecular decomposition of $Fe(Cp)_2$ are in agreement with literature values showing some influence of surface-catalyzed kinetics, as reported by Dyagileva et al. [106]. In addition to the unimolecular decomposition kinetics of $Fe(Cp)_2$, also the kinetics of adding 10% of hydrogen as reactive gas were investigated. This is because adding hydrogen to ferrocene was reported to have advantageous outcome on the film quality by removing ligand fragments from the reaction area. The results of the kinetic analysis demonstrate that for the latter case a reduction in activation energy for the gas-phase reaction regime from

$247.6 \pm 20\,\mathrm{kJ\,mol^{-1}}$ to $88.0 \pm 14.6\,\mathrm{kJ\,mol^{-1}}$ was observed. The considerably lower activation energy for the reduction of ferrocene is primarily caused by a bimolecular reaction of ferrocene with hydrogen leading to a change in branching ratio and composition of the products observed.

In sum, by analyzing the microreactors flow field and thanks to the strength of the applied setup, a methodology to obtain comprehensive mechanistic information on the thermal decomposition of three model precursors $Al(acac)_3$, $Zr(acac)_4$ and $Fe(Cp)_2$ was devised. It was also demonstrated that with a knowledge of the flow field, reasonable kinetic parameters can be derived. The presented findings add to a limited body of literature on the gas-phase kinetics of CVD precursors which is needed to model reactive systems and avoid time-consuming experiments to find optimum parameters for maximizing the growth rate and quality of the desired thin film or functional material. This work provides an encouragement for a novel way to perform kinetic analysis in microreactors utilizing the i^{2}PEPICO technique with all its advantages. It was demonstrated that i^{2}PEPICO is a well-suited analytical technique for thermal decomposition studies of CVD precursors. The data of this thesis could serve as a basis for future studies on the gas-phase kinetics of CVD precursors by using well-defined reaction conditions in continuous flow reactors.

7.2 Open Questions and Further Perspectives

The synthesis of thin films is a combination of gas-phase and surface reaction steps. Although conditions were chosen, such that surface reactions are minimized in the present work, it cannot be denied that these, to some extent, also play a role in the decomposition mechanism. This interference especially becomes apparent when surface-catalyzed kinetics, such as for ferrocene, are a significant factor. Since the current study was not specifically designed to investigate these phenomena, additional work needs to be done to quantify or further minimize their impact and only probe the gas-phase kinetics. Possible strategies could be the usage of alternative reactor concepts or changing the volume-to-surface ratio to efficiently quantify the effect of surface reactions. As far as the present microreactor setup is concerned, experiments with species that tend to generate catalytic intermediates on the surface are not ideal and future investigations should concentrate on those that are not catalytic. Examples for suitable precursors could even be more complex compounds than the ones investigated in the course of this thesis, such as $Zr(tmhd)_4$. Their decomposition mechanism is likely to be even more multifaceted than the one of the precursors having a relatively simple acetylacetone ligand. Yet, the present thesis showed that their kinetic and mechanistic analysis seems to be possible. In this context, first experiments covering the decomposition of $Al(tmhd)_3$ and $Zr(tmhd)_4$ show promising preliminary results which can be combined with the insights gained from the acetylacetonate based metal β-diketonates. This knowledge will enhance the understanding of role of ligand structure in the decomposition processes.

As demonstrated for the addition of H_2, oxidizing reactions are also of interest for synthesis processes. The effect of oxygen on the decomposition mechanism has been investigated by adding 10% O_2 to $Al(acac)_3$ and $Fe(Cp)_2$. When using ferrocene a slow, but steady reduction of resistivity was observed during the experiments due to a formation of a non-conductive coating on the inner walls of the reactor. Additionally an excessive particle formation was noticed. The oxidizing conditions were extremely difficult to control, but the presented findings and various literature sources suggest that the addition of oxidizing reagents could lower the decomposition barrier of both precursors by a considerable amount. Consequently, follow-up research has to be done to fully understand the influence of oxygen on the reaction mechanism. A possible chance to prevent the precursor from being exposed to oxygen before the thermal decomposition takes place may lie in the usage of alternative oxygen sources having lower decomposition temperatures than the precursor to be investigated. An example for this could be nitrous oxide N_2O when the influence of oxygen on the decomposition of ferrocene should be elucidated.

Clearly, the scope of this study was to determine the decomposition mechanistically in a first step including the recording of temperature-dependent species profiles, but in a second step a quantification of those intermediates is extremely valuable for mechanism development and modeling of the process. This, however, affords a calibration of the species of interest, for which ionization cross sections, especially of the detected metal-containing intermediates, are desperately needed. Future research aiming on the measurement or simulation of these cross sections would help to fill these gaps.

The presented results on the kinetics of the investigated precursors have some constraints, such as the instrument-dependent maximum step size for the temperature increments in the microreactor or the overlap between surface and gas-phase reactions at some point. Also using carrier gases with unfavorable thermal properties, such as argon compared to helium, can lead to an inhomogeneous temperature profile and special care must be taken when combining experimental and numerical data for the interpretation of kinetic rates. Despite this, this work is an important step towards further kinetic investigations in microreactor setups, especially using helium, for which it was demonstrated by CFD that the flow field approaches plug-flow like character with respect to the temperature field. However, the current simple approach of fitting two straight lines for the surface and gas-phase reaction rates to the data of $Al(acac)_3$ and $Fe(Cp)_2$ could be replaced by a more suitable approach using a regression function for the reaction rate constants k_{surf} and k_{gas} considering the arbitrary consecutive reaction mechanism A $\rightarrow$ B $\rightarrow$ C as follows:

$$k_{tot} = \frac{k_{surf} \cdot k_{gas}}{k_{surf} + k_{gas}}. \tag{7.1}$$

Given that at a specific temperature T_{12} the reaction rate constant $k_{surf} = k_{gas} = k_{12}$ leads to the following regression function:

$$k_i = k_{12} \cdot \exp\left(\frac{-E_i}{R} \cdot \left(\frac{1}{T} - \frac{1}{T_{12}}\right)\right), \tag{7.2}$$

where the regressions parameters k_{12}, T_{12}, E_{surf} and E_{gas} can be determined from experimental data. This approach has recently proven to reach promising results for the determination of activation energies, having a high influence on the higher barrier reaction, here the gas-phase reaction, which was corrected by the factor of two [386].

The data suggests that, at least for $Zr(acac)_4$, the precursor gas composition is not necessarily constant for the long run (>10 h). While this issue has been accounted for in the second presented study (see Sec. 5.2.2), a monitoring of the feed concentration is highly desired. Research into solving this problem is in progress, where optical absorption spectroscopy is used to track and control the precursor concentration before the composition enters a plug-flow reactor. If this system can be downsized to fit the present microreactor setup, kinetic rate data could be obtained with higher precision. This is because one must not rely on approximations on the inlet concentrations of the precursor, when a real time monitoring of the precursor concentration is available.

The simulation results suggest that due to the thermal properties of the gas and advantageous properties of the resulting molecular beam, as well as lower residence times in the reactor, helium is superior over argon as carrier gas and should, whenever possible, be used in future experiments. However only limited experimental characterization on the flow conditions can be found in the literature. Baraban et al. measured the the temperature of NO at different flow conditions using *in-situ* laser-induced fluorescence detection in an optical accessible reactor [262]. Additionally, density profiles were obtained by Tranter et al. using X-ray fluorescence detection [329]. Consequently, more research on the measurement of flow properties, such as inserting probes or using optical systems to measure temperature or density in a microreactor system, would help to calibrate the calculations more precisely. In comparison to the simple approach described here, which relies on surface temperature measurements as a linkage between simulation and experiment, experimentally obtained flow conditions of the whole flow field would clearly improve the simulation results. In addition, one could concentrate on a more profound analysis of the large body of flow field data by using volume-averaged temperatures and residence times.

Although there are several challenges when using of the high-temperature microreactor that complicate the interpretation of experimental data, given the circumstances that only limited data is available and that the presented kinetic parameters are close to the ones measured in comparable systems, the introduced approach marks a good starting point to exploit microreactor data for mechanistic investigations and kinetic rate measurements of simple unimolecular dissociation reactions.

Bibliography

[1] Verified Market Research, *Global Chemical Vapor Deposition (CVD) Market Size By Category (CVD Equipment, CVD Materials, CVD Services), By Application (Microelectronics, Data Storage, Solar Products), By Geographic Scope And Forecast*, March 2022, https://www.verifiedmarketresearch.com/product/chemical-vapor-deposition-cvd-market/.

[2] X.-T. Yan and X. Yongdong, *Chemical vapour deposition: An integrated engineering design for advanced materials*, Springer, New York and London, 1st edn., 2010.

[3] J. E. Crowell, *Journal of Vacuum Science & Technology A: Vacuum, Surfaces, and Films*, 2003, **21**, S88–S95.

[4] A. B. Leese and A. R. Mills, in *Chemical Vapour Deposition*, ed. M. L. Hitchman and A. C. Jones, Royal Society of Chemistry, Cambridge, UK, 2009, pp. 535–570.

[5] P. Luo, S. Zhou, W. Xia, J. Cheng, C. Xu and Y. Lu, *Advanced Materials Interfaces*, 2017, **4**, 1600970.

[6] J. A. Raiford, S. T. Oyakhire and S. F. Bent, *Energy & Environmental Science*, 2020, **13**, 1997–2023.

[7] Q. Wang, Y. Lei, Y. Wang, Y. Liu, C. Song, J. Zeng, Y. Song, X. Duan, D. Wang and Y. Li, *Energy & Environmental Science*, 2020, **13**, 1593–1616.

[8] L. Qiu, S. He, Y. Jiang and Y. Qi, *Journal of Materials Chemistry A*, 2021, **9**, 22759–22780.

[9] N. Bellomo, M. Michel, B. R. Pistillo, R. J. White, E. Barborini and D. Lenoble, *ChemElectroChem*, 2022, **9**, 31.

[10] G. Zhang, X. Xiao, B. Li, P. Gu, H. Xue and H. Pang, *Journal of Materials Chemistry A*, 2017, **5**, 8155–8186.

[11] Z. Cai, B. Liu, X. Zou and H.-M. Cheng, *Chemical Reviews*, 2018, **118**, 6091–6133.

[12] C. A. Banciu, F. Nastase, A.-I. Istrate and L. M. Veca, *Molecules*, 2022, **27**, 3634.

[13] Z. Shi, H. Ci, X. Yang, Z. Liu and J. Sun, *ACS Nano*, 2022, **16**, 11646–11675.

[14] L. Yu, D. El-Damak, U. Radhakrishna, X. Ling, A. Zubair, Y. Lin, Y. Zhang, M.-H. Chuang, Y.-H. Lee, D. Antoniadis, J. Kong, A. Chandrakasan and T. Palacios, *Nano Letters*, 2016, **16**, 6349–6356.

[15] F. Lo Presti, A. L. Pellegrino and G. Malandrino, *Advanced Materials Interfaces*, 2022, **9**, 2102501.

[16] A. Rajib, A. Kuddus, K. Yokoyama, T. Shida, K. Ueno and H. Shirai, *Journal of Applied Physics*, 2022, **131**, 105301.

[17] H. Liu, C. Y. You, J. Li, P. R. Galligan, J. You, Z. Liu, Y. Cai and Z. Luo, *Nano Materials Science*, 2021, **3**, 291–312.

[18] F. Shen, Z. Zhang, Y. Zhou, J. Ma, K. Chen, H. Chen, S. Wang, J. Xu and Z. Chen, *Nature Communications*, 2022, **13**, 5597.

[19] Y. Yin, Y. Guo, D. Liu, C. Miao, F. Liu, X. Zhuang, Y. Tan, F. Chen and Z.-x. Yang, *Advanced Optical Materials*, 2022, **10**, 2102291.

[20] Y.-L. Hong, Z. Liu, L. Wang, T. Zhou, W. Ma, C. Xu, S. Feng, L. Chen, M.-L. Chen, D.-M. Sun, X.-Q. Chen, H.-M. Cheng and W. Ren, *Science*, 2020, **369**, 670–674.

[21] S. T. Vagge and S. Ghogare, *Materials Today: Proceedings*, 2022, **56**, 1201–1216.

[22] S. Wu, Y. Zhao, W. Li, W. Liu, Y. Wu and F. Liu, *Coatings*, 2021, **11**, 79.

[23] J. G. Thakare, C. Pandey, M. M. Mahapatra and R. S. Mulik, *Metals and Materials International*, 2021, **27**, 1947–1968.

[24] H. Fukui, *SEI Technical Review*, 2016, 39–45.

[25] N. Schalk, M. Tkadletz and C. Mitterer, *Surface and Coatings Technology*, 2022, **429**, 127949.

[26] F. Ghaemi, M. Ali, R. Yunus and R. N. Othman, in *Synthesis, Technology and Applications of Carbon Nanomaterials*, ed. S. A. Rashid, R. N. I. Raja Othman and M. Z. Hussein, Elsevier, Amsterdam, Netherlands, 2019, pp. 1–27.

[27] P.-X. Hou, F. Zhang, L. Zhang, C. Liu and H.-M. Cheng, *Advanced Functional Materials*, 2022, **32**, 2108541.

[28] N. Zhao, Q. Wu, X. Zhang, T. Yang, D. Li, X. Zhang, C. Ma, R. Liu, L. Xin and M. He, *Carbon*, 2022, **187**, 29–34.

[29] A. C. Jones and M. L. Hitchman, in *Chemical Vapour Deposition*, ed. M. L. Hitchman and A. C. Jones, Royal Society of Chemistry, Cambridge, UK, 2009, pp. 1–36.

[30] M. J. Hampden-Smith and T. T. Kodas, *Chemical Vapor Deposition*, 1995, **1**, 8–23.

[31] K. J. Hüttinger, *Chemical Vapor Deposition*, 1998, **04**, 151–158.

[32] W. O. Filtvedt, A. Holt, P. A. Ramachandran and M. C. Melaaen, *Solar Energy Materials and Solar Cells*, 2012, **107**, 188–200.

[33] H. Komiyama, Y. Shimogaki and Y. Egashira, *Chemical Engineering Science*, 1999, **54**, 1941–1957.

[34] I. Utke, P. Swiderek, K. Höflich, K. Madajska, J. Jurczyk, P. Martinović and I. B. Szymańska, *Coordination Chemistry Reviews*, 2022, **458**, 213851.

[35] H. Matsumura, *Catalytic Chemical Vapor Deposition: Technology and Applications of Cat-CVD*, Wiley-VCH, Weinheim, Germany, 2019.

[36] A. Yanguas-Gil, Y. Yang, N. Kumar and J. R. Abelson, *Journal of Vacuum Science & Technology A: Vacuum, Surfaces, and Films*, 2009, **27**, 1235–1243.

[37] H. Pedersen, *Chemistry of Materials*, 2016, **28**, 691–699.

[38] A. A. Onischuk and V. N. Panfilov, *Russian Chemical Reviews*, 2001, **70**, 321–332.

[39] L. Zhou, Z. Pan, Z. Liu and W. Wang, *JOM*, 2020, **72**, 1273–1278.

[40] M. D. Allendorf, T. M. Besmann, R. J. Kee and M. T. Swihart, in *Chemical Vapour Deposition*, ed. M. L. Hitchman and A. C. Jones, Royal Society of Chemistry, Cambridge, UK, 2009.

[41] K. Otsuka, R. Ishimaru, A. Kobayashi, T. Inoue, R. Xiang, S. Chiashi, Y. K. Kato and S. Maruyama, *ACS Nano*, 2022, 5627–5635.

[42] I. Ohkubo, T. Aizawa, K. Nakamura and T. Mori, *Frontiers in Chemistry*, 2021, **9**, 642388.

[43] A. Gupta, S. Nigam and V. M. Shinde, *Journal of the American Ceramic Society*, 2022, **105**, 3885–3895.

[44] H. O. Pierson, *Handbook of Carbon, Graphite, Diamond, and Fullerenes: Properties, Processing, and Applications*, Noyes Publications, Park Ridge, N.J, 1993.

[45] W. S. Rees, *CVD of Nonmetals*, Wiley, Weinheim and New York, 1996.

[46] A. Gupta, S. Nigam and V. M. Shinde, *Journal of the American Ceramic Society*, 2022, **105**, 3885–3895.

[47] A. Devi, *Coordination Chemistry Reviews*, 2013, **257**, 3332–3384.

[48] K. E. Lewis and G. P. Smith, *Journal of the American Chemical Society*, 1984, **106**, 4650–4651.

[49] K. Choy, *Progress in Materials Science*, 2003, **48**, 57–170.

[50] J. G. Hulkko, R. Qiu, O. Bäcke, A. Forslund, M. Halvarsson, H. Larsson and M. Boman, *Surface and Coatings Technology*, 2022, **438**, 128394.

[51] H. Simka, M. Hierlemann, M. Utz and K. F. Jensen, *Journal of the Electrochemical Society*, 1996, **143**, 2646–2654.

[52] M. D. Allendorf and C. F. Melius, *Surface and Coatings Technology*, 1998, **108-109**, 191–199.

[53] T. Nakajima, M. Nakamoti and K. Yamashita, *Molecular Physics*, 2003, **101**, 267–276.

[54] P. Raghunath, Y.-M. Lee, S.-Y. Wu, J.-S. Wu and M.-C. Lin, *International Journal of Quantum Chemistry*, 2013, **113**, 1735–1746.

[55] A. A. Apeke and N. A.-D. Kyame, in *Nanomaterials via Single-Source Precursors*, ed. A. Barron, A. Hepp and A. Apblett, Elsevier, San Diego, 2021, pp. 123–161.

[56] J. Lei, Y. Xie and B. I. Yakobson, *ACS Nano*, 2021, **15**, 10525–10531.

[57] N. Sato, Y. Funato, K. Shima, H. Sugiura, Y. Fukushima, T. Momose, M. Koshi and Y. Shimogaki, *International Journal of Chemical Kinetics*, 2021, **53**, 638–645.

[58] B. Song, B. Gao, P. Han, Y. Yu and X. Tang, *Materials*, 2021, **14**, 7532.

[59] K. C. Topka, H. Vergnes, T. Tsiros, P. Papavasileiou, L. Decosterd, B. Diallo, F. Senocq, D. Samelor, N. Pellerin, M.-J. Menu, C. Vahlas and B. Caussat, *Chemical Engineering Journal*, 2022, **431**, 133350.

[60] N. Cheimarios, G. Kokkoris and A. G. Boudouvis, *Chemical Engineering Science*, 2010, **65**, 5018–5028.

[61] I. G. Aviziotis, T. Duguet, K. Soussi, G. Kokkoris, N. Cheimarios, C. Vahlas and A. G. Boudouvis, *Physica Status Solidi C*, 2015, **12**, 923–930.

[62] G. M. Psarellis, I. G. Aviziotis, T. Duguet, C. Vahlas, E. D. Koronaki and A. G. Boudouvis, *Chemical Engineering Science*, 2018, **177**, 464–470.

[63] G. P. Gakis, S. Termine, A.-F. A. Trompeta, I. G. Aviziotis and C. A. Charitidis, *Chemical Engineering Journal*, 2022, **445**, 136807.

[64] P. Papavasileiou, E. D. Koronaki, G. Pozzetti, M. Kathrein, C. Czettl, A. G. Boudouvis, T. J. Mountziaris and S. P. Bordas, *Chemical Engineering Research and Design*, 2022, **186**, 314–325.

[65] J. Wang, T.-C. Luo, Y.-c. He, J. Li and G. Wang, *Ceramics International*, 2022, **48**, 25302–25313.

[66] G. D. Papasouliotis and S. V. Sotirchos, *Journal of the Electrochemical Society*, 1994, **141**, 1599–1611.

[67] Y. Liu, N. Lim, T. Smith, X. Sang and J. P. Chang, *Journal of Vacuum Science & Technology B*, 2022, **40**, 012201.

[68] M. E. Coltrin, P. Ho, H. K. Moffat and R. J. Buss, *Thin Solid Films*, 2000, **365**, 251–263.

[69] M. D. Allendorf, C. F. Melius and A. H. McDaniel, *MRS Proceedings*, 1998, **555**, 16.

[70] H. Pedersen and S. D. Elliott, *Theoretical Chemistry Accounts*, 2014, **133**, 111.

[71] V. M. Shinde and P. Pradeep, *Journal of Analytical and Applied Pyrolysis*, 2021, **154**, 104998.

[72] R. C. Lucas, D. Morgan and T. F. Kuech, *The Journal of Physical Chemistry A*, 2020, **124**, 1682–1697.

[73] M. D. Allendorf, T. H. Osterheld and C. F. Melius, *MRS Proceedings*, 1993, **334**, 71.

[74] B. H. Weiller, *MRS Proceedings*, 1993, **334**, 357.

[75] O. Féron, F. Langlais and R. Naslain, *Chemical Vapor Deposition*, 1999, **5**, 37–47.

[76] P. Carminati, T. Buffeteau, N. Daugey, G. Chollon, F. Rebillat and S. Jacques, *Thin Solid Films*, 2018, **664**, 106–114.

[77] T. Ohba, T. Suzuki, H. Yagi, Y. Furumura and T. Hatano, *Journal of the Electrochemical Society*, 1995, **142**, 934–938.

[78] L. Decosterd, K. C. Topka, B. Diallo, D. Samelor, H. Vergnes, F. Senocq, B. Caussat, C. Vahlas and M.-J. Menu, *Physical Chemistry Chemical Physics*, 2021, **23**, 10560–10572.

[79] V. G. Minkina, *Inorganic Materials*, 1993, **29**, 1400–1401.

[80] A. F. Bykov, A. E. Turgambaeva, I. K. Igumenov and P. P. Semyannikov, in *Proceedings of the Tenth European Conference on Chemical Vapour Deposition: Volume 1*, ed. G. A. Battistion, R. Gerbasi, M. Porchia and G. A. Battiston, Journal de Physique IV and Éd. de Physique, Les Ulis, 1995, vol. 05, pp. C5–191–C5–197.

[81] J. V. Hoene, R. G. Charles and W. M. Hickam, *The Journal of Physical Chemistry*, 1958, **62**, 1098–1101.

[82] E. I. Tsyganova and L. M. Dyagileva, *Russian Chemical Reviews*, 1996, **65**, 315–328.

[83] A. Devi, S. A. Shivashankar and A. G. Samuelson, *Le Journal de Physique IV*, 2002, **12**, 139–146.

[84] S. K. Pradhan, P. J. Reucroft and Y. Ko, *Surface and Coatings Technology*, 2004, **176**, 382–384.

[85] N. Bahlawane, K. Kohse-Höinghaus, P. A. Premkumar and D. Lenoble, *Chemical Science*, 2012, **3**, 929–941.

[86] A. Nebatti, C. Pflitsch, B. Curdts and B. Atakan, *Materials Science in Semiconductor Processing*, 2015, **39**, 467–475.

[87] A. E. Turgambaeva, V. V. Krisyuk, A. F. Bykov and I. K. Igumenov, in *Proceedings of the Twelfth European Conference on Chemical Vapour Deposition*, ed. A. Figueras, EDP Sciences, Les Ulis, 1999, vol. 09 of Journal de physique 4, Proceedings, pp. Pr8–65–Pr8–72.

[88] I. K. Igumenov, A. E. Turgambaeva and P. P. Semyannikov, *Le Journal de Physique IV*, 2001, **11**, Pr3–505–Pr3–515.

[89] J. S. Kim, H. A. Marzouk, P. J. Reucroft, J. D. Robertson and C. E. Hamrin, *Thin Solid Films*, 1993, **230**, 156–159.

[90] M. C. Rhoten and T. C. DeVore, *Chemistry of Materials*, 1997, **9**, 1757–1764.

[91] C. Dubourdieu, S. B. Kang, Y. Q. Li, G. Kulesha and B. Gallois, *Thin Solid Films*, 1999, **339**, 165–173.

[92] B. Atakan, V. Khlopyanova, S. Mausberg, F. Mumme, A. Kandzia and C. Pflitsch, *Physica Status Solidi C*, 2015, **12**, 878–885.

[93] A. M. Torres-Huerta, M. A. Domínguez-Crespo, E. Ramírez-Meneses and J. R. Vargas-García, *Applied Surface Science*, 2009, **255**, 4792–4795.

[94] L. J. Espinoza-Pérez, E. López-Honorato and L. A. González, *Ceramics International*, 2020, **46**, 15621–15630.

[95] H. M. Ismail, *Powder Technology*, 1995, **85**, 253–259.

[96] M. V. F. Schlupp, J. Martynczuk, M. Prestat and L. J. Gauckler, *Advanced Energy Materials*, 2013, **3**, 375–385.

[97] P. Madkikar, X. Wang, T. Mittermeier, A. H. A. Monteverde Videla, C. Denk, S. Specchia, H. A. Gasteiger and M. Piana, *Journal of Nanostructure in Chemistry*, 2017, **7**, 133–147.

[98] M. Schlupp, S. Binder, J. Martynczuk, M. Prestat and L. J. Gauckler, *Thin Solid Films*, 2012, **522**, 58–65.

[99] Y. M. Manawi, A. Samara, T. Al-Ansari and M. A. Atieh, *Materials*, 2018, **11**, year.

[100] A. Leonhardt, S. Hampel, C. Müller, I. Mönch, R. Koseva, M. Ritschel, D. Elefant, K. Biedermann and B. Büchner, *Chemical Vapor Deposition*, 2006, **12**, 380–387.

[101] A. Barreiro, S. Hampel, M. H. Rümmeli, C. Kramberger, A. Grüneis, K. Biedermann, A. Leonhardt, T. Gemming, B. Büchner, A. Bachtold and T. Pichler, *The Journal of Physical Chemistry B*, 2006, **110**, 20973–20977.

[102] S. Y. Moon, W. S. Kim and C. S. Kim, *RSC Advances*, 2018, **8**, 25815–25818.

[103] P. J. Zandstra, *The Journal of Chemical Physics*, 1964, **40**, 612.

[104] D. K. Russell, *Chemical Vapor Deposition*, 1996, **2**, 223–233.

[105] D. Lysenkov, J. Engstler, A. Dangwal, A. Popp, G. Müller, J. J. Schneider, V. M. Janardhanan, O. Deutschmann, P. Strauch, V. Ebert and J. Wolfrum, *Small*, 2007, **3**, 974–985.

[106] L. M. Dyagileva, V. P. Mar'in, E. I. Tsyganova and G. A. Razuvaev, *Journal of Organometallic Chemistry*, 1979, **175**, 63–72.

[107] P. Srisuma, N. Suwattanapongtada, N. Opasanon, P. Charoensuppanimit, K. Kerdnawee, C. Termvidchakorn, W. Tanthapanichakoon and T. Charinpanitku, *Engineering Science and Technology, an International Journal*, 2021, **44**, 1621.

[108] C. N. R. Rao and A. Govindaraj, *Nanotubes and Nanowires*, Royal Society of Chemistry, London England, 3rd edn., 2022, vol. no. 52.

[109] W. Ren, F. Li, S. Bai and H.-M. Cheng, *Journal of Nanoscience and Nanotechnology*, 2006, **6**, 1339–1345.

[110] C. Liu and H.-M. Cheng, *Materials Today*, 2013, **16**, 19–28.

[111] F. Senocq, F.-D. Duminica, F. Maury, T. Delsol and C. Vahlas, *Surface and Coatings Technology*, 2006, **153**, G1025.

[112] K. Kuwana and K. Saito, *Proceedings of the Combustion Institute*, 2007, **31**, 1857–1864.

[113] T. Yamada, A. Maigne, M. Yudasaka, K. Mizuno, D. N. Futaba, M. Yumura, S. Lijima and K. Hata, *Nano Letters*, 2008, **8**, 4288–4292.

[114] G. Dormans, *Journal of Crystal Growth*, 1991, **108**, 806–816.

[115] J.-H. Luo, R.-Y. Luo and W.-G. Zhang, *Chemical Vapor Deposition*, 2007, **13**, 574–580.

[116] S. I. Futko, B. G. Shulitskii, V. A. Labunov and E. M. Ermolaeva, *Journal of Engineering Physics and Thermophysics*, 2015, **88**, 1432–1441.

[117] Y. Xu, Y. Ma, Y. Liu, S. Feng, D. He, P. Haghi-Ashtiani, A. Dichiara, L. Zimmer and J. Bai, *The Journal of Physical Chemistry C*, 2018, **122**, 6437–6446.

[118] C. R. Kleijn, in *Chemical Physics of Thin Film Deposition Processes for Micro- and Nano-Technologies*, ed. Y. Pauleau, Springer Netherlands, Dordrecht, 2002, pp. 119–144.

[119] C. R. Kleijn, R. Dorsman, K. J. Kuijlaars, M. Okkerse and H. van Santen, *Journal of Crystal Growth*, 2007, **303**, 362–380.

[120] C. Vahlas, B. Caussat, F. Senocq, W. L. Gladfelter, L. Aloui and T. Moersch, *Chemical Vapor Deposition*, 2007, **13**, 123–129.

[121] P. Chen, S. D. Colson, W. A. Chupka and J. A. Berson, *The Journal of Physical Chemistry*, 1986, **90**, 2319–2321.

[122] P. Hemberger, J. A. van Bokhoven, J. Pérez-Ramírez and A. Bodi, *Catalysis Science & Technology*, 2020, **10**, 1975–1990.

[123] J. M. Dyke, *Physical Chemistry Chemical Physics*, 2019, **21**, 9106–9136.

[124] T. Baer and R. P. Tuckett, *Physical Chemistry Chemical Physics*, 2017, **19**, 9698–9723.

[125] Z. Zhang, Y. Pan, J. Yang, Z. Jiang and H. Fang, *Journal of Crystal Growth*, 2017, **473**, 6–10.

[126] N. Bahlawane, P. A. Premkumar, Z. Tian, X. Hong, F. Qi and K. Kohse-Höinghaus, *Chemistry of Materials*, 2010, **22**, 92–100.

[127] K. Shao, Y. Tian and J. Zhang, *The Journal of Physical Chemistry A*, 2022, **126**, 1085–1093.

[128] K. Shao, J. Brunson, Y. Tian and J. Zhang, *International Journal of Mass Spectrometry*, 2022, **482**, 116933.

[129] S. Grimm, S.-J. Baik, P. Hemberger, A. Bodi, A. M. Kempf, T. Kasper and B. Atakan, *Physical Chemistry Chemical Physics*, 2021, **23**, 15059–15075.

[130] S. Grimm, S.-J. Baik, P. Hemberger, T. Kasper, A. M. Kempf and B. Atakan, *Journal of Materials Research*, 2022, **37**, 1558–1575.

[131] S. Grimm, P. Hemberger, T. Kasper and B. Atakan, *Advanced Materials Interfaces*, 2022, **9**, 2200192.

[132] G. P. Williams, *Vacuum*, 1982, **32**, 333–345.

[133] W. Knop, P. K. Pranzas and P. Schreiner, in *Neutrons and Synchrotron Radiation in Engineering Materials Science*, ed. W. Reimers, Wiley-VCH, Weinheim and Chichester, 2008.

[134] G. Margaritondo, *Journal of Vacuum Science & Technology A*, 2022, **40**, 033204.

[135] James Clerk Maxwell, *Philosophical Transactions of the Royal Society of London*, 1865, **155**, 459–512.

[136] A. Liénard, *L'Eclairage Electrique*, 1898, **16**, 5–53.

[137] H. C. Pollock, *American Journal of Physics*, 1983, **51**, 278–280.

[138] D. Iwanenko and I. Pomeranchuk, *Physical Review*, 1944, **65**, 343.

[139] F. R. Elder, A. M. Gurewitsch, R. V. Langmuir and H. C. Pollock, *Physical Review*, 1947, **71**, 829–830.

[140] J. Schwinger, *Physical Review*, 1949, **75**, 1912–1925.

[141] H. Baumgärtel, *Chemie in unserer Zeit*, 1994, **28**, 6–18.

[142] P. Willmott, *An Introduction to Synchrotron Radiation: Techniques and Applications*, Wiley, Hoboken New Jersey, Second edition edn., 2019.

[143] Z. Zhao, in *Synchrotron Radiation in Materials Science*, ed. C. Fan and Z. Zhao, Wiley-VCH, Weinheim, Germany, 2018.

[144] M. Böge, Proceedings of the 8th European Particle Accelerator Conference, 2002, pp. 39–43.

[145] M. Johnson, A. Bodi, L. Schulz and T. Gerber, *Nuclear Instruments and Methods in Physics Research Section A: Accelerators, Spectrometers, Detectors and Associated Equipment*, 2009, **610**, 597–603.

[146] S. Suga, A. Sekiyama and C. A. Tusche, *Photoelectron Spectroscopy: Bulk and Surface Electronic Structures*, Springer, Cham, Switzerland, Second edition edn., 2021, vol. volume 72.

[147] H. Hertz, *Annalen der Physik und Chemie*, 1887, **267**, 983–1000.

[148] E. Illenberger, *Gaseous Molecular Ions: An Introduction to Elementary Processes Induced by Ionization*, Steinkopff, Heidelberg, 1992, vol. 2.

[149] W. C. Wiley and I. H. McLaren, *Review of Scientific Instruments*, 1955, **26**, 1150–1157.

[150] G. H. Wannier, *Physical Review*, 1953, **90**, 817–825.

[151] G. Vall-Llosera, M. A. Huels, M. Coreno, A. Kivimäki, K. Jakubowska, M. Stankiewicz and E. Rachlew, *ChemPhysChem*, 2008, **9**, 1020–1029.

[152] P. Hemberger, A. Bodi, C. Schon, M. Steinbauer, K. H. Fischer, C. Kaiser and I. Fischer, *Physical Chemistry Chemical Physics*, 2012, **14**, 11920–11929.

[153] P. Hemberger, A. Bodi, T. Bierkandt, M. Köhler, D. Kaczmarek and T. Kasper, *Energy & Fuels*, 2021, **35**, 16265–16302.

[154] J. Z. Yang and Combustion Team, *Photoionization Cross Section Database (Version 2.0)*, 2017, http://flame.nsrl.ustc.edu.cn/database/.

[155] *NIST Chemistry WebBook, NIST Standard Reference Database 69*, ed. P. J. Linstrom and M. G. Mallard, 1997.

[156] T. A. Cool, J. Wang, K. Nakajima, C. A. Taatjes and A. Mcllroy, *International Journal of Mass Spectrometry*, 2005, **247**, 18–27.

[157] J. Wang, B. Yang, T. A. Cool, N. Hansen and T. Kasper, *International Journal of Mass Spectrometry*, 2008, **269**, 210–220.

[158] J. Pieper, S. Schmitt, C. Hemken, E. Davies, J. Wullenkord, A. Brockhinke, J. Krüger, G. A. Garcia, L. Nahon, A. Lucassen, W. Eisfeld and K. Kohse-Höinghaus, *Zeitschrift für Physikalische Chemie*, 2018, **232**, 153–187.

[159] A. M. Ellis, *Electronic and Photoelectron Spectroscopy: Fundamentals and Case Studies*, Cambridge University Press, Cambridge, 2005.

[160] D. Rösch, R. Almeida, B. Sztáray and D. L. Osborn, *The Journal of Physical Chemistry A*, 2022, **126**, 1761–1774.

[161] M. C. R. Cockett, *Chemical Society Reviews*, 2005, **34**, 935–948.

[162] D. Villarejo, *The Journal of Chemical Physics*, 1968, **48**, 4014–4026.

[163] T. Baer, W. B. Peatman and E. W. Schlag, *Chemical Physics Letters*, 1969, **4**, 243–247.

[164] W. B. Peatman, T. B. Borne and E. W. Schlag, *Chemical Physics Letters*, 1969, **3**, 492–497.

[165] R. Stockbauer, *International Journal of Mass Spectrometry and Ion Physics*, 1977, **25**, 89–101.

[166] W. Peatman, G. B. Kasting and D. J. Wilson, *Journal of Electron Spectroscopy and Related Phenomena*, 1975, **7**, 233–246.

[167] G. C. King, M. Zubek, P. M. Rutter and F. H. Read, *Journal of Physics E: Scientific Instruments*, 1987, **20**, 440–443.

[168] B. Tsai, T. Baer and M. L. Horovitz, *Review of Scientific Instruments*, 1974, **45**, 494–498.

[169] A. T. J. B. Eppink and D. H. Parker, *Review of Scientific Instruments*, 1997, **68**, 3477–3484.

[170] D. S. Baer, J. B. Paul, M. Gupta and A. O'Keefe, *Applied Physics B*, 2002, **75**, 261–265.

[171] B. Sztáray and T. Baer, *Review of Scientific Instruments*, 2003, **74**, 3763–3768.

[172] A. Bodi, M. Johnson, T. Gerber, Z. Gengeliczki, B. Sztáray and T. Baer, *Review of Scientific Instruments*, 2009, **80**, 034101.

[173] A. Bodi, P. Hemberger, T. Gerber and B. Sztáray, *Review of Scientific Instruments*, 2012, **83**, 083105.

[174] B. Sztáray, K. Voronova, K. G. Torma, K. J. Covert, A. Bodi, P. Hemberger, T. Gerber and D. L. Osborn, *The Journal of Chemical Physics*, 2017, **147**, 013944.

[175] W. Claassen, J. Bloem, W. Valkenburg and C. van den Brekel, *Journal of Crystal Growth*, 1982, **57**, 259–266.

[176] C. Kelly, D. Garg and P. N. Dyer, *Thin Solid Films*, 1992, **219**, 103–108.

[177] Z. J. Hu and K. J. Hüttinger, *Chemical Vapor Deposition*, 2000, **6**, 77–82.

[178] S. Ponton, H. Vergnes, D. Samelor, D. Sadowski, C. Vahlas and B. Caussat, *AIChE Journal*, 2018, **64**, 3958–3966.

[179] A. Kantrowitz and J. Grey, *Review of Scientific Instruments*, 1951, **22**, 328–332.

[180] G. B. Kistiakowsky and W. P. Slichter, *Review of Scientific Instruments*, 1951, **22**, 333–337.

[181] H. Haberland, U. Buck and M. Tolle, *Review of Scientific Instruments*, 1985, **56**, 1712–1716.

[182] D. R. Miller, in *Atomic and molecular beam methods*, ed. G. Scoles, Oxford Univ. Press, New York, 1988, pp. 14–53.

[183] Y. Tsutsumi, M. Ikegawa, T. Usui, Y. Ichikawa, K. Watanabe and J. Kobayashi, *Journal of Vacuum Science & Technology A: Vacuum, Surfaces, and Films*, 1996, **14**, 2337–2342.

[184] J. B. Anderson and J. B. Fenn, *Review of Scientific Instruments*, 1965, **8**, 780.

[185] H. Beijerinck and N. F. Verster, *Physica B+C*, 1981, **111**, 327–352.

[186] J. B. Anderson, *AIAA Journal*, 1972, **10**, 112.

[187] W. L. Hsu, M. C. McMaster, M. E. Coltrin and D. S. Dandy, *Japanese Journal of Applied Physics*, 1994, **33**, 2231–2239.

[188] D. Brinks, R. Hildner, E. M. H. P. van Dijk, F. D. Stefani, J. B. Nieder, J. Hernando and N. F. van Hulst, *Chemical Society Reviews*, 2014, **43**, 2476–2491.

[189] A. A. Onischuk, V. P. Strunin, M. A. Ushakova and V. N. Panfilov, *International Journal of Chemical Kinetics*, 1998, **30**, 99–110.

[190] M. Fikri, A. Makeich, G. Rollmann, C. Schulz and P. Entel, *The Journal of Physical Chemistry A*, 2008, **112**, 6330–6337.

[191] A. Desenfant, G. Laduye, G. L. Vignoles and G. Chollon, *Journal of Industrial and Engineering Chemistry*, 2021, **94**, 145–158.

[192] C. van den Brekel and L. Bollen, *Journal of Crystal Growth*, 1981, **54**, 310–322.

[193] A. A. Onischuk, V. P. Strunin, M. A. Ushakova and V. N. Panfilov, *Journal of Aerosol Science*, 1997, **28**, 207–222.

[194] K. Tonokura and M. Koshi, *Current Opinion in Solid State and Materials Science*, 2002, **6**, 479–485.

[195] N. Yang, S. K. Youn, C. E. Frouzakis and H. G. Park, *Carbon*, 2018, **130**, 607–613.

[196] S. Schröder, A. M. Hinz, T. Strunskus and F. Faupel, *The Journal of Physical Chemistry A*, 2021, **125**, 1661–1667.

[197] Y. Zhang, J. Xia, Q. Fang and Y. Li, *Combustion and Flame*, 2022, **237**, 111900.

[198] D. K. Russell, *Chemical Society reviews*, 1990, **19**, 407.

[199] D. K. Russell, G. P. Mills, J. B. Raynor and A. D. Workman, *Chemical Vapor Deposition*, 1998, **4**, 61–67.

[200] D. K. Russell and A. Yee, *New Journal of Chemistry*, 2005, **29**, 485–492.

[201] R. A. Berrigan, J. B. Metson and D. K. Russell, *Chemical Vapor Deposition*, 1998, **4**, 23–28.

[202] Q. Guan, K. N. Urness, T. K. Ormond, D. E. David, G. Barney Ellison and J. W. Daily, *International Reviews in Physical Chemistry*, 2014, **33**, 447–487.

[203] P. J. Weddle, C. Karakaya, H. Zhu, R. Sivaramakrishnan, K. Prozument and R. J. Kee, *International Journal of Chemical Kinetics*, 2018, **50**, 473–480.

[204] M. V. Zagidullin, R. I. Kaiser, D. P. Porfiriev, I. P. Zavershinskiy, M. Ahmed, V. N. Azyazov and A. M. Mebel, *The Journal of Physical Chemistry A*, 2018, **122**, 8819–8827.

[205] K. Shao, Y. Tian and J. Zhang, *International Journal of Mass Spectrometry*, 2021, **460**, 116476.

[206] X. Liu, J. Zhang, A. Vazquez, D. Wang and S. Li, *The Journal of Physical Chemistry A*, 2019, **123**, 10520–10528.

[207] J. M. Lemieux and J. Zhang, *International Journal of Mass Spectrometry*, 2014, **373**, 50–55.

[208] J. M. Lemieux, S. D. Chambreau and J. Zhang, *Chemical Physics Letters*, 2008, **459**, 49–53.

[209] S. Arrhenius, *Zeitschrift für Physikalische Chemie*, 1889, **4U**, 96–116.

[210] S. Arrhenius, *Zeitschrift für Physikalische Chemie*, 1889, **4U**, 226–248.

[211] K. Schwetlick, H. Dunken, G. Pretzschner, K. Scherzer and H.-J. Tiller, *Chemische Kinetik: Lehrbuch 6*, Dt. Verl. für Grundstoffindustrie, Leipzig, 5th edn., 1989, vol. 6.

[212] F. A. Lindemann, S. Arrhenius, I. Langmuir, N. R. Dhar, J. Perrin and W. C. McC. Lewis, *Transactions of the Faraday Society*, 1922, **17**, 598–606.

[213] C. N. Hinshelwood, *Proceedings of the Royal Society of London A: Mathematical and Physical Sciences*, 1926, **113**, 230–233.

[214] T. Bierkandt, P. Hemberger, P. Oßwald, D. Krüger, M. Köhler and T. Kasper, *Proceedings of the Combustion Institute*, 2019, **37**, 1579–1587.

[215] M. Hoener, D. Kaczmarek, T. Bierkandt, A. Bodi, P. Hemberger and T. Kasper, *Review of Scientific Instruments*, 2020, **91**, 045115.

[216] D. Schleier, E. Reusch, M. Gerlach, T. Preitschopf, D. P. Mukhopadhyay, N. Faßheber, G. Friedrichs, P. Hemberger and I. Fischer, *Physical Chemistry Chemical Physics*, 2021, **23**, 1539–1549.

[217] D. W. Kohn, H. Clauberg and P. Chen, *Review of Scientific Instruments*, 1992, **63**, 4003–4005.

[218] F. Holzmeier, I. Fischer, B. Kiendl, A. Krueger, A. Bodi and P. Hemberger, *Physical Chemistry Chemical Physics*, 2016, **18**, 9240–9247.

[219] T. Bierkandt, P. Hemberger, P. Oßwald, M. Köhler and T. Kasper, *Proceedings of the Combustion Institute*, 2017, **36**, 1223–1232.

[220] T. K. Ormond, A. M. Scheer, M. R. Nimlos, D. J. Robichaud, T. P. Troy, M. Ahmed, J. W. Daily, T. L. Nguyen, J. F. Stanton and G. B. Ellison, *The Journal of Physical Chemistry A*, 2015, **119**, 7222–7234.

[221] J. Bouwman, H. R. Hrodmarsson, G. B. Ellison, A. Bodi and P. Hemberger, *The Journal of Physical Chemistry A*, 2021, **125**, 1738–1746.

[222] D. L. Osborn, C. C. Hayden, P. Hemberger, A. Bodi, K. Voronova and B. Sztáray, *The Journal of Chemical Physics*, 2016, **145**, 164202.

[223] A. Bodi, B. Sztáray, T. Baer, M. Johnson and T. Gerber, *Review of Scientific Instruments*, 2007, **78**, 084102.

[224] P. Hemberger, X. Wu, Z. Pan and A. Bodi, *The Journal of Physical Chemistry A*, 2022, **126**, 2196–2210.

[225] F. Vietmeyer, *Diplomarbeit*, Universität Bielefeld, Bielefeld, 2009.

[226] Andras Bodi, *i(2)PEPICO software tools*, 15.10.2019, https://www.psi.ch/en/sls/vuv/pepico.

[227] T. Zhang, J. Wang, T. Yuan, X. Hong, L. Zhang and F. Qi, *The Journal of Physical Chemistry A*, 2008, **112**, 10487–10494.

[228] M. A. Siddiqi, R. A. Siddiqui and B. Atakan, *Surface and Coatings Technology*, 2007, **201**, 9055–9059.

[229] N. B. Morozova, S. V. Sysoev, I. K. Igumenov and A. N. Golubenko, *Journal of Thermal Analysis*, 1996, **46**, 1367–1373.

[230] S. Lau and B. Atakan, *Journal of Chemical & Engineering Data*, 2020, **65**, 1211–1221.

[231] W. A. Chupka, *The Journal of Chemical Physics*, 1993, **98**, 4520–4530.

[232] X. Wu, X. Zhou, S. Bjelić, P. Hemberger, B. Sztáray and A. Bodi, *Physical Chemistry Chemical Physics*, 2022, **24**, 1437–1446.

[233] J. Cui, M. G. Kast, B. A. Hammann, Y. Afriyie, K. N. Woods, P. N. Plassmeyer, C. K. Perkins, Z. L. Ma, D. A. Keszler, C. J. Page, S. W. Boettcher and S. E. Hayes, *Chemistry of Materials*, 2018, **30**, 7456–7463.

[234] Z. Li, Y. Xin, Y. Liu, H. Liu, D. Yu and J. Xiu, *Coatings*, 2021, **11**, 389.

[235] D. Samelor, L. Baggetto, R. Laloo, V. Turq, T. Duguet, D. Monceau and C. Vahlas, *Materials Science Forum*, 2018, **941**, 1846–1852.

[236] S. Zhang, L. Zheng, G. Wei, L. Guo, J. Li, R. Tu, L. Zhang, T. Goto and H. Ohmori, *International Journal of Applied Ceramic Technology*, 2019, **16**, 1356–1363.

[237] A. Michau, Y. Gazal, F. Addou, F. Maury, T. Duguet, R. Boichot, M. Pons, E. Monsifrot, H. Maskrot and F. Schuster, *Surface and Coatings Technology*, 2019, **375**, 894–902.

[238] J. S. Pérez, F. J. López and E. S. Pérez, *Journal of Applied Research and Technology*, 2020, **18**, 95–100.

[239] R. Tu, Y. Yuan, L. Guo, J. Li, S. Zhang, M. Yang, Q. Li, L. Zhang, T. Goto, H. Ohmori, J. Shi and H. Li, *International Journal of Applied Ceramic Technology*, 2019, **16**, 2265–2272.

[240] *Chemical Vapour Deposition: Precursors, Processes and Applications*, ed. M. L. Hitchman and A. C. Jones, Royal Society of Chemistry, Cambridge, UK, 2009.

[241] L. G. Hubert-Pfalzgraf, *Applied Organometallic Chemistry*, 1992, **6**, 627–643.

[242] M. Danzinger, R. Haubner and B. Lux, *International Journal of Refractory Metals and Hard Materials*, 1996, **14**, 59–67.

[243] C. Pflitsch, A. Muhsin, U. Bergmann and B. Atakan, *Surface and Coatings Technology*, 2006, **201**, 73–81.

[244] A. Ito, R. Tu and T. Goto, *Surface and Coatings Technology*, 2010, **204**, 2170–2174.

[245] P. Rodriguez, B. Caussat, C. Ablitzer, X. Iltis and M. Brothier, *Chemical Engineering Research and Design*, 2013, **91**, 2477–2483.

[246] S. Li, Di He, X. Liu, S. Wang and L. Jiang, *Journal of Nuclear Materials*, 2012, **420**, 405–408.

[247] T. Goto, *Journal of Wuhan University of Technology-Materials Science Edition*, 2016, **31**, 1–5.

[248] F. A. D. Battaglin, E. S. Prado, L. Caseli, T. F. d. Silva, M. H. Tabacniks, N. C. d. Cruz and E. C. Rangel, *Materials Research*, 2017, **20**, 926–936.

[249] N. Hansen, W. Li, M. E. Law, T. Kasper, P. R. Westmoreland, B. Yang, T. A. Cool and A. Lucassen, *Physical Chemistry Chemical Physics*, 2010, **12**, 12112–12122.

[250] D. Felsmann, K. Moshammer, J. Krüger, A. Lackner, A. Brockhinke, T. Kasper, T. Bierkandt, E. Akyildiz, N. Hansen, A. Lucassen, P. Oßwald, M. Köhler, G. A. Garcia, L. Nahon, P. Hemberger, A. Bodi, T. Gerber and K. Kohse-Höinghaus, *Proceedings of the Combustion Institute*, 2015, **35**, 779–786.

[251] T. Wang, S. Li, B. Yang, C. Huang and Y. Li, *The Journal of Physical Chemistry B*, 2007, **111**, 2449–2455.

[252] T. Zhang, L. Zhang, X. Hong, K. Zhang, F. Qi, C. K. Law, T. Ye, P. Zhao and Y. Chen, *Combustion and Flame*, 2009, **156**, 2071–2083.

[253] A. Bodi, P. Hemberger, D. L. Osborn and B. Sztáray, *The Journal of Physical Chemistry Letters*, 2013, **4**, 2948–2952.

[254] J. Bourgalais, Z. Gouid, O. Herbinet, G. A. Garcia, P. Arnoux, Z. Wang, L.-S. Tran, G. Vanhove, M. Hochlaf, L. Nahon and F. Battin-Leclerc, *Physical Chemistry Chemical Physics*, 2020, **22**, 1222–1241.

[255] M. J. Frisch, G. W. Trucks, H. B. Schlegel, G. E. Scuseria, M. A. Robb, J. R. Cheeseman, G. Scalmani, V. Barone, G. A. Petersson, H. Nakatsuji, X. Li, M. Caricato, A. V. Marenich, J. Bloino, B. G. Janesko, R. Gomperts, B. Mennucci, H. P. Hratchian, J. V. Ortiz, A. F. Izmaylov, J. L. Sonnenberg, D. Williams-Young, F. Ding, F. Lipparini, F. Egidi, J. Goings, B. Peng, A. Petrone, T. Henderson, D. Ranasinghe, V. G. Zakrzewski, J. Gao, N. Rega, G. Zheng, W. Liang, M. Hada, M. Ehara, K. Toyota, R. Fukuda, J. Hasegawa, M. Ishida, T. Nakajima, Y. Honda, O. Kitao, H. Nakai, T. Vreven, K. Throssell, Montgomery, Jr., J. A., J. E. Peralta, F. Ogliaro, M. J. Bearpark, J. J. Heyd, E. N. Brothers, K. N. Kudin, V. N.

Staroverov, T. A. Keith, R. Kobayashi, J. Normand, K. Raghavachari, A. P. Rendell, J. C. Burant, S. S. Iyengar, J. Tomasi, M. Cossi, J. M. Millam, M. Klene, C. Adamo, R. Cammi, J. W. Ochterski, R. L. Martin, K. Morokuma, O. Farkas, J. B. Foresman and D. J. Fox, *Gaussian 16 Revision A.03*, 2016.

[256] J. A. Montgomery, M. J. Frisch, J. W. Ochterski and G. A. Petersson, *The Journal of Chemical Physics*, 2000, **112**, 6532–6542.

[257] L. A. Curtiss, P. C. Redfern and K. Raghavachari, *The Journal of Chemical Physics*, 2007, **126**, 084108.

[258] C. Peng and H. Bernhard Schlegel, *Israel Journal of Chemistry*, 1993, **33**, 449–454.

[259] T. Yu, X. Wu, X. Zhou, A. Bodi and P. Hemberger, *Combustion and Flame*, 2020, **222**, 123–132.

[260] V. A. Mozhayskiy and A. I. Krylov, *ezSpectrum*, http://iopenshell.usc.edu/downloads.

[261] R. Bauernschmitt and R. Ahlrichs, *Chemical Physics Letters*, 1996, **256**, 454–464.

[262] J. H. Baraban, D. E. David, G. B. Ellison and J. W. Daily, *Review of Scientific Instruments*, 2016, **87**, 014101.

[263] K. Huang, *Statistical Mechanics*, New York, Wiley, 2nd edn., 1987.

[264] Ansys® Academic Multiphysics, Release 19.1.

[265] C. J. Geankoplis, *Transport Processes and Unit Operations*, PTR Prentice Hall, Engelwood Cliffs, N.J., 3rd edn., 1993.

[266] P. L. Roe, *Annual Review of Fluid Mechanics*, 1986, **18**, 337–365.

[267] E. Bich, J. Millat and E. Vogel, *Journal of Physical and Chemical Reference Data*, 1990, **19**, 1289–1305.

[268] A. Ustinov, V. I. Vovna and O. M. Ustinova, *Journal of Electron Spectroscopy and Related Phenomena*, 1998, **88-91**, 103–108.

[269] M. J. Lacey and J. S. Shannon, *Organic Mass Spectrometry*, 1972, **6**, 931–937.

[270] I. Antonov, K. Voronova, M.-W. Chen, B. Sztáray, P. Hemberger, A. Bodi, D. L. Osborn and L. Sheps, *The Journal of Physical Chemistry A*, 2019, **123**, 5472–5490.

[271] P. Hemberger, V. B. F. Custodis, A. Bodi, T. Gerber and J. A. van Bokhoven, *Nature Communications*, 2017, **8**, 15946.

[272] S. Liang, P. Hemberger, N. M. Neisius, A. Bodi, H. Grützmacher, J. Levalois-Grützmacher and S. Gaan, *Chemistry*, 2015, **21**, 1073–1080.

[273] B. K. Cunha de Miranda, C. Alcaraz, M. Elhanine, B. Noller, P. Hemberger, I. Fischer, G. A. Garcia, H. Soldi-Lose, B. Gans, L. A. V. Mendes, S. Boyé-Péronne, S. Douin, J. Zabka and P. Botschwina, *The Journal of Physical Chemistry A*, 2010, **114**, 4818–4830.

[274] A. W. Potts and T. A. Williams, *Journal of Electron Spectroscopy and Related Phenomena*, 1974, **3**, 3–17.

[275] B. Niu, D. A. Shirley and Y. Bai, *The Journal of Chemical Physics*, 1993, **98**, 4377–4390.

[276] M. S. Banna and D. A. Shirley, *Journal of Electron Spectroscopy and Related Phenomena*, 1976, **8**, 255–270.

[277] P. Hemberger, M. Lang, B. Noller, I. Fischer, C. Alcaraz, B. K. Cunha de Miranda, G. A. Garcia and H. Soldi-Lose, *The Journal of Physical Chemistry A*, 2011, **115**, 2225–2230.

[278] Z. Z. Yang, L. S. Wang, Y. T. Lee, D. A. Shirley, S. Y. Huang and W. A. Lester, *Chemical Physics Letters*, 1990, **171**, 9–13.

[279] J. Krüger, G. A. Garcia, D. Felsmann, K. Moshammer, A. Lackner, A. Brockhinke, L. Nahon and K. Kohse-Höinghaus, *Physical Chemistry Chemical Physics*, 2014, **16**, 22791–22804.

[280] B. Niu, Y. Bai and D. A. Shirley, *The Journal of Chemical Physics*, 1993, **99**, 2520–2532.

[281] E. E. Rennie, A.-M. Boulanger, P. M. Mayer, D. M. P. Holland, D. A. Shaw, L. Cooper and L. G. Shpinkova, *The Journal of Physical Chemistry A*, 2006, **110**, 8663–8675.

[282] G. Y. Matti, O. I. Osman, J. E. Upham, R. J. Suffolk and H. W. Kroto, *Journal of Electron Spectroscopy and Related Phenomena*, 1989, **49**, 195–201.

[283] A. J. Yencha, M. R. Siggel-King, G. C. King, A. E. Malins and M. Eypper, *Journal of Electron Spectroscopy and Related Phenomena*, 2013, **187**, 65–71.

[284] G. Bieri, F. Burger, E. Heilbronner and J. P. Maier, *Helvetica Chimica Acta*, 1977, **60**, 2213–2233.

[285] P. Masclet, G. Mouvier and J. F. Bocquet, *Journal de Chimie Physique*, 1981, **78**, 99–106.

[286] G. Bieri, J. D. Dill, E. Heilbronner, J. P. Maier and J. L. Ripoll, *Helvetica Chimica Acta*, 1977, **60**, 629–637.

[287] N. Hansen, S. J. Klippenstein, J. A. Miller, J. Wang, T. A. Cool, M. E. Law, P. R. Westmoreland, T. Kasper and K. Kohse-Höinghaus, *The Journal of Physical Chemistry A*, 2006, **110**, 4376–4388.

[288] F. Brogli, E. Heilbronner, V. Hornung and E. Kloster-Jensen, *Helvetica Chimica Acta*, 1973, **56**, 2171–2178.

[289] S. Soorkia, A. J. Trevitt, T. M. Selby, D. L. Osborn, C. A. Taatjes, K. R. Wilson and S. R. Leone, *The Journal of Physical Chemistry A*, 2010, **114**, 3340–3354.

[290] J. Bouwman, A. Bodi, J. Oomens and P. Hemberger, *Physical Chemistry Chemical Physics*, 2015, **17**, 20508–20514.

[291] M. Gerlach, A. Bodi and P. Hemberger, *Physical Chemistry Chemical Physics*, 2019, **21**, 19480–19487.

[292] P. Bischof, R. Gleiter, H. Hopf and F. T. Lenich, *Journal of the American Chemical Society*, 1975, **97**, 5467–5472.

[293] T. Veszprémi, L. Nyulászi and J. Nagy, *Journal of Organometallic Chemistry*, 1987, **331**, 175–180.

[294] L. Klasinc, B. Kovac and H. Gusten, *Pure and Applied Chemistry*, 1983, **55**, 289–298.

[295] T. Kobayashi and S. Nagakura, *Bulletin of the Chemical Society of Japan*, 1974, **47**, 2563–2572.

[296] H. W. Jochims, H. Rasekh, E. Rühl, H. Baumgärtel and S. Leach, *Chemical Physics*, 1992, **168**, 159–184.

[297] T. Kobayashi, K. Yokota and S. Nagakura, *Journal of Electron Spectroscopy and Related Phenomena*, 1973, **2**, 449–454.

[298] J. P. Maier and D. W. Turner, *Journal of the Chemical Society, Faraday Transactions 2*, 1973, **69**, 196–206.

[299] V. Galasso, F. P. Colonna and G. Distefano, *Journal of Electron Spectroscopy and Related Phenomena*, 1977, **10**, 227–237.

[300] M. Meot-Ner, *The Journal of Physical Chemistry*, 1980, **84**, 2716–2723.

[301] A. Bodi, T. Baer, N. K. Wells, D. Fakhoury, D. Klecyngier and J. P. Kercher, *Physical Chemistry Chemical Physics*, 2015, **17**, 28505–28509.

[302] J. G. Thakare, C. Pandey, M. M. Mahapatra and R. S. Mulik, *Metals and Materials International*, 2021, **27**, 1947–1968.

[303] S. Wu, Y. Zhao, W. Li, W. Liu, Y. Wu and F. Liu, *Coatings*, 2021, **11**, 79.

[304] I. Stambolova, O. Dimitrov, M. Shipochka, S. Yordanov, V. Blaskov, S. Vassilev, B. Jivov, S. Simeonova, K. Balashev, N. Grozev and L. Lakov, *Journal of Physics: Conference Series*, 2020, **1492**, 012025.

[305] A. Méndez-López, O. Zelaya-Ángel, M. Toledano-Ayala, I. Torres-Pacheco, J. F. Pérez-Robles and Y. J. Acosta-Silva, *Crystals*, 2020, **10**, 454.

[306] J. H. Lee, B.-E. Park, D. Thompson, M. Choe, Z. Lee, I.-K. Oh, W.-H. Kim and H. Kim, *Thin Solid Films*, 2020, **701**, 137950.

[307] M. A. Mohammed, *NeuroQuantology*, 2020, **18**, 22–27.

[308] J. P. B. Silva, K. C. Sekhar, H. Pan, J. L. MacManus-Driscoll and M. Pereira, *ACS Energy Letters*, 2021, **6**, 2208–2217.

[309] L. Yao, F. Liang, J. Jin, B. V. Chowdari, J. Yang and Z. Wen, *Chemical Engineering Journal*, 2020, **389**, 124403.

[310] S. Codato, G. Carta, G. Rossetto, G. A. Rizzi, P. Zanella, P. Scardi and M. Leoni, *Chemical Vapor Deposition*, 1999, **5**, 159–164.

[311] R. C. Smith, T. Ma, N. Hoilien, L. Y. Tsung, M. J. Bevan, L. Colombo, J. Roberts, S. A. Campbell and W. L. Gladfelter, *Advanced Materials for Optics and Electronics*, 2000, **10**, 105–114.

[312] V. V. Srdić and M. Winterer, *Journal of the European Ceramic Society*, 2006, **26**, 3145–3151.

[313] F. Jasim, *Journal of Thermal Analysis*, 1991, **37**, 149–153.

[314] V. V. Rodaev, S. S. Razlivalova, A. O. Zhigachev, V. M. Vasyukov and Y. I. Golovin, *Polymers*, 2019, **11**, 1067.

[315] R. M. Mahfouz, G.-W. Ahmed, A. I. Al-Wassil, M. Siddiqui and A. M. Al-Otaibi, *Radiation Effects and Defects in Solids*, 2013, **168**, 950–958.

[316] H. Wang, C. Xia, G. Meng and D. Peng, *Materials Letters*, 2000, **44**, 23–28.

[317] L. J. Espinoza-Pérez, E. López-Honorato, L. A. González and V. García-Montalvo, *Ceramics International*, 2021, **47**, 4611–4624.

[318] X. Liu, J. Zhang, A. Vazquez, D. Wang and S. Li, *Physical Chemistry Chemical Physics*, 2018, **20**, 18782–18789.

[319] M. Pulver and G. Wahl, in *Proceedings of the Fourteenth International Conference and EUROCVD-11; held as part of the 192nd Electrochemical Society Meeting in Paris, France, September 5 - 9, 1997*, ed. M. D. Allendorf and C. Bernard, Electrochemical Society, Pennington, New Jersey, 1997, pp. 960–967.

[320] L. K. L. Dean, G. C. DiDonato, T. D. Wood and K. L. Busch, *Inorganic Chemistry*, 1988, **27**, 4622–4627.

[321] E. A. Fogleman, H. Koizumi, J. P. Kercher, B. Sztáray and T. Baer, *The Journal of Physical Chemistry A*, 2004, **108**, 5288–5294.

[322] I. Fischer and S. T. Pratt, *Physical Chemistry Chemical Physics*, 2022, **24**, 1944–1959.

[323] J. A. Miller and S. J. Klippenstein, *The Journal of Physical Chemistry A*, 2003, **107**, 7783–7799.

[324] S. E. Stein, J. A. Walker, M. M. Suryan and A. Fahr, *Symposium (International) on Combustion*, 1991, **23**, 85–90.

[325] W. von Niessen, G. Bieri and L. Åsbrink, *Journal of Electron Spectroscopy and Related Phenomena*, 1980, **21**, 175–191.

[326] T. Kobayashi and S. Nagakura, *Journal of Electron Spectroscopy and Related Phenomena*, 1975, **7**, 488–491.

[327] I. Fragala, G. Condorelli, A. Tondello and A. Cassol, *Inorganic Chemistry*, 1978, **17**, 3175–3179.

[328] S. Gozem and A. I. Krylov, *WIREs Computational Molecular Science*, 2021, **7**, 551.

[329] R. S. Tranter, A. L. Kastengren, J. P. Porterfield, J. B. Randazzo, J. P. Lockhart, J. H. Baraban and G. B. Ellison, *Proceedings of the Combustion Institute*, 2017, **36**, 4603–4610.

[330] T. J. Kealy and P. L. Pauson, *Nature*, 1951, **168**, 1039–1040.

[331] S. A. Miller, J. A. Tebboth and J. F. Tremaine, *Journal of the Chemical Society (Resumed)*, 1952, 632.

[332] D. Astruc, *European Journal of Inorganic Chemistry*, 2017, **2017**, 6–29.

[333] H. Werner, *Angewandte Chemie (International ed. in English)*, 2012, **51**, 6052–6058.

[334] M. Mukaida, I. Hiyama, T. Tsunoda and Y. Imai, *Thin Solid Films*, 2001, **381**, 214–218.

[335] T. Gao, C. Zhou, Y. Zhang, Z. Jin, H. Yuan and D. Xiao, *Journal of Materials Chemistry A*, 2018, **6**, 21577–21584.

[336] X. Liu, X. Liang, H. Lou, H. Wang, H. Li, S. Zhang, S. Zhu, W. Han and B. Zhou, *Sustainable Energy & Fuels*, 2021, **5**, 1067–1074.

[337] A. E. Elwardany, M. N. Marei, Y. Eldrainy, R. M. Ali, M. Ismail and M. M. El-kassaby, *Fuel*, 2020, **270**, 117574.

[338] T. Hirasawa, C.-J. Sung, Z. Yang, A. Joshi and H. Wang, *Combustion and Flame*, 2004, **139**, 288–299.

[339] S. Huang, R. Yang, J. Wang, S. Chang, X. Gou, C. Hua and J. Zhao, *Journal of Heterocyclic Chemistry*, 2020, **57**, 2854–2861.

[340] D. R. Chen, M. Chitranshi, M. Schulz and V. Shanov, *Nano LIFE*, 2019, **09**, 1930002.

[341] H. W. Zhu, C. L. Xu, D. H. Wu, B. Q. Wei, R. Vajtai and P. M. Ajayan, *Science*, 2002, **296**, 884–886.

[342] A. Moisala, A. G. Nasibulin, D. P. Brown, H. Jiang, L. Khriachtchev and E. I. Kauppinen, *Chemical Engineering Science*, 2006, **61**, 4393–4402.

[343] M. D. Yadav, A. W. Patwardhan, J. B. Joshi and K. Dasgupta, *Chemical Engineering Journal*, 2019, **377**, 119895.

[344] V. Y. Iakovlev, D. V. Krasnikov, E. M. Khabushev, A. A. Alekseeva, A. K. Grebenko, A. P. Tsapenko, B. Y. Zabelich, J. V. Kolodiazhnaia and A. G. Nasibulin, *Chemical Engineering Journal*, 2020, **383**, 123073.

[345] E. M. Khabushev, D. V. Krasnikov, J. V. Kolodiazhnaia, A. V. Bubis and A. G. Nasibulin, *Carbon*, 2020, **161**, 712–717.

[346] S. Zghal, I. Jedidi, M. Cretin, S. Cerneaux and M. Abdelmouleh, *Diamond and Related Materials*, 2020, **101**, 107557.

[347] M. D. Yadav and K. Dasgupta, *Industrial & Engineering Chemistry Research*, 2021, **60**, 2187–2196.

[348] R. Bhatia and V. Prasad, *Solid State Communications*, 2010, **150**, 311–315.

[349] P. Lassègue, L. Noé, M. Monthioux and B. Caussat, *Physica Status Solidi C*, 2015, **12**, 861–868.

[350] A. Peña, J. Puerta, A. Guerrero, E. Cañizales and J. L. Brito, *Journal of Nanotechnology*, 2012, **2012**, 1–5.

[351] S. A. Rashid, M. Z. A. Rashid, M. A. Musa and S. H. Othman, *Asia-Pacific Journal of Chemical Engineering*, 2013, **8**, 254–261.

[352] M. D. Yadav, K. Dasgupta, A. W. Patwardhan, A. Kaushal and J. B. Joshi, *Chemical Engineering Science*, 2019, **196**, 91–103.

[353] K. Kuwana and K. Saito, *Carbon*, 2005, **43**, 2088–2095.

[354] D. He, H. Li and J. Bai, *Carbon*, 2011, **49**, 5359–5372.

[355] K. Elihn and K. Larsson, *Thin Solid Films*, 2004, **458**, 325–329.

[356] L. M. Dyagileva, E. I. Tsyganova and Y. A. Aleksandrov, *Russian Chemical Reviews*, 1988, **57**, 316–325.

[357] W. Wasel, K. Kuwana, P. T. Reilly and K. Saito, *Carbon*, 2007, **45**, 833–838.

[358] P. Schissel, D. J. McAdoo, E. Hedaya and D. W. McNeil, *The Journal of Chemical Physics*, 1968, **49**, 5061–5066.

[359] A. Révész, L. Szepes, T. Baer and B. Sztáray, *Journal of the American Chemical Society*, 2010, **132**, 17795–17803.

[360] J. Opitz and P. Härter, *International Journal of Mass Spectrometry and Ion Processes*, 1992, **121**, 183–199.

[361] S.-J. Han, M. Yang, C. Hwang, D. Woo, J. Hahn, H. Kang and Y. Chung, *International Journal of Mass Spectrometry*, 1998, **181**, 59–66.

[362] J. Wang, L. Sheng and Y. Zhang, *Chinese Journal of Chemical Physics*, 2004, **17(2)**, 121–125.

[363] T. G. Rowland, B. Sztáray and P. B. Armentrout, *The Journal of Physical Chemistry A*, 2013, **117**, 1299–1309.

[364] A. K. Vasiliou, K. M. Piech, B. Reed, X. Zhang, M. R. Nimlos, M. Ahmed, A. Golan, O. Kostko, D. L. Osborn, D. E. David, K. N. Urness, J. W. Daily, J. F. Stanton and G. B. Ellison, *The Journal of Chemical Physics*, 2012, **137**, 164308.

[365] R. Gleiter, M. C. Bohm and R. D. Ernst, *Journal of Electron Spectroscopy and Related Phenomena*, 1984, **33**, 269–278.

[366] B. Sztáray, A. Bodi and T. Baer, *Journal of Mass Spectrometry*, 2010, **45**, 1233–1245.

[367] J. M. Dyke, B. W. J. Gravenor, R. A. Lewis and A. Morris, *Molecular Physics*, 1982, **15**, 4523–4534.

[368] P. Hemberger, G. da Silva, A. J. Trevitt, T. Gerber and A. Bodi, *Physical Chemistry Chemical Physics*, 2015, **17**, 30076–30083.

[369] C. Cauletti, J. C. Green, M. Kelly, P. Powell, J. van Tilborg, J. Robbins and J. Smart, *Journal of Electron Spectroscopy and Related Phenomena*, 1980, **19**, 327–353.

[370] C. Baker and D. W. Turner, *Proceedings of the Royal Society of London, Series A: Mathematical and Physical Sciences*, 1968, **308**, 19–37.

[371] F. Brogli, E. Heilbronner, J. Wirz, E. Kloster-Jensen, R. G. Bergman, K. P. C. Vollhardt and A. J. Ashe, *Helvetica Chimica Acta*, 1975, **58**, 2620–2645.

[372] M. F. Ryan, J. R. Eyler and D. E. Richardson, *Journal of the American Chemical Society*, 1992, **114**, 8611–8619.

[373] M. Swart, *Inorganica Chimica Acta*, 2007, **360**, 179–189.

[374] X. Wu, Z. Pan, S. Bjelić, P. Hemberger and A. Bodi, *Journal of Analytical and Applied Pyrolysis*, 2022, **161**, 105410.

[375] L. Brissonneau, R. Sahnoun, C. Mijoule and C. Vahlas, *Journal of the Electrochemical Society*, 2000, **147**, 1443.

[376] Z. Pan, A. Puente-Urbina, A. Bodi, J. A. van Bokhoven and P. Hemberger, *Chemical Science*, 2021, **12**, 3161–3169.

[377] A. E. Long, S. S. Merchant, A. G. Vandeputte, H.-H. Carstensen, A. J. Vervust, G. B. Marin, K. M. van Geem and W. H. Green, *Combustion and Flame*, 2018, **187**, 247–256.

[378] C. Cavallotti, D. Polino, A. Frassoldati and E. Ranzi, *The Journal of Physical Chemistry A*, 2012, **116**, 3313–3324.

[379] B. Yang, J. Wang, T. A. Cool, N. Hansen, S. Skeen and D. L. Osborn, *International Journal of Mass Spectrometry*, 2012, **309**, 118–128.

[380] C. R. Brundle and M. B. Robin, *Journal of the American Chemical Society*, 1970, **92**, 5550–5555.

[381] T. K. Ormond, P. Hemberger, T. P. Troy, M. Ahmed, J. F. Stanton and G. B. Ellison, *Molecular Physics*, 2015, **113**, 2350–2358.

[382] A. Lifshitz and M. Frenklach, *The Journal of Physical Chemistry*, 1975, **79**, 686–692.

[383] I. V. Tokmakov, L. V. Moskaleva and M. C. Lin, *International Journal of Chemical Kinetics*, 2004, **36**, 139–151.

[384] L. Brissonneau, A. Reynes and C. Vahlas, *Chemical Vapor Deposition*, 1999, **5**, 281–290.

[385] G. T. Linteris, M. D. Rumminger, V. Babushok and W. Tsang, *Proceedings of the Combustion Institute*, 2000, **28**, 2965–2972.

[386] J. Kohout, *Molecules*, 2021, **26**, 7162.

[387] G. A. Bird, *Molecular Gas Dynamics and the Direct Simulation of Gas Flows*, Clarendon Press, Oxford, Reprinted. edn., 2003, vol. 42.

[388] Morris, Hannon and Garcia, *Physical Review A: Atomic, Molecular, and Optical Physics*, 1992, **46**, 5279–5281.

[389] E. N. Fuller, P. D. Schettler and J. C. Giddings, *Industrial & Engineering Chemistry*, 1966, **58**, 18–27.

[390] N. S. Hush, M. K. Livett, J. B. Peel and G. D. Willett, *Australian Journal of Chemistry*, 1987, **40**, 599.

[391] G. Karniadakis, *Microflows and Nanoflows: Fundamentals and Simulation*, Springer, New York, NY, 2005, vol. v.29.

Appendix A

Supplementary Material Chapter 4

Reprint of the supplementary material of the $Al(acac)_3$ paper [129] with permission from the Royal Society of Chemistry (RSC) with minor modifications to adhere to the overall style of this thesis.

A.1 Numerical Simulation of the Microreactor

A.1.1 General Equations and Assumptions

The Navier-Stokes equations contain mass continuity and momentum conservation written as:

$$\frac{\partial \rho}{\partial t} + \frac{\partial(\rho \bar{u}_i)}{\partial x_i} = 0, \tag{A.1}$$

$$\frac{\partial(\rho \bar{u}_i)}{\partial t} + \frac{\partial(\rho \bar{u}_i \bar{u}_j)}{\partial x_j} = -\frac{\partial p}{\partial x_j} + \frac{\partial}{\partial x_j}\left[\mu\left(\frac{\partial u_i}{\partial x_j} + \frac{\partial u_j}{\partial x_i}\right) - \rho\overline{u_i' u_j'}\right], \tag{A.2}$$

where μ is the dynamic viscosity. In the present work, the Knudsen number (Kn) is used as key parameter to determine the rarefaction level of the flow field region. The Reynolds and Mach number define the local Kn as follows:

$$Kn = \frac{\lambda}{L}, \tag{A.3}$$

$$Re = \frac{\rho u D}{\mu}. \tag{A.4}$$

Generally, depending on the value of Kn, the flow region can be divided into a continuous flow region (Kn<0.01), a slip flow region (0.01<Kn<0.1), a transition flow region (0.1<Kn<10), and a freemolecular flow region (Kn>10). Detailed transition of flow regimes based on the Knudsen number can be found elsewhere

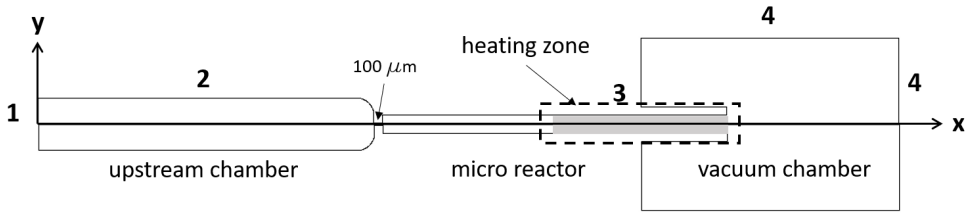

Figure A.1: Two-dimensional axisymmetric geometry for the present simulation.

[387]. By applying slip boundary condition, a simple approximation for slip fluid velocity at the wall is:

$$v_{\text{slip}} = l_{\text{s}} \frac{\partial v}{\partial n}, \tag{A.5}$$

where n denotes the normal vector to the wall, and l_{s} is the slip length. The main difficulty to define the slip velocity comes from the treatment of the slip length. In the present work, the slip length is l_{s} calculated according to Morris et al. [388]:

$$l_{\text{s}} = \alpha \cdot L \cdot Kn. \tag{A.6}$$

The model constant α is suggested as 1.15 in their work. The heated length (10 mm) of the reactor is used as the characteristic length L.

A.1.2 Computational Domain and Numerical Setup

The computational domain is set up as axisymmetric two-dimensional geometry as shown in Fig. A.1 with detailed boundary conditions listed in Tab. A.1.

In the present work, a cell size of 10 µm is used for the complete computational domain, in order to assure accurate results, while keeping the computational costs at a minimum. Applying this grid size gives us more than ten nodes in radial direction to resolve the flow field of a tiny pinhole (100 µm), which represents the connection between evaporator (see Fig. A.1 No. 2) and reactor (see Fig. A.1 No. 3). To test the influence of a further refinement of the mesh size on the simulation results, we halved the cell size. There is no significant difference of the calculated flow field properties, as demonstrated in Fig. A.2. Thus, we conclude that the

Table A.1: Boundary conditions for the domain in Fig. A.1.

No.	**Boundary** type	**Pressure** [mbar]	**Temperature** [K]
1	Inlet	550, 1600	293.15
2	No-slip wall	–	405.15
3	Slip wall	–	423.15 –1273.15
4	Outlet	6×10^{-5}	–
5	Symmetric	–	–

cell size of 10 µm is sufficient to resolve the present computational domain at the conditions evaluated in this study.

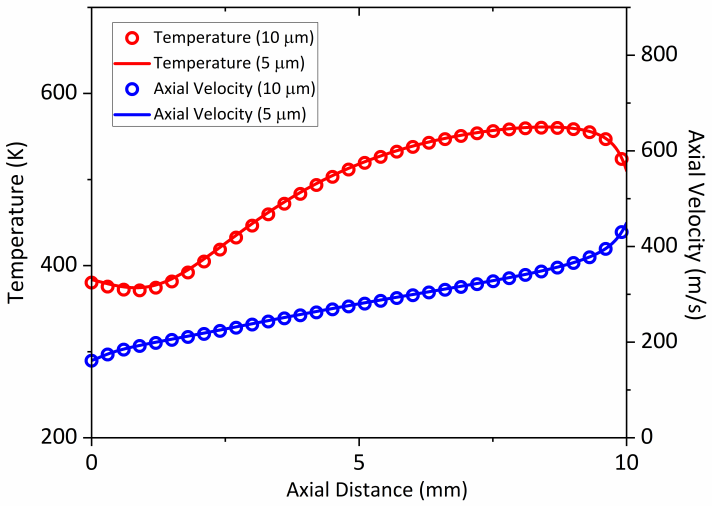

Figure A.2: Axial profiles of the temperature and axial velocity for an outer surface temperature of 623 K at two grid sizes, 5 µm and 10 µm.

A.1.3 Flow Regime Characteristics in the Heated Zone

Figure A.3 shows the axial profiles of Kn in the heated zone of the reactor at wall temperatures of 553.15, 673.15 and 833.15 K. If the outer surface temperature is increased, the flow in the heating zone has a higher Kn. Since the range of Kn at the experimental outer surface temperatures of 348–1273 K is $0.005 \leq Kn \leq 0.02$, we can assume that the flow in microreactor is located in the slip flow region.

A.1.4 Validation of the Simulation

To validate the feasibility of the present simulation method, additional simulations were performed with the same conditions that were used for the simulation of a microreactor by Weddle et al. [203]. A detailed description of the geometry and operating parameters can be found elsewhere [203]. Our simulation reproduced Weddle's conditions fairly well and shows a good agreement for important flow properties, as temperature and axial velocity, as shown in Fig. A.4. The deviations at the outlet section of the reactor ($x > 30$ mm) can be explained by the simulation domain used in both studies. Our domain does include the downstream vacuum chamber (see Fig. A.1 No. 4), in which the flow is expanded, whereas the reference test case does only consider the microreactor as simulation domain.

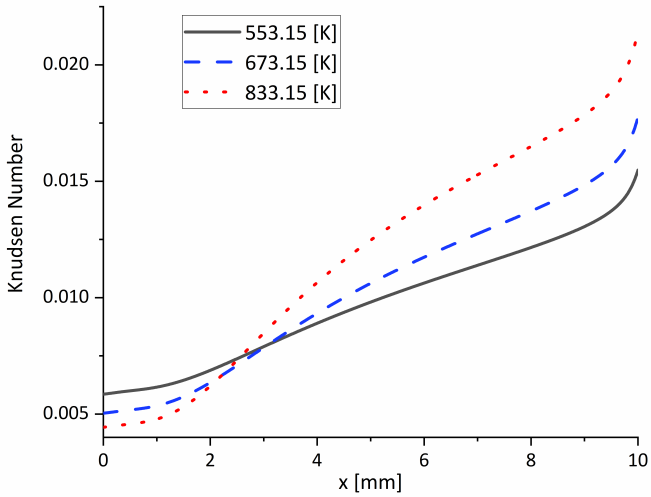

Figure A.3: Axial profile of the local Knudsen number for various experimental surface temperatures.

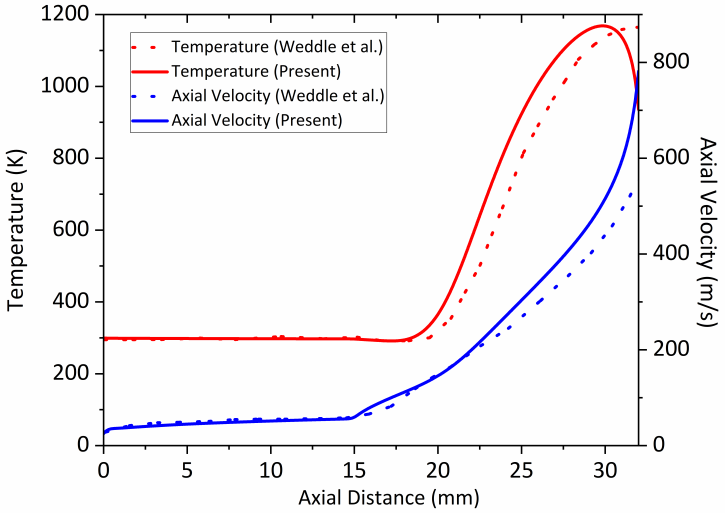

Figure A.4: Axial centerline profiles of temperature (red) and axial velocity (blue) for a wall temperature of 1500 K and 1700 K. Data from Weddle et al. [203]: dotted; our simulation: lines.

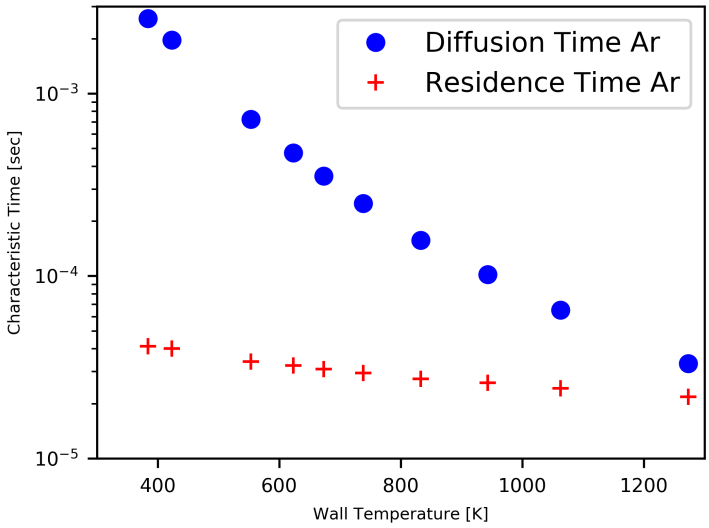

Figure A.5: Comparison of residence and diffusion time for $Al(C_5H_7O_2)_3$ in argon.

A.1.5 Effect of Wall Reactions

Even though the residence time in the reaction (heating) zone is significantly smaller than in typical flow reactors, it is necessary to check whether surface reactions may dominate the mechanism under the experimental conditions. Guan et al. [202] tried to explain the influence of wall reactions by a comparison between the residence time and the characteristic time for radial diffusion expressed as $\tau_{diff} = r^2/D$. We also used this approach for our conditions, where r is the radius of the SiC microreactor and D is denoted as the diffusion coefficient of aluminium acetylacetonate in argon. Since, to our knowledge, there is no available data in the literature for the diffusion coefficient (aluminum acetylacetonate in argon), we approximated the diffusion coefficient with a correlation equation [389]. This correlation equation estimates the binary diffusion coefficient with empirical constants (so-called atomic diffusion volumes) found from experimental data. However, since the original equation does not contain the metal component, we adjusted the equation constants by the previous observation from Siddiqi et al. (aluminium acetylacetonate in nitrogen) [228]. Figure A.5 displays that the residence time in the reaction zone is much smaller than the diffusion time scale except for wall temperatures higher than 1200 K. Therefore, we can assume that the surface reaction at the wall is rather small in the present temperature range used in our study, which is <1000 K.

A.2 Temperature-Dependent Gas Expansion Factor

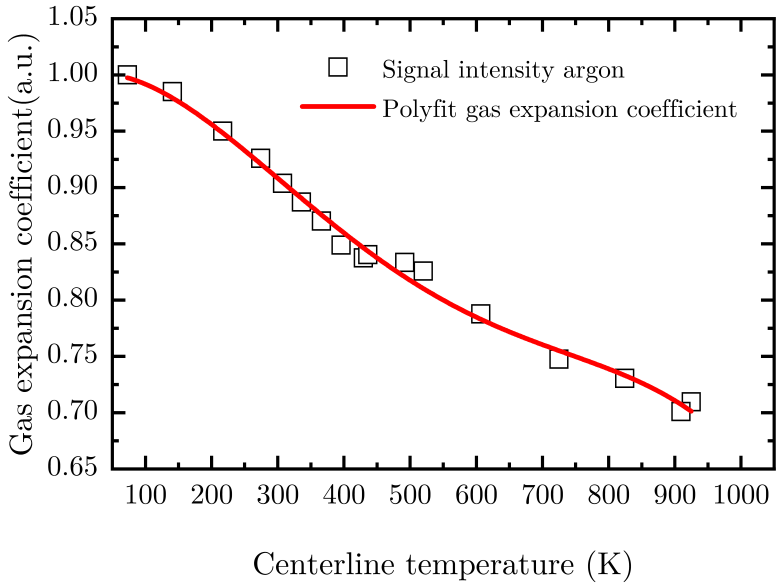

Figure A.6: Gas expansion factor as a function of calculated centerline temperature according to the numerical simulation.

A.3 Assignment of m/z 224, $Al(C_5H_7O_2)(C_5H_6O_2)$

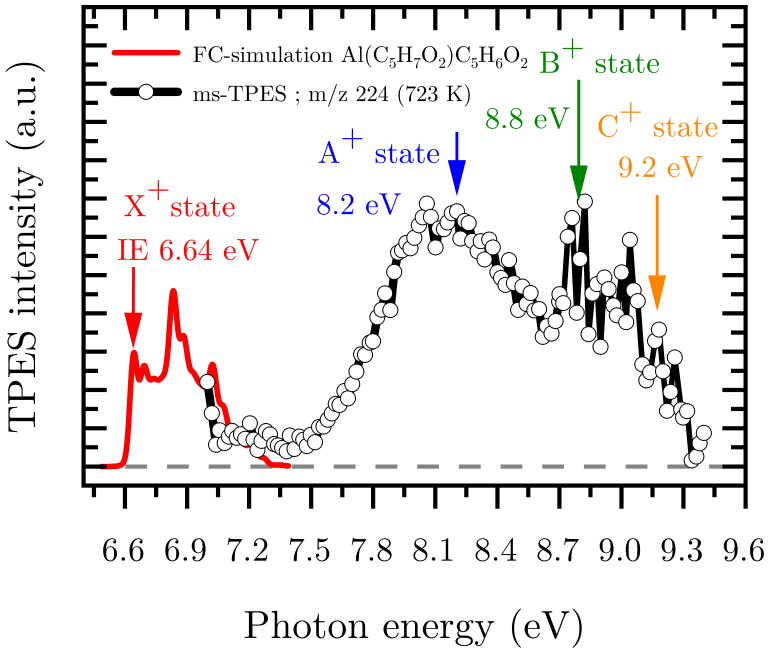

Figure A.7: Assignment of the ms-TPES at m/z 224 (dotted black curve) to $Al(C_5H_7O_2)(C_5H_6O_2)$, based on computed IEs from Franck-Condon simulations of $Al(C_5H_7O_2)(C_5H_6O_2)$ (red curve). Blue, green and yellow notations belong to calculated excited states of the molecule.

A.4 Species Assignments of Further Decomposition Products

At 9.82 eV, a clear peak in the ms-TPES of *m/z* 15 emerges, which corresponds to the published ionization potential of the methyl radical (IE = 9.84 eV [273]) (see Fig. A.8 (a)). The spectrum in Fig. A.8 (b) is consistent with the reported spectrum of acetylene (C_2H_2) [156] and the experimental data in (c) is in line with the spectrum obtained by others for the photoionization of formaldehyde (CH_2O) at IE = 8.71 eV [275]. Strong evidence of a mixture of vinyl alcohol [282] and acetaldehyde [283] was found at the *m/z* 44 channel by comparing the ms-TPE spectrum to reference spectra in Fig. A.8 (d).

Additional assignments have been made for C_4-C_5 hydrocarbons revealing that beneath the pyrolysis products vinylacetylene [284] is present (see Fig. A.9 (a)). The ms-TPE spectrum for the *m/z* 54 channel reveals the contribution of at least four isomers of C_4H_6, 1,3-butadiene (IE = 9.07 eV [285]), 1,2 butadiene (IE = 9.33 eV [155]), 2-butyne (IE = 9.59 eV [284]) and 1-butyne (IE = 10.18 eV [155]), which were assigned by their literature values and PES (see Fig. A.9 (b)). The cyclopentadienyl radical has been identified among the pyrolysis products with an ionization onset of 8.42 eV by a literature PIE curve [287]. At least three species reside on the *m/z* 66 channel, where strong evidence has been found for 1,3-cyclopentadiene [291] and 1,2,4-pentatriene [290] by a comparison to literature ms-TPES. Additionally, at 9.0 eV, evidence in the ms-TPES for 1-penten-3-yne [284] has been found.

As far as the C_5-C_{10} hydrocarbons as secondary decomposition products of the pyrolysis of $Al(C_5H_7O_2)_3$ are concerned, we found evidence for 2-pentanone *m/z* 86 ($C_5H_{10}O$) [155], phenol *m/z* 94 (C_6H_6O) [155], anisole *m/z* 108 (C_7H_6O) [294] and azulene *m/z* 128 ($C_{10}H_8$) [296] in the ms-TPE spectra (see Fig. A.10).

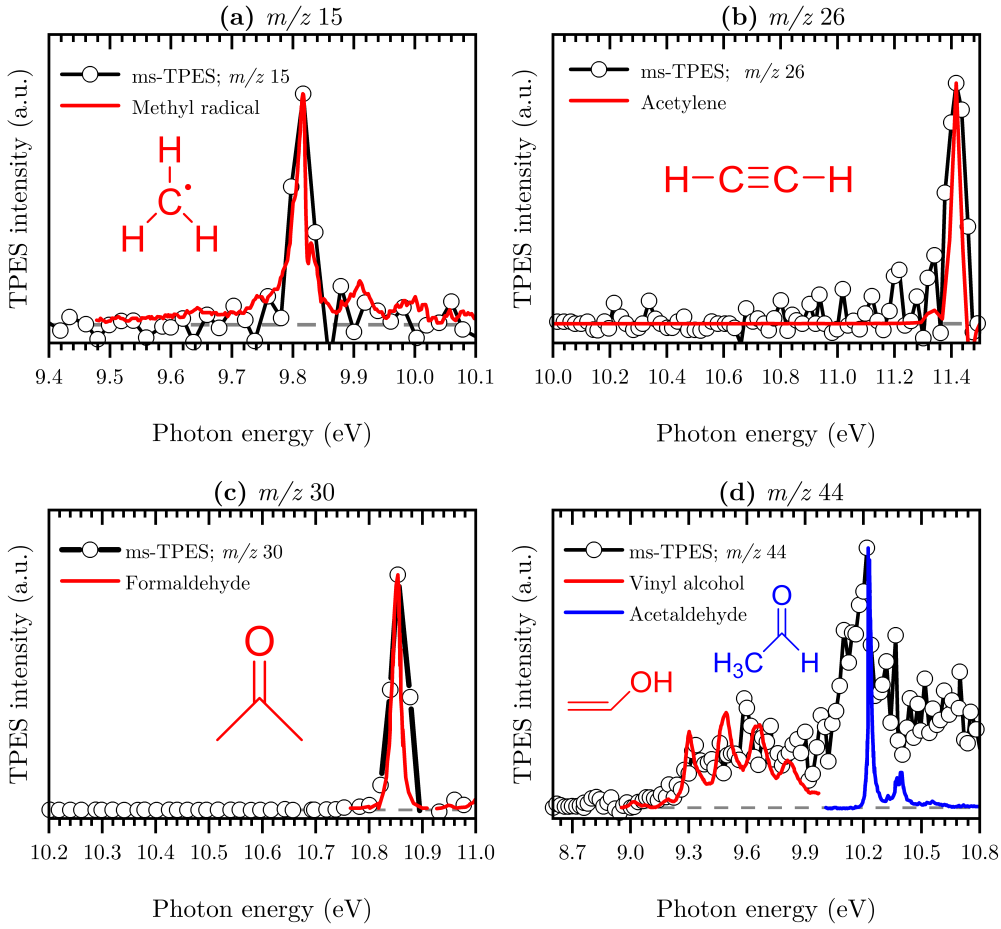

Figure A.8: Representative examples of product species identification and assignment for C_1-C_3 hydrocarbons and oxygenated species in the pyrolysis of $Al(C_5H_7O_2)_3$ using ms-TPE spectra (black lines, dot symbol); Literature reference spectra (red, blue) are as follows: (a) *m/z* 15 (CH_3) [273] (b) *m/z* 26 (C_2H_2) [156] (c) *m/z* 30 (CH_2O) [275] and (d) *m/z* 44 (C_2H_3OH) [282] and (C_2H_4O) [283].

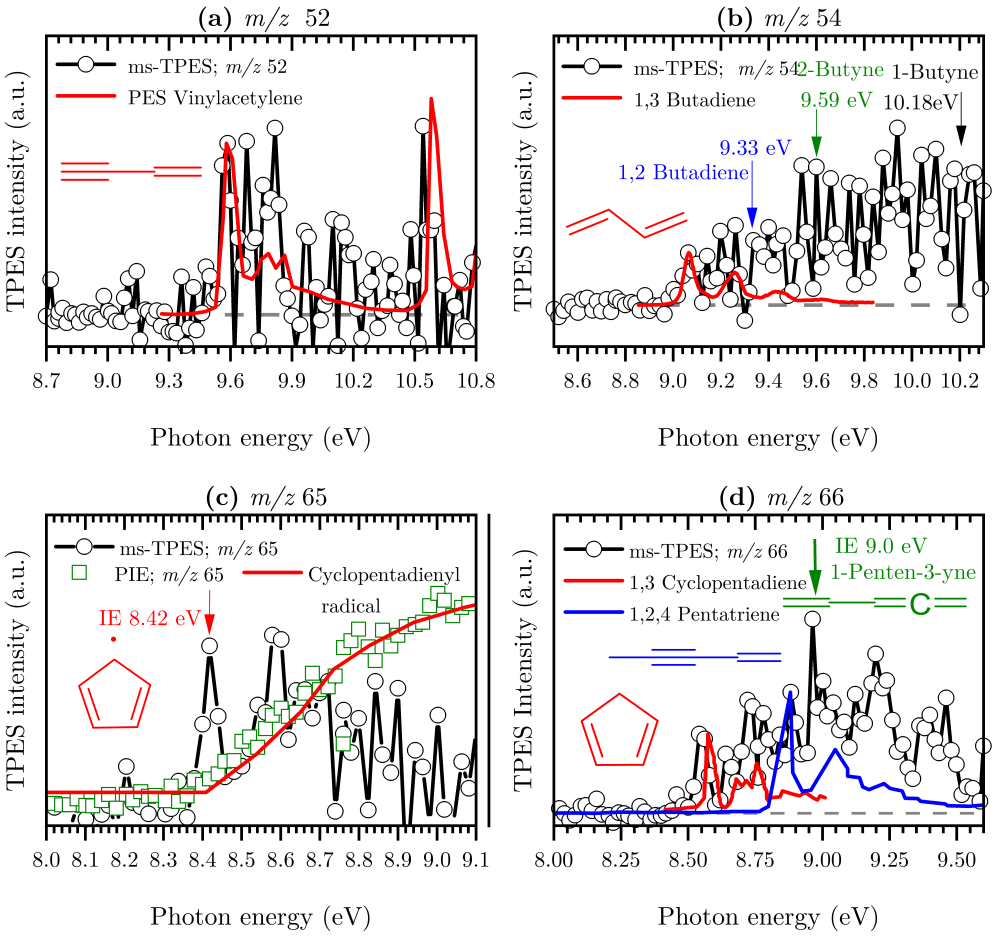

Figure A.9: Representative examples of product species identification and assignment for C_4-C_5 hydrocarbons and oxygenated species in the pyrolysis of $Al(C_5H_7O_2)_3$ using ms-TPE spectra (a-d) and PIE curves (c) (black lines, dot symbol); Literature reference spectra (red, blue) and cross sections (red) are as follows: (a) m/z 52 (C_4H_4) [284] (b) m/z 54 (C_4H_6) [155, 284, 285] (c) m/z 65 (C_5H_5) [287] and (d) m/z 66 (C_5H_6) [284, 290, 291].

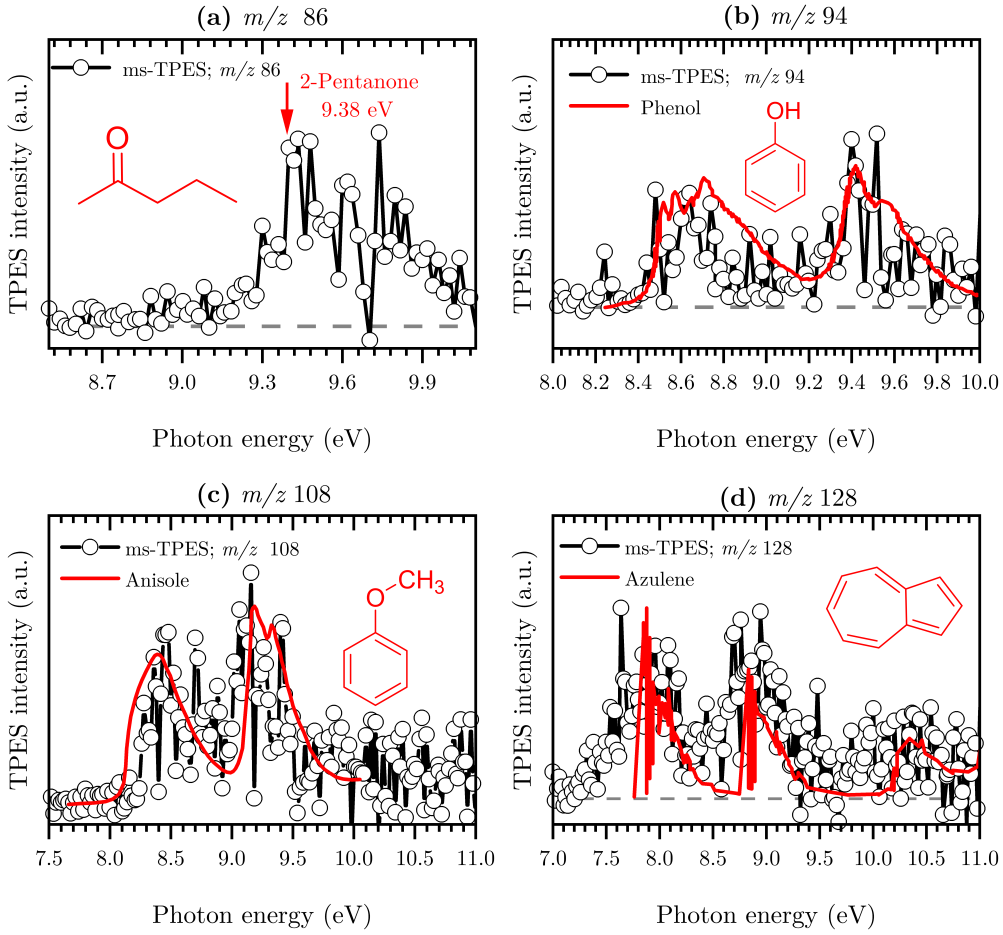

Figure A.10: Representative examples of product species identification and assignment for C_5-C_{10} hydrocarbons and oxygenated species in the pyrolysis of $Al(C_5H_7O_2)_3$ using ms-TPE spectra (black lines, dot symbol); Literature reference spectra (red) are as follows: (a) m/z 86 ($C_5H_{10}O$) [155] (b) m/z 94 (C_6H_6O) [155] (c) m/z 108 (C_7H_6O) [294] and (d) m/z 128 ($C_{10}H_8$) [296].

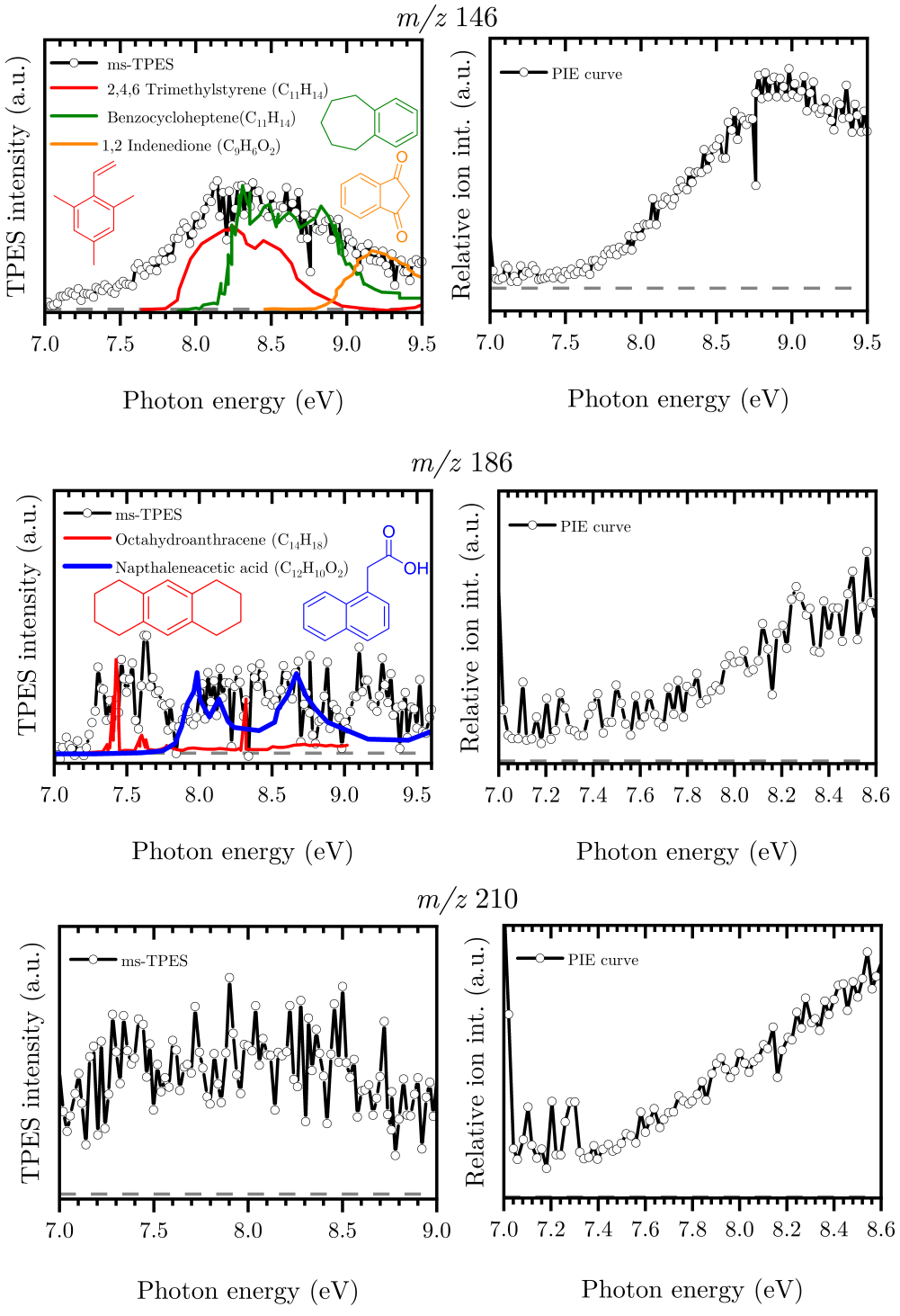

Figure A.11: Possible product species identification and assignment for m/z 146 and 186 formed by pyrolysis of $Al(C_5H_7O_2)_3$ with the aid of ms-TPES (black lines, dot symbol) as well as ms-TPES and their respective PIE curves for m/z 146, 186, and 210; Literature reference spectra (red, blue and orange) are as follows: (top) m/z 146 ($C_{11}H_{14}$); red [297]; green [298]) and ($C_9H_6O_2$; orange [299]); (middle) m/z 186 ($C_{14}H_{18}$) [300] and ($C_{12}H_{10}O_2$ [294]).

A.5 DPI of Important Pyrolysis Products

The shape of the ms-TPES in Fig. A.12 are in good agreement with the reference spectrum of acetylacetone ($C_5H_8O_2$) in its 97% enol (IE = 8.9 eV) [270] and 3% diketo (IE = 9.5 eV) [270] tautomers at 300 K. The signal does not follow the reference photoelectron spectrum at photon energies >10.0 eV, due to DPI, leading to the formation of the major fragments m/z 43, 58, 72 and 85 [270]. Because of keto-enol tautomerism, gaseous acetylacetone exists primarily in its enol form (first band 8.9 eV) at room temperature, whereas at higher temperatures, the equilibrium shifts to more gaseous diketo-acetylacetone (second band 10.2 eV) [270, 390]. The central band at 9.5 eV represents a superposition of both tautomer signals. Antonov et al. [270] stated that the m/z 43 peak is due to the DPI of diketone-acetylacetone. At temperatures higher than 600 K the equilibrium constant is around unity [270], representing similar concentrations of enol- and keto-acetylacetone in the gas phase. This leads to enhanced formation in pyrolysis conditions due to DPI of m/z 100.

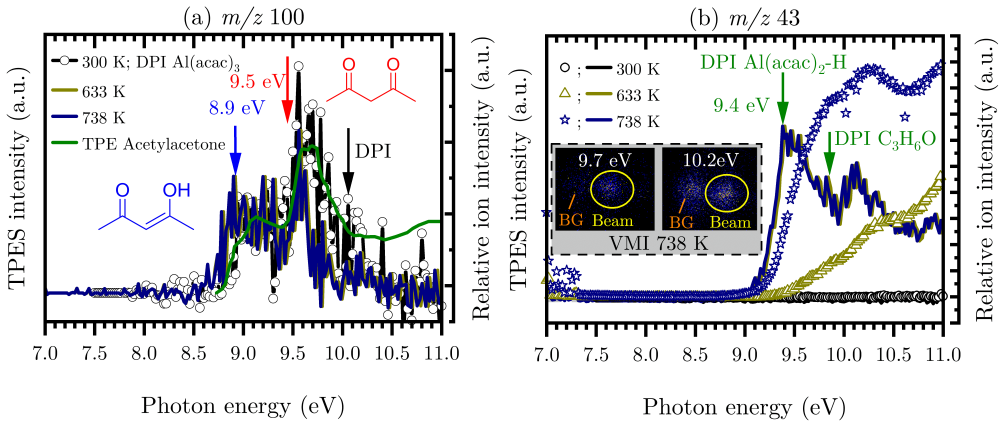

Figure A.12: Temperature dependent ms-TPE spectra for m/z 100 (left) and m/z 43 (right). Important dissociative ionization energies of possible fragments are denoted by green arrows and labeled with their respective parent molecule. The literature reference spectrum is taken from Antonov et al. [270].

A.6 Influence of Surface Reactions on the Formation of m/z 164

According to a review study by Igumenov et al. [88] significant amounts of m/z 164 ($C_{10}H_{12}O_2$) may also be formed by heterogeneous surface reactions. Since these reactions are controlled by the $Al(C_5H_7O_2)_3$ feed concentration, we carried out experiments with different evaporation temperatures. A significant difference in the decomposition behavior was observed supporting the idea that, at low temperatures, surface reactions are dominant in the pyrolysis tube (see Fig. A.13). The strong increase at 673 K implies that another gas-phase process is also responsible for the formation of m/z 164.

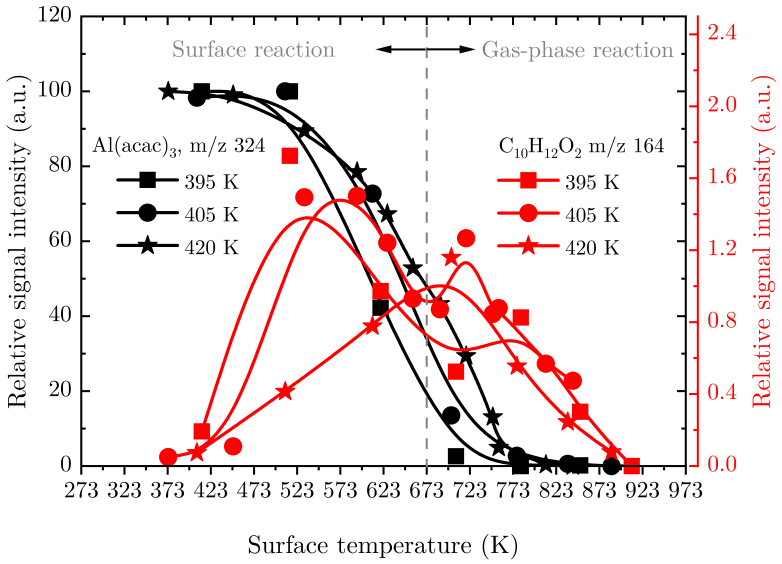

Figure A.13: Influence of the precursor inlet concentration by different evaporation temperatures of 395/405 and 420 K on the reaction mechanism, leading to the formation of $C_{10}H_{12}O_2$.

Appendix B

Supplementary Material Chapter 5

Reprint of the supplementary material of the $Zr(acac)_4$ paper [130] with permission from Springer Nature. This appendix contains minor modifications to adhere to the overall style of this thesis.

B.1 Numerical Modeling of the Microreactor

B.1.1 Governing Equations

The Reynolds averaged Navier-Stokes (RANS) equations contain mass and momentum conservation written as:

$$\frac{\partial \rho}{\partial t} + \frac{\partial (\rho \bar{u}_i)}{\partial x_i} = 0, \tag{B.1}$$

$$\frac{\partial (\rho \bar{u}_i)}{\partial t} + \frac{\partial (\rho \bar{u}_i \bar{u}_j)}{\partial x_j} = -\frac{\partial p}{\partial x_j} + \frac{\partial}{\partial x_j}\left[\mu\left(\frac{\partial u_i}{\partial x_j} + \frac{\partial u_j}{\partial x_i}\right) - \rho\overline{u_i^{'} u_j^{'}}\right], \tag{B.2}$$

where μ is the dynamic viscosity. The velocity was decomposed with a time-averaged component $\overline{u_i}$ and a fluctuating component $u_i^{'}$, as $u_i = \overline{u_i} + u_i^{'}$. In the present work, based on the observed flow characteristic in our previous study [129] (see Chap. 4 and Appendix A), the RANS equations combined with a slip (boundary) condition were used to investigate the flow in the microreactor under conditions relevant to interpret the experimental data.

For the slip boundary implementation in the simulation, a simple model for the slip fluid velocity at the wall was used, which can be expressed as:

$$v_{\text{slip}} = l_{\text{s}} \frac{\partial v}{\partial n}, \tag{B.3}$$

where l_{s} is the slip length and n denotes the normal vector to the wall. In the present work, the slip length l_{s} is calculated using the approach suggested by Morris et al. [388]:

$$l_s = \alpha \cdot L \cdot Kn. \tag{B.4}$$

The local Knudsen number Kn is defined with the Mach Number Ma and the Reynolds number Re as: $Kn = (\sqrt{\gamma\pi}Ma)/(\sqrt{2}Re)$ [391]. The model constant α in Eq. B.4 was suggested to be 1.15 [388] and the diameter of the microreactor was used as the characteristic length L.

B.1.2 Boundary Conditions

Table B.1: Boundary conditions for the CFD simulation of the microreactor. Roman numerals are in accordance with Fig. 5.9 in the main text.

Nr.	Boundary type	Pressure [mbar]	Temperature [K]	
I	Inlet	214	293	
II	No-slip wall	–	403	
III	Slip wall	–	Helium: 423	−903 (12 points)
		–	Argon: 423	, 671, 803
IV	Outlet	5×10^{-5}	–	

B.1.3 Local Residence Time and Temperature Distribution

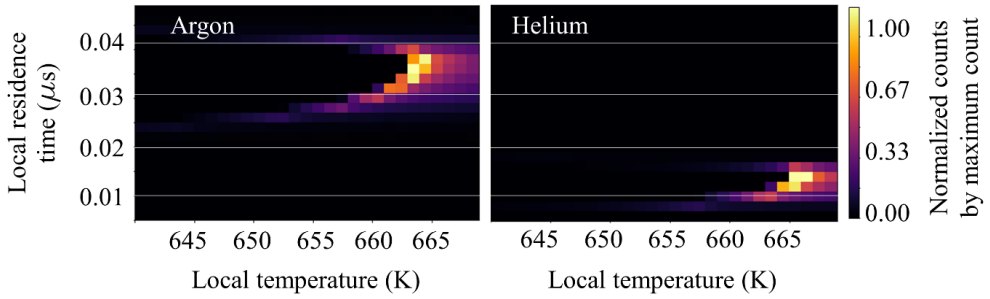

Figure B.1: Joint histogram between local residence time and temperature from each CFD cell from the simulation at a surface temperature of 671 K.

Figure B.1 shows a histogram of the combined local residence time and temperature in the heated area of the microreactor at a a surface temperature of 671 K. In the present study, an axisymmetric 2D simulation contains 50.000 equidistant cells (10 µm x 10 µm) within the heated area (x = 10 mm y = 0.5 mm). Therefore, the local residence time, which refers to how long the fluid stays in the specific computational cell, can be estimated easily from the cell width divided by the local axial velocity in the specific cell. As shown, the argon flow exhibits a longer residence time in the heated zone as compared to helium. Furthermore, we can

confirm that using helium as a dilution gas shows more plug-flow like conditions with respect to the temperature field is achieved. This is additionally shown in Fig. 5.1 of the main text.

B.1.4 Comparison of the Temperature Profiles Using Different Dilution Gases

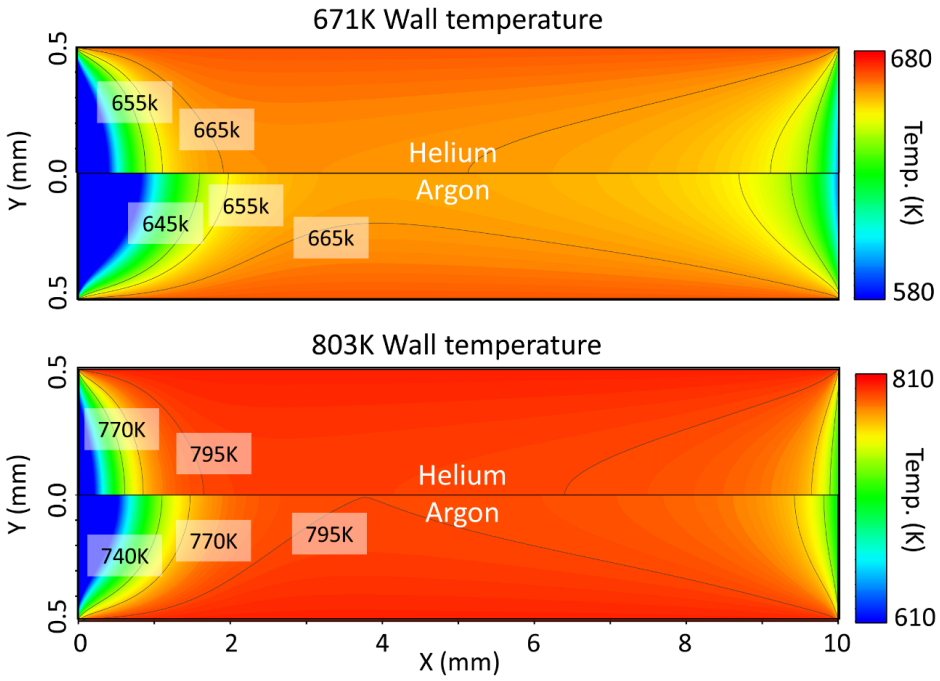

Figure B.2: Contour plots of the reactor temperature field obtained from CFD calculations in helium (top side) and argon (bottom side) at surface temperatures of 671 and 803 K. At these temperatures most of the intermediate species were observed upon pyrolysis of $Zr(acac)_4$.

In order to correctly interpret the temperature onset of the formation of the detected intermediate species and interpret the chemical pathways to their formation more precisely, we performed two different simulation sets with the same boundary conditions, but using helium and argon as dilution gas. Considering the flow field, the main difference between helium and argon can be explained by a higher heat conductivity of helium, which in turn is responsible for more efficient heat transfer in the reactor by conduction and convection and therefore leads to a more plug-flow like temperature profile in the microreactor. Additionally, we found that a lower inlet pressure (here ca. 214 mbar) leads to a more uniform temperature profile in comparison to the results obtained in our previous study (ca. 160 mbar), since the density of the gas is six times smaller [129]. This should lead to an increase in signal intensity as well as an accurate interpretation of the temperature-dependence of the collected experimental data with respect to chemical mechanisms and kinetics.

B.1.5 Flow Field in the Microreactor

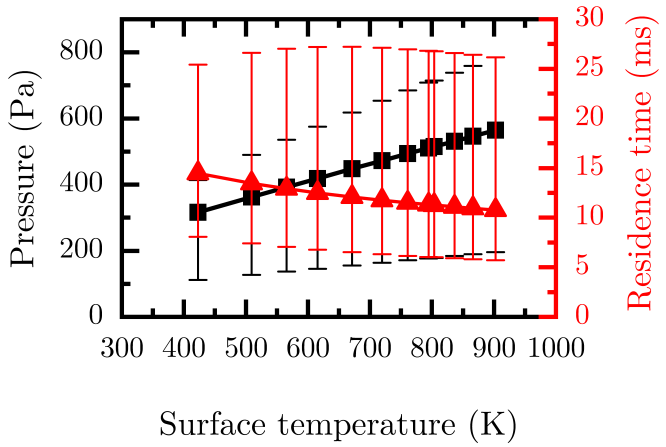

Figure B.3: Average pressure and residence time inside the heated area as a function of surface temperature using helium as dilution gas. The error bars indicate the maximum and minimum values along the axial centerline of the microreactor.

Figure B.3 shows the averaged pressure and residence time for the heated zone (10 mm length) from each simulation with surface temperatures ranging from 400 to 900 K, which correspond to the measured values in the experiment. Pressure and residence time profiles show an almost linear course upon a variation of the surface temperature. We report here average residence times of $\approx$ 10.5–14.5 µs in the case of helium used as dilution gas, which is in accordance with previous studies that hint on the beneficial properties of helium for the derivation of reaction kinetics in such small pyrolysis reactors [202, 203, 204].

B.2 Precursor Stability at Room Temperature

B.2.1 Dissociative Photoionization

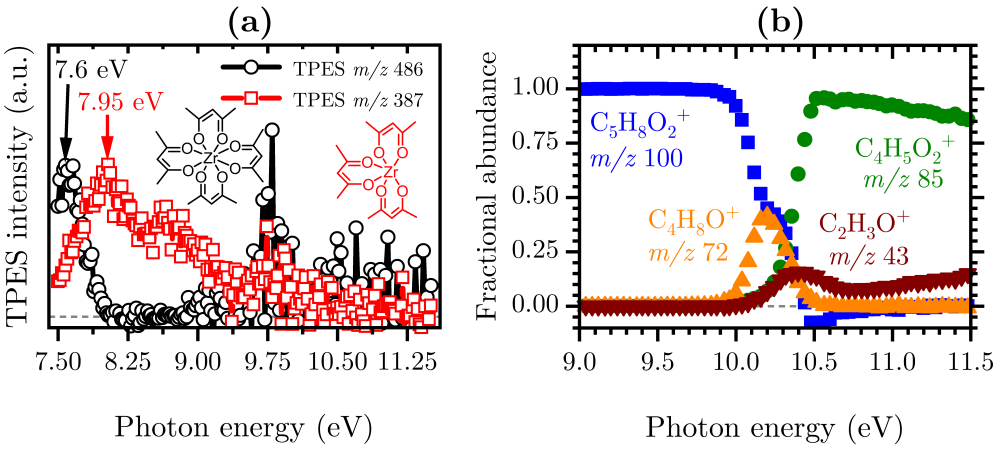

Figure B.4: (a) Mass-selected threshold photoelectron spectra (ms-TPES) recorded at room temperature in the 7.5–11.4 eV photon energy range. The main dissociative ionization product at m/z 387 is denoted in red whereas the parent molecule $Zr(C_5H_7O_2)_4$ is shown in black along with the vertical ionization energies; (b) Breakdown diagram of $C_5H_8O_2$ at 403 K shows the dissociative ionization of acetylacetone.

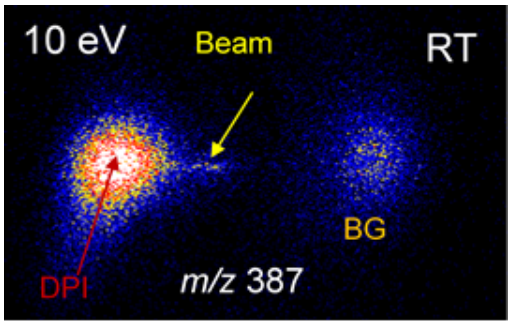

Figure B.5: Room temperature ion image of m/z 387 at an evaporator temperature of 403 K and a photon energy of 10 eV. A broad kinetic energy distribution hints that m/z 387 ($Zr(acac)_3^+$) is the main fragment formed by dissociative ionization of $Zr(acac)_4$.

B.2.2 Threshold Photoelectron Spectrum of *m/z* 60 Acetic Acid

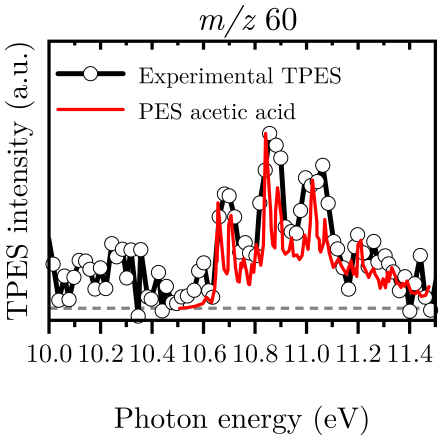

Figure B.6: Threshold photoelectron spectrum of *m/z* 60 at an evaporator temperature of 403 K (black symbols and line). The literature reference spectrum of $C_2H_3O_2$ (acetic acid) [325] is shown in red and is in good agreement with the bands observed here.

B.3 Species Assignment of Minor Decomposition Products

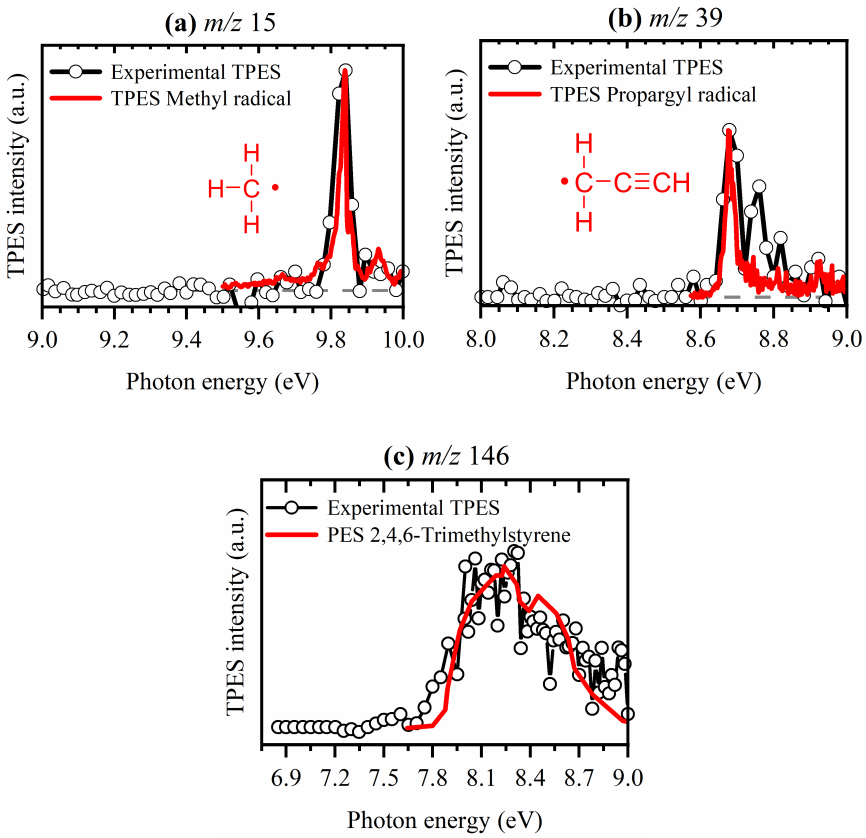

Figure B.7: Mass-selected threshold photoelectron spectra (ms-TPES) of minor decomposition products at a temperature of 803 K (a) and (b) and 776 K (c). Literature references in red are as follows: (a) m/z 15 methyl radical (CH_3) [273], (b) m/z 39 propargyl radical (C_3H_3) [277] and (c) m/z 146 2,4,6-trimethylstyrene ($C_{11}H_{14}$) [326].

B.4 Velocity Map Images of Some of the Detected Zr-Species

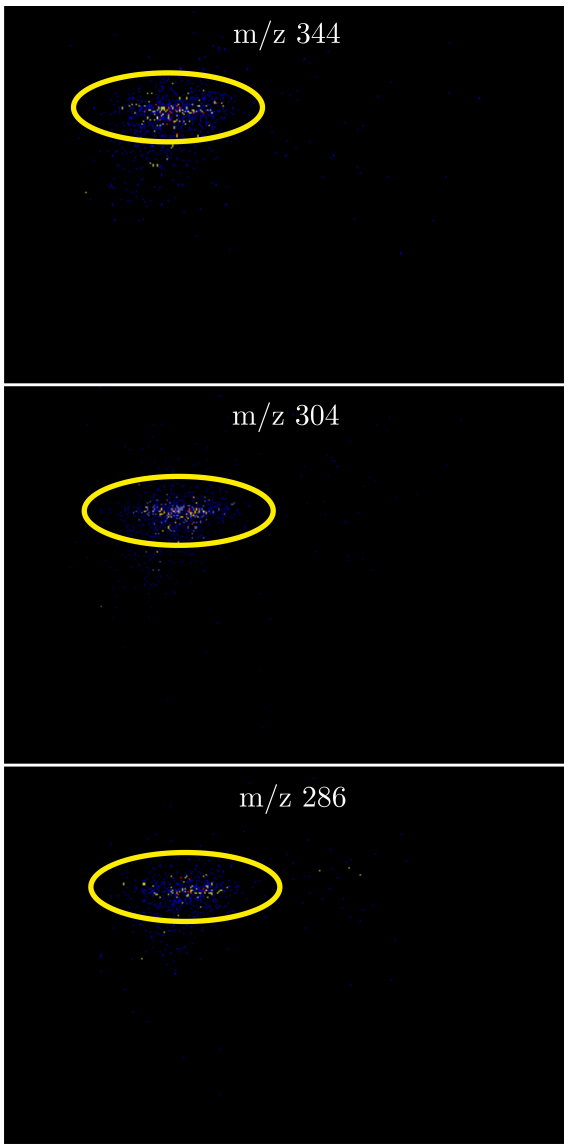

Figure B.8: Ion velocity map images of the most abundant Zr-species m/z 344, 304 and 286 at a temperature of 776 K, recorded at 8.5 eV.

Appendix C

Supplementary Material Chapter 6

Reprint of the supplementary material of the $Fe(Cp)_2$ paper [131] with permission from Wiley. This appendix contains minor modifications to adhere to the overall style of this thesis.

C.1 VMI Images of a Focused Molecular Beam

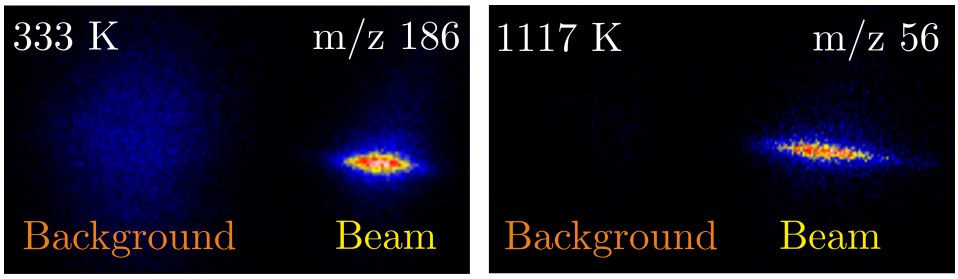

Figure C.1: Ion images of a molecular beam at a photon energy of 9.0 eV, recorded by velocity map imaging (VMI). The specific images of the mass channels are displayed which belong to the precursor ferrocene (m/z 186) (left) at 333 K and atomic iron (right), as a major decomposition product on m/z 56 at 1117 K. The narrow kinetic energy distribution, represented by a narrow beam component, can easily be identified which adds an additional analytical dimension. This enables us to unequivocally distinguish between dissociatively and directly ionized species.

C.2 Origin of the Impurity at m/z 80 Cyclopentadienone

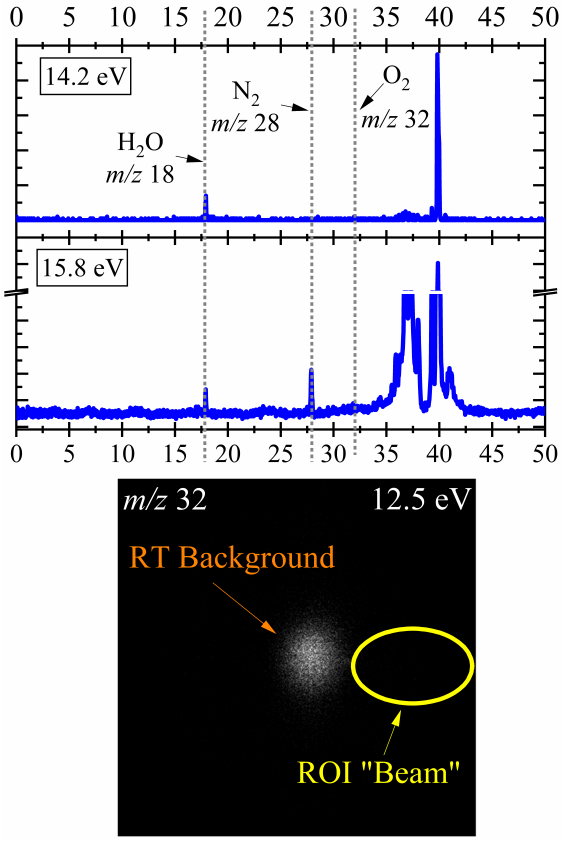

Figure C.2: Top: Exemplary mass spectra at 14.2 and 15.8 eV in order to identify possible signals of water (IE = 12.62 eV), nitrogen (IE = 15.58 eV) and oxygen (IE = 12.07 eV) [155]. Bottom: Velocity map images of ions from an exemplary measurement at a photon energy of 12.5 eV which only consider the mass channel m/z 32. The color orange denotes the room temperature background, thus no signal from the sample, yellow denotes the region of interest (ROI) for the molecular beam component. Since almost no ions are observable in the beam, we conclude that the contribution of oxygen impurity in the sample is at most very low.

Here we briefly discuss the origin of the signal at m/z 80 in our mass spectra at 11.5 eV in Fig. 6.2 of the main text. This peak is assigned to cyclopentadienone. Since we did not add oxygen as reactive gas in our experiments, this species is considered to be an impurity. Small amounts of 1-butene-3-yne may also stem from a decarbonylation of cyclopentadienone [220]. One source could be O-atoms attached to the walls of the reactor or the solid sample in the evaporator, another could be small traces of O_2 in the gas sample by small amounts of solvents (e.g. ethanol) that are used for cleaning the evaporator after each experiment. Nevertheless, we believe that our results are not affected by the oxygen contamination (see ion image in Fig. C.2) since the amount of oxygen in the gas sample is relatively low in

comparison to the signal intensity of ferrocene. In addition, the ionization cross section of cyclopentadienone at 10.5 eV is approximately three times larger than the one for the cyclopentadienyl radical [155]. As a result, the absolute concentration of m/z 80 is significantly smaller than the concentrations of the major pyrolysis products.

C.3 Minor Products of Ferrocene Pyrolysis at 1117 K

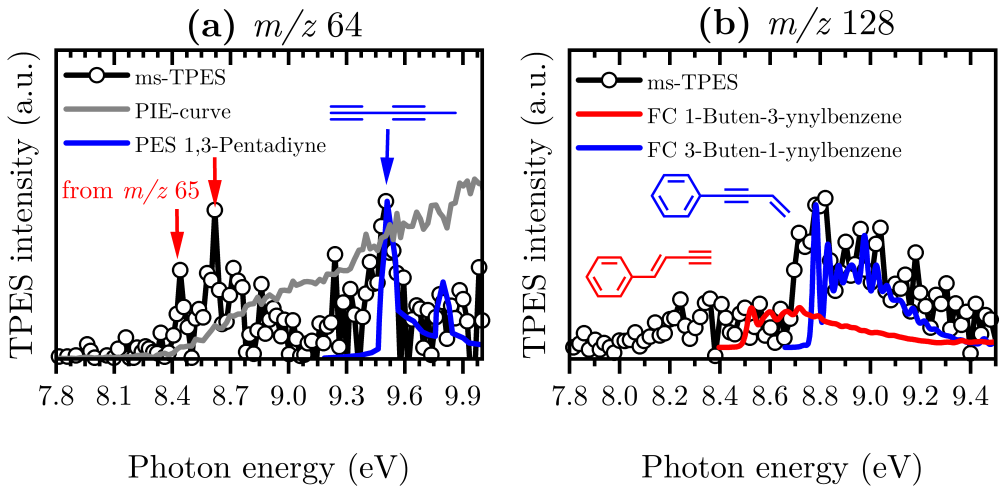

Figure C.3: Representative examples of species identification and assignment of the minor decomposition products using experimental obtained ms-TPES (black dots and lines) at 1117 K; species are either characterized by literature reference spectra, by specific ionization onsets in the gray PIE curve (a) or Frank-Condon simulations (FC) in (b). References are as follows: (a) m/z 64 red: contributions from m/z 65, blue: 1,3-pentadiyne [288], (b) m/z 128 red: 1-buten-3-ynylbenze [376], blue: 3-Buten-1-ynylbenzene [376].

The ms-TPES of m/z 64 is depicted in Fig. C.3 (a). Given the ionization energies of 8.42 and 8.67 eV for c-C_5H_4 [287], it is tempting to assign the signal to the cyclopentadienylide carbenes, however the peaks coincide with transitions of the cyclopentadienyl radical. Due to the large abundance of the cyclopentadienyl radical (C_5H_5, m/z 65), a small signal interference cannot be avoided which also results in an artificial signal contribution due to mass separation in the ms-TPES. However, we detected small contributions of the acyclic isomer 1,3 pentadiyne represented by 9.50 eV [288]. In addition, also larger hydrocarbons were identified in the spectra at m/z 128 shown in Fig. C.3 (b), however again in relatively small abundances. Here, the comparison with Frank-Condon simulations obtained from Pan et al. [376] revealed that 3-butene-1-ynylbenzene with an IE at 8.74 eV explains the majority of the ms-TPE signal in Fig. C.3 (b) whereas a small contribution of 1-butene-3-ynylbenzene (IE = 8.53 eV) is identified.

C.4 Threshold Photoelectron Spectrum of m/z 54 at 1079 K

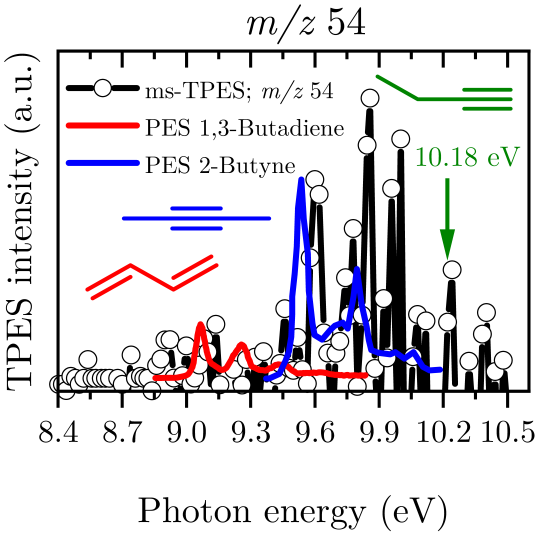

Figure C.4: Mass-selected threshold photoelectron spectrum (ms-TPES) of mass channel 54 along with the assignment to the following C_4H_6 isomers by literature references at 1079 K; red: 1,3-butadiene [284], blue: 2-butyne [285], green: 1-butyne [155].

C.5 Temperature-Dependent Gas Expansion Factor $\lambda(T)$

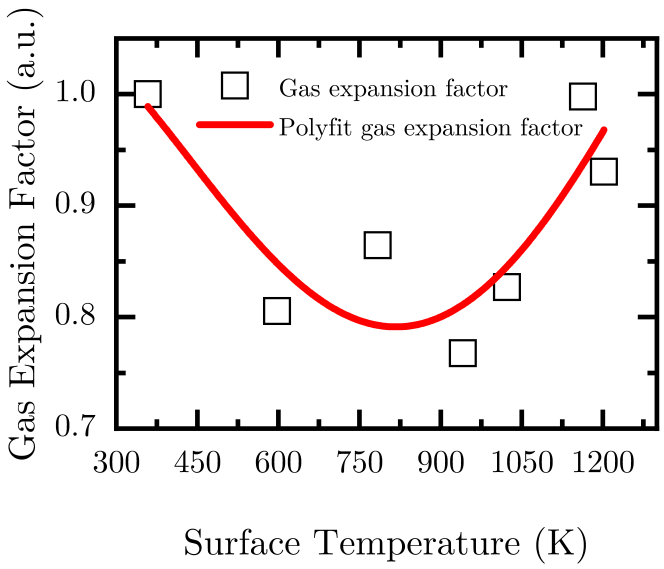

Figure C.5: Gas expansion factor as a function of surface temperature at the pyrolysis of $Fe(Cp)_2$.

DOI: 10.17185/duepublico/78661
URN: urn:nbn:de:hbz:465-20230705-173451-2